The formation of Hongge Fe-Ti-V oxide deposit hosted in layered intrusion, Emeishan Large Igneous Province, Southwest China

Von der Naturwissenschaftlichen Fakultät der

Gottfried Wilhelm Leibniz Universität Hannover

zur Erlangung des Grades

Doktor der Naturwissenschaften

(Dr. rer. nat.)

genehmigte Dissertation

von

Dachuan Wang, gongcheng shuoshi

(Master of Engineering)

(China University of Geosciences)

Referent: Prof. Dr. rer. nat François Holtz (Leibniz Universität Hannover)

Koreferent: Prof. Dr. Tong Hou (China University of Geosciences, Beijing)

Tag der Pomotion: 16.02.2023

Acknowledgements

As a foreign Ph.D. student in Germany, I received so much kind help and encouragement from different friendly people over the past five years. Before the end of this journey, I would like to say the most sincere thanks from my heart. So many kind people, and so many memorable moments, I will appreciate all of you forever. Studying in Germany and getting a doctorate here is one of my life's most beautiful periods.

First, I express the most profound appreciation to my venerable supervisor Prof. François Holtz, who provided me the chance to come to the institute and led me to experience the art of experimental petrology. He is always patient, open-minded, and prepared to help with all my coming questions, both in science and in my personal life. Without his guidance and unrestricted support, this project would have been impossible. Besides my advisor, I would like to thank my Chinese supervisor: Prof. Tong Hou, who designed this wonderful research project with Prof. François Holtz and Prof. Roman Botcharnikov and guided me over the past five years. He is always energetic and full of creativity. The thoughtful discussion and cooperation with him significantly promote the level of this research. I am grateful to Prof. Roman Botcharnikov and Prof. Stefan Weyer, who contribute their expertise in experimental studies and isotope geochemistry. Their critical inspirations and constructive recommendations help to clarify many essential scientific questions in this project. Prof. Harald Behrens and Prof. Jürgen Koepke were also thanked for their professional suggestions and assistance when I came to ask for help.

I want to show great appreciation for all my colleagues in the institute, especially in our Petrology Group. From the first day I arrived at the institute, sectaries Sabine Kropp and Kristin Kortlang gave their kind assistance on document preparation for my registration in the university and kept helping with the paper works in the past five years. Thanks for their kind help. Dr. Insa Cassens is thanked for her kind help and suggestions to adapt to life in Germany and room renting at the early stage. Many thanks to Dr. Renat Almeev, Dr. Dominik Mock, Dr. Marina Lazarov, and Dr. Ingo Horn, who gave professional instructions with microprobe, SEM, and laser analyses. Thanks to Julian Feige, Ulrich Kroll, and Adreas Reimer for their help with sample preparations and equipment maintenance. Special thanks to our IHPV group, Dr. Felix Marxer, Dr. Julie Michaud, Florian Pohl, Sarah Haselbach, and Stepan Krasheninnikov, who were greatly appreciated. Thanks to Philipp Beckmann, Phillip Wiegel, Antonia Simon, Christian Singer, Sven Merseburger, Dr. Filippo Ridolfi, and Dr. Diego González-García for their selfless help both in science and life. In addition, I would like to express my gratitude toward my most kind officemate-Artur Engelhardt, who gave me countless help in the past few years. We shared opinions both on science and different cultures, and his contributions broadened my study and life horizons.

Many thanks to our interesting “Chinese research group in Hannover”. Thanks to Dr. Chao Zhang, Dr. Xiaoyan Li, Dr. Lianxun Wang, Dr. Nuo Li, Dr. Qongmei Qi, Dr. Zhenhua Zhou, Dr. Lining Cheng, Xu Gao, Wang Liao, and Ronghao Pan to share the memorable memory in Hannover. With all your company and encouragement, life in Hannover never felt lonely. Last but not least, I want to thank my parents, who always supported, motivated, and encouraged me to keep going. For them, no matter how much gratitude is never over too much.

Thanks also go to Germany and Leibniz Universität Hannover. Without your kindness and open-minded attitude towards international students, I would not have had the chance to finish my study here. I wish Germany and our university to be better and better. Thanks to my motherland China and China Scholarship Council, who have given me financial support over the past few years. Your contribution deserves me to spend my lifetime to feedback. Finishing a Ph.D. study is not the final aim of life. It is just a small break and a new start for the further expeditions in the future. I will always memorize this colorful journey and stay brave in the future.

Abstract

The origin of Fe-Ti-V oxide ore layers, especially the monomineralic Fe-Ti-V oxide ores, in layered intrusions remains controversial. To reveal the Fe-Ti-V oxide mineralization processes, we had chosen the giant Hongge Fe-Ti-V oxide deposit in Emeishan Large Igneous Province, Southwest China, to carry out detailed mineralogical, petrological, geochemical and experimental research.

Detailed microprobe analyses on cumulus minerals (olivine, clinopyroxene, and plagioclase) from the Hongge drill core samples had shown that a broad normal fraction crystallization trend is largely absent in Hongge intrusion. Instead, from the bottom upwards, the anorthite content (An) of plagioclase and forsterite content (Fo) of olivine show frequent reversals, indicating open magma chamber processes with frequent replenishment of more primitive magmas during the solidification.

Crystallization experiments using a high-Ti basaltic composition were conducted under crustal conditions with various temperatures, pressure, oxygen fugacity, and water activity. As a result, the compositions of experimental minerals (olivine, clinopyroxene, and plagioclase) show good agreements with Hongge natural samples, convincing high suitability of high-Ti basalts as parental magmas. Moreover, according to the phase relationships obtained from the experiments, the crystallization conditions of Hongge layered intrusions can be determined at ~1150-1000 ℃, 200-300 MPa, QFM-1 to +1, and relatively high water activity.

Based on petrological observations and *in-situ* Fe isotope studies, we proposed a new magmatic-hydrothermal model to explain the formation of monomineralic ore layers. Textural evidence shows that hydrothermal dissolution and re-precipitation of Fe-Ti-V oxides were critical in forming high-grade massive ores. Furthermore, Rayleigh modeling on Fe isotopes indicates that ~20-30 % of Fe from Fe-Ti-V oxides in the lower Units was hydrothermally removed and subsequently re-precipitated into the major ore layers in the MZ, which is expected to significantly increase ore tonnages and grades, forming thick massive or even monomineralic ore layers.

Keywords: Hongge Fe-Ti-V oxides deposit, layered intrusion, monomineralic ore layers, open magma chamber processes, crystallization experiments, *in-situ* Fe isotope analyses, hydrothermal reworking

Kurzzusammenfassung

Der Ursprung von Fe-Ti-V-Oxiderzschichten, insbesondere der monomineralischen Fe-Ti-V-Oxiderze, in geschichteten Intrusionen bleibt jedoch umstritten. Um die Fe-Ti-V-Oxidmineralisierungsprozesse aufzudecken, haben wir die riesige Hongge-Fe-Ti-V-Oxidlagerstätte in der großen magmatischen Provinz Emeishan im Südwesten Chinas ausgewählt, um detaillierte mineralogische, petrologische, geochemische und experimentelle Untersuchungen durchzuführen.

Detaillierte Mikrosondenanalysen von Kumulusmineralien (Olivin, Klinopyroxen und Plagioklas) aus den Bohrkernproben von Hongge haben gezeigt, dass ein breiter normaler Kristallisationstrend in der Hongge-Intrusion weitgehend fehlt. Stattdessen zeigen der Anorthitgehalt (An) von Plagioklas und der Forsteritgehalt (Fo) von Olivin von unten nach oben häufig Umkehrungen, was auf offene Magmakammerprozesse mit häufigem Nachfüllen primitiverer Magmen während der Erstarrung hinweist.

Kristallisationsexperimente mit einer basaltischen Zusammensetzung mit hohem Ti-Gehalt wurden unter Krustenbedingungen bei verschiedenen Temperaturen, Drücken, Sauerstoffflüchtigkeit und Wasseraktivität durchgeführt. Als Ergebnis zeigen die Zusammensetzungen der experimentellen Minerale (Olivin, Klinopyroxen und Plagioklas) gute Übereinstimmungen mit natürlichen Hongge-Proben, was die gute Eignung von Hoch-Ti-Basalten als Ausgangsmagmen bestätigt. Darüber hinaus können gemäß den aus den Experimenten erhaltenen Phasenbeziehungen die Kristallisationsbedingungen der geschichteten Hongge-Intrusionen bei ~1150–1000 ℃, 200–300 MPa, QFM-1 bis +1 und relativ hoher Wasseraktivität bestimmt werden.

Basierend auf petrologischen Beobachtungen und In-situ-Fe-Isotopenstudien haben wir ein neues magmatisch-hydrothermales Modell vorgeschlagen, um die Bildung monomineralischer Erzschichten zu erklären. Texturelle Hinweise zeigen, dass die hydrothermale Lösung und erneute Ausfällung von Fe-Ti-V-Oxiden entscheidend für die Bildung hochgradiger Massiverze waren. Darüber hinaus zeigt

die Rayleigh-Modellierung von Fe-Isotopen, dass ca. 20–30 % des Fe aus Fe-Ti-V-Oxiden in den unteren Einheiten hydrothermal entfernt und anschließend wieder in die größeren Erzschichten in der MZ ausgefällt wurden, was voraussichtlich zu einer enormen Erhöhung von Erzmengen und –anreicherungen führt, die massive oder sogar monomineralische Erzschichten bilden.

Schlüsselwörter: Hongge Fe-Ti-V-Oxidlagerstätte, Schichtintrusion, monomineralische Erzschichten, offene Magmakammerprozesse, Kristallisationsexperimente, In-situ-Fe-Isotopenanalysen, hydrothermale Nachbearbeitung

Table of Contents

Chapter 1: Introduction

Iron (Fe), the fourth enriched element in the Earth's crust, is one of the earliest used metals in human history. In different cultures, records of the use of iron products can date back to 2000-3000 years ago. As human civilization has entered the industrial society, especially in the last 20 years, iron consumption has dramatically increased. In China, for example, the crude steel production has increased about sevenfold in the last decade (Fig. 1.1). Titanium (Ti) and vanadium (V), although initially identified by scientists in the late 18th and early 19th century, much later than Fe, due to their importance as alloying elements in the steel industry, are widely applied in many fields, especially in the aerospace and navigation industry.

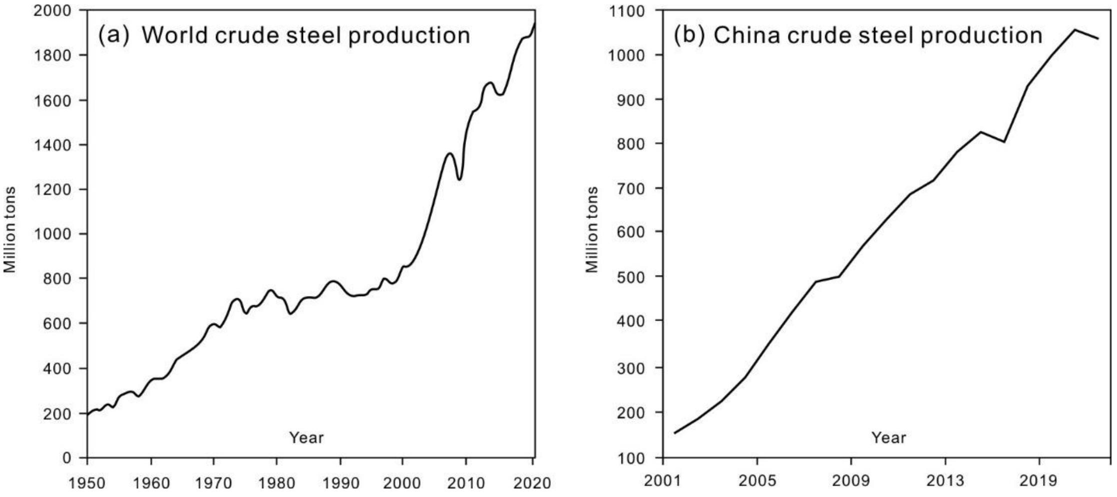

Fig. 1.1 (a) World crude steel productions from 1950 to 2020. The data source is from world steel organization. (b) The production of crude steel in China from 2001-2022. Data are from China steel organization.

As the demand for Fe, Ti, and V increases yearly, exploration of their high-grade deposits becomes essential for economic geologists and mining companies. According to previous studies (e.g., Zhang et al., 2014, 2015), the Fe resource can be mined from multiple types of Fe deposits, e.g., banded iron formation, magmatic Fe-Ti-V oxide deposit, skarn Fe deposit, etc (Fig. 1.2). Compared to the diverse Fe resources, the source of Ti is much limited, ~92% from ilmenite deposits and 8% from rutile deposits. Vanadium is a trace element in magma, and no independent V minerals are formed. Thus, the main sources for V are from Fe-Ti-V oxides which can contain economically valuable amounts of vanadium. Magmatic iron ore from layered intrusions is one of the major sources for Fe, Ti, and V metals used in industrial processes and other applications (e.g., Eales and Cawthron, 1996; Zhou et al., 2005). Thus, understanding the crystallization and Fe-Ti-V oxides mineralization process of these Fe-Ti-V oxide ore-bearing layered intrusions is not just of science but also of great economic interest.

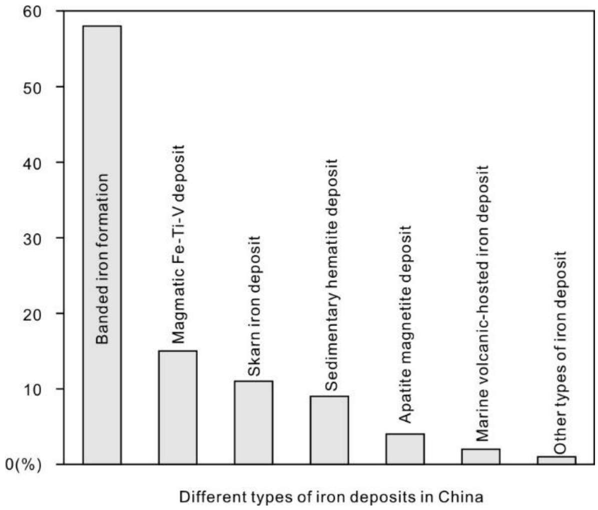

Fig. 1.2 The main Fe-deposit types in China

1.1 Layered intrusions

Layered intrusion, systematically clarified in the classical book “Layered Igneous Rocks”, describes the solidified magma chambers with compositional, mineralogical, and textural layering textures in vertical sections (Wager and Brown, 1968). They are generally box-shaped, funnel-shaped, or sheet-shaped and occur in the crust at various depths, from several hundred to thousand meters thick and several square kilometers to tens of thousands square kilometers (Table 1.1). The most common types of layering include modal layering, phase layering, and cryptic layering (Charlier et al., 2015). Many of the layered intrusions are temporally and spatially associated with large-scale basaltic magmatism in what is known as Large Igneous Provinces (LIPs), for example, Skaergaard intrusion with Columbia River flood basalts (e.g., Hunter and Sparks, 1987; Thy et al., 2009; Holness et al., 2017); Muskox intrusion with Coppermine River basalts (e.g., Baragar and Annells, 1969; Kerans, 1983), and Panxi intrusions with Emeishan flood basalts (e.g., Zhou et al., 2005; Zhang et al., 2006). In addition, some layered intrusions are also found in the post-orogenic extensional environment (e.g., Wilson et al., 1996) or greenstone belts (Maier et al., 2003). In the geological history, layered intrusions mainly occurred in Archaean and Proterozoic (Scoates and Wall, 2015), such as Stella layered intrusion at 3.03 Ga (Maier et al., 2003) and Stillwater layered intrusion at 2.7 Ga (DePalo and Wasserburg, 1979; Wall et al., 2010). During the Paleozoic, Mesozoic, and Cenozoic periods, there were also scatted distributed layered intrusions, for instance, Panxi intrusions (~ 260 Ma, Zhong et al., 2007), Rum intrusion (~60.5 Ma; Hamilton et al., 1998). Parental magmas of these layered intrusions are mainly tholeiitic or picritic basalts (e.g., Barnes and Hoatson, 1994; McBirney, 1996), but sometimes can also be andesite or diorite (Fischer, 2018). The most fundamental reason made layered intrusions unique from others is that layered intrusions host abundant substantial magmatic ore reserves such as Fe, Ti, V, Cr, Ni, Cu, and platinum-group elements (PGEs) (Naldrett et al., 1987; Barnes et al., 2004; Charlier et al., 2007; Yao and Mungall, 2022).

Due to the unique tectonic settings, typical rhythmic textures, and abundant hosted metal sources, layered intrusions immediately attracted the interest of geologists since the 1970s (e.g., Henderson and Suddaby, 1971; Parsons and Becker, 1987) and is still a hot topic today (e.g., Charlier et al., 2015; Boudreau, 2016, 2019). Furthermore, as the differentiation products of mafic-ultramafic magmas in the crust, layered intrusions detailed record the information of temperature (T), pressure (P), oxygen fugacity (fO_2), and other physical-chemical factors during the magma crystallization-differentiation processes (Naldrett, 1989; Barling et al., 2000; Zhong et al., 2007). In particular, the determination of the P, T, and fO_2 controlling their differentiation has been a major step in deciphering the diversity of liquid lines of descent. Thus, abundant geologists believe that layered intrusions are excellent natural laboratories for studying magma differentiations in broad P-T-fO_2 conditions (Wager et al., 1960; Hunter, 1996; Naslund and McBirney, 1996; Boudreau, 2016). Besides, to explain the different types of layering textures (e.g., striped texture, laminated texture, and rhythmic texture) in layered intrusions, the dynamic studies during magma differentiations have been developed rapidly. The main dynamic models include crystal setting (Wager and Brown, 1968), *in-situ* crystallization (Kruger and Latypov, 2022), convection (Kerr and Tait, 1985; Sparks et al., 1985), double-diffusive convection (McBirney and Noyes, 1979), etc. Our current knowledge about mantle magma evolution and deep-seated magma chamber processes is mainly based on the studies of layered intrusions (Marsh, 1989; Campbell, 1996).

1.2 Magmatic Fe-Ti-V oxide deposits

Fe-Ti-V oxide deposits are one of the crucial magmatic ore types and are widely observed in mafic-ultramafic layered intrusions, including Bushveld in South Africa (Eales and Cawthorn, 1996), Sept Iles in Canada (Namur et al., 2012), Bjerkreim-Sokndal in Norway (Wilson et al., 1996), etc. According to the USGS, about 92% of the Ti and almost all the V resources come from magmatic Fe-Ti-V oxide deposits. Fe-Ti-V oxide deposits in layered intrusions are mainly displayed in three different forms: 1) Fe-Ti-V oxide ore mineralization in the upper gabbro, norite, and diorite zones of large layered intrusions (e.g., the magnetite layers in the Upper Zone of Bushveld Complex, Fischer et al., 2016; Yuan et al., 2017); 2) Fe-Ti-V oxide ore layers existing in the bottom olivine clinopyroxenite, clinopyroxenite, and gabbro zones of layered intrusions (e.g., massive Fe-Ti-V oxide ore layers in Panzhihua intrusion, Pang et al., 2008a, 2008b); 3) Fe-Ti-V oxide ore layers hosted by anorthosite, norite, troctolite, and gabbro zones (e.g., Bjerkreim-Sokndal and Tellnes deposit in Norway, Lee, 1996; Charlier et al., 2006). According to the previous studies, the former two types of Fe-Ti-V oxide deposits are mainly related to mantle plume activities, and their parental magmas are tholeiitic ferrobasalts or picritic basalts

(Barnes and Hoatson, 1994; Mathison and Ahmat, 1996; Wilson et al., 1996) while the latter is genetically related to aluminum-rich tholeiitic basalts and formed in the post-orogenic extension environment (Wilmart et al., 1989; Charlier et al., 2010).

1.3 Models for Fe-Ti-V oxide ore layer formation

The origin of magmatic Fe-Ti-V oxide deposits in layered intrusions has been debated for decades, and multiple mechanisms have been proposed over the years due to increased numerical and experimental simulations. However, the most important models are summarized as follows:

(1) Fractional crystallization and crystal sorting as a function of mineral density, size and, magma viscosity might result in modally graded layers commonly observed in layered intrusions (Cawthorn et al., 2005; Bai et al., 2012). The sharp base and gradational upper contacts of the magnetite layers are often taken as evidence supporting gravity-driven crystal settling and sorting.

(2) Magma addition and mixing. Previous studies found that the residual magma mixed with more primitive replenishing magmas may drive the composition of the hybrid magma into the single spinel stability field and result in monomineralic layers (Naslund and McBirney, 1996; Howarth and Prevec, 2013a). Although this process lacks experimental support, this process may also apply to magnetite layers if the addition of new magma results in Fe-Ti oxide saturation.

(3) Formation of a dense Fe-rich immiscible liquid from a ferrobasaltic parental magma, which sinks towards the base of the intrusion (Namur et al., 2012; Fischer et al., 2016). Silicate liquid immiscibility was almost immediately applied to explain the formation of magnetite layers once proposed by Philpotts (1967). Through experimental works, a eutectic oxide: apatite ratio of 2:1 has been distinguished by different researchers (Reynolds, 1985; Von Gruenewaldt, 1993) as critical petrological evidence for the existence of immiscibility processes.

(4) Changes in fO_2 or pressure (Osborn, 1978; Klemm et al., 1985). Abundant experimental studies have already proved that high fO_2 can promote the crystallization

of Fe-Ti-V oxides (Toplis and Carrol, 1995; Botcharnikov et al., 2008). Based on V features of the magnetite grains in massive magnetite layers and disseminated magnetite layers in Bushveld Complex, Klemm et al. (1985) concluded that the massive magnetite layers must be crystallized under higher fO_2 conditions than the disseminated magnetite. The mechanism of pressure fluctuation was proposed by Osborn (1978), who found out that an increase in pressure results in an increase in the stability of spinel and pyroxene fields at the expense of plagioclase and olivine. In light of experimental works, Cameron (1978) concluded that chromite layers in the Bushveld Critical Zone crystallized due to a change in pressure. This process may also be applied to magnetite layers.

(5) *In-situ* bottom crystallization (Campbell, 1978; Cawthorn and McCarthy, 1980) and double-diffusive layering (Kruger and Smart, 1987; Tegner et al., 2006; Yao and Mungall, 2022). These two models have been invoked to account for strong vertical and horizontal Cr gradients of magnetite separates collected from several profiles through the massive magnetite layers. Cr is a highly compatible element in magnetite ($D_{\mathrm{Cr}}^{\mathrm{Mt/melt}}$=20-340, Dare et al., 2014). Thus, magnetite crystallization can quickly decrease the Cr content in the magma and lead to heterogeneous crystallization in either vertical or horizontal directions. Cawthorn and McCarthy (1980) have attributed observed Cr gradients and reversals in Cr content of the massive magnetite layers to this sort of diffusion-controlled bottom crystallization within an inhomogeneous magma.

Although abundant studies are conducted, no unique mechanism can account for all field, petrographic and geochemical features observed from the Fe-Ti-V oxide deposits. Thus, there is still plenty of research space to be filled regarding the petrogenesis and metallogenesis of Fe-Ti-V oxide ore-bearing layered intrusions. This information is bound to be useful for future exploration of magmatic Fe-Ti-V oxide ore deposits.

Table 1.1 Major layered intrusions worldwide and their related ore deposits

Name	Location	Age	Size	Tectonic Setting	Related deposit
Bushveld Complex	South Africa	2.06 Ga	65,000 km^2, 7-9 km thick	Mantle-plume related	Cr-PGE-Fe-Ti-V deposit
Stillwater Complex	The United States	2.7 Ga	47 km long, 8 km wide, 6 km thick	Mantle-plume related	PGE-Cu-Ni-Cr deposit
Sept Iles	Canada	564 Ma	5000 km2, 80 km long, 7 km thick	Intracontinental Rift	Fe-Ti-P deposit
Great Dyke intrusion	Zimbabwe	2.46 Ga	550 km long, 4-11 km wide, 1.9-3.3 km wide	Mantle-plume related	Cr-PGE-Cu-Ni deposit
Skaergaard intrusion	East Greenland	55 Ma	11 km long, 7 km wide, 3.5 km thick	Large Igneous Province	PGE-Au deposit
Duluth Complex	The United States	1.1 Ga	5,000 km^2, 3-5 km thick	Intracontinental Rift	Cu-Ni-PGE deposit
Muskox intrusion	Canada	1.27 Ga	125 km long, 11 km wide, 1.8 km thick	Large Igneous Province	Ni-Cu-PGE deposit
Bjerkreim-Sokndal intrusion	Norway	930 Ma	40 km long, 15 km wide, 1.8 km thick	Post-orogenic extension	Fe-Ti deposit
Fongen-Hyllingen intrusion	Norway	426 Ma	160 km^2, 40 km long, 6 km wide	Post-orogenic extension	–
Tellnes intrusion	Norway	930 Ma	2.7 km long, 400 m thick	Post-orogenic extension	Fe-Ti deposit
Munni Munni Complex	Australia	2.93 Ga	25 km long, 9 km wide, 5.5 km thick	Intracontinental Rift	PGE-Cu-Ni deposit
Penikat Complex	Finland	2.44 Ga	23 km long, 1.5-3.5 wide, 2-3 km thick	Intracontinental Rift	Cu-Ni-PGE deposit
Portimo Complex	Finland	2.43 Ga	20 km long, 15 km wide, 1.2 km thick	Intracontinental Rift	Cu-Fe-Ni-PGE deposit
Federov Pansky intrusion	Russia	2.5 Ga	250 km^2, 4 km thick	Intracontinental Rift	Cu-Ni-PGE deposit
Rum Complex	The United Kingdom	60 Ma	10 km long, 10 km wide, 800 m thick	Large Igneous Province	–

Panzhihua intrusion	China	260 Ma	19 km long, 2 km wide, 2.5 km thick	Large Igneous Province	Fe-Ti-V deposit
Baima intrusion	China	260 Ma	24 km long, 2-6.5 wide	Large Igneous Province	Fe-Ti-V deposit
Taihe intrusion	China	260 Ma	3.7 km long, 3.5 km wide, 1.2 km thick	Large Igneous Province	Fe-Ti-V deposit
Hongge intrusion	China	260 Ma	15 km long, 6 km wide, 1.7 km thick	Large Igneous Province	Fe-Ti-V deposit
Xinjie intrusion	China	260 Ma	7 km long, 1.5 km wide, 1.2 km thick	Large Igneous Province	Fe-Ti-V deposit

(modified after Zhong et al. 2007 and Namur et al. 2010)

1.4 Role of hydrothermal reworking on Fe-Ti-V oxide deposits and aims of this study

Hydrothermal reworking textures are commonly observed in layered intrusions and were traditionally considered as late-stage hydrothermal alterations (e.g., Luan et al., 2014a, 2014b; Xing and Wang, 2017). However, based on recent studies on the hydrothermal enrichment of Ni-Cu, Cr, and PGE in layered intrusions (Boudreau, 2019 and reference therein), contributions from hydrothermal reworking to the Fe-Ti-V oxide mineralization in layered intrusions could be highly underestimated. Thus, systematic studies on the influence of hydrothermal reworking for the Fe-Ti-V oxide ore-bearing layered intrusions provide us with a new approach to understanding the formation of thick massive ore layers, especially monomineralic ore layers. With these questions, we selected Hongge layered intrusion from the Panxi region, which hosts the largest Fe-Ti-V oxide deposit in China, as our example to explore the crystallization and Fe-Ti-V oxide mineralization conditions, expecting to provide new understandings of the extraordinary Fe-Ti-V oxides enrichment processes. The three main objects and work plans are addressed as follows:

(1) In Chapter 2, a detailed mineralogical and petrological study of Hongge layered intrusion was carried out to constrain the dynamic processes of Hongge intrusion. This part of study is mainly based on the samples from a drill core that covers the wall rocks and all the lithological units. A total of 110 samples were prepared for rock powders and determined major elements and several trace element compositions with X-ray fluorescence. The cumulus minerals in 170 samples from the drill core (including olivine, clinopyroxene, and plagioclase) were analyzed with microprobe. Finally, the chemical compositions from bulk rock and cumulus minerals were applied to determine the magma chamber processes.

(2) In Chapter 3, a series of experimental studies using a high-Ti basaltic composition from Emeishan Large Igneous Province (ELIP) were conducted under variable temperature (T), pressure (P), oxygen fugacity (fO_2), and water activity

(aH_2O) conditions. The experiments were conducted with internally heated pressure vessels (IHPV), and experimental products were analyzed with microprobe. Experimental results were furtherly applied to determine phase equilibria under different T-P-fO_2-aH_2O conditions and to compare with natural samples. According to this part of study, we can understand the crystallization and mineralization conditions of Hongge layered intrusion, and obtain information about the high-Ti differentiation processes under crust conditions.

(3) In Chapter 4, systematic *in-situ* Fe isotope studies on magnetite and ilmenite were applied to explore the contributions of hydrothermal reworking in the formation of massive monomineralic Fe-Ti-V oxide ores. Fe isotopes have already been confirmed as an efficient tool to trace the ore formation processes in abundant previous studies (e.g., Angerer et al., 2013; Knipping et al., 2015; Troll et al., 2019) and during magmatic and hydrothermal processes, the fractionations of Fe isotopes among different minerals show distinct characteristics. Therefore, based on the newly obtained high-precision *in-situ* Fe isotope data, we quantitatively estimated the hydrothermal contributions in the formation of thick massive ore layers and came up with a new ore formation model for the Fe-Ti-V oxide deposits in layered intrusion.

Chapter 2: New constraints on the open magma chamber processes in the formation of giant Hongge Fe-Ti-V oxide deposit

Dachuan Wang[1], Tong Hou[2], Meng Wang[2], François Holtz[1]

[1] Institut für Mineralogie, Leibniz Universität Hannover, Callinstr. 3, 30167 Hannover, Germany

[2] State Key Laboratory of Geological Process and Mineral Resources, China University of Geosciences, Beijing 100083, China

(Published by Lithos, 2020, 374, 105704)

DOI: 10.1016/j.lithos.2020.105704

Abstract

The Hongge layered intrusion in Emeishan Large Igneous Province (ELIP), SW China, contains the largest Fe-Ti-V oxide deposit in China (4500Mt ore reserve). The mechanism by which million tons of Fe-Ti-V oxide concentrated is debated. In this study, new petrography, mineral chemistry (~3600 microprobe analyses for olivine, clinopyroxene and plagioclase) and bulk rock major element chemistry (108 samples) are presented from samples collected over a 940 m drill core (ZK11003) in the southern part of the Hongge layered intrusion. In contrast to the Bushveld and Skaergaard layered intrusions, a broad normal fractionation trend upwards recorded by cumulus clinopyroxene and plagioclase is absent, whereas frequent reversals to more primitive compositions are observed in the Hongge intrusion. According to the mineral reversals, we divided the entire intrusion into eleven stratigraphic units. Notably, in the Middle Zone (MZ) and Lower Zone (LZ), the appearance of Fe-Ti-V oxide ore layers are closely related to these reversals. These distinct units are regarded as indicators for major replenishments of primitive high-Ti ferrobasaltic/picritic magmas. In these samples, various clinopyroxene populations with both low and high Mg# are also observed and phases with high Mg# are interpreted to be inherited from the replenishing magmas.

Previous studies have proposed that the replenishing magma might be anhydrous. However, the presence of a considerable amount of hydrous cumulus minerals including phlogopite and hornblende indicates that there is a high water content in melts at some stages of the formation of the Hongge layered intrusion, especially in the LZ and MZ. Contamination of crustal materials (e.g., introduction of aqueous fluids) or replenishing magmas with different water contents could lead to high water activities in the shallow crystallizing magma chamber. As a consequence, mixing of hydrous residual melts with replenishing magmas would trigger large scale precipitation of Fe-Ti-V oxide ores. Relatively high water activity, which could suppress the crystallization of cumulus plagioclase, would also explain the absence of this phase in the LZ and MZ. Thus, based on all these observations, we propose that the Hongge layered intrusion was formed by multiple emplacements of crystal-laden magmas that carried olivine and clinopyroxene already crystallized in deep-seated chambers.

Keywords: Hongge; layered intrusion; magma replenishment; Fe-Ti-V oxide ore; crystal-laden magma.

2.1 Introduction

Magmatic iron ore hosted by mafic-ultramafic layered intrusions is one of the most important sources for Fe, Ti and V metals used in industrial processes and other applications. Such layered intrusions are commonly large, sill-like bodies that exhibit compositional, mineralogical and textural layering indicating the role of magma differentiation processes (e.g., Cawthorn, 1996). Specifically, the Fe-Ti-V oxide ore-bearing layered intrusions are widespread and include Bushveld Complex in South Africa (e.g., Eales and Cawthorn, 1996), Duluth and Stillwater in America (e.g., Parks and Hill, 1986; Miller and Ripley, 1996), Bjerkreim-Sokndal in Norway (e.g., Wilson et al., 1996), and Panxi region in China (e.g., Zhou et al., 2005). The Panxi region, between the cities of Panzhihua and Xi Chang, of southern Sichuan province, is an important area within the Emeishan Large Igneous Province (ELIP) because plutonic and hypabyssal rocks host several world-class orthomagmatic Fe-Ti-V oxide deposits which were collectively called Panxi deposits (c.f., Shellnutt et al., 2011a, 2011b). In spite of extensive research, the origin of thick Fe-Ti-V oxide-rich layers, especially the monomineralic magnetite layers, in layered intrusions is still unclear and intensively debated.

In the case of the Panxi deposits, there is a general consensus that the parental magma of the mafic layered intrusions is high-Ti ferrobasaltic in composition which had been derived from more primitive (ferro-) picritic magmas (Zhou et al., 2013). However, the origin of the Fe-Ti-V oxide-rich layers has been intensively debated and is virtually unknown (Pang et al., 2010). Specifically, at least three main models have been proposed so far for the formation of the Fe-Ti-V oxide ore layers in these Panxi deposits: 1) Formation of a dense Fe-rich immiscible liquid from a ferrobasaltic parental magma, which sinks towards the base of the intrusion because of gravity settling (e.g., Zhou et al., 2005); 2) Early crystallization and accumulation of Fe-Ti-V oxides, either due to high water content (1.5 wt.% H_2O) in the parental magma (Pang et al., 2008a, 2008b) or due to an increase in magma fO_2 related to CO_2-degassing of the footwall carbonates (Ganino et al., 2008); and 3) Magnetite accumulation due to intrusion of H_2O-rich and Ti-magnetite crystal-rich magmas into a dry crystallizing gabbroic magma chamber in the magmatic plumbing system (e.g., Howarth and Prevec, 2013a).

The Panxi layered mafic intrusions in Emeishan Large Igneous Province (ELIP), Southwestern China host large Fe-Ti-V deposits in the form of massive Fe-Ti-V oxide ore layers at the base or in the lower part of the intrusions, which have been mined continuously for the last three decades and are still being mined (Fig. 2.1). The Panxi oxide ores represent world-class resources of Fe, Ti and V with total reserves of ~7209 Mt Fe, ~559 Mt TiO_2 and ~17.4 Mt V_2O_5 (e.g., Ma et al., 2003; Zhou et al., 2005; Pang et al., 2009; Song et al., 2013). The Panxi intrusions became only recently the subject of detailed studies (e.g., Zhou et al., 2005; Ganino et al., 2008; Pang et al., 2009; Zhang et al., 2012; Song et al., 2013; Shellnutt, 2014). Very good exposures as well as drill cores in mined areas and the unusually thick monomineralic Fe-Ti-V oxide layers present within the intrusions provide an excellent material case for geological research.

Among the Panxi deposits, the Hongge Fe-Ti-V oxide deposit is the largest one in the Panxi district (Fig. 2.1). New drill cores covering the whole sequence of the layered intrusion are available, thus providing a good opportunity to carry out new systematic investigations and sampling for petrological and geochemical studies and to constrain the petrogenesis and metallogenesis of the deposit. Accordingly, in this paper, we present a representative characterization of one drill core, based on microscopy, mineral chemistry, major and trace element bulk geochemistry. A total of 172 samples were analyzed and were used to constrain the petrogenesis of the layered mafic rocks and the mechanism of Fe-Ti-V oxide ore formation and its relationship with the host intrusion.

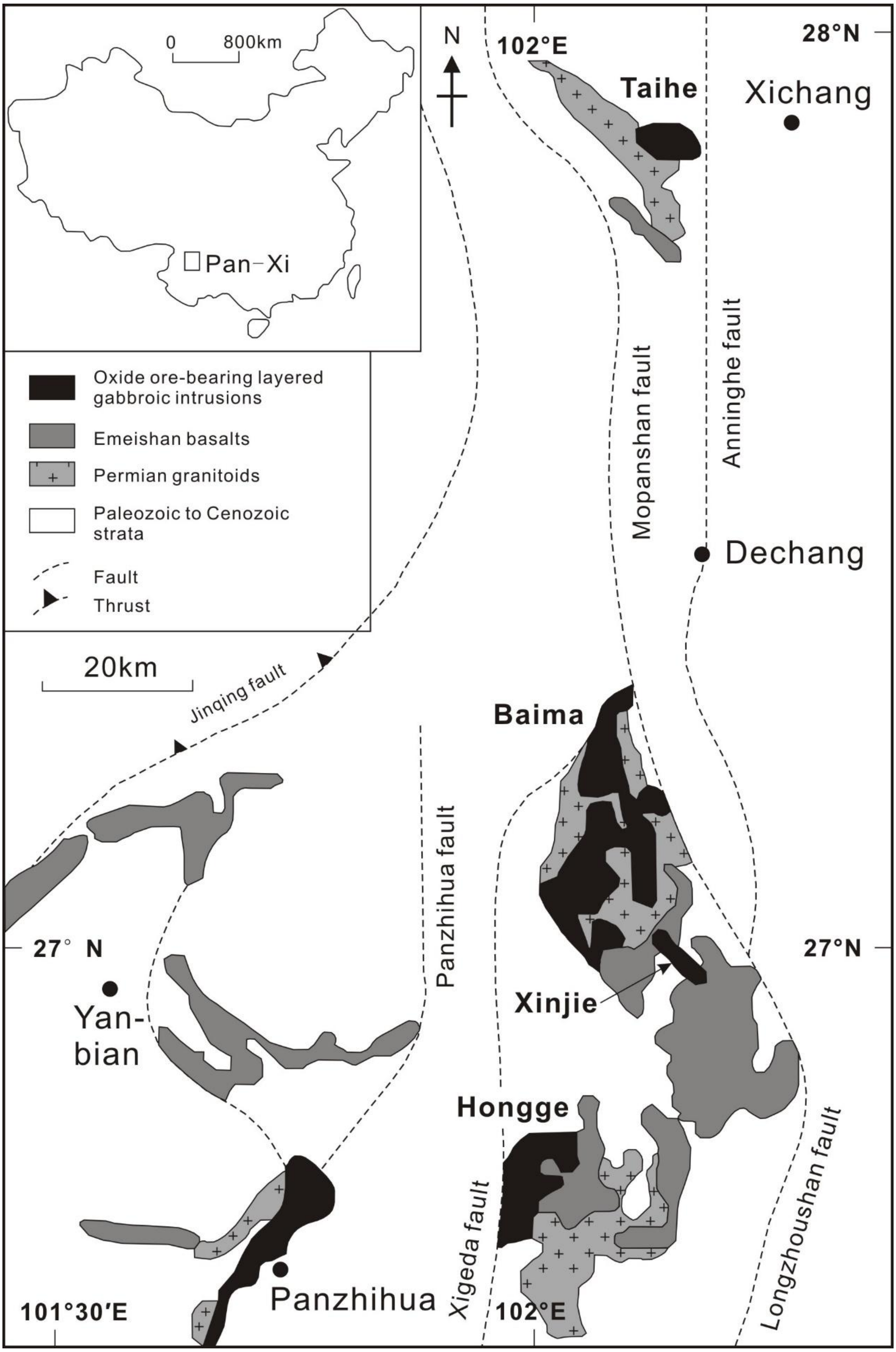

Fig. 2.1. Geological map of the Panxi region, showing the distribution of Fe-Ti-V oxide deposits and related Emeishan basalts (modified from Liu et al., 1985).

2.2 Geological setting

2.2.1 Regional geology

The ELIP covers a large portion of the western Yangtze block, with an extension to Northern Vietnam and covers an area of more than 5×10^5 km^2 (e.g., Chung and Jahn, 1995; Song et al., 2001; Xu et al., 2001; Zhou et al., 2002a; Xiao et al., 2004a, 2004b). Proterozoic rocks composed the basement of the Yangtze block, mainly including 1) the Huili Group or its equivalents, the Yanbian or Kunyang Groups formed in Paleo- to Mesoproterozoic period, which are mainly low-grade metasedimentary rocks interbedded with felsic and mafic metavolcanic rocks, and 2) the Neoproterozoic Kangding Complex, mainly composed of granitic and metamorphic rocks (Panxi Geological Party, 1984). The ELIP consists primarily of the Emeishan flood basalts, mafic-ultramafic layered intrusions as well as minor silicic igneous rocks. The origins of the silicic rocks are varied and are derived by: 1) partial melting of crust, 2) differentiation of mafic magmas similar in composition to the Emeishan basalt, and 3) by mingling between crustal and mantle melts (Shellnutt et al., 2011a). The thickness of the Emeishan basalts varies greatly across the ELIP and can range from several hundred meters to a maximum of ~5 km (e.g., Chung and Jahn, 1995; Song et al., 2001; Xu et al., 2001; Zhou et al., 2002a; Zhang et al., 2006, 2008, 2009, 2014). The main part of the ELIP is located within the broad region of Cenozoic uplift caused by the India–Eurasian collision (Chung and Jahn, 1995). As a consequence, the lava pile is deeply dissected and exposed, especially in the western parts of the province. Erosional remnants of the flood basalts are distributed over an area of $\sim 2.5 \times 10^5$ km^2 (e.g., Hou et al., 2012). The ELIP flood basalts were likely emplaced at or close to sea level (Ukstins Peate and Bryan, 2009). Compared to the flood basalts in Siberian Traps, which erupted at a relatively high northern latitude, the emplacement of the Emeishan flood basalts occurred near the equator (Enkin et al., 1992). Overall, the province appears to be slightly older than the ~251 Ma Siberian Traps, with high precision zircon ages of 256.3 ± 0.4 Ma to 259.6 ± 0.5 Ma (Shellnutt et al., 2012, 2020; Zhong et al., 2014, 2020). According to the geochemical features and based on Ti contents, Emeishan flood basalts are divided into two series (Xu et al., 2001; Hou et al., 2011): high-Ti series (Ti/Y>500 or Ti>2.5wt. %) and low-Ti series (Ti/Y<500 or Ti<2.5 wt.%). High-Ti basalts occur both in the inner and outer ELIP zone and are considered as products of lower degree (1.5%) of partial melting of garnet-bearing-lherzolitic mantle, followed by assimilation of crust (e.g., Qi and Zhou, 2008; Song et al., 2009). Low-Ti basalts are mainly located in the inner zone of ELIP and interpreted to result from higher degree (up to 16%) of partial melting of sub-continental lithospheric mantle with assimilation of crust (e.g., Xu et al., 2001, 2003; Xiao et al., 2004a; Song et al., 2009). However, high degrees of mantle partial melting for the high-Ti volcanic rocks in the ELIP (~10-20%; Qi and Zhou, 2008; Song et al., 2009) have also been proposed. High-Ti basalts, especially those of ferrobasaltic composition are considered to have a strong genetic relationship with the giant Fe-Ti-V oxide ore-hosted layered intrusions, while low-Ti basalts are more closely associated to the smaller mafic-ultramafic intrusions which host Ni-Cu deposits (Zhou et al., 2008). Along the Mopanshan-Yuanmao and Panzhihua trending faults, numerous mafic-ultramafic layered intrusions hosting Fe-Ti-V oxide as well as Cu-Ni-(PGE) deposits are clustered. From north to the south, these intrusions are named as Taihe (262±3 Ma, Guo et al., 2004), Baima (262±3 Ma, Zhou et al., 2008; Shellnutt et al., 2009), Xinjie (259±3 Ma, Zhou et al., 2002b), Hongge (259±1.3 Ma, Zhong and Zhu, 2006) and Panzhihua (263±3 Ma, Zhou et al., 2005; 259±0.8 Ma, Hou et al., 2012; 261.4±4.6 Ma, Hou et al., 2013). According to the different assemblages of rock types, these ore-bearing rocks can be divided into two categories: (1) mafic-ultramafic (gabbroic to pyroxenitic/dunitic) intrusions, such as Hongge and Xinjie intrusions; (2) mafic (gabbroic) intrusions, such as Panzhihua, Taihe and Baima intrusions (c.f., Wang et al., 2008). The Fe-Ti-V oxide ore-bearing Hongge layered mafic-ultramafic intrusion is the largest intrusion with exposed area ~60 km^2 in the Panxi region (Fig. 2.1).

2.2.2 Main units and wall rocks of the Hongge layered intrusion

Horizontally, the Hongge layered intrusion is ~16 km long, 5 to 10 km wide and 0.6-2.7 km thick, with a total outcrop area ~60 km^2 (Panxi Geological Party, 1984). The footwall belongs to the Paleoproterozoic Hekou Formation which is mainly low to medium grade metamorphic rocks, such as mica- and plagioclase-bearing quartz schist, dolomitic marble, amphibolite, phyllite, and greenschist. The hanging wall is combined of Hekou Formation and Sinian Deingying Formation, which consists of amphibolites, greenschists and dolomitic limestone, dolomite, respectively (Fig. 2.2). A series of faults with NS-, NE-, and NW-trends cut off the intrusion and footwall rocks in different parts.

Based on the mineral assemblage, changes of mineral modal proportions, occurrence or disappearance of cumulus minerals as well as texture and structure of the rocks, the Hongge layered intrusion is usually divided into a Lower Zone (LZ), a Middle Zone (MZ) and an Upper Zone (UZ) from bottom to top (e.g., Zhong et al., 2002; Fig. 2.3), and they are predominantly composed of olivine clinopyroxenite (±hornblende), magnetite clinopyroxenite (±olivine) and gabbro (±apatite), respectively. The LZ is characterized by the presence of ~5 to 15 vol.% hornblende and phlogopite; MZ is characterized by the occurrence of thick Fe-Ti-V oxide ore layers; while UZ is featured by considerable amounts of euhedral apatite (e.g., Luan et al., 2014a, 2014b; Liao et al., 2015). Generally, the rocks from LZ and MZ were emplaced into the Mesoproterozoic schist and metamorphic sandstone in the north, and Neoproterozoic dolomitic limestone in the south. Notably, gabbros of the UZ intruded into the Emeishan basalts in the NE part of the intrusion. Late-stage granites and syenites are sometimes located between the mafic Hongge intrusion and the metamorphic wall rocks.

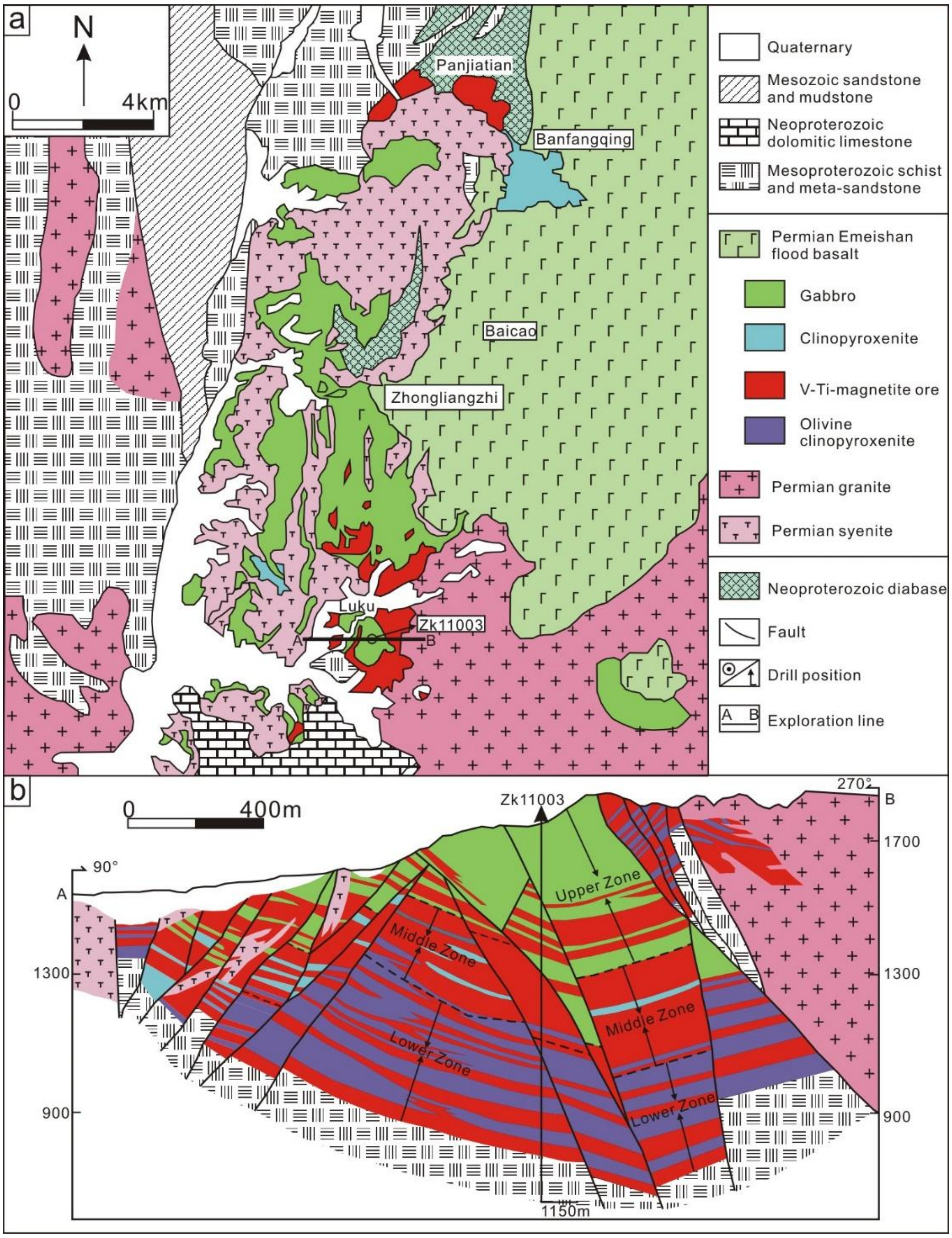

Fig. 2.2. a: Geological map of the Hongge layered intrusion; b: cross section of the exploration line. Modified from Sichuan Geological Survey (2010).

2.3 Analytical methods

2.3.1 Bulk rock compositions

Bulk rock compositions were measured with X-ray fluorescence (XRF) at the University of Liège, Belgium. All the rock samples were firstly carefully crushed into small pieces and milled in agate mortars. An ARL PERFORM-X 4200 was used to determine major and some trace elements which are enriched in mafic rocks (e.g., Cr and V, the detection limit is *c*.5 ppm and 8 ppm). Major elements (i.e., Si, Ti, Al, Fe, Mn, Mg, Ca, Na, K, P) were measured on lithium tetra- and metaborate fused discs. Traill-Lachance algorithm was used for matrix correction with the raw data. Pressed powder pellets were made by powders for trace elements measurement. Compton peak monitoring was used for the correction of matrix effects with trace elements raw data. Detailed data for bulk-rock element analyses are presented in Supplementary Table 2.1.

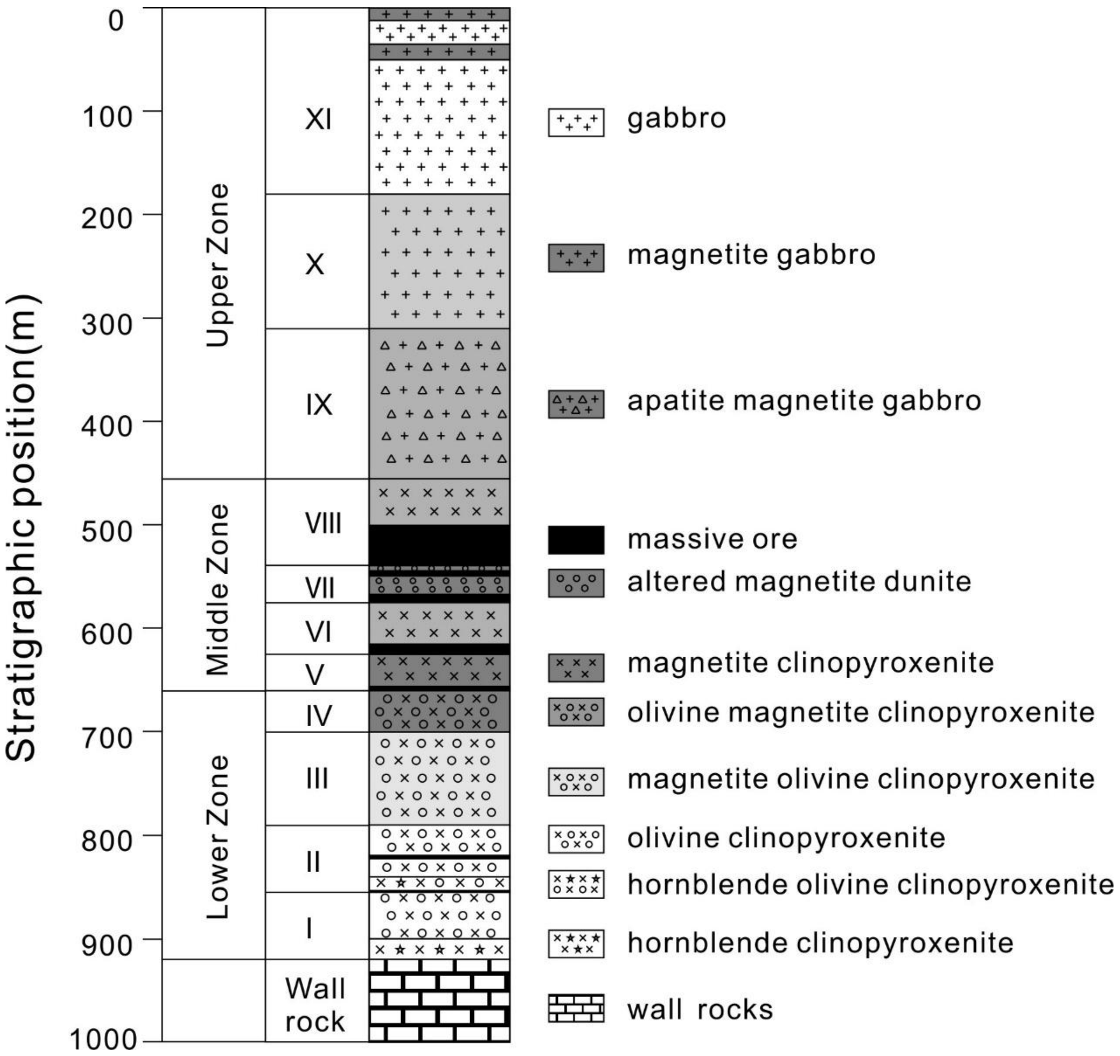

Fig. 2.3. Stratigraphy of the Hongge layered intrusion based on petrographic observations of the samples from drill core ZK11003.

2.3.2 Mineral chemistry

The chemical compositions of olivine, clinopyroxene and plagioclase were obtained with a Cameca SX100 electron microprobe at the Institute of Mineralogy, Leibniz Universtät Hannover (Germany). The working condition for the microprobe during measurement is 15kV for acceleration voltage and 15 nA for beam current. Beam size was set up for 1 μm and the counting time for each element was 10 s. PAP procedures were used for correcting the raw data. Synthetic materials or natural minerals are used for standards, including Woll MAC (Si and Ca), jadeite (Na), kyanite (K) and synthetic TiO_2, Fe_2O_3, MgO and Mn_3O_4. Detailed results are listed in Supplementary Table 2.2.

2.3.3 Mineral mode determination by SEM

Mineral proportions in thin sections were determined using a JEOL-7610F Field Emission Scanning Electron Microscope (SEM) at the Institute of Mineralogy, Leibniz Universtät Hannover (Germany). The total number of the investigated samples is 150. Because of the limitation of software for SEM, one mosaic element mapping job is usually less than 10 mm ×10 mm, and we selected two or three representative areas for each sample. For the mappings, every single picture was measured independently and finally scrabbled up to a mosaic map. The obtained mosaic maps were imported into the Photoshop software and representative elements were used for calculation of the mineral proportions, such as Mg for olivine, Fe for magnetite and Ti for ilmenite. Detailed results of mineral modes can be checked in Supplementary Table 2.3. The main cumulus and intercumulus mineral modes are shown in Fig. 2.4.

2.4 Sampling and petrography of drilling core ZK11003

172 samples were collected along the ZK11003 drilling core (see location in Fig. 2.2) and selected to obtain a detailed section of the layered intrusion with an average

spacing between samples of less than 5 m. For the ore layers or if the lithological layering was pronounced, we selected more closely spaced samples. Some previous work has been done on samples of this deposit (e.g., Bai et al., 2012, 2014; Luan et al., 2014b; Liao et al., 2015). However, so far no systematic integrating detailed petrography, bulk rock and mineal major element compositions have been presented. Here we present a detailed description of the LZ, MZ and UZ.

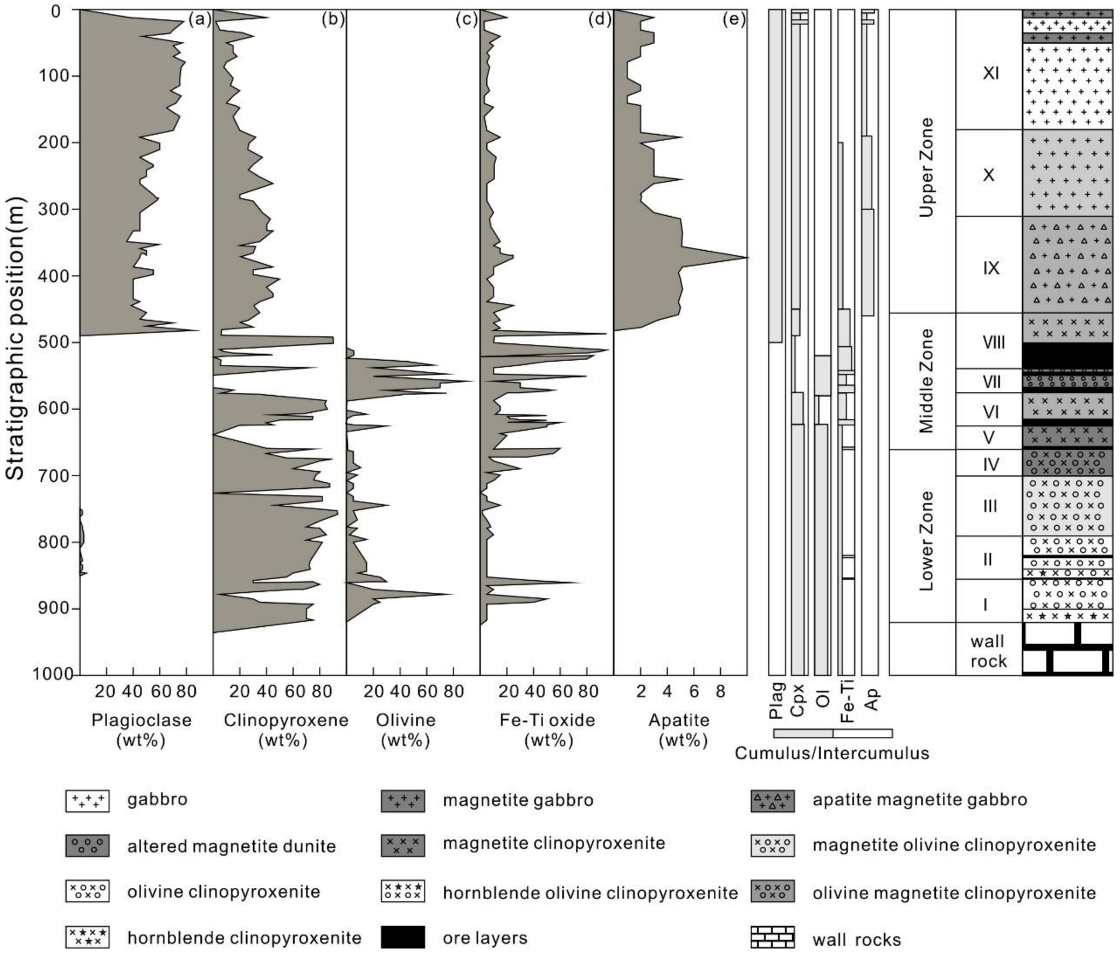

Fig. 2.4. Mineral modes in cumulates from the Hongge layered intrusion for (a) plagioclase, (b) clinopyroxene, (c) olivine, (d) Fe-Ti-V oxides, (e) apatite. To the right is the stratigraphy of cumulus (grey) and intercumulus (white) phases.

2.4.1 Lower Zone (LZ)

The thickness of LZ is ~260 m (from depth 920 to 660 m) in the investigated drilling core. The typical mineral assemblage includes hornblende, clinopyroxene, olivine, Fe-Ti-V oxides as well as minor apatite, plagioclase, phlogopite and minor sulfides. According to Wager et al. (1960), cumulus minerals usually have coarse-grained size and relatively idiomorphic shape. Intercumulus minerals usually crystallized later from the trapped liquids or residual melts and have subhedral shapes and poikilitic texture. In general, the main cumulus minerals in LZ are coarse-grained olivine and clinopyroxene (grain size between 0.25-0.5 cm; Fig. 2.5a and b) as well as minor phlogopite and hornblende, which are magmatic in origin (Luan et al., 2014a). Subhedral magnetite and ilmenite (in average ratio ~1 to 1) and subsequently crystallized fine-grained olivine and clinopyroxene (grain size between 0.05-0.1 cm) are major intercumulus minerals (Fig. 2.5a and i). Apatite and sulfides are usually rare. Spotted veins mainly composed of Ab-rich plagioclase (described as albite in the following paper) and K-feldspar in the LZ are also observed. From bottom to the top, according to the mineral modes and changes of mineral assemblage, four different lithological units can be further identified in the LZ.

Unit I mainly contains a 20 m thick layer of hornblende clinopyroxenite at the bottom and a 40 m thick layer of olivine clinopyroxenite on the top. In the hornblende clinopyroxenite layers, hornblende content can reach up to 15 vol.%. Fe-Ti-V oxides content is usually lower than 15 vol.%. Clinopyroxene is the main cumulus mineral in hornblende clinopyroxenite layers, with proportions usually higher than 70 vol.%. The olivine clinopyroxenite layer on top of Unit I mainly contains 10-30 vol.% olivine, 10-15 vol.% Fe-Ti-V oxides and 50-70 vol.% clinopyroxene. Additionally, minor apatite (<1 vol.%), phlogopite and plagioclase (<2 vol.%) are occasional present in these two layers.

Unit II is composed of a very thin disseminated ore layer at the bottom, then followed by a 10 m thick hornblende olivine clinopyroxenite layer and a 40 m thick olivine clinopyroxenite layer. In this paper, we defined disseminated ore layers as rocks with proportions of 40-50 vol.% Fe-Ti-V oxides (and even up to 60 %) and massive ore layers as rocks with more than 60 vol.% oxide. In the middle part of the olivine clinopyroxenite layer, another thin disseminated Fe-Ti-V oxide ore layer has also been recognized. Compared to Unit I, hornblende olivine clinopyroxenite layers in Unit II (Fig. 2.5c and d) contain more olivine (15-30 vol.%) and less hornblende (<10 vol.%) and clinopyroxene (30-60 vol.%).

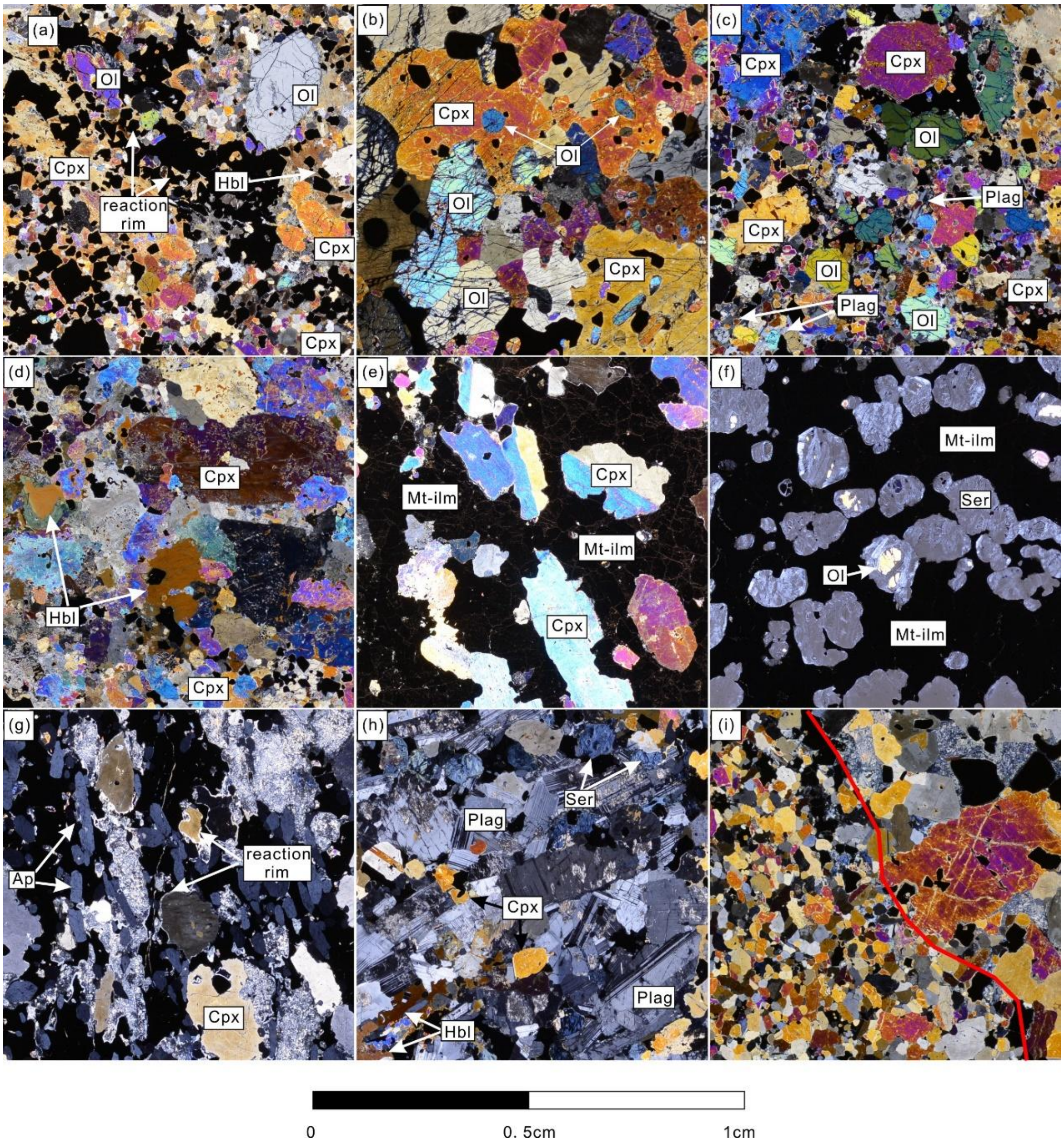

Fig. 2.5. Representative photomicrographs showing the main cumulus and intercumulus assemblages of rocks from the drilling core of the Hongge layered intrusion. (a) Magnetite olivine clinopyroxenite in the LZ (Unit III) containing coarse-grained olivine and clinopyroxene as well as fine-grained olivine and clinopyroxene. Fe-Ti-V oxides are enclosed around clinopyroxene and olivine. Hornblende reaction rim can be found along early formed clinopyroxene. (b) Olivine clinopyroxenite (Unit II) contains euhedral to subhedral coarse-grained clinopyroxene and olivine. In the coarse-grained cumulus phases, fine-grained clinopyroxene and olivine as well as Fe-Ti-V

oxides are enclosed in. (c) Olivine clinopyroxenite (Unit II) contains both cumulus and intercumulus olivine and clinopyroxene. Intercumulus plagioclase can also be observed in this unit. (d) Hornblende clinopyroxenite (Unit II) contains euhedral to subhedral coarse-grained clinopyroxene and poikilitic texture hornblende. (e) Magnetite clinopyroxenite (Unit VI) contains lineation and orientation of clinopyroxene and massive Fe-Ti-V oxides. (f) Altered magnetite dunite (Unit VII) contains massive Fe-Ti-V oxides and serpentine with remaining fresh olivine core. (g) Apatite magnetite gabbro (Unit IX) contains abundant euhedral apatite, euhedral to subhedral clinopyroxene and altered plagioclase. (h) Magnetite gabbro (Unit X), dominated by large lath-shaped plagioclase and euhedral to subhedral clinopyroxene with a few serpentine crystals; Fe-Ti-V oxides drops down to a low percentage. (i) Magnetite clinopyroxenite (Unit V) shows a distinguishing line between coarse-grained clinopyroxene and fine-grained clinopyroxene. Plag, plagioclase; Cpx, clinopyroxene; Ol, olivine; Hbl, hornblende; Mt-ilm, Fe-Ti-V oxides; Ap, apatite; Ser, serpentine.

Unit III and Unit IV are composed of olivine- and magnetite-bearing clinopyroxenites. The content of olivine and magnetite in Unit III and Unit IV ranges between 10-30 vol.%. Nevertheless, the modal proportions of Fe-Ti-V oxides mark the boundary between Unit III and IV, i.e. Unit III has more olivine than Fe-Ti-V oxides (named magnetite olivine clinopyroxenite), whereas Unit IV contains more Fe-Ti-V oxides than olivine (named olivine magnetite clinopyroxenite). In the rocks of these two units, the hornblende content is usually less than 5 vol.%. In addition, there are several syenitic or granitic dykes ranging from 2 m to 5 m in thickness in the LZ.

2.4.2 Middle Zone (MZ)

The 200 m thick MZ (range from depth 660 m to 460 m) contains ore layers with variable thickness ranging from 5 to 40 m. From bottom to the top, four main lithological units (V, VI, VII and VIII) were identified. In each unit, the Fe-Ti-V oxide ore layer with variable thickness (5-30 m) appears at the bottom, prior to magnetite-bearing clinopyroxenite or dunite. Specifically, Units V and VI are mainly composed of magnetite clinopyroxenite with the presence of thin disseminated ore layers (5-10 m). Unit VII is composed of altered magnetite-bearing dunite and on top of the dunite, there is a ~10 m thick ore layer. Unit VIII is composed of magnetite clinopyroxenite with thick massive ore layers (>30 m).

In contrast to the LZ rocks, the MZ rocks contain only a minor amount of hornblende (<3 vol.%), and the content of olivine is also significantly lower (<10 vol.%), except for the magnetite-bearing dunite layers in Unit VII. In addition, lineation and orientation of clinopyroxene are observed in the magnetite clinopyroxenite layers on top of the MZ (Fig. 2.5e). Unlike the Fe-Ti-V oxides in the LZ, magnetite and ilmenite in the ore layers of the MZ are euhedral and cumulus phases. Sulfides are rare and their proportion is lower than in the LZ. In Unit V and VI, magnetite clinopyroxenite layers contain about 10-30 vol.% Fe-Ti-V oxides, less than 5 vol.% olivine and 65-85 vol.% clinopyroxene. In the samples from Unit VII, olivine is mostly rounded and replaced by serpentine, with only tiny fresh remnants left in the former core of the minerals (Fig. 2.5f). In Unit VIII, adjacent to the thick ore layers, we observed a sharp decrease in the clinopyroxene content in the upper part compared to Unit V and VI. In contrast, plagioclase (which is deeply altered) starts to be presented in the upper part of Unit VIII. Apatite appears in the uppermost part of Unit VIII. Two layers (609-625 m and 490-500 m) of massive ores only containing Fe-Ti-V oxides with minor oriented spotted clinopyroxene, which could be interpreted as flow texture, can be observed in Unit VI and VIII and show a gravity settling structure (Fig. 2.5e).

2.4.3 Upper Zone (UZ)

The UZ is about 460 m thick and can be divided into three units from bottom to the top, named apatite-magnetite-bearing gabbro Unit IX, magnetite-bearing gabbro Unit X and gabbro Unit XI. The rocks are usually deeply altered. Coarse-grained plagioclase and clinopyroxene are the main cumulus phases in Unit IX and X (Fig.

2.5g and h). Euhedral apatite is usually surrounded by Fe-Ti-V oxides (Fig. 2.5g). Sometimes, poikilitic apatite can also be found in the coarse-grained clinopyroxene and plagioclase. Intercumulus phases are composed of fine-grained plagioclase and clinopyroxene which can also be included in intercumulus magnetite and ilmenite (ratio ~ 1 to 3). In the UZ, coarse-grained clinopyroxene and plagioclase usually have a clear hornblende reaction rim. The clinopyroxene content sharply decreases compared to the MZ and LZ and is usually less than 40 vol.%, whereas plagioclase content is usually higher than 50 vol.%. The difference between apatite-magnetite-bearing gabbro and magnetite-bearing gabbro is the content of apatite and Fe-Ti-V oxides. Plagioclases in magnetite-bearing gabbro layers are only slightly altered and show no obvious zonation under the microscope (Fig. 2.5h). Coarse-grained clinopyroxene is often associated with large lath-shaped plagioclase, but fine-grained clinopyroxene is usually associated with apatite and Fe-Ti-V oxides surrounding cumulus minerals. Hornblende is also presented in this zone with about 5-10 vol.%. All the plagioclase in Unit XI is deeply altered and only albite can be found as unaltered phases. Clinopyroxene in Unit XI shows the same texture and structure as in other units in the UZ. Two mafic dykes that intruded into Unit XI were identified.

2.5 Analytical results

2.5.1 Bulk rock composition

The 108 selected samples for bulk rock analyses are relatively fresh as confirmed under the microscope before analysis and as indicated by their low loss-on-ignition (LOI) values. Generally, samples in the Hongge layered intrusion have large compositional variations for most of the major elements (Fig. 2.6, data from Supplementary Table 2.1). For example, Fe_2O_3 varies from 11.8 to 70.0 wt.% and shows a negative linear relationship with SiO_2 (0.85-48.9 wt.%). The TiO_2 concentrations (1.5 to 27.7 wt.%) are positively correlated with Fe_2O_3 and display the same negative relationship with SiO_2. The strong variations of Fe_2O_3 and TiO_2 and the negative correlations with SiO_2 and other major elements can be explained by the different proportions of oxide phases and silicate phases in the investigated samples. Stratigraphically, Fe_2O_3(t)+TiO_2 content shows a strong increase in the transition between the LZ and MZ. The variations of Fe_2O_3(t)+TiO_2 within the UZ and LZ units are large and are in the range of 13.8-80.4 wt%. The highest values are observed at the bottom of the LZ and MZ, with values of 80.4 and 87.8 wt.%, respectively (Fig. 2.7a).

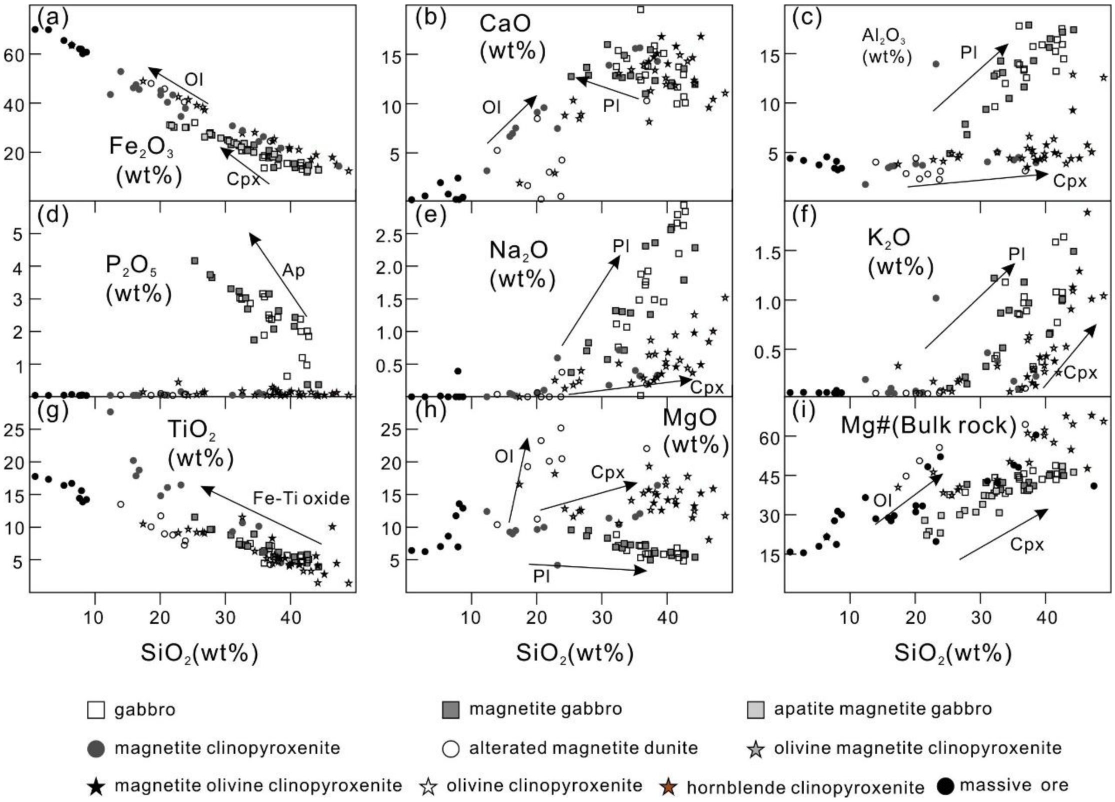

Fig. 2.6. Major element distribution diagrams from bulk rock analyses from the Drill core in the Hongge layered intrusion. Data are from Supplementary Table 1. The arrows show the differentiation effects of main cumulus minerals in each zone.

CaO ranges from 0.1 to 20.0 wt.% and the extremely low CaO content samples are oxide-rich or massive ore rocks; Al_2O_3 changes from 1.7 to 18.0 wt.% and shows two different correlations with SiO_2. The Na_2O concentrations vary from 0 to 2.9 wt.% and increase up section (highest values are in the UZ units). K_2O ranges from 0 to 1.9 wt.% and is correlated with SiO_2 in the LZ and MZ. MgO is systematically higher in the LZ and MZ when compared with the UZ. An average MgO value for the LZ and MZ is 13.3 wt.%, with concentrations up to 25.2 wt.% in some dunite samples, whereas the maximum concentration in the UZ is lower than 9.6 wt.%. As a consequence of the general inverse relationship between Fe and Mg as a function of SiO_2, whole rock Mg# values show a positive trend with SiO_2 in the three units, ranging from 15.2 to 68.2 (Fig. 2.6i).

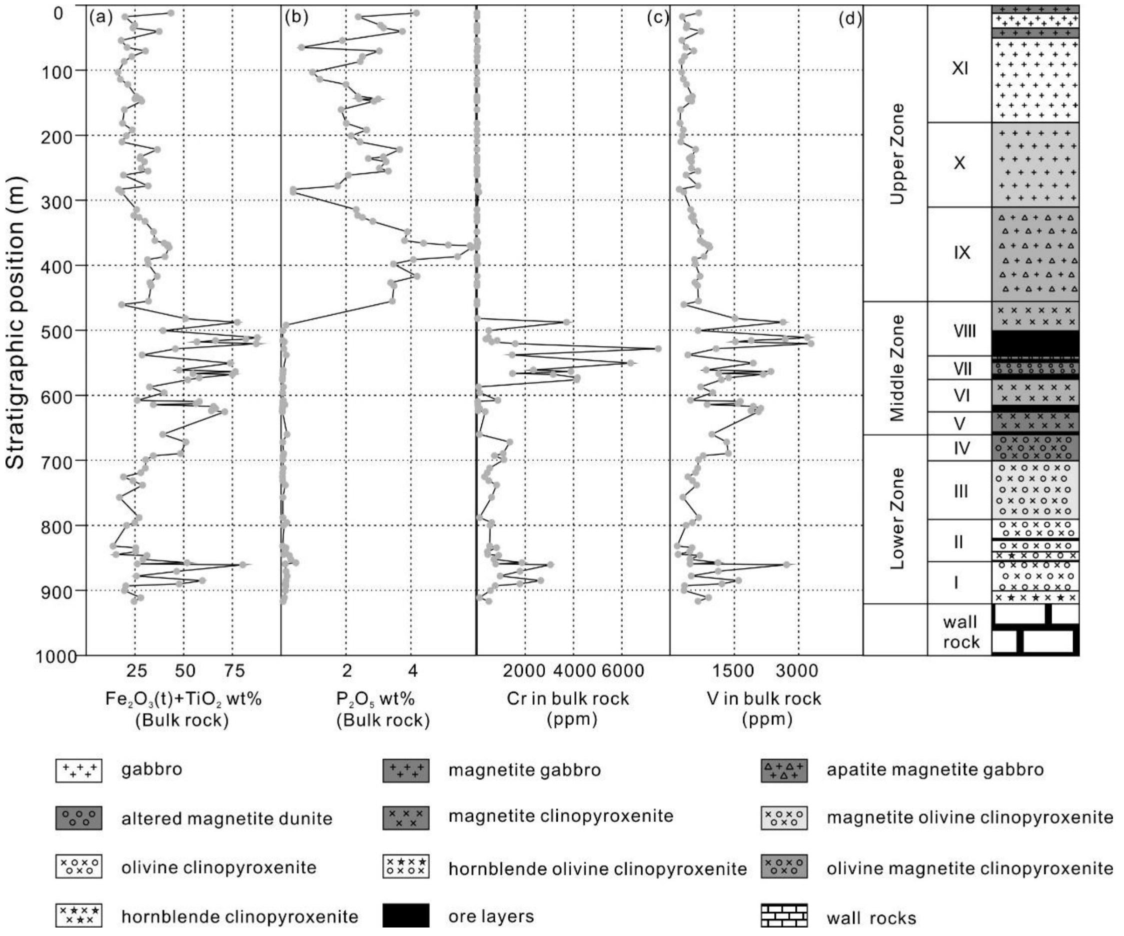

Fig. 2.7. Stratigraphic evolution of bulk rock compositions for (a) Fe_2O_3+TiO_2 (wt.%) in bulk rock, (b) P_2O_5 (wt.%) in bulk rock, (c) Cr (ppm) in bulk rock and (d) V (ppm) in bulk rock.

P_2O_5 ranges from 0 to 5.9 wt.% and the high values are in the rocks of the UZ. The phosphorus content in the samples from the LZ and MZ is relatively low. However, the analysis of the UZ Units IX and X show that the phosphorus content gradually increases from the bottom to the middle and then decreases from the middle to the top (Fig. 2.7b).

The evolution of Cr and V, as a function of the stratigraphic position, is presented in Fig. 2.7c and d. The Cr and V contents usually reach the highest values in magnetite-rich layers in the LZ and MZ. Above Unit VIII in the MZ, the Cr content in the UZ is below the detection (≤ 5 ppm). The maximum value of V is at ~3200 ppm. There is a clear positive correlation between V and Cr for the samples in the LZ. However, there is no systematic and clear correlation in the MZ. In particular, some samples with high V contents have Cr contents below the detection limit in the UZ.

2.5.2 Mineral composition

Previous studies have already confirmed that most layered intrusions experienced a slow cooling process (e.g., Holness et al., 2007). Thus, mineral assemblages, especially cumulus minerals crystallized from the original parental magma, can undergo several post-crystallization processes during cooling, which we take into consideration in the discussion below. Thus in this study, only the core compositions of these minerals could be used to gain information about the parental magma as the rim composition could have been re-equilibrated with trap liquids in the crystal mush. In this study, care was taken to analyze systematically the mineral composition in the core.

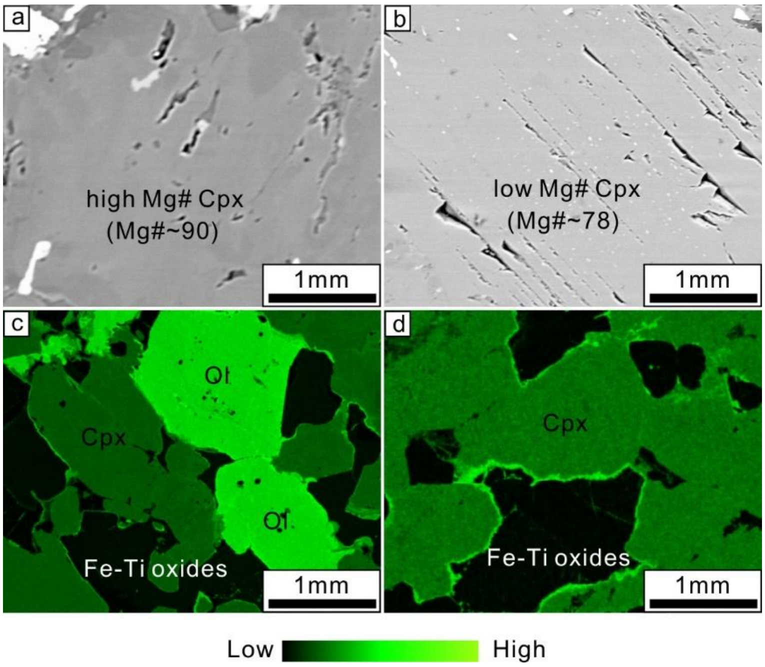

Fig. 2.8. (a) BSE image of high Mg# clinopyroxene, (b) BSE image of low Mg# clinopyroxene, (c) SEM image of olivine and clinopyroxene for Mg mapping in the MZ, (d) SEM image of clinopyroxene for Mg mapping in MZ.

2.5.2.1 Olivine

Olivine from the Hongge intrusion has Fo contents [molar 100×Mg/(Fe+Mg)] ranging from 71 to 85 (see Supplementary Table 2.2). No obvious zonation is found in individual olivine crystals. There is also no obvious compositional variation between cumulus olivine and intercumulus olivine in the same thin section. Variations of the Fo contents within one thin section is 2 mol.% (see error bar in Fig. 2.9a). The Ni contents in olivine are usually lower than 0.2 wt.%.

2.5.2.2 Clinopyroxene

Clinopyroxene is primarily augite based on the end-member calculations. The Mg# [molar 100×Mg/(Mg+Fe)] varies from 73 to 90 (see Supplementary Table 2.2). Based on our analyses, there is no obvious difference for the Mg# of clinopyroxene between core and rim (variation of Mg# is 1 to 2 mol.%). As described above, two different types of clinopyroxene with two different phases are observed in the Hongge layered intrusion (cumulus and intercumulus clinopyroxene), but in most samples, there is no difference in Mg# between the two types. However, in some thin sections which are usually close to the ore layers, additional populations with higher Mg# can be found. According to the different Mg#, we classified the clinopyroxenes into two different populations, named as low Mg# clinopyroxene (<80; major) and high Mg# clinopyroxene (>80, some crystals have Mg# as high as ~90; minor). The populations with high Mg# usually have no oxide lamellae (Fig. 2.8a) and are indicated as red dots in Fig. 2.9b.

The TiO_2 contents in the low Mg# clinopyroxene vary from 0.6 to 2.7 wt.% and are mostly higher than 1 wt.%. In contrast, the high Mg# clinopyroxenes have much lower TiO_2 content (mainly <0.9 wt.%). Al_2O_3, Cr_2O_3 and MnO_2 contents in the low

Mg# clinopyroxene are also higher compared to the contents in the high Mg# clinopyroxene. For SiO_2 and CaO content, the high Mg# clinopyroxene is about 2-3 wt.% higher (absolute values) compared to the low Mg# clinopyroxene (see Supplementary Table 2.2).

2.5.2.3 Plagioclase

Plagioclase is mainly observed in two zones. The first occurrence is within a small interval in the LZ as an intercumulus phase and the second occurrence starts from the top of MZ and covers the entire UZ as a dominant cumulus phase (Fig. 2.9c). Plagioclase in the LZ has anorthite contents (An) [molar 100×Ca/(Ca+Na)] ranging from 58 to 70 mol.% (see Supplementary Table 2.2), except for one sample (collected at the depth of 846.3m). In this sample, a large variation of An content was observed, ranging from 44 to 59 mol.%. The An content in plagioclase of the UZ varies significantly from 40 to 80 mol.%. However, no clear trend could be found (e.g., the trend typical for fractional crystallization). In Unit IX and X of UZ, An content of plagioclase shows a maximum in the central part of the unit and lower values at the bottom and at the top (Fig. 2.9c). Most of the plagioclases in the UZ have no zoning, however, in some samples, there are irregular compositional changes from the core to the rim (up to 15 mol.%; Fig. 2.10). More importantly, in some thin sections (such as No. 283 and 287), 2 or 3 populations of plagioclases with different An content (Fig. 2.9c; black and grey dots) can be found, similar to samples No. 846.3 mentioned above, although no clear textural differences between each population were noted. This phenomenon can be found in 6 samples in the UZ.

2.5.2.4 Albite

Ab-rich plagioclase (albite) is one of the main accessory minerals in the LZ and MZ in Hongge layered intrusion. It firstly appears at the bottom of the LZ with a low percentage and was also identified in the upper part of MZ. However, when albite occurs in the UZ, especially in Unit XI, almost all the plagioclase is replaced by albite. The Ab content in albite [molar 100×Na/(Ca+Na)], is usually high (~93 mol.%) (Fig.

2.9d). Variation of the Ab content in individual samples is mostly between 0.5 to 5.2 mol.%.

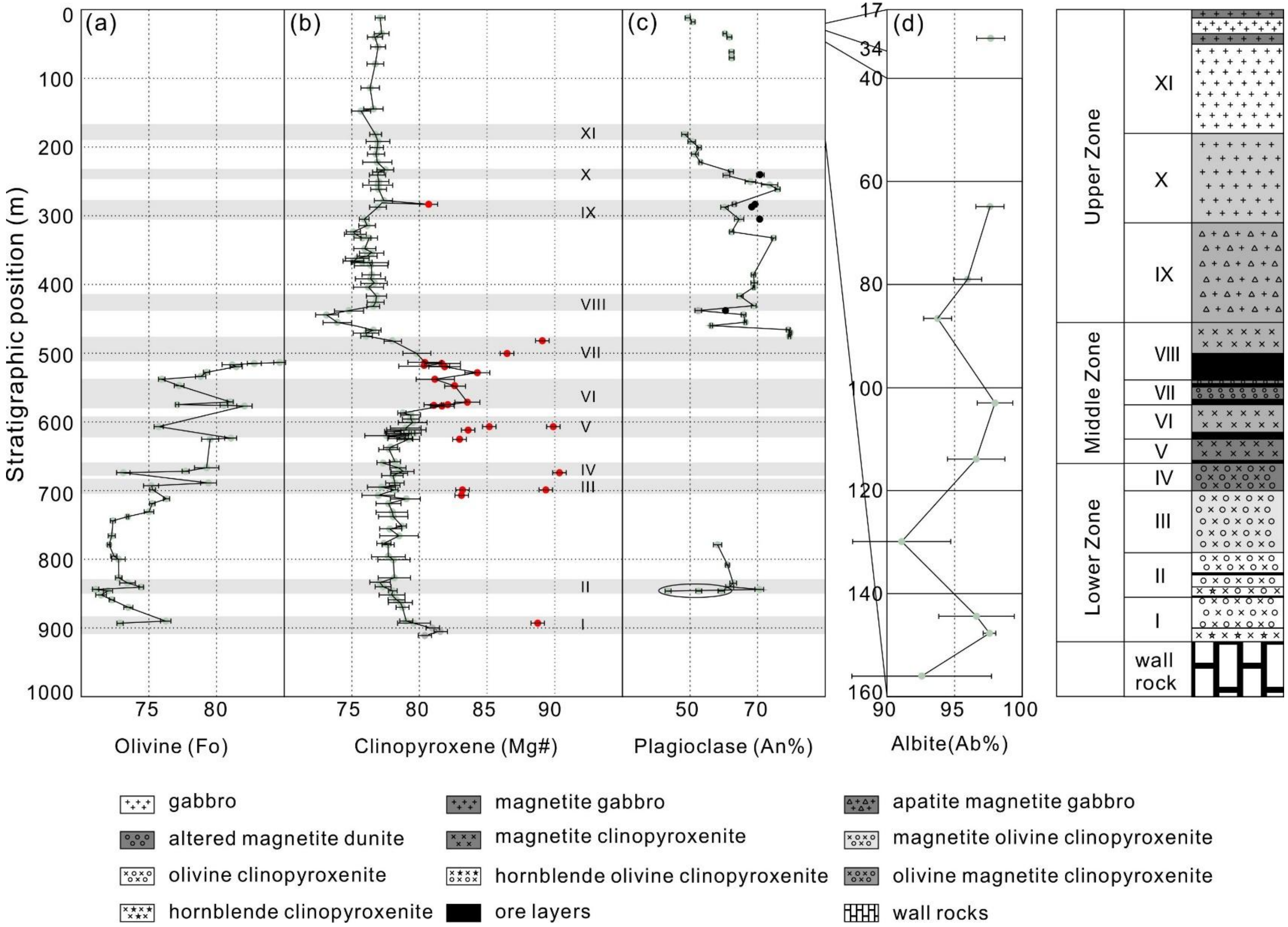
(a)
(b)
(c)
(d)
Stratigraphic position (m)
0
100
200
300
400
500
600
700
800
900
1000
Olivine (Fo)
75
80
Clinopyroxene (Mg#)
75
80
85
90
Plagioclase (An%)
50
70
Albite(Ab%)
90
95
100
17
34
40
60
80
100
120
140
160
XI
X
IX
VIII
VII
VI
V
IV
III
II
I
Upper Zone
Middle Zone
Lower Zone
wall rock
gabbro
altered magnetite dunite
olivine clinopyroxenite
hornblende clinopyroxenite
magnetite gabbro
magnetite clinopyroxenite
hornblende olivine clinopyroxenite
ore layers
apatite magnetite gabbro
magnetite olivine clinopyroxenite
olivine magnetite clinopyroxenite
wall rocks

Fig. 2.9. Compositional variations of (a) olivine (Fo%), (b) clinopyroxene (Mg#), (c) plagioclase (An%) and (d) albite (Ab%), with stratigraphic position in the Hongge layered intrusion. Red dots represent the high Mg# clinopyroxene. Black dots represent the high An content plagioclase. Grey zones represent 11 magma replenishment events identified in the Hongge intrusion.

2.5.2.5 Stratigraphic variation of dominant minerals and correlation between mineral compositions

Figure 2.9 shows the variations of the main mineral compositions (olivine, clinopyroxene, plagioclase, and albite) as a function of the depth of the drill cores. Throughout the stratigraphy, clinopyroxene is the dominant crystalline phase, while olivine mainly occurs in the LZ and MZ. In contrast, plagioclase only appears from the top of the MZ and predominantly occurs as a major cumulus phase in the UZ. Notably, thin layers of interstitial plagioclase-bearing clinopyroxenite have also been observed in the LZ.

A variation of mineral compositions along the drill core can be observed, especially for olivine and plagioclase. From bottom to top, the olivine composition varies significantly as reflected by at least three reversals in Fo content (an increase of Fo content from bottom to top) in the LZ and four reversals in the MZ. For the low Mg# clinopyroxene population, the Mg# remains nearly constant in the LZ and MZ (~78 ±1), except for Unit I and VIII. The clinopyroxene Mg# in these two units is higher in the lower part (81-84) and then decreases to the top, reaching the Mg# of 78 for Unit I and Mg# of 73 for Unit VIII, which could be explained by fractional crystallization. There is no correlation of the Fo content of olivine with the low Mg# clinopyroxenes in the LZ and MZ (e.g., positive correlation between Fo content and Mg#). As discussed above, in some samples, except the low Mg# clinopyroxene population, there is another population of clinopyroxene with high Mg#. The presence of the high Mg# clinopyroxene population seems to always be correlated with reversals in olivine composition. The samples containing the high Mg# clinopyroxene population tend to have low Fo content of olivine (Fig. 2.11a and c). The An content of plagioclase in the UZ also shows several compositional reversals while the Mg# of clinopyroxene in the UZ remains almost constant (76±1) except for one sample (No. 283 with Mg# 82). Thus, plagioclase compositional reversals in the UZ have no clear genetic correlation with Mg# of clinopyroxene.

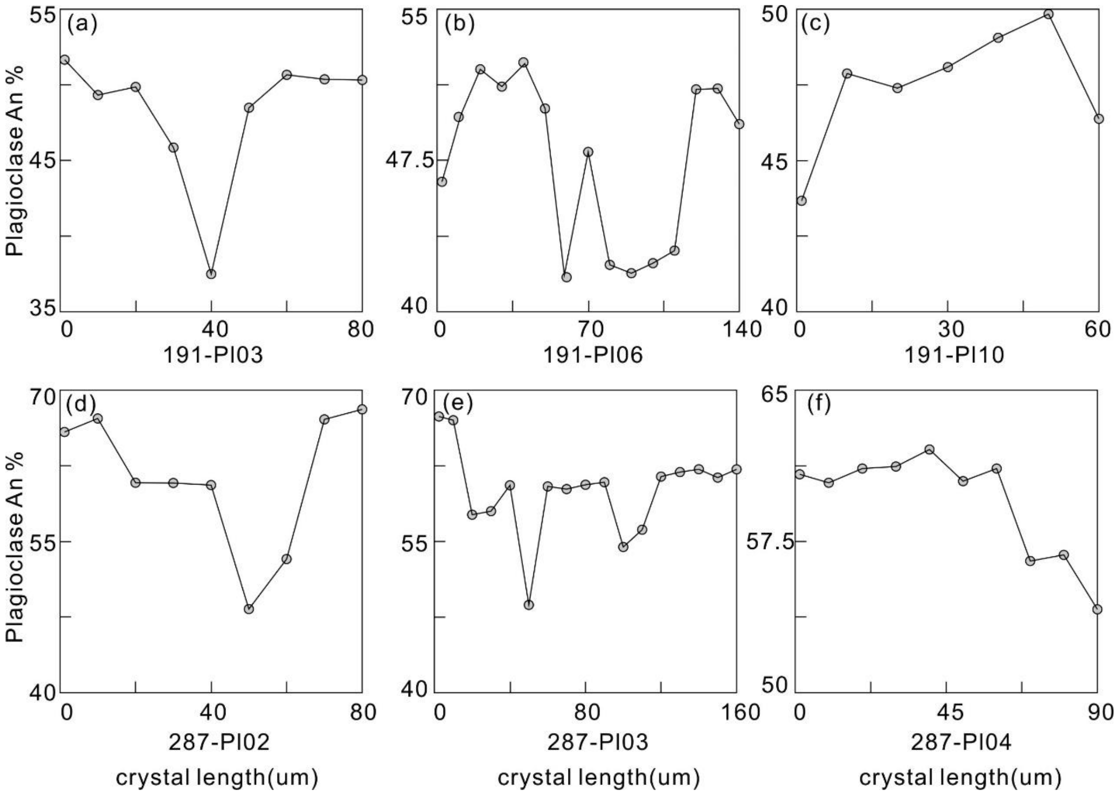

Fig. 2.10. An content changes for plagioclase in representative samples in the UZ from rim-core-rim. (a) (b) (c) are samples at the depth 191m from Unit X. (d)(e)(f) are samples at depth 287m from Unit IX.

2.6 Discussion

2.6.1 Factors affecting the stratigraphic variation of mineral compositions

Compositional changes of silicate minerals are often observed within the stratigraphy of layered intrusions. In many cases, there is a general decrease of Mg# of mafic minerals from bottom to top or there are episodic reversals. Different processes were proposed and at least four major mechanisms including crystal fractionation processes in a magma body formed by a single injection (e.g., McBirney, 1996), trapped liquid shifts (e.g., Barnes et al., 1986), sub-solidus re-equilibrations (e.g., Frost et al., 1988, 1991) and replenishment of more primitive magmas (e.g., Yuan et al., 2017). In the case of the Panxi region, several previous studies incorporating crystal fractionation process have been proposed for explaining the crystallization order of cumulus minerals in these layered intrusions (Pang et al., 2008a, 2008b; Shellnutt et al., 2009, Shellnutt and Jahn, 2010; Shellnutt et al., 2011b; Zhang et al., 2012; Song et al., 2013; Luan et al., 2014b; Tao et al., 2015; Zhang et al., 2020). However, multiple mineral reversals (especially olivine) and bulk rock trace elements reversals (e.g., Cr) in the entire Hongge intrusion strongly suggest that the Hongge cumulates do not follow simple fractional crystallization trends (c.f., Wager and Brown, 1968), and the evolution of the liquid line of descent (Toplis and Carroll, 1995, 1996). Since the rationality and inadequacy of crystal fractionation in the Hongge intrusion are discussed in previous studies, thus only the three other hypotheses mentioned before are discussed below.

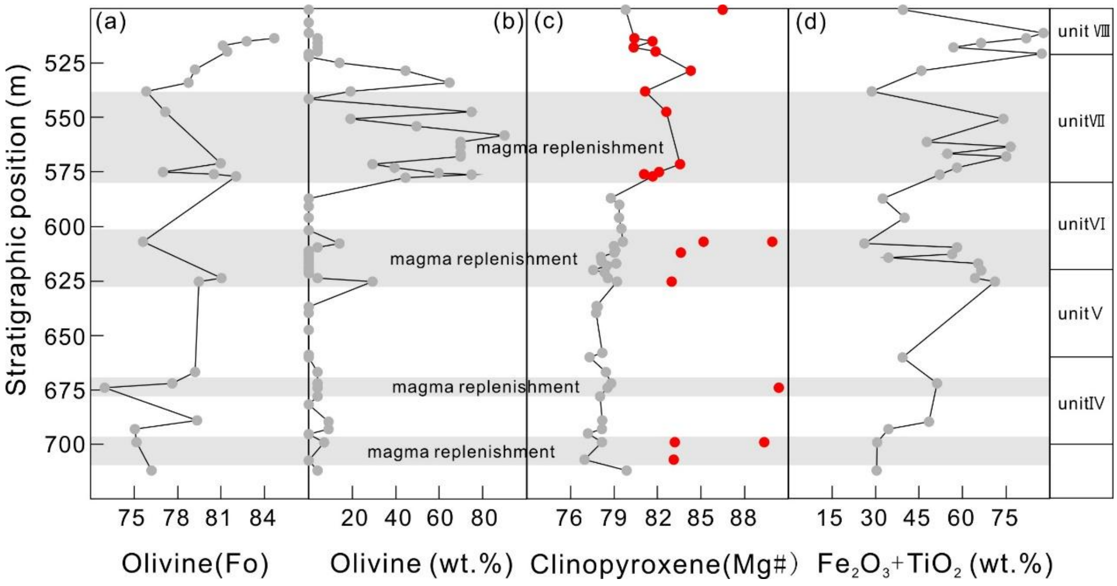

Fig. 2.11. Details of units in the upper part of LZ and units in the MZ, showing the concomitant reversals in Fo content in olivine (a) and modal proportions of olivine (b), and low and high Mg# clinopyroxene (c), and Fe_2O_3+TiO_2 content in bulk rocks (d). Grey zones represent magma

replenishment events.

2.6.2 Trapped liquid shift

Trapped liquid shift effects have a clear influence on the composition of mafic minerals in layered intrusions especially for the Mg# of pyroxene and Fo content in olivine (e.g., Barnes et al., 1986). One line of evidence for a large volume of trapped liquid is the compositional zoning of cumulus mineral phases with decreasing An content in plagioclase or Mg# of both olivine and clinopyroxene towards the rim (e.g., Namur et al., 2014; Namur and Humphreys, 2018). For the Panzhihua layered intrusion, Pang et al. (2009) estimated the amount of trapped liquid using bulk Zr concentrations. Based on their estimation, the crystallization of trapped liquid in a crystal mush (or cumulate) is responsible for shifts of ~7 mol.% in the Mg# of clinopyroxene and ~5 mol.% Fo in olivine towards more Fe-rich compositions. However, for our samples, such systematic zoning in cumulus phases is not observed. Specifically, microprobe analyses at both the core and rim of major cumulus minerals, i.e., olivine and clinopyroxene, show no obvious compositional differences. Hence, this indicates that the trapped liquid effect did not play a major role in causing the stratigraphic compositional variations in the Hongge layered intrusion. Moreover, this inference is clearly evidenced by our observations that coarse-grained cumulus minerals are dominant phases (>85 vol.%) in both the LZ and MZ compared to that of the intercumulus minerals. A small amount of trapped liquid across the stratigraphy of the Hongge intrusion is consistent with the observations of Bai et al. (2014) that were estimated by bulk La content (i. e., 5 % trapped liquid). Although compositionally zoned plagioclase is present in the UZ, the compositional changes could not result from trapped liquid shift effects. As emphasized by Grove et al. (1984), the diffusion of cations in plagioclase is too slow to re-equilibrate with respect to An content. In addition, the complex compositional variations of individual plagioclases that are observed in some (but not all) samples are not consistent with a trapped liquid shift effect either (Fig. 2.10) because some grains have a higher An content in the rim.

Therefore, based on our observations, the variation of Mg# in mafic phases and of An content in plagioclase cannot be only explained by the effects of re-equilibration with trapped liquids.

2.6.3 Sub-solidus re-equilibration

Sub-solidus re-equilibration between oxides and mafic silicate minerals might be another important mechanism to explain the changes of cumulus mineral compositions, especially in Fe-Ti oxide-rich systems. Frost et al. (1988, 1991) proposed the following reactions involving the exchange of Mg^{2+} and Fe^{2+} between Fe-Ti oxides and mafic silicate minerals:

$2MgFe_2O_4$(in Mt)+Fe_2SiO_4(in Ol)=$2Fe_3O_4$(in Mt)+Mg_2SiO_4(in Ol) (1)

$2MgTiO_3$(in Ilm)+Fe_2SiO_4(in Ol)=$2FeTiO_3$(in Ilm)+Mg_2SiO_4(in Ol) (2)

Usually decreasing temperature and increasing Fe-Ti-V oxides contents will promote the reaction towards the right direction, causing an increase of Mg# in clinopyroxene and Fo content in olivine (Frost et al., 1988, 1991). In the LZ, the bulk Fe-Ti-V oxides content is relatively low and the amount of mafic minerals, especially clinopyroxene is high. Thus, sub-solidus re-equilibrations are not expected to significantly modify the Mg# of the clinopyroxenes as well as Fo content in olivine. However, a positive correlation between the Fo content in olivine and the amount of Fe-Ti-V oxides can be noted along the stratigraphic column in the MZ (Fig. 2.11a and d). In each unit of the MZ, the highest Fo content in olivine always occurs in samples that were collected within or close to the ore layers. Meanwhile, Fe-Ti-V oxides in the ore layers of Hongge MZ also have higher Mg contents and lower FeO_t content compared to those in the associated magnetite clinopyroxenite layers in the same unit which will promote the Fe-Mg exchange with olivine (Fe-Ti-V oxides data referred from Luan et al., 2014b and our unpublished data). Mn and Ni in these high Fo content olivine layers are more compatible in oxides compared to other layers, which could be explained by sub-solidus reactions (see the above reactions). A similar phenomenon is found in the Kiglapait intrusion in which Fe-Ti oxides enriched ore layers have higher

Fo content olivine compared to the silicate-rich layers (c.f., Morse 1980). The two most representative units in the Hongge intrusion showing the inverse evolution of Fo content in olivine and Fe_2O_3+TiO_2 in the bulk rocks are Unit VI and VIII (Fig. 2.11). Since olivine grains in the MZ show no internal zoning (Fig. 2.8c), this would also imply that this phase was completely re-equilibrated at low temperatures. In contrast to olivine, strong compositional changes of the low Mg# clinopyroxene population along the stratigraphic column from the MZ are not observed in these units (Fig. 2.11c, grey dots), which could be explained by a much faster Fe-Mg equilibration of olivine compared to clinopyroxene (c.f., Zhang et al., 2010). If clinopyroxene would only re-equilibrate partially, an inverse compositional zoning (higher Mg# of the rim) could be expected but such a feature was not observed, which could indicate that the cooling of the intrusion was fast enough to avoid such type of sub-solidus reaction in the MZ (Fig. 2.8d). This further indicates that the different populations of clinopyroxene observed in some samples (red points in Figs. 2.9 and 2.11) must be related to magmatic (primitive) processes. Although Cr_2O_3, MnO_2, TiO_2 and Al_2O_3 contents in the low Mg# clinopyroxene are higher compared to the high Mg# clinopyroxene which might be taken for the products from sub-solidus re-equilibration with Fe-Ti-V oxides, however, the appearance of high Mg# clinopyroxene shows no correlation with the bulk Fe_2O_3+TiO_2 content changes, particularly for Unit III and VI (Fig. 2.11c and d). In these units, high Mg# clinopyroxenes are observed but, the Fe_2O_3+TiO_2 content in bulk rocks remains constant across the stratigraphy (Unit III) or even decreases (Unit VI) to the top. In addition, compared to clinopyroxene, olivine is more easily influenced by sub-solidus re-equilibration, however, Fo content of olivine in high Mg# clinopyroxene samples is relatively low, strongly indicating that the high Mg# clinopyroxene population is not formed by sub-solidus re-equilibration. Higher SiO_2 and CaO content in high Mg# clinopyroxene also cannot be explained by sub-solidus re-equilibration with oxides for the reason that these elements are both rare in oxides and have low diffusion rate. The observations described above suggest that sub-solidus re-equilibration effects in the Hongge intrusion are mainly concentrated in the MZ and might have more influence on the composition of olivine compared to clinopyroxene.

Previous studies have revealed that clinopyroxene in the Hongge layered intrusion contains abundant oxide lamellae along its prismatic cleavages (e.g., Luan et al., 2014b) which might also influence the Mg# of clinopyroxene (Fig. 2.8b). However, in our samples, the high Mg# clinopyroxene is usually about 10 % higher than the low Mg# clinopyroxene. If the high Mg# clinopyroxene populations (Mg# = ~90) are the products of late-stage oxide exsolution under slow cooling conditions, then these crystals should have a significant volume of oxide lamellae. However, Fig. 2.8a shows that the high Mg# clinopyroxenes (Mg# = ~90) almost have no oxide lamellae compared to the low Mg# clinopyroxenes. Thus we conclude that the high Mg# clinopyroxene population is not caused by oxide exsolution.

2.6.4 Primitive magma replenishment

Replenishment of more primitive magma (compared to the residual melts in shallow magma chamber) is another possible mechanism to explain the mineral compositional reversals in layered intrusions (e.g., Namur et al., 2010; Yuan et al., 2017). Usually, plagioclase is an ideal mineral to detect a replenishment event, because its composition would not be easily affected by trapped liquid shift or sub-solidus re-equilibration as stated above (Grove et al., 1984). However, plagioclase in the investigated core mainly occurs in the UZ, and compositional reversals of olivine and clinopyroxene need to be analyzed to find evidence for magma replenishment events in the MZ and LZ. As discussed above, variations of Fo content in olivine in the MZ may be related to sub-solidus reactions, so the olivine composition reversals in the MZ cannot accurately reflect magma replenishment events. The most typical feature for clinopyroxene in the MZ and LZ of Hongge intrusion is that in some samples especially near the boundary of the lithological units, two clinopyroxene populations with different Mg# could be identified. In order to check the equilibration between olivine and clinopyroxene in the Hongge intrusion, we selected olivine in the LZ that is less influenced by sub-solidus re-equilibration to estimate the Mg# of clinopyroxene in the same horizon. Based on the expected K_D $(FeO/MgO)^{olivine}/(FeO/MgO)^{liquid}$ of 0.3 for basaltic systems at shallow depths (Roeder and Emslie, 1970), we selected the highest Fo content of olivine in the LZ (~80 mol % in sample No. 689) to calculate the Mg# of the equilibrated clinopyroxene within the sample. Calculations show that the Mg# of clinopyroxene equilibrated with olivine in the LZ is about 81 which is almost the same as we observed in our sample (Mg# 78 in sample No. 689). Hence, these olivines (Fo80) and clinopyroxenes (Mg# =~78) could crystallize from basaltic melts in a shallow magma chamber. On the other hand, the high Mg# clinopyroxene population (Mg# =~90) in the LZ cannot crystallize together with the olivine (Fo80) in the same sample. Thus, we conclude that these high Mg# clinopyroxenes crystallized from a more primitive magma that differentiated at depth prior to the emplacement into the current chamber. Such a hypothesis was proposed by Tao et al. (2015) in the ELIP magmatic plumbing system, suggesting that the high Mg# clinopyroxene phenocryst (Mg# =~90) crystallized from picrite at a deeper magma chamber (20~30km) and high temperature (1190-1275 ℃). Kamenetsky et al. (2012) also found that the high Mg# clinopyroxenes (Mg# =~90) in picrites in ELIP have less TiO_2 and more CaO compared to the low Mg# clinopyroxene (Mg# =~75 to 80) in basalts. These studies are both consistent with the high Mg# clinopyroxene population in our samples. Thus, we conclude that the high Mg# clinopyroxenes in our samples crystallized from picritic magma in a deeper-seated magma chamber and were carried to the shallow magma chamber by magma replenishment events. Magma replenishment is also needed to explain the repeated variation of oxide proportions along the LZ and MZ (marked by the bulk Fe_2O_3+TiO_2 content; Fig. 2.11d). In this case, the domains with high bulk Fe_2O_3+TiO_2 could reflect domains particularly affected by replenishing magmas (Song et al., 2013). MELTS modeling results from Song et al. (2013) show that extensive fractionation crystallization of high Mg# minerals (e.g., olivine and clinopyroxene, etc.) in picritic magma would lead a Fe-Ti enrichment in the fractionated melts. The domains in which strong variations of oxide contents are observed are also those in which there is a strong fluctuation of the Mg# of clinopyroxene and in which different populations of clinopyroxenes are observed. In both Units IX and X, the An content of plagioclase firstly shows an increasing trend and then a gradual decrease towards the top of the core, which can be also interpreted as a record of magma replenishment, similar to the Bushveld Complex as reported by Yuan et al. (2017). Therefore, we believe that the occurrence of different populations of clinopyroxenes within one sample (some with high Mg#) and the evolution of the An content of plagioclase are mainly caused by magma replenishment events. Cumulus albite in Unit XI is another important indicator for possible magma replenishment event. Usually, relatively Fe-rich mafic silicates and Na-rich plagioclase (or albite) occurrence resemble a Sandwich horizon in layered intrusions (McBirney, 1996). One typical feature for the Sandwich horizon is the enrichment of incompatible elements due to mass balance such as Zr. However, in our samples, Zr content in Unit XI shows no enrichment compared to other units that argue against the typical Sandwich horizon (see Supplementary Table 2.1). One possible explanation is that the uppermost UZ marks the level at which the loss of residual melt occurred (Pang et al., 2009). Mineral compositions associated with the reversal at the base of Unit XI clearly show that the liquid did not differentiate to complete the evolution (Fig. 2.9b and c). Therefore, the loss of residual melt was likely concurrent with the major recharge of magma at the base of Unit XI, which displaced and pushed the liquid out of the chamber. The missing residual melt probably underwent further differentiation and eventually crystallized to form a coeval peralkaline granite similar to those intimately associated with the Panzhihua, Baima and Taihe layered intrusions (Shellnutt and Zhou, 2007; Shellnutt et al., 2009, 2011a; Shellnutt and Jahn, 2010). Accordingly, from bottom to the top, at least eleven sections along the core ZK11003 can be identified in which the fluctuations of mineral modes and compositions are indicative of replenishment events involving more primitive magmas. The samples recording these magma mixing events are marked in grey in Figs. 2.9 and 2.11.

Based on the above discussion, primitive replenishing magma events would be the most possible explanation controlling the composition reversals and occurrence of different cumulus mineral populations. The high Mg# clinopyroxenes were not formed by *in-situ* crystallization but precipitated in another deep-seated reservoir. A similar scenario, in which replenishing magmas may carry a certain proportion of phases that crystallized in less evolved deep-seated magma chambers, has also been advocated in other layered intrusions such as the Sept Iles intrusion and Bushveld Complex (e.g., Namur et al., 2010; Yuan et al., 2017). In the Hongge intrusion, evidence of replenishments by crystal-laden magmas is also provided by the existence of samples with very high olivine modal proportions in the MZ (Unit VII).

In the LZ and MZ, high Fo olivine has not been observed in the Hongge intrusion. One possible explanation is that due to their high density (3.2 g/cm^3, data from Song et al., 2013), the early-crystallized olivines sank to the bottom of the deep-seated chamber and thus were not carried upwards into the shallow chamber. Alternatively, if olivine formed in the deep-seated chamber then it may have been carried together with high Mg# clinopyroxene, such olivine would re-equilibrate with the hybrid melts formed by the mixing between replenishing magma and residual melts due to the relatively fast diffusion of Fe and Mg, and different olivine populations would not be expected in the shallow magma chamber. However, high Mg# clinopyroxenes mainly occur in core sections in which modal proportions of olivine change strongly and in which olivine composition reversals are observed (Fig. 2.11b and c). The high Mg# clinopyroxenes are observed in samples with the lowest Fo content in olivine or just below in the stratigraphy. In these samples, the modal proportion of olivine reaches the highest value. This is best displayed in Units VI and VII. The high modal proportion of olivine in some samples may also indicate that the replenishing magma carried some olivine from the deep magma chamber, in addition to the high Mg# clinopyroxene. Similar to clinopyroxene, for the plagioclase in the UZ, two populations of plagioclase with distinct An content can be observed within a single sample, and the occurrence of different plagioclase populations (high and low An content) simultaneously in the same thin sections is correlated to high modal proportions of plagioclase in these samples. Since the diffusivities of cations in plagioclase are much lower compared to that in olivine and clinopyroxene (Grove et al., 1984), these high An content plagioclases (An content =~69 in sample No. 283) may also be carried by replenishing magmas. For some plagioclase-rich samples such as No. 287 and 193 in the UZ, complex irregular compositional changes from the rim to the core can be also found (Fig. 2.10). Among these plagioclases, some of them show a clear compositional change from Ab-rich core to An-rich rim. This reversal may be interpreted by a crystallization An-rich rim from a more primitive Ca-rich magma.

2.6.5 Onset of Fe-Ti-V oxide crystallization and mineralization in the Hongge intrusion

As discussed above, it is likely that magmas from different reservoirs (shallow and deep-seated magma chambers) became more evolved. Based on MELTS modeling, Luan et al. (2014b) suggested that the nominally dry picritic magma in the deep chamber (estimated to be at ~5kbar) crystallized olivine as the liquidus phase, followed by spinel and clinopyroxene. Following the calculation of Luan et al. (2014b), extensive fractionation of these minerals would lead to a residual melt gradually enriched in Fe and Ti, containing up to ~18 wt. % Fe_2O_{3T} and 4 wt.% TiO_2. The composition of the melt after fractionation in the deep magma chamber is usually considered to be compositionally similar to the high-Ti ferrobasalts (c.f., Shellnutt, 2014). Multiple magma replenishment events seem to be an efficient mechanism to supply continuously primitive magmas with Fe-Ti enriched melts. When these fractionated Fe-Ti-rich melts carrying high Mg# clinopyroxene are transferred from the deep-seated chamber into the shallow magma chamber by replenishment, the water content in the replenishing magmas is supposed to be relatively low because the parental picritic magmas were probably nearly dry.

On the other hand, the widespread occurrence of magmatic hornblende and minor phlogopite both in the LZ and MZ indicate that the crystallizing magmas are hydrous at some stage and that the melt water contents may be high enough in late crystallization stages to promote the formation of hydrous phases (Howarth and Prevec, 2013b). The general absence of plagioclase both in the LZ and MZ also support a hydrous system, as water could suppress the crystallization of plagioclase (e.g., Gaetani and Grove, 1998; Botcharnikov et al., 2008; Feig et al., 2010; Almeev et al., 2012). If the recharging primitive magmas are almost anhydrous as proposed by Liao et al. (2015 and reference therein), then the hydrous nature of the ore-forming magma could be related to an external introduction of water, e.g., by assimilation from wall rocks (e.g., Ganino et al. 2008, 2013). Ganino et al. (2008) also suggested that the interaction with wall rocks (e.g. carbonate) could also elevate the oxygen fugacity (QFM to QFM+1.5), which would also promote precipitation of Fe-Ti-V oxides (Pang et al., 2007, 2008b).

Experimental results show that high water activity in ferrobasatic magma would promote the formation of Fe-Ti oxides during early crystallization stages (Botcharnikov et al., 2008). In the MZ, the replenishing magma from the deep-seated chamber is mainly composed of high Mg# clinopyroxene and possibly olivine as well as relatively Fe-Ti enriched melt due to early fractionation. Thus mixing between the replenishing magma and hydrous residual melts from the LZ could facilitate the precipitation of oxides and contribute to the formation of thick ore layers. In addition, mixing between replenishing primitive magma (nominally dry) and hydrous residual melts can destabilize silicate minerals. This may also explain why the massive ores at Hongge intrusion exclusively occur in the MZ.

Hence, we propose a multistage Fe-Ti-V oxide enrichment model involving the continuous replenishment of crystal-laden primitive magma from a deep-seated chamber. Although the origin of the water is not very clear so far (magmatic or external source), a mixing between a water-poor more primitive magma with a Fe-Ti enriched melt due to fractionation and a crystallizing magma with hydrous residual melt under oxidizing conditions are among the key factors leading to the precipitation of large volume of thick massive Fe-Ti-V oxide ores in the MZ.

2.7 Conclusions

New systematic bulk-rock compositions, precise mineral modes determined with SEM, and detailed microprobe analyses of plagioclase, clinopyroxene, and olivine from drill core of the Hongge layered intrusion allow us to come up with the following conclusions.

The formation of the Hongge layered intrusion is the result of several replenishment events. At least eleven major primitive magma replenishment events have been identified. Lithological units correlate well with compositional reversals of minerals. The occurrence of various mineral populations suggests that the replenishing magmas are crystal-laden magmas, containing i.e, high Mg# clinopyroxenes in the transporting melt. Due to extensive fractionation of the primitive minerals, a Fe-Ti enriched residual melt (transporting melt) is expected. The mixing between hydrous residual melts in the shallow chamber and replenishing magma with Fe-Ti enriched melts may be the key factor controlling the precipitation of high amounts of Fe-Ti-V oxides. Multiple magma replenishment events seem to be an efficient mechanism to supply continuously Fe and Ti to form the massive Fe-Ti-V oxide mineralization in the MZ. This process can also be reconciled with the cyclic units observed in the Hongge layered intrusion.

Chapter 3: Experimental constraints on the crustal differentiation of high-Ti basalts in Emeishan Large Igneous Province, SW China: Implications for the formation of Fe-Ti oxide ore-bearing layered intrusions

Dachuan Wang[1], Tong Hou[2], Roman Botcharnikov[3], Sarah Haselbach[1], Andreas Klügel[4], Meng Wang[2], Zhaochong Zhang[2], François Holtz[1]

[1]Institut für Mineralogie, Leibniz Universität Hannover, Hannover, Germany; [2]State Key Laboratory of Geological Processes and Mineral Resources, China University of Geosciences, Beijing, China; [3]Institut für Geowissenschaften, Johannes Gutenberg Universtät Mainz, Mainz, Germany; [4]Fachbereich Geowissenschaften, Universtät Bremen, Germany

Abstract

Several late Permian mafic-ultramafic layered intrusions host giant Fe-Ti oxide ore deposits in Emeishan Large Igneous Province (ELIP), SW China. Their metallogenesis is enigmatic and hotly debated. Nevertheless, they are believed to have a parental magma with composition resemble to the coeval erupted high-Ti flood basalts. Hence, the crustal differentiation of such magmas had unanimously played an important role during the formation of ore deposits. Here we report the crystallization experiments carried in internally heated pressure vessels using a representative high-Ti basaltic composition to investigate its differentiation at crustal depths. The experiments were conducted in the temperature interval 950-1200 ℃ at both 300 and 100 MPa with variable water activities (aH_2O = 0-1). The oxygen fugacity (fO_2) was controlled and varied from QFM-1 to QFM+3.3 log units (whereas QFM corresponds to quartz-fayalite-magnetite). The comparison of the natural basalts differentiation trends with the experimental melts allow us to constrain the differentiation conditions of Emeishan high-Ti basalts. The results indicate that the high-Ti basalts could form in a temperature range of ~ 1150 to 950 ℃, within a wide range of redox condition, i.e., QFM-1 to QFM+2, and at shallow depth (~3-10 km). In addition, water activity during differentiation of high-Ti basalts could vary widely from nominally dry to water-saturated conditions. Compositions of experimental minerals are in good agreement with those minerals from Fe-Ti oxide ore-bearing layered intrusions, confirming that high-Ti basaltic magma can represent the parental to the Fe-Ti oxide ore-bearing layered intrusions. Thus, the experimental phase equilibria could be used to determine the P-T-fO_2-aH_2O conditions of Panzhihua and Hongge layered intrusion in ELIP. The comparison of experimental cotectics and natural mineral assemblages indicate that Panzhihua intrusion formed in a high fO_2, low T-P-aH_2O condition while Hongge intrusion crystallized from a low fO_2, high T-P-aH_2O conditions.

Key words: Emeishan Large Igneous Province; high-Ti basalts; Fe-Ti oxides; layered intrusions; crystallization experiments.

3.1 Introduction

The Emeishan Large Igneous Province (ELIP) in southwestern China, is believed to be genetically related to a Permian mantle plume (e.g., Chung and Jahn 1995; Zhang et al., 2006; Xu et al., 2007). It covers about 5×10^6 km^2 (Song et al., 2001; Boven et al., 2002; Ali et al., 2004; Xiao et al., 2004a, 2004b), and comprises flood continental basalts, mafic-ultramafic intrusions, and contemporaneous felsic and calc-alkaline rocks (e.g., Xu et al., 2001; Zhou et al., 2002b; Shellnutt and Zhou, 2008; Shellnutt et al., 2009; Song et al., 2009). According to the TiO_2 contents and Ti/Y ratios, Xu et al. (2001) divided the flood basalts into two types: 1) the high-Ti series [TiO_2 (wt.%) > 2.5, Ti/Y > 500] and 2) the low-Ti series [TiO_2 (wt.%) < 2.5, Ti/Y < 500]. Cotemporaneous mafic-ultramafic intrusions (~ 260 Ma, Zhong et al., 2006) are important parts of ELIP and contain several World-class Fe-Ti oxide deposits, as well as several Cu-Ni-(PGE) sulfide deposits (e.g. Zhang et al., 2009 and references therein). Among these ore-bearing intrusions, Fe-Ti oxide mineralization is always considered to be genetically related to high-Ti basalts (e.g., Zhou et al., 2005; Hou et al., 2011; Song et al., 2013) Although the formation mechanisms of these Fe-Ti oxide ore-bearing layered intrusions in ELIP had been studied since the 80s last century, the timing of the onset of Fe-Ti oxides and the origin of Fe-Ti oxide-rich layers are still controversial. Proposed models include: 1) fractional crystallization coupled with gravity sorting (e.g., Song et al., 2013); 2) silicate liquid immiscibility from the high-Ti basalts (e.g., Zhou et al., 2005; Wang et al., 2017); 3) magma replenishment and mixing under hydrous condition with variation in redox condition or pressure (e.g., Howarth and Prevec, 2013a, b), and 4) diffusion controlled crystallization (e.g., Dong et al., 2022). However, the above models still cannot fully interpret the formation of massive Fe-Ti oxide ores. This is because a comprehensive understanding of differentiation of high-Ti basalts in the crust is lacking as most studies rely only on field or microscopic observations and thermodynamic modelling (e.g., Song et al., 2013). In other words, the absence of experimental constraints on the differentiation of the high-Ti basaltic magmas in the crust is a significant limitation for models explaining the Fe-Ti oxide mineralization in ELIP. Since the Fe-Ti oxide ore-bearing layered intrusions formed at a relatively shallow depth (~3 to 10 km; Song et al., 2013; Luan et al., 2014b), crystallization experiments of the high-Ti basalts at upper crustal pressure, i.e., ranging from 100 to 300 MPa, can significantly improve our understanding of the crustal differentiation of high-Ti basalts and the Fe-Ti oxides mineralization.

Previous studies proposed that H_2O contents in ELIP flood basalts are relatively low (~0.5 to 0.7 wt.%, Hanski et al., 2010), similar to those related to non-subduction-related plumes (e.g., Hawaiian, Hauri, 2002; Kerguelen, Wallace, 2002). Nevertheless, a recent study on Emeishan picrites (Liu et al., 2017) indicate that the volcanic rocks in ELIP might evolve in relatively hydrous conditions, especially during the formation of the Fe-Ti oxide ore-bearing layered intrusions. Volatiles, and especially water, have a dramatic effect on the crystallization temperatures, phase relations and compositions of minerals, which could shift the tholeiitic evolution to a calc-alkaline trend (e.g., Sisson and Grove, 1993; Botcharnikov et al., 2008). Hence, any accurate interpretation of natural data and modelling of differentiation processes of high-Ti basaltic magmas absolutely requires systematic experimental quantification of the role of volatiles during crystallization processes in the crust. Although some experimental studies using ferrobasaltic compositions have been conducted at both dry and hydrous conditions (e.g., Sisson and Grove, 1993; Toplis and Corrall, 1995; Feig et al., 2006, 2010; Botcharnikov et al., 2008; Husen et al., 2016), these starting compositions are rather different from the Emeishan high-Ti basalt, especially in terms of TiO_2 and Al_2O_3 contents (Supplementary Table 3.1). Hence, new systematic experiments under crustal pressure with the Emeishan high-Ti basalt is needed, especially in the presence of volatiles. The results, including crystallization sequence, melt evolution, and especially the stability field of Fe-Ti oxides, are expected to improve our understanding on the formation of the Fe-Ti oxide ore-bearing layered intrusions in ELIP.

To systematically determine the effect of intensive parameters [including temperature (T), pressure (P), oxygen fugacity (fO_2), and water activity (aH_2O)] on the liquid line of descent (LLD) during the crustal differentiation of the Emeishan high-Ti basalts, a series of crystallization experiments were conducted with internally heated pressure vessels (IHPV) at various P-T-fO_2-aH_2O conditions. In addition to constraints on LLDs, the obtained data are applied to discuss the role of these intensive parameters on crystallization sequence and stability fields of mineral. In addition, at the end of the paper, a mineralogical comparison between the Fe-Ti oxide ore-bearing layered intrusions and the experimental products provides important information for the understanding Fe-Ti oxides mineralization in ELIP.

3.2 Experimental methods

3.2.1 Starting material

The composition of Emeishan high-Ti basalts varies in a relatively wide range (e.g., GEOROC database). Since this study mainly aims at exploring the crystallization conditions of Fe-Ti oxide ore-bearing layered intrusions, we used the average composition of the high-Ti basalts from the Longzhoushan section (Qi et al., 2008), both temporally and spatially close to the Fe-Ti oxide ore-bearing layered intrusions, as analog to prepare (see Table 3.1).

A synthetic starting glass powder was prepared from a mixture of oxides (SiO_2, TiO_2, Al_2O_3, Fe_2O_3, MgO, P_2O_5) and carbonates ($CaCO_3$, Na_2CO_3, K_2CO_3). According to the natural samples from the marginal or bottom zones of the Fe-Ti oxide ore bearing layered intrusions (e.g., Wang et al., 2008; Bai et al., 2019), chromite is invariably observed as inclusions in cumulus olivine and clinopyroxene. To enhance the crystallization of such Cr-bearing oxides, ~ 0.5 wt. % Cr_2O_3 was added to the starting composition. The starting components were first ground in a rotary mortar and then melted 3 times in a Pt crucible at 1600 ℃, 1 atm, and at the air oxygen condition (log fO_2 = -0.68) to obtain a homogeneous composition. After the third melting, several pieces of glass chips were picked up randomly to check for the homogeneity of the silicate glass with electron microprobe (composition variations expressed as 1 sigma standard deviation are listed in Table 3.1), and the remaining part was ground into fine powder (100-200 μm) with a ball mill machine.

3.2.2 Experimental design

As mentioned above, the Fe-Ti oxide ore-bearing layered intrusions formed at a relatively shallow depth (~3-10 km) through observations of contact relationships with the overlying basalts (e.g., Pang et al., 2008a; Song et al., 2013; Luan et al., 2014b). Hence, in this study, two pressures of 300 MPa and 100 MPa were set to evaluate the possible pressure effects on the formation of the layered intrusions. According to the thermometry studies of Emeishan high-Ti basalts and MELTS simulations on the differentiation of Fe-Ti oxide ore-bearing layered intrusions in ELIP (e.g., Zhang et al., 2013; Liao et al., 2015; Tao et al., 2015), the explored temperature range was set from 1200 to 950 ℃ and experiments were conducted with an interval of 50 ℃. We applied a wide range of water activities to check all the possible conditions in natural systems, i.e., nominally dry to water-saturated conditions. The water activity was varied by conducting fluid present experiments with different proportions of H_2O-CO_2-bearing. Based on the solubility study of H_2O-CO_2-bearing fluids in tholeiitic basalts (Shishkina et al., 2010), added fluid contents were 10 wt.% and 5 wt.% (equivalent to total pure water) for 300 MPa and 100 MPa experiments, respectively, to ensure the presence of a free fluid phase during the experiments. The initial mole fraction of H_2O (X^{fl}_{H2Oini}) was adjusted by adding different proportions of H_2O and silver oxalate (source for CO_2) and varied from $X^{fl}_{H2Oini} = 0$ (nominally dry, pure CO_2 in the fluid) to 1.0 (water saturated, pure H_2O added). To determine the influence of fO_2 variations in our system, two different fO_2 ranges corresponding to QFM + 1 and QFM + 3.3 at water-saturated conditions were applied.

3.2.3 Capsule preparation

All experiments were conducted using $Au_{80}Pd_{20}$ capsules (2.8 mm internal diameter with 0.2 mm thick). The capsule tubes were first annealed in a furnace at 950 ℃ for 10 minutes, then cleaned with distilled water and cut into 15 mm lengths for experiments. Previous studies pointed out that a certain amount of Fe could be lost from starting powders into the capsules during high T-P experiments, especially under reducing conditions and near liquidus conditions (e.g., Botcharnikov et al., 2005, 2008; Almeev et al., 2013). To minimize the Fe loss during experiments, all capsules are pre-saturated with ~0.2-0.3 wt.% Fe following van der Laan and Koster van Groos (1991). The inner surface of the capsules was coated with Fe using an electroplating bath. After electroplating, the preprocessed capsules were annealed in an oven for 48 hours under an $Ar-H_2$ atmosphere at 950 ℃ and 1 atm pressure. This Fe pre-saturation procedure for $Au_{80}Pd_{20}$ capsules has been proved to be a practical way to minimize the influence of Fe loss (e.g., Husen et al., 2016; Veksler and Hou, 2020).

3.2.4 Experimental techniques

Glass powders were firstly put overnight in an oven (110 ℃) before being loaded into the capsules to minimize the amount of adsorbed water. Each Fe pre-saturated capsule was filled with 0-4 μl deionized H_2O with ~36 mg glass powder for 300 MPa experiments and 0-2 μl deionized H_2O with ~38 mg glass powder for 100 MPa. X^{fl}_{H2Oini} was controlled by adding a certain amount of silver oxalate (0-17 mg at 300 MPa and 0-9 mg at 100 MPa). After loading the glass powders and fluid phases, capsules were welded with a graphite arc-welder and then put overnight in an oven at 110 ℃ to ensure that the capsules were well shut. Capsules with loss of weight were discarded for further high-pressure experiments.

High T-P experiments were conducted by internally heated pressure vessels (IHPV) oriented vertically (technical details in descriptions of Berndt et al., 2002). The total pressure was measured and recorded continuously with an uncertainty of about 1 MPa using a strain gauge manometer. The variations of pressure during the experiments were less than 5 MPa. The temperature was monitored with four unsheathed S-type ($Pt-Pt_{90}Rh_{10}$) thermocouples over a length of about 30 mm with an error of less than 5 ℃. Pure argon gas (Ar) was used as a pressure medium in an IHPV for oxidizing experiments. In such experiments, the intrinsic fO_2 of the vessel was determined using a NiPd solid sensor (Schuessler et al., 2008) to be 3.3 log units above the fO_2 of the QFM (quartz-fayalite-magnetite) solid assemblage (hereafter labeled as QFM + 3.3) under water-saturated conditions. The experiments designed for reducing conditions were conducted in a second IHPV pressurized with a mixture of Ar and H_2 gases to adjust the required fH_2 in the vessel and to perform experiments at the desired redox conditions corresponding to the nominal oxygen buffers of QFM + 1 at water-saturated conditions (calculation of fO_2 values is based on the equation of Schwab and Kuestner, 1981). The fH_2 prevailing in the IHPV at high P-T was controlled with a Shaw-membrane (e.g., Scaillet et al., 1992; Berndt et al., 2002). The hydrogen fugacity within the capsule is adjusted as a result of an inward diffusion of hydrogen, and in turn, the oxygen fugacity inside the capsule is buffered through the equilibrium reaction of water formation ($H_2+1/2O_2=H_2O$). Thus, only the water-saturated capsules ($aH_2O = 1$) have the redox conditions of QFM + 1 and QFM + 3.3. In the capsules with $aH_2O < 1$, the oxygen fugacities were more reduced than the intrinsic conditions.

To start the experiments, the capsules were pre-pressurized to about 50 to 80 MPa below the desired pressure due to the gas expansion during the heating procedure and readjusted to the target pressure after the heating process. The temperature was increased from room temperature to 50 ℃ below the target temperature at a rate of 30 ℃/min, then increased slowly to the target temperature at a rate of 10 ℃/min to avoid overheating. To determine the Cr equilibrium distribution between minerals and melts, experiments were carried out for a relatively long duration (5 days) when compared to other reported experiments with basaltic systems (e.g., Berndt et al., 2005; Botcharnikov et al., 2008). Minerals formed from crystallization experiments using glass powder as starting material have usually a relatively small size, especially at high undercooling and dry conditions, leading to problems for an accurate analysis of mineral compositions. In order to grow crystals that are large enough for analysis, temperature cycling was applied, as this procedure was demonstrated to efficiently coarsen the crystallized phases (e.g., Mills and Glazner, 2013; Silva et al., 2017). In this study, the experiments were conducted at constant temperature for the first 24 hours, a cycling of ± 10 ℃ was applied for the following 72 hours and temperature was constant again for the last 24 hours. Using this procedure, we expected that small-size crystals during cycling would dissolve during the high temperature phase, and that crystallization around the large phases would occur at low temperature. At the end of the experiments, the capsules were quenched using a sample holder equipped with a rapid quench facility (Berndt et al., 2002). Although the size of the capsules and T-P conditions inside the vessel would influence the quench rate, abundant successful studies have proved that it was sufficiently fast to avoid quench effects with a rate of about 150 K/s (e.g., Feig et al., 2006, 2010; Botcharnikov et al., 2008).

3.3 Analytical Techniques

3.3.1 Determination of $a\mathrm{H_2O}$ after experiments

After finishing the experiments, the capsules were weighted to ensure that no capsules failed during the experiment. To determine the H_2O and CO_2 content in the existing fluid phase after experiments, the capsules were punctured and weighted following the weight loss method (detailed description see Botcharnikov et al. 2008). The determined fluid phase composition was expressed as X^{fl}_{H2O} [$H_2O/(H_2O+CO_2)$ in mole fraction]. The relationship between X^{fl}_{H2O} and $a\mathrm{H_2O}$ has been derived from abundant empirical and thermodynamic models (e.g., Aranovich and Newton, 1999; Churakov and Gottschalk, 2003; Duan and Zhang, 2006), and the results show that at the investigated pressures the difference between determined X^{fl}_{H2O} and calculated *a*H_2O is within analytical uncertainty for X^{fl}_{H2O}. Thus, for simplicity, the *a*H_2O in this study was assumed to be approximately equal to the determined X^{fl}_{H2O}, and the results for the experiments performed at different T, P, and *f*O_2 are listed in Table 3.2. Because the final X^{fl}_{H2O} in the system relies on multiple parameters such as the initial mole fraction of water added in the capsule, the degree of crystallinity, and the residual melt compositions, the determined results could vary over a wide range and were sometimes significantly different from the desired values. For easy comparison of the experimental results, we will discuss the products based on the initial mole fraction of H_2O (X^{fl}_{H2Oini}) in the fluids.

3.3.2 Calculations of *f*O_2

As mentioned above, the oxygen fugacity inside the capsules was buffered by the diffusion of H_2 through the capsule walls. Hence, the redox conditions of the capsules depend on the external redox conditions in the IHPV and the redox reactions in the capsules. With the determined *a*H_2O values, the *f*O_2 in the experimental capsules was calculated using the equation: $\log fO_2^{capsule} = \log fO_2^{apparent} + 2\log(aH_2O)$ (e.g., Scaillet et al., 1995; Botcharnikov et al., 2005) where $\log fO_2^{apparent}$ is the oxygen fugacity expected in the system at $aH_2O = 1$. The *f*O_2 values (Table 3.2) were also used to calculate the ferric-ferrous ratio in residual melts according to the model of Kress and Carmichael (1991).

3.3.3 Electron microprobe analyses

Experimental products were analyzed using Cameca and JEOL iHP200F microprobe at University of Bremen and Leibniz University Hannover, respectively, with an acceleration voltage of 15 kV. Experimental minerals were analyzed with a 1 μm focused beam and 15 nA current, while glass analysis was conducted with 12 μm defocused beam and 10 nA current. Na and K were analyzed first to minimize the loss with counting times of 8 s, while other elements were fixed at 10 s. Synthetic and natural standards were used for calibrations, including Fe_2O_3, MgO, Al_2O_3, TiO_2, albite (Na), orthoclase (K), chromite (Cr), wollastonite (Si and Ca), and rhodochrosite (Mn).

H_2O concentration in the experimental glasses was determined following the "by difference" method described in Devine et al. (1995) using a series of Mutnovsky basaltic glass standards (Shishkina et al., 2010) containing different H_2O contents (0-7.56 wt.% H_2O). The obtained calibration lines, established for each microprobe session, were used to calculate the actual H_2O concentration of the individual sample (See Supplementary Fig. 3.1, where an example of the calibration line is provided). The uncertainty ranged from ± 0.5 to 0.9 wt% H_2O. Mass balance calculations for phase proportions and estimation of Fe loss or gain from the capsules were determined with an Excel VBA program developed by Li et al. (2020). Glass compositions were not needed to normalize to 100% to exclude the H_2O dissolved in the melt. To quantify the extent of Fe-loss or Fe-gain, the input matrix can be modified by adding an additional column and setting a new artificial "Fe" phase with an assigned composition of 100% FeO. The sum of squared estimate of errors (SSE) for the calculated mass proportions of coexisting phases yields a smaller value. The calculation results are listed in Table 3.2.

3.3.4 Attainment of equilibrium

As mentioned above, the experimental duration of our experiments was significantly longer than that applied for similar crystallization experiments using basaltic systems, implying that kinetic problems due to sluggish crystal growth are not expected. Several lines of evidence support our experiments had reached near-equilibrium conditions. 1) Mineral phase distributions are relatively homogeneous through the capsules, and the minerals have idiomorphic shapes. 2) The samples do not have quench phases or minerals with quench textures (e.g., tails or skeletal forms). 3) Compositions of mineral phases are also homogeneous within the analytical uncertainty. 4) Phase equilibria, and chemical trends of experimentally produced glasses exhibit compositional variations that are consistent with results of

H_2O-bearing experiments obtained in other studies. 4) Mineral-melt and mineral-mineral partitioning coefficients of elements are comparable with previous relevant studies for most runs (see discussions below).

Table 3.1 The composition of starting high-Ti basaltic glass

N	**SiO_2**	**TiO_2**	**Al_2O_3**	**Cr_2O_3**	**FeO**	**MnO**	**MgO**	**CaO**	**Na_2O**	**K_2O**	**P_2O_5**	**Total**
20	49.85±0.16	3.29±0.06	11.05±0.13	0.47±0.01	12.74±0.06	0.21±0.05	7.84±0.07	10.35±0.10	1.99±0.08	1.35±0.03	0.29±0.01	99.41±0.35

N: number of analyses

Table 3.2 Experimental conditions and phase relations

Run	T (℃)	P (MPa)	fH_2 (bar)	X^{fl}_{H2Oini}	aH_2O	Log fO_2	ΔQFM_{calc}	Phases assemblages and proportions	SSE	Fe loss or gain (%)
	ΔQFM nominal = +3.3									
EM01	1200	300	—	1	1	-4.8	3.3	Gl(100)	0.34	+12
EM02	1200	300	—	0.6	0.6	-5.2	2.9	Gl(98.3), Mt(1.7)	0.12	+14
EM03	1200	300	—	0.2	0.13	-6.6	1.5	Gl(98.6), Mt(1.4)	0.17	+14
EM04	1200	300	—	0	0.07	-7.1	1.0	Gl(98.5), Mt(1.5)	0.23	+15
EM05	1150	300	—	1	1	-5.4	3.3	Gl(97.0), Mt(3.0)	0.22	+14
EM06	1150	300	—	0.6	0.26	-6.5	2.1	Gl(97.6), Mt(2.4)	0.17	+10
EM07	1150	300	—	0.2	0.1	-7.4	1.3	Gl(88.2), Mt(2.3), Cpx(10.0), Ol(-0.5)	0.03	+7
EM08	1150	300	—	0	0.04	-8.2	0.5	Gl(85.5), Mt(1.7), Cpx(13.8), Ol(-1.1)	0.05	-2
EM09	1100	300	—	1	1	-6.0	3.3	Gl(95.6), Mt(4.4)	0.21	+8

EM10	1100	300	—	0.6	0.38	-6.8	2.5	Gl(81.7), Mt(6.3), Cpx(12.0)	0.10	+7
EM11	1100	300	—	0.2	0.13	-7.8	1.5	Gl(64.6), Mt(6.5), Cpx(30.4), Opx(-1.49)	0.04	+5
EM12	1100	300	—	0	0.05	-8.6	0.7	Gl(62.7), Mt(4.6), Cpx(33.1), Opx(-0.94), Pl(0.54)	0.05	-2
EM13	1050	300	—	1	1	-6.7	3.3	Gl(77.7), Mt(4.6), Cpx(12.7), Hm(5.0)	0.13	+8
EM14	1050	300	—	0.6	0.49	-7.3	2.7	Gl(61.2), Mt(4.0), Cpx(28.3), Ilm(6.47)	0.12	-1
EM15	1050	300	—	0.2	0.21	-8.0	1.9	Gl(37.8), Mt(6.2), Cpx(37.2), Ilm(5.6), Opx(0.22), Pl(13.0)	0.15	+6
EM16	1050	300	—	0	0.04	-9.5	0.5	Close to solidus	—	—
EM17	1000	300	—	1	1	-7.4	3.3	Gl(62.2), Mt(2.8), Cpx(25.0), Hm(10.0)	0.33	+4
EM18	1000	300	—	0.6	0.63	-7.8	2.9	Gl(45.2), Mt(5.6), Cpx(36.2), Hm(7.33), Opx(0.64), Pl(4.89), Ap(0.09)	0.05	+9
EM19	1000	300	—	0.2	0.28	-8.5	2.2	Close to solidus	—	—
EM20	1000	300	—	0	0.19	-8.9	1.9	Close to solidus	—	—
	ΔQFM nominal = +1									
EM21	1200	300	14.45	1	1	-7.1	1	Gl(99.2), Chr(0.8)	0.13	+21

EM22	1200	300	14.45	0.6	0.54	-7.6	0.5	Gl(99.3), Chr(0.7)	0.20	+1
EM23	1200	300	14.45	0.2	0.3	-8.1	-0.1	Gl(99.4), Chr(0.6)	0.17	-9
EM24	1200	300	14.45	0	0.12	-8.9	-0.8	Gl(99.2), Chr(0.8)	0.16	-10
EM25	1150	300	13.64	1	1	-7.7	1	Gl(99.2), Chr(0.8)	0.15	+2
EM26	1150	300	13.64	0.6	0.49	-8.3	0.4	Gl(99.2), Chr(0.8)	0.17	-9
EM27	1150	300	13.64	0.2	0.25	-8.9	-0.2	Gl(97.9), Chr(0.8), Cpx(2.0), Ol(-0.7)	0.09	-28
EM28	1150	300	13.64	0	0.23	-9.0	-0.3	Gl(98.6), Chr(0.8), Cpx(1.5), Ol(-0.9)	0.09	-26
EM29	1100	300	12.81	1	1	-8.3	1	Gl(98.7), Chr(1.3)	0.26	+5
EM30	1100	300	12.81	0.6	0.49	-8.9	0.4	Gl(83.1), Chr(0.7), Cpx(11.5), Ol(4.7)	0.02	-2
EM31	1100	300	12.81	0.2	0.26	-9.5	-0.2	Gl(67.1), Chr(0.7), Cpx(24.9), Ol(7.3)	0.15	-3
EM32	1100	300	12.81	0	0.24	-9.5	-0.2	Gl(67.4), Chr(0.8), Cpx(22.9), Ol(8.9)	0.10	-8
EM33	1050	300	11.95	1	1	-9.0	1	Gl(86.1), Mt(4.4), Cpx(8.1), Ol(1.5)	0.07	+10
EM34	1050	300	11.95	0.6	0.53	-9.5	0.5	Gl(68.4), Mt(4.9), Cpx(24.8), Ol(1.4), Ilm(0.5)	0.05	-2
EM35	1050	300	11.95	0.2	0.31	-10.0	0	Gl(65.9), Mt(3.0), Cpx(27.6), Ol(2.3), Ilm(1.2)	0.02	-5
EM36	1050	300	11.95	0	0.17	-10.5	-0.5	Gl(48.6), Mt(1.7), Cpx(41.9), Ol(-0.9), Ilm(3.0), Opx(0.8), Pl(5.0)	0.06	-9
EM37	1000	300	11.06	1	1	-9.7	1	Gl(66.4), Mt(8.2), Cpx(23.2), Ol(1.6), Ilm(0.7)	0.10	+8

EM38	1000	300	11.06	0.6	0.52	-10.3	0.4	Gl(55.9), Mt(5.3), Cpx(38.5), Ol(5.9), Ilm(2.5), Opx(-7.9), Pl(-0.3)	0.01	-1
EM39	1000	300	11.06	0.2	0.21	-11.1	-0.4	Gl(33.9), Mt(3.9), Cpx(41.3), Ol(2.6), Ilm(3.1), Opx(1.0), Pl(13.6), Ap(0.73)	0.02	+0
EM40	1000	300	11.06	0	0.1	-11.7	-1	Close to solidus	—	—
EM41	950	300	10.15	1	1	-10.5	1	Gl(46.2), Mt(6.2), Cpx(32.3), Ilm(2.1), Opx(-1.0), Ap(0.2), Am(14.0)	0.01	+2
EM42	950	300	10.15	0.6	0.63	-10.9	0.6	Close to solidus	—	—
	ΔQFM nominal = +3.3									
EM43	1200	100	—	1	1	-4.9	3.3	Gl(97.8), Mt(2.2)	0.19	+16
EM44	1200	100	—	0.6	0.54	-5.5	2.8	Gl(98.1), Mt(1.9)	0.16	+10
EM45	1200	100	—	0.2	0.24	-6.2	2.1	Gl(98.7), Mt(1.3)	0.17	+10
EM46	1200	100	—	0	0.1	-6.9	1.3	Gl(99.1), Mt(0.9)	0.20	+2
EM47	1150	100	—	1	1	-5.5	3.3	Gl(95.8), Mt(4.2)	0.13	+19
EM48	1150	100	—	0.6	0.42	-6.3	2.6	Gl(96.6), Mt(3.7), Ol(-0.3)	0.03	+19
EM49	1150	100	—	0.2	0.24	-6.8	2.1	Gl(98.0), Mt(1.7), Ol(0.3)	0.30	+19

EM50	1150	100	—	0	0.03	-8.6	0.3	Gl(98.3), Mt(1.5), Ol(0.2)	0.20	+15
EM51	1100	100	—	1	1	-6.2	3.3	Gl(94.8), Mt(5.2)	0.13	+6
EM52	1100	100	—	0.6	0.37	-7.0	2.4	Gl(79.2), Mt(7.5), Cpx(13.3)	0.13	+7
EM53	1100	100	—	0.2	0.13	-7.9	1.5	Gl(71.4), Mt(6.5), Cpx(22.6), Ol(-0.5)	0.03	+7
EM54	1100	100	—	0	0.1	-8.2	1.3	Gl(70.8), Mt(4.4), Cpx(24.4), Ol(0.4)	0.02	-2
EM55	1050	100	—	1	1	-6.9	3.3	Gl(65.0), Mt(14.67), Cpx(23.0), Hm(-9.2), Psb(6.6)	0.16	-5
EM56	1050	100	—	0.6	0.5	-7.5	2.7	Gl(59.0), Mt(9.7), Cpx(30.6), Hm(-1.2), Psb(3.4), Opx(-1.6)	0.06	+4
EM57	1050	100	—	0.2	0.28	-8.0	2.2	Gl(43.1), Mt(10.8), Cpx(36.7), Hm(-6.2), Psb(6.4), Opx(0.9), Pl(9.5)	0.05	+8
EM58	1050	100	—	0	0.15	—	—	Gl(36.8), Mt(16.8), Cpx(38.2), Hm(-14.1), Psb(9.3), Opx(-0.6), Pl(13.6)	0.01	+2
EM59	1000	100	—	1	1	-7.6	3.3	Gl(53.1), Mt(13.8), Cpx(32.9), Hm(-6.2), Psb(6.4)	0.11	-4
EM60	1000	100	—	0.6	0.58	-8.1	2.8	Gl(36.9), Mt(11.8), Cpx(35.8), Hm(-3.7), Psb(5.8), Opx(1.1), Pl(12.1)	0.04	+6

EM61	1000	100	–	0.2	0.16	-9.2	1.7	Close to solidus	–	–
EM62	1000	100	–	0	0.1	-9.6	1.3	Close to solidus	–	–
EM63	950	100	–	1	1	-8.5	3.3	Gl(34.9), Cpx(35.3), Hm(15.3), Psb(-1.7), Opx(4.2), Pl(11.5), Ap(0.5)	0.08	+5
EM64	950	100	–	0.6	0.6	–	–	Close to solidus	–	–
	ΔQFM nominal = +1									
EM65	1200	100	5.13	1	1	-7.2	1	Gl(98.9), Chr(1.1)	0.16	+18
EM66	1200	100	5.13	0.6	0.46	-7.9	0.3	Gl(99.1), Chr(0.9)	0.18	+19
EM67	1200	100	5.13	0.2	0.25	-8.4	-0.2	Gl(99.3), Chr(0.7)	0.16	-4
EM68	1200	100	5.13	0	0.14	-8.9	-0.7	Gl(99.3), Chr(0.7)	0.16	-13
EM69	1150	100	4.92	1	1	-7.8	1	Gl(99.0), Chr(1.0)	0.13	+4
EM70	1150	100	4.92	0.6	0.56	-8.3	0.5	Gl(99.7), Chr(1.2), Ol(-0.9)	0.14	-4
EM71	1150	100	4.92	0.2	0.26	-9.0	-0.2	Gl(98.7), Chr(1.0), Ol(0.3)	0.02	-10
EM72	1150	100	4.92	0	0.2	-9.2	-0.4	Gl(98.2), Chr(0.9), Ol(0.9)	0.03	-14
EM73	1100	100	4.69	1	1	-8.5	1	Gl(96.7), Chr(2.1), Ol(1.2)	0.08	+7
EM74	1100	100	4.69	0.6	0.52	-9.0	0.4	Gl(88.3), Chr(1.8), Cpx(7.6), Ol(2.3)	0.07	-5

EM75	1100	100	4.69	0.2	0.33	-9.4	0	Gl(82.7), Chr(1.6), Cpx(13.1), Ol(2.6)	0.08	-9
EM76	1100	100	4.69	0	0.2	-9.9	-0.4	Gl(78.7), Chr(1.2), Cpx(17.7), Ol(2.5)	0.06	-5
EM77	1050	100	4.47	1	1	-9.2	1	Gl(76.4), Mt(6.2), Cpx(15.6), Ol(1.8)	0.05	+8
EM78	1050	100	4.47	0.6	0.53	-9.7	0.5	Gl(67.9), Mt(5.4), Cpx(24.4), Ol(2.4)	0.02	-1
EM79	1050	100	4.47	0.2	0.28	-10.3	-0.1	Gl(56.3), Mt(4.5), Cpx(30.2), Ol(3.4), Ilm(1.1), Pl(4.5)	0.01	-6
EM80	1050	100	4.47	0	0.22	-10.5	-0.3	Gl(49.4), Mt(2.6), Cpx(35.2), Ol(3.2), Ilm(2.3), Pl(7.5)	0.03	-6
EM81	1000	100	4.23	1	1	-9.9	1	Gl(56.9), Mt(11.1), Cpx(30.7), Ol(0.6), Ilm(0.85)	0.03	+7
EM82	1000	100	4.23	0.6	0.6	-10.3	0.56	Gl(34.3), Mt(9.0), Cpx(40.1), Ol(-0.9), Opx(0.6), Ilm(2.1), Pl(14.0), Ap(0.2)	0.01	+3
EM83	1000	100	4.23	0.2	0.21	—	-0.4	Close to solidus	—	—
EM84	1000	100	4.23	0	0.1	—	-1	Close to solidus	—	—
EM85	950	100	3.98	1	1	-10.7	1	Gl(38.4), Mt(9.8), Cpx(37.6), Ol(1.6), Opx(0.6), Ilm(2.7), Pl(8.9), Ap(0.4)	0.03	+5
EM86	950	100	3.98	0.6	0.55	—	0.48	Close to solidus	—	—

—, not determined.

3.4 Results

3.4.1 General remarks

The phase relations obtained at 300 MPa and 100 MPa are listed in Table 3.2. The crystallizing phases (Supplementary Figs. 3.2, 3.3) include chromite (Chr), magnetite (Mt), olivine (Ol), clinopyroxene (Cpx), ilmenite (Ilm), hematite (Hm), pseudobrookite (Psb), orthopyroxene (Opx), plagioclase (Pl), apatite (Ap) and amphibole (Am) and were successfully analyzed in most of the runs except several samples with high crystallinity or tiny crystals (< 2 μm).

Although the starting materials and capsules were pre-dried and immediately welded shut, microprobe analyses with glass compositions in the nominally dry experiments still revealed the presence of water (0.1-1.1 wt.% in quench glass, Supplementary Table 3.2). There are several possible explanations for the incorporation of water in the experimental runs. One is relative to the hydrogen diffusion through the capsule wall, producing water inside the capsule. Another one is due to the reduction of Fe^{3+} to Fe^{2+}, releasing oxygen that forms water with the hydrogen of the buffer (e.g., Feig et al., 2006, 2010), since the prevailing fO_2 during the experiments is lower than the fO_2 during the synthesis of the starting material. Moreover, due to the relatively long run duration in this study (5 days) compared to the previous studies on basaltic systems, Fe gain or loss is evident in several runs, especially at near-liquidus conditions (Table 3.2). Hence, special attention should be paid to these samples, especially regarding the Fe evolution in glasses. Additionally, the phase proportions calculated for some experiments are sometimes negative. This does not imply disequilibrium conditions in our experiments, but is probably a result of Fe gain or loss as stated above, which would change the bulk Fe content in the system and lead to the problems for the mass balance calculation.

Opx and Psb were observed in the experiments, however, they are not observed in natural high-Ti basalts. These minerals are regarded as formed via peritectic reactions (e.g., Akimoto et al., 1957; Haggerty and Lindsley, 1970; Koepke et al., 2003; Almeev et al., 2013; Veksler and Hou, 2020). These peritectic reactions can be described by the following equations:

$$\text{(Mg,Fe)}_2\text{SiO}_4 \text{ (Ol)} + 2\text{SiO}_2 = 2\text{(Mg,Fe)SiO}_3 \text{ (Opx)}, \qquad (1)$$

and

$$\text{(Fe,Ti)O}_3 \text{ (Ilm-Hm)} + \text{TiO}_2 = \text{(Fe,Ti}_2\text{)O}_5 \text{ (Psb)}. \qquad (2)$$

Specifically, the influences on phase proportions or glass compositions on these peritectic reactions were mentioned in literature (e.g., Irving and Wyllie 1975; Abbott, 1978; Villiger et al., 2004; Erdmann et al., 2014). Such peritectic reactions mainly influence the proportions of the phase involved in the reaction (melt compositions would be changed), but minor changes in the proportions or compositions of other mineral phases are expected. Thus, in the following, the compositions of Opx and Psb were mentioned but these phases were not discussed for further interpretation.

3.4.2 Phase relations

3.4.2.1 300 MPa experiments under oxidizing conditions

Mt is the liquidus phase in all experimental runs (Fig. 3.1a), followed by Ol or Cpx. The Ol crystallization interval is restricted to around 1150 ℃ with lower X^{fl}_{H2Oini} (≤ 0.2), and at lower temperatures, Ol is replaced by Opx due to a peritectic reaction as mentioned before. Cpx reaches saturation in the system at a similar temperatures than Ol for lower X^{fl}_{H2Oini} (≤ 0.2), but is also the second phase to crystallize at higher X^{fl}_{H2Oini}. Cpx crystallized at water-saturated conditions at 1050 ℃ and below. Pl joins the silicate phases assemblage between 1100 ℃ at nominally dry conditions (~0.1 wt.% H_2O in melt). Its crystallization is below 1000 ℃ at water-saturated conditions. At 1050 ℃ and below, Hm joins the mineral assemblage, independently of water activity. Ap is the latest phase to crystallize and was only observed in one experiment at 1000 ℃ and X^{fl}_{H2Oini} at ~0.6.

3.4.2.2 300 MPa experiments under reducing conditions

Under reducing conditions (Fig. 3.1b), Chr (instead of Mt at higher fO_2)

precipitates first at all melt H_2O concentrations. However, with the temperature dropping down to ~1050 °C, Chr disappears and is replaced by Mt. Ol joins the mineral assemblage ~1150 °C and lower X^{fl}_{H2Oini} (≤ 0.2), but has a much wider stability field under reducing conditions than the oxidizing experiments. The stability field of Ol extends water-saturated conditions. At such conditions, Ol is observed at 1050 °C and 1000 °C. However, this phase is not any more stable at 950 °C. Within the investigated temperature interval of 50 °C, there is no difference for the crystallization temperature of Ol and Cpx, and the upper boundary curve for Cpx crystallization was assumed to be parallel and nearly identical to that of Ol under reducing conditions. However, Cpx is still stable in the low temperature experiment at 950 °C. Another notable feature for reducing experiments is the presence of Ilm instead of Hm at 1050 °C (X^{fl}_{H2Oini} < 1) to 950 °C (X^{fl}_{H2Oini} = 1). Pl is observed from 1050 °C at low X^{fl}_{H2Oini} (≤ 0.2) instead of 1100 °C at oxidizing conditions. However, the crystallization temperature of Pl under water-saturated conditions is not well bracketed at high water activities. The crystallization temperature of Opx in reducing conditions is about ~ 50 °C lower than that at the oxidizing conditions. Ap is still the last crystallizing phase at 1000 °C and X^{fl}_{H2Oini} of 0.2. Am was only obtained in one run at 950 °C and water-saturated conditions.

3.4.2.3 100 MPa experiments at oxidizing conditions

Similarly to the results at 300 MPa, Mt is the primary liquidus phase at all melt water contents (Fig. 3.1c). The Ol crystallization interval is restricted to around 1150 °C – 1100 °C for X^{fl}_{H2Oini} less than 0.6 (melt water contents < 2 wt.% H_2O). At lower temperatures, Ol is also replaced by Opx at lower temperatures, but compared to oxidizing experiments at 300 MPa, Ol has a wider stability field at 100 MPa. The Cpx crystallization temperature is about 50 °C lower at 100 MPa compared to 300 MPa. Hm crystallization seems to be independent of pressure and starts crystallizing at 1050 °C, similar to the 300 MPa samples. One significant difference for oxide phases at 100 MPa and oxidizing conditions is that from 1050 °C, Psb joins the oxides crystallization until 950 °C. Pl is observed at 1050 °C with X^{fl}_{H2Oini} of ~ 0.2 and crystallizes between 1000 and 950 ℃ at water-saturated conditions. Ap is always the latest phase among all the experimental products. Ap is presented at 1000 ℃ and X^{fl}_{H2Oini} of ~ 0.6 and starts to crystallize between 1000 and 950 ℃ at water-saturated conditions.

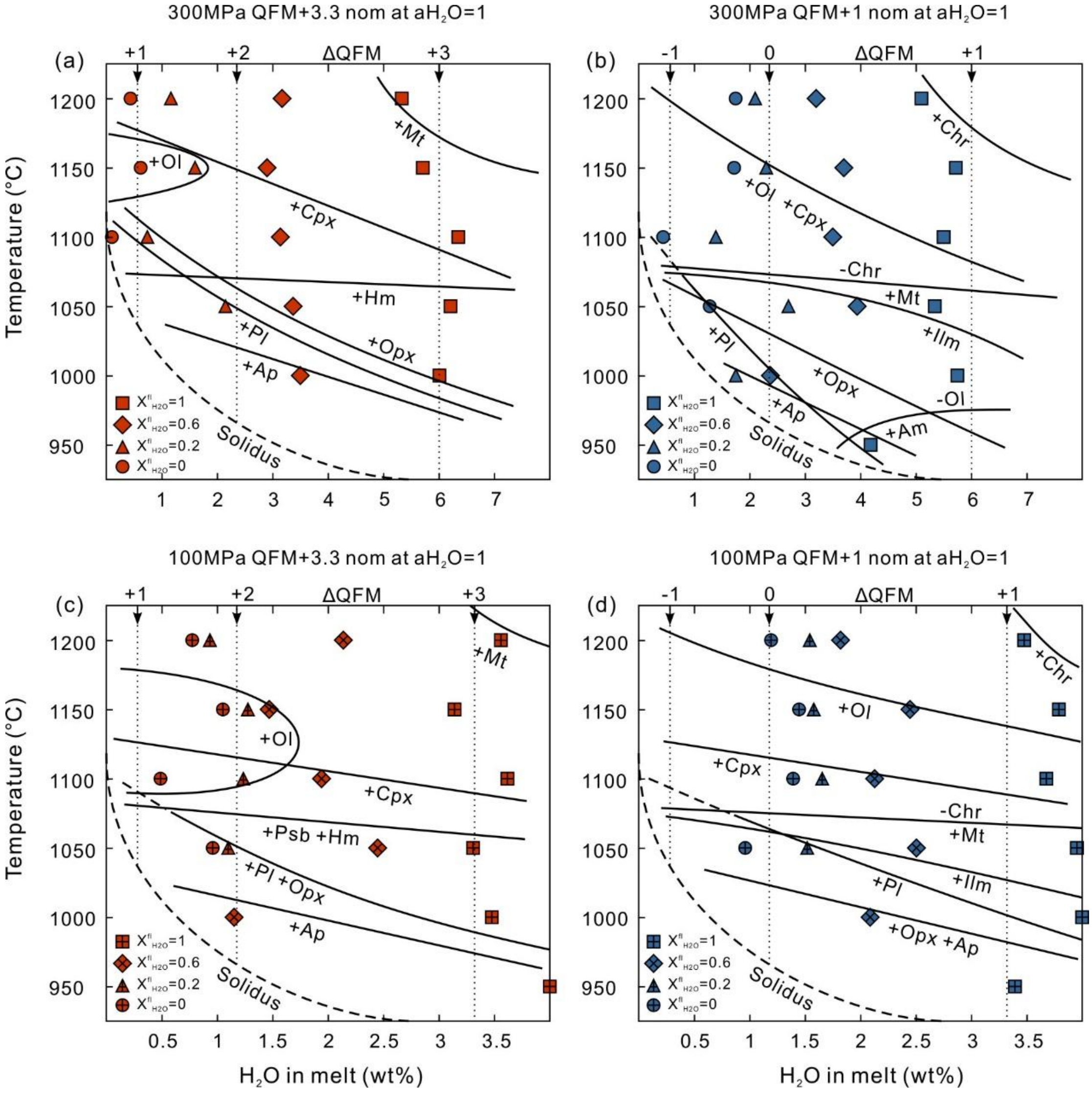

Fig. 3.1. Phase diagrams of the Emeishan high-Ti basalts as a function of pressure, temperature and water content of the melt. The nominal redox conditions are (a) and (c) QFM + 3.3, and (b) and (d) QFM + 1, with fixed hydrogen fugacities and $aH_2O = 1$. Black arrows and vertical dotted lines represent estimated redox conditions in the experiments (as shown above each diagram in ΔQFM notation). Continuous lines represent the stability fields of mineral phases and dashed lines illustrate the expected solidus in the system. Part of the stability lines of Pl in (b-d) are marked by dashed lines since the liquidus of Pl is presumed to extend at 1100 ℃ under extremely dry

condition as in (a). The curve of stability lines of Ol in (b) and (d) are estimated according to Almeev et al. (2007). Abbreviations: Ol-olivine; Cpx-clinopyroxene; Chr-chromite; Mt-magnetite; Ilm-ilmenite; Hm-hematite; Psb-pseudobrookite; Opx-orthopyroxene; Pl-plagioclase; Ap-apatite; Am-amphibole.

3.4.2.4 100 MPa experiments at reducing conditions

The crystallization sequence for reducing experiments at 100 MPa follows the trend observed from 300 MPa experimental results at similar redox conditions (Fig. 3.1d). Chr is the liquidus phase and is replaced by Mt in the experiments at 1050 ℃ and below. Ilm joins the mineral assemblage at 1050 ℃ and low X^{fl}_{H2Oini} (≤ 0.2), similarly to the 300 MPa results ($X^{fl}_{H2Oini} \leq 0.6$). The main differences between 300 and 100 MPa are also noted for the silicate phases. At similar melt water content, the crystallization temperature of the beginning of crystallization of olivine is not very different from that at 300 MPa. The lower crystallization of Ol at 300 MPa and water-saturated conditions may be related to the higher water contents that can be reached at 300 MPa. In contrast to data at 300 MPa, Ol is still a stable phase at 950 ℃, 100 MPa and water-saturated conditions. More importantly, the temperature of the beginning of crystallization temperature of Cpx at 100 MPa is similar to that of oxidizing experiments at 100 MPa, but ~ 50 ℃ lower than the 300 MPa experiments under reducing conditions. At similar redox conditions and melt water content, decreasing pressure also results in a slight increase of the crystallization of Pl. The stability field of Opx at 100 MPa and reducing condition is narrow compared to the other three investigated conditions. At similar redox conditions and melt water content, pressure also affects the crystallization temperature of Opx that is decreasing from 1050 ℃ at 300 MPa to 1000 ℃ at 100 MPa (for melt with 2 wt.% H_2O).

To summarize, for the multiple parameters determined in our system, as expected, the stability of oxide minerals are barely affected by pressure and are more sensitive to the prevailing redox conditions. In contrast, the stability of silicate minerals, and mainly Cpx and Pl show an obvious dependence on pressure variations. Specifically, both Ol and Pl have a larger stability fields at low pressure, while Cpx and Opx show the opposite trends. Ol is the only silicate phase in our system that is strongly sensitive to fO_2, and it has a much wider stability field under reducing conditions due to the higher ratio of ferrous/ferric iron in the silicate melt. Furthermore, the stability of all silicate phases (Ol, Cpx, Pl and Opx) are also sensitive to the aH_2O. Increasing aH_2O in the melt decreases the crystallization temperature of these phases. Ap crystallization in our system shows no apparent correlations with pressure or fO_2, and may be only controlled by temperature and melt compositions.

3.4.3 Phase proportions

The proportions of each crystalline phase are listed and illustrated in Table 3.2 and Fig. 3.2 with a sum of squared estimate of errors (SSE) less than 0.5, showing a high reliability of calculation. At given pressure and fO_2, the melt fraction decreases with decreasing temperature (at constant water content) and decreasing water contents in the melt (at isothermal conditions) (Fig. 3.2a-b) down to ~ 30 wt.% at ~1000 ℃ at the lowest X^{fl}_{H2Oini}. The crystallinity (in wt.%) at water-saturated conditions increases nearly with decreasing temperature between 1100 and 950 ℃ with an increase of ~ 0.4 wt.% crystals/℃. This linear trend is the result of the co-crystallization of Cpx and Fe-Ti oxides at this condition. With ongoing cooling, Pl would also join the crystal assemblage at water-saturated conditions which would furtherly enhance the crystallinity.

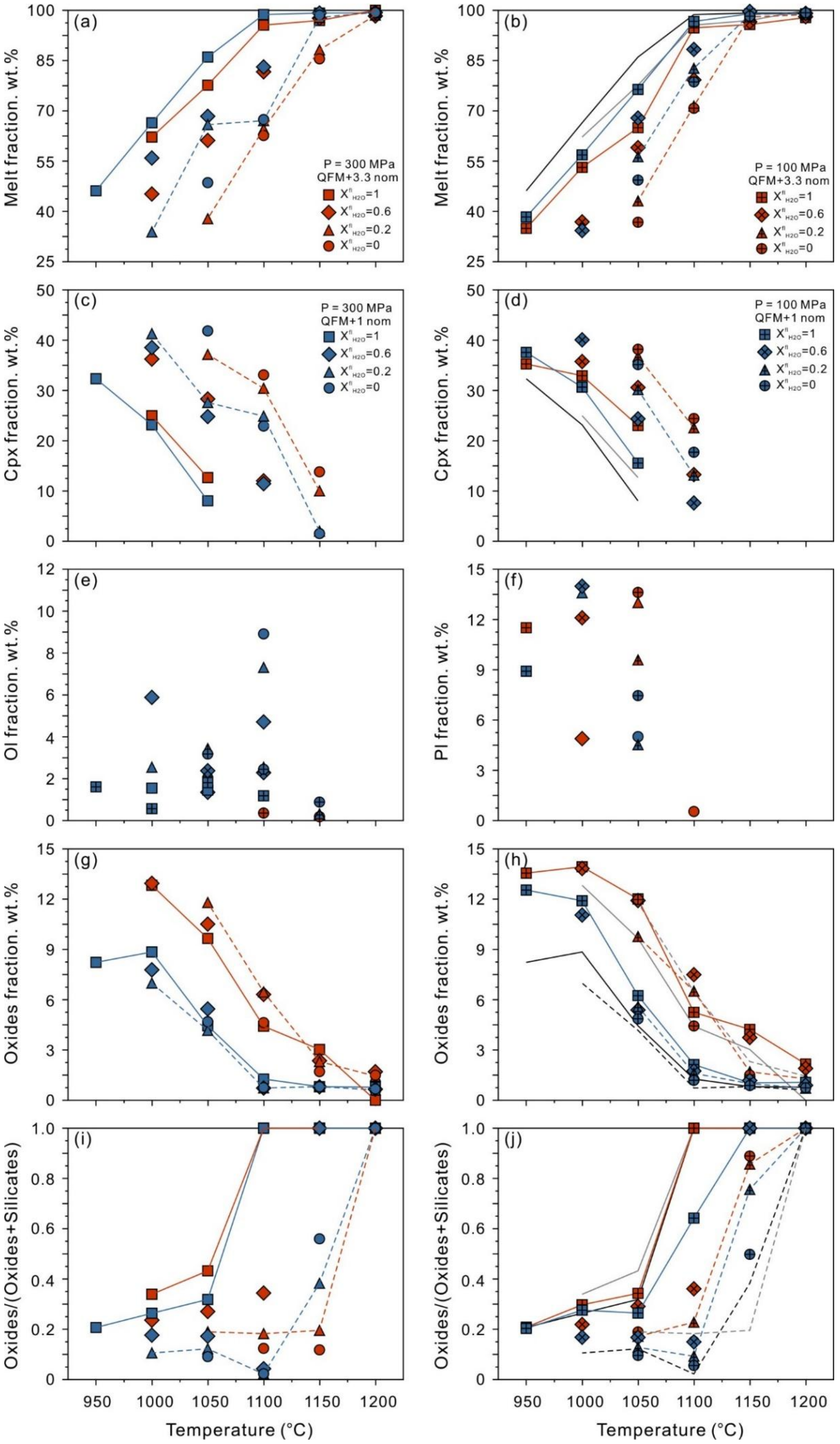
(a)
(b)
(c)
(d)
(e)
(f)
(g)
(h)
(i)
(j)
Melt fraction. wt.%
Cpx fraction. wt.%
Ol fraction. wt.%
Pl fraction. wt.%
Oxides fraction. wt.%
Oxides/(Oxides+Silicates)
Temperature (°C)
P = 300 MPa
QFM+3.3 nom
P = 100 MPa
QFM+3.3 nom
P = 300 MPa
QFM+1 nom
P = 100 MPa
QFM+1 nom
X^{fl}_{H2O}=1
X^{fl}_{H2O}=0.6
X^{fl}_{H2O}=0.2
X^{fl}_{H2O}=0
950
1000
1050
1100
1150
1200

Fig. 3.2. Phase proportions as a function of temperature and X^{fl}_{H2Oini}. The left and right column are the results for 300 and 100 MPa experiments, respectively. The solid lines (red and blue) connected the variations of water-saturated experiments along the temperature changes and dashed lines (red and blue) illustrated the low X^{fl}_{H2Oini} (=0.2) experiments variations with ongoing cooling. The dark solid and dashed line in the right column are mirrored from the red solid and dashed lines from the left column while the grey solid and dashed lines are mirrored from the blue solid and dashed lines from the left column.

Melts proportions are always lower under oxidizing conditions than under reducing conditions and the gap between oxidized and reduced experiments becomes more apparent with decreasing aH_2O and temperatures (e.g., Botcharnikov et al., 2008; Feig et al., 2010). Pressure effects on melt fractions show two different trends. At water-saturated conditions, the proportions of melts in 100 MPa experiments are obviously lower than in 300 MPa experiments. However, at low X^{fl}_{H2Oini} (e.g., = 0.2), the fractions of melt in 300 MPa experiments become lower than in 100 MPa experiments (except one sample EM35 with relatively high aH_2O). This general observation can be explained by the change of the slope of melting temperatures in the P-T diagram. At dry conditions, the solidus temperatures increase with pressure (Green and Ringwood, 1966; Holloway and Burnham, 1972). In contrast, at high aH_2O, the solidus decreases with pressure, which is due to an increasing melt water content with pressure for a given water activity (water solubility increases with pressure). These observations also show that our mass balance calculations are consistent with what is expected.

Cpx proportions increase with decreasing X^{fl}_{H2Oini} at a given temperature and show an overall increasing trend with decreasing temperature up to about 45 wt.% (Fig. 3.2c-d). Considering the high proportions of Cpx compared with other phases, it can be noted that the crystallinity in the investigated system is mainly controlled by Cpx. The influence of fO_2 on Cpx proportions becomes more pronounced at low X^{fl}_{H2Oini} at a given P-T condition. At water-saturated conditions, Cpx proportions are only lightly higher under oxidizing conditions. However, at low X^{fl}_{H2Oini} (e.g., = 0.2), the proportions of Cpx become significantly higher under oxidizing conditions than reducing conditions. As mentioned above, crystallization of Cpx is strongly pressure-dependent. Thus, the proportions of Cpx at two different pressures show clear difference. At water-saturated conditions, Cpx proportions in 100 MPa experiments are higher than in 300 MPa experiments at both oxidizing and reducing conditions. In contrast, at low X^{fl}_{H2Oini} (e.g., = 0.2), Cpx proportions become lower in 100 MPa experiments than in 300 MPa experiments.

Ol mainly crystallizes under reducing conditions in the system and its proportion is controlled by the peritectic reaction (1). Hence, it shows a scattering of the data if plotted as a function of temperature and $a\mathrm{H_2O}$ in Fig. 3.2e. In general, the proportions of Ol are higher in 300 MPa experiments than 100 MPa experiments. The maximum amounts that are observed are ~ 10 wt%. Pl is only observed in a few runs at low temperatures. Thus, only a few data are plotted in Fig. 3.2f and at given P-T conditions, the proportions of Pl increase with decreasing $a\mathrm{H_2O}$ (at constant intrinsic $f\mathrm{O_2}$ and P) and with increasing $f\mathrm{O_2}$ (at constant X^{fl}_{H2Oini} and P). Oxide species in our system show rather complex compositional variations. Thus, only total weight fractions of oxides in the experimental products, instead of individual separated oxide species, are plotted in Fig. 3.2g-h. At oxidizing conditions, the fraction of total oxides firstly shows an increasing trend to ~ 13 wt.% until ~ 1050 °C, and then keeps constant. At a given P-T condition, the total oxides fractions are significantly higher in oxidizing experiments than reducing experiments. Similar to silicate minerals, pressure variation also affects the oxides proportions and oxides proportions are higher in 100 MPa experiments. The oxides fraction among the total solid phases is an indicator to model potential oxide enrichment in the magmatic systems, and the highest proportions of oxide minerals (oxides / total mineral phases) can reach up to 43 wt.% at oxidizing and water-saturated conditions (Fig. 3.2i-j).

3.4.4 Phase chemistry

The chemical compositions of experimental products were obtained with electron microprobe and summarized in Supplementary Table 3.2. In addition, natural Ol, Cpx, Pl and Fe-Ti oxides compositions from Panzhihua and Hongge layered intrusion (Pang et al., 2008a; Chen et al., 2017; Bai et al., 2019; Wang et al., 2020) are displayed in histograms or pseudo-triangle diagrams for comparison.

3.4.4.1 Melt

The general variation trends with increasing crystallization (decreasing temperature) are similar for experiments under both 100 and 300 MPa, and plotted in Fig. 3.3. The SiO_2 contents in the experimental melts steadily increase with decreasing temperature. At a given temperature, significant differences in SiO_2-content in melts can be observed and this is related to a change of crystal content in the experimental products at reducing and oxidizing conditions and also to different modes of the crystal population (especially proportions of Ol, Cpx and Pl; Scaillet and McDonald, 2003). The SiO_2 content increases at a constant temperature with decreasing aH$_2$O (Fig. 3.3a-b). Oxygen fugacity strongly influences the SiO_2 contents in experimental melts. Under oxidizing conditions, the melts of two different pressures have a higher SiO_2 content than observed under reducing conditions. The effect of pressure on the SiO_2 content of residual melt is depending on the aH$_2$O, which is consistent with the evolution of melts fractions mentioned above. At water-saturated conditions, the SiO_2 contents in 100 MPa melts are higher than in 300 MPa melts. However, at low X^{fl}_{H2Oini} (e.g., = 0.2), 100 MPa experimental melts have lower SiO_2 contents than 300 MPa products.

The evolution of TiO_2 contents in Fig. 3.3c-d shows a maximum at 1100 ℃ at low X^{fl}_{H2Oini} ($\leq$ 0.2) and reducing conditions. No pronounced TiO_2 enrichment is observed in water-rich reducing experiments and in oxidizing experiments. The maximum concentration of TiO_2 is about 4.3 wt.% in the low X^{fl}_{H2Oini} experiments and the concentration peak almost disappears in water-saturated melts. Such a behavior is related to crystallization history of Fe-Ti oxides, and in particular Ilm.

Melt Al_2O_3 contents are sensitive to the onset and abundance of Pl crystallization, and thus to pressure. At 300 MPa, Al_2O_3 contents exhibit an enrichment trend with ongoing cooling and decreasing $a$$H_2O$ (Fig. 3.3e). At 100 MPa, melt Al_2O_3 concentrations continue to rise until ~ 17.0 wt.%, followed by a plateau due to crystallization of Pl at water-saturated conditions (Fig. 3.3f).

Eliminating the samples with high Fe gain or loss from the capsules, FeO contents of experimental melts at two given pressures reveal a plateau at high temperatures and a pronounced decrease initiating between 1100 and 950 ℃ related to the extensive crystallization of Fe-Ti oxides (Fig. 3.3g-h). As mentioned before, fO_2 has a strong influence on the crystallization of Fe-Ti oxides, and thus FeO contents in the melts. Under oxidizing conditions, the FeO content decreases strongly with decreasing temperatures compared to reducing conditions. A similar trend of FeO evolution in the melts is observed in abundant previous studies (e.g., Berndt et al., 2005; Freise et al., 2009). Behaviors of MgO and CaO in our system are mainly controlled by the presence of Cpx due to the low proportions of Ol and late crystallization of Pl. MgO (Fig. 3.3i-j) and CaO (Fig. 3.3k-l) contents in the water-saturated melts are approximately constant at high temperatures (≥1100 °C) and a nearly linear decrease is observed with ongoing cooling. With decreasing $a$$H_2O$, due to the crystallization of Cpx, MgO and CaO strongly decreases at both 300 and 100 MPa melts. As discussed above, the stability field and proportion of Cpx are related to pressure. This leads to a stronger decrease in the melt MgO and CaO contents of water-saturated samples in the low-pressure runs and low $a$$H_2O$ samples in the high-pressure runs. The alkalis, Na_2O (Fig. 3.3m-n) and K_2O (Fig. 3.3o-p), are incompatible elements for all crystallized phases in our system. Thus, similar increasing trends are observed for both crystallization series with decreasing temperature.

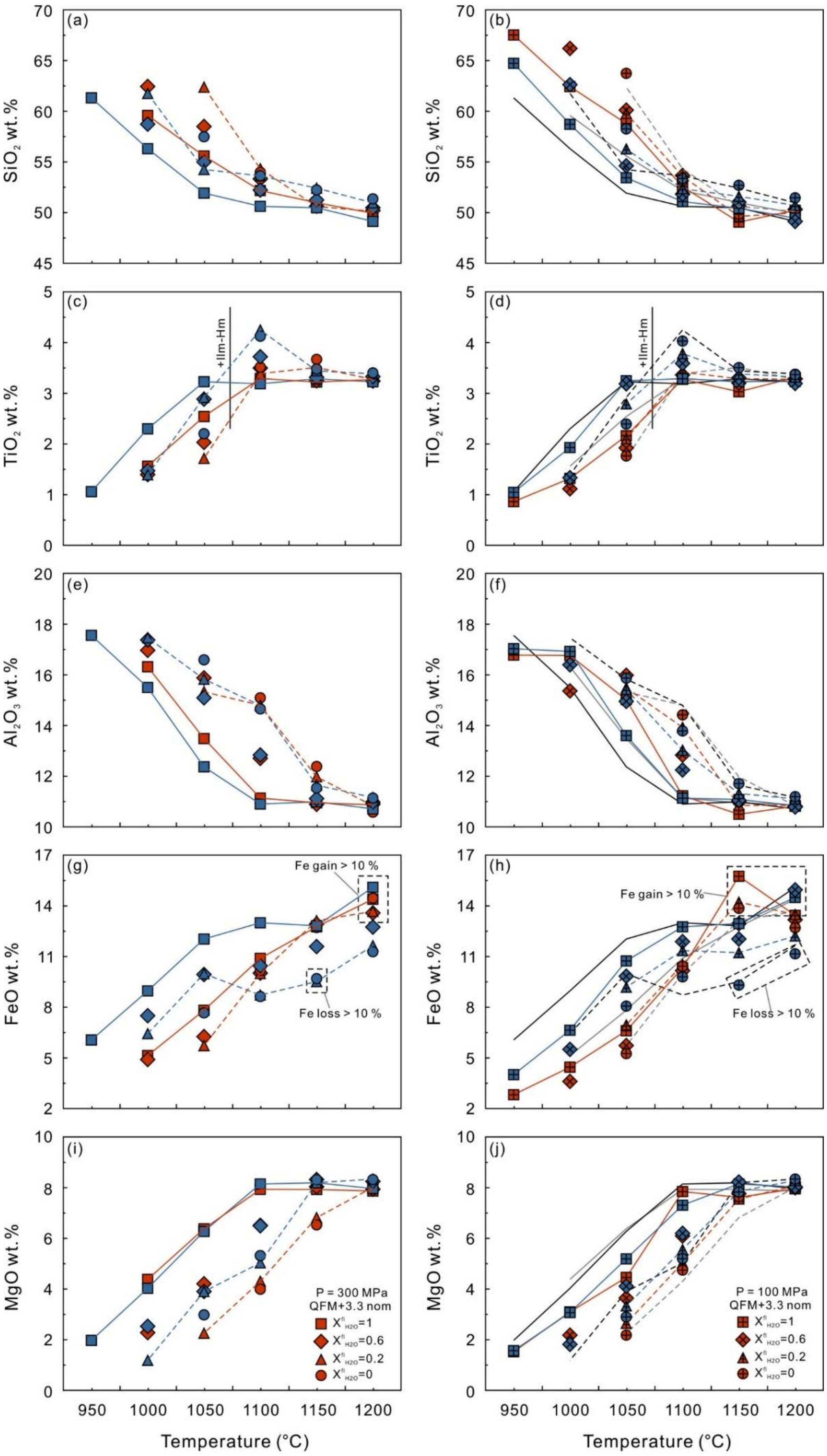(a)
(b)
SiO$_2$ wt.%
70
65
60
55
50
45
(c)
(d)
TiO$_2$ wt.%
+Ilm-Hm
5
4
3
2
1
0
(e)
(f)
Al$_2$O$_3$ wt.%
20
18
16
14
12
10
(g)
(h)
FeO wt.%
Fe gain > 10 %
Fe loss > 10 %
17
14
11
8
5
2
(i)
(j)
MgO wt.%
10
8
6
4
2
0
P = 300 MPa
QFM+3.3 nom
P = 100 MPa
QFM+3.3 nom
X^{fl}_{H2O}=1
X^{fl}_{H2O}=0.6
X^{fl}_{H2O}=0.2
X^{fl}_{H2O}=0
950
1000
1050
1100
1150
1200
Temperature (°C)

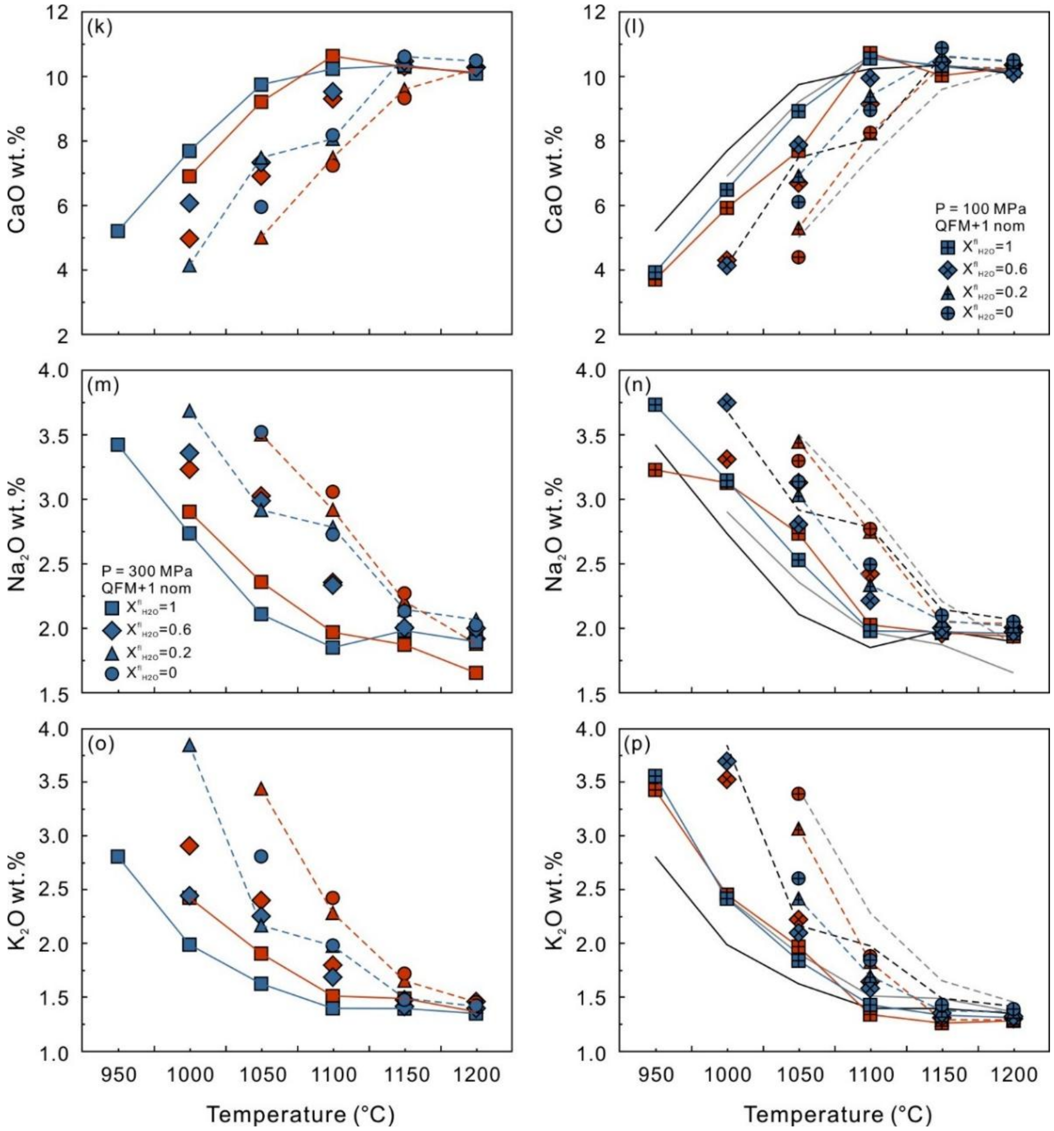

Fig. 3.3. Composition of experimental melts as a function of temperature (all compositions are normalized to 100 %). The left and right column are the results for 300 and 100 MPa experiments, respectively. Solid red and blue lines in both side represent the evolution trends of water-saturated experiments under oxidizing and reducing conditions while dashed red and blue lines represent the evolution trends of experiments with X^{fl}_{H2Oini} = 0.2 under oxidizing and reducing conditions. The solid dark and grey lines in the right column are mirrored from the water-saturated experiments under reducing and oxidizing experiments in the left column. The dashed dark and grey lines in the right column are mirrored from the X^{fl}_{H2Oini} = 0.2 experiments under reducing and oxidizing experiments in the left column.

3.4.4.2 Olivine

The forsterite content of Ol [Fo = molar 100×Mg/(Mg+Fe)] shows an overall decreasing trend with ongoing cooling and varies from 84 to 56, consistent with the natural compositions of Ol from both Panzhihua and Hongge intrusion (Fig. 3.4). In general, no pronounced pressure effect was observed on the Fo content. However, at given temperature, increasing aH_2O could dramatically increase the Fo content (up to ~ 20 %) of olivine. This effect can partly be ascribed to the increase in melt fraction due to water and the increase of fO_2, which directly controls the Fe^{2+} content in the melts (e.g., Toplis and Carroll, 1995; Berndt et al., 2005; Feig et al., 2006). Specifically, the Fo contents of Ol show a good correlation with the temperature at given aH_2O (Fig. 3.4a). However, at lower aH_2O, the variation is much steeper than at water-saturated conditions, reflecting the positive effect of aH_2O on the temperature range of crystallization of Ol. When compositions of experimental Ol are compared with Mg# of coexisting melt, which is defined by Mg# = molar 100×Mg/(Mg+Fe^{2+}) [Fe^{2+} /Fe^{3+} ratios in the melts were calculated from the model of Kress and Carmichael (1991)], the variation is in agreement with data from Berndt et al. (2005, Fig. 3.4b), supporting that olivine was in equilibrium with melts in our experiments. This is also supported by the $Kd_{Ol-melt}^{Fe-Mg}$ values of our experiments, which vary from 0.27 to 0.37 (except one sample EM72 with value 0.41; Roeder and Emslie, 1970). In addition to the Fo content, CaO content in Ol varies from ~0.20 to 0.61 wt.% and shows an increasing trend with decreasing X^{fl}_{H2Oini} at a given P-T condition.

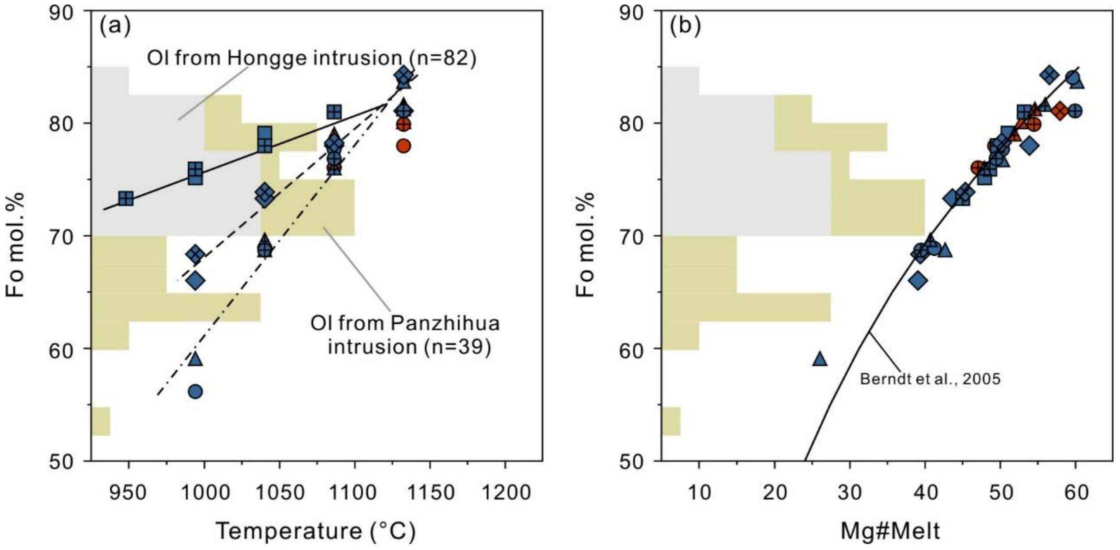

Fig. 3.4. Forsterite content (Fo) in experimental olivine as a function of (a) temperature and aH_2O, (b) magnesium number of the coexisting melt and aH_2O. Continuous, dashed and dashed-dotted lines in (a) are the regression trends for the H_2O-saturated, hydrous ($X^{fl}_{H2Oini} = 0.6$) and low aH_2O ($X^{fl}_{H2Oini} \leq 0.2$) experiments. Continuous line in (b) is the empirical trends for basaltic magmas proposed by Berndt et al. (2005). The histograms of natural olivine compositions from Panzhihua and Hongge layered intrusion are provided along the vertical axis for comparison. Symbols as per Fig. 3.1.

3.4.4.3 Clinopyroxene

The compositions of Cpx vary from $En_{42}Fs_{24}Wo_{34}$ to $En_{52}Fs_9Wo_{39}$ (Fig. 3.5a). Mg# [Mg# = molar 100 × Mg/(Mg+Fe)] of Cpx displays a general decreasing trend with temperature decrease and changes from 87 to 64, covering the main variation range of the Cpx in both Hongge and Panzhihua intrusions (Fig. 3.5b). At given P-T conditions, higher aH_2O results in higher Mg# of Cpx, similar to the observations made for Ol. In addition to aH_2O, redox conditions also affect the Mg# and $XCaO/XFeO_t$ ratios of Cpx (XCaO and $XFeO_t$ represent the mole fraction of CaO and total FeO content; Fig. 3.5c-d), as higher Fe^{3+}/Fe^{2+} ratios are expected in the oxidized system. Pressure variation between 100 and 300 MPa have no obvious effects on the Mg# of Cpx.

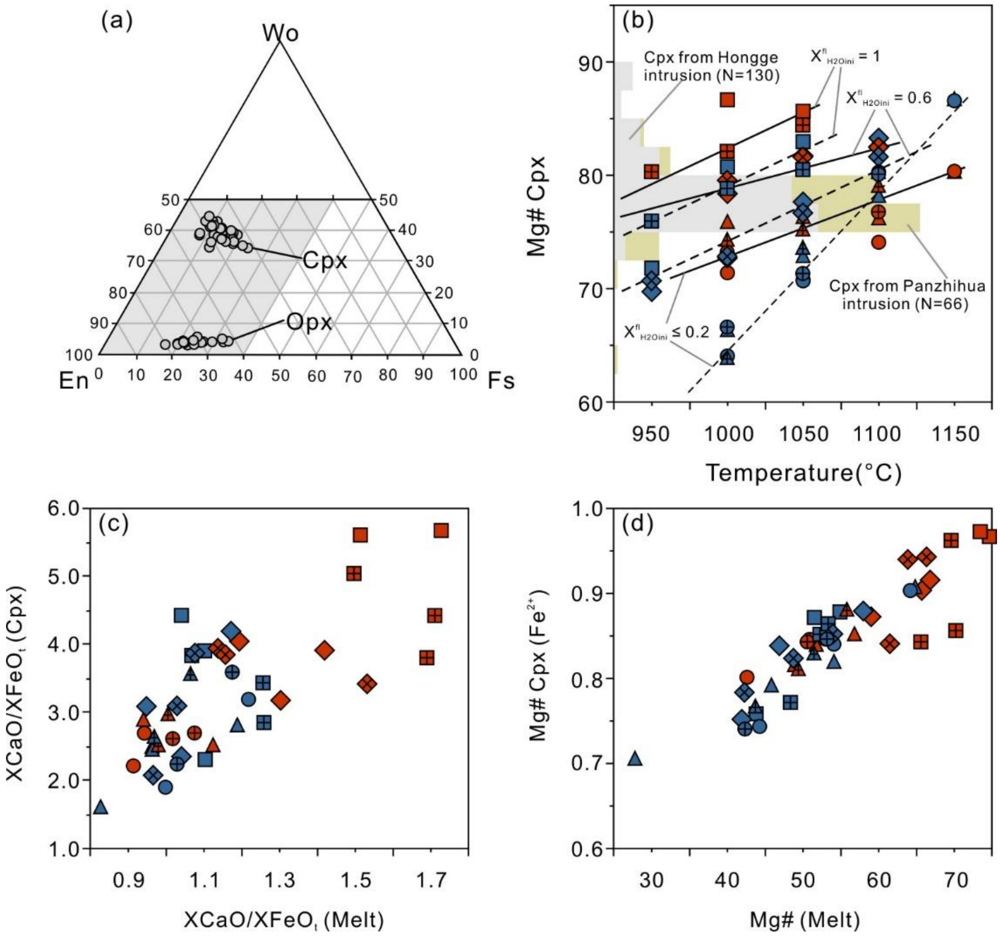

Fig. 3.5. (a) Pyroxene quadrilateral and the experimental Cpx and Opx. (b) Clinopyroxene magnesium number (Mg#) variations as a function of temperature and X^{fl}_{H2Oini}. Solid lines are the regression trends for the different X^{fl}_{H2Oini} at oxidizing conditions and dashed lines are the regression trends for the different X^{fl}_{H2Oini} at reducing conditions. (c) Partitioning of CaO and FeO between clinopyroxene and coexisting silicate melts as a function of aH$_2$O. (d) The relationship between Mg#(Fe^{2+}) of Cpx and Mg# of the melt as a function of X^{fl}_{H2Oini}. It should be noted that the total FeO$_t$ content in both Cpx and melt is used in plotting the data in (c), whereas only Fe^{2+} is used in (d). Symbols as per Fig. 3.1.

3.4.4.4 Orthopyroxene

Compositions of Opx are shown in Figs. 3.5a and 3.6. Opx only occurs in a few samples. However, even based on the limited number of Opx-bearing samples, Mg# of Opx (Mg# = 100×Mg/(Mg+Fe) in mol %) varies significantly as a function of fO$_2$ and aH$_2$O. Opx has much higher Mg# in oxidizing conditions than in reducing conditions and the highest Mg# of Opx is obtained in the water-saturated sample at 950 ℃ and oxidizing conditions. Two values at low aH_2O conditions and reducing conditions (1050 and 1000 ℃) do not fit to this general trend (blue dots in Fig. 3.6). We suspect that the main reasons for this discrepancy are analytical problems in these samples with high crystallinity, which could be related to the presence of oxides as tiny inclusions in the Opx phases.

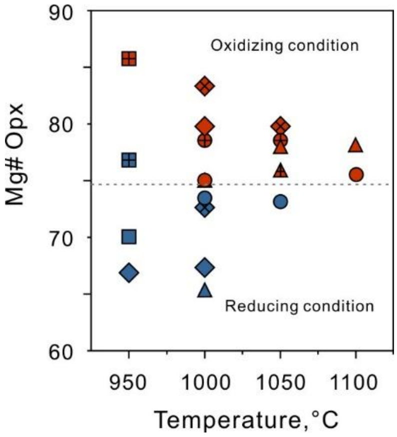

Fig. 3.6. Orthopyroxene magnesium number (Mg#) variations as a function of temperature and X^{fl}_{H2Oini}. The dotted line divides the boundary of oxidizing and reducing experiments. Symbols as per Fig. 3.1.

3.4.4.5 Plagioclase

The compositions of Pl are shown in Fig. 3.7a as a function of temperature and nominal aH_2O in the system. According to previous studies on the composition of Pl in basaltic systems (e.g., Sisson and Grove, 1993; Berndt et al., 2005; Feig et al., 2006), the An values of Pl (An = 100×Ca/(Ca+Na) in mol %) increase significantly with increasing aH_2O. The maximum An content (~70) in this study is determined in the water-saturated experiment performed at 950 ℃, 300 MPa, and reducing conditions. Different from the mafic silicate minerals, variations of fO_2 have a negligible influence on the An content of Pl (< 3 %). In the investigated pressure range, a no notable effect of pressure on the An content cannot be detected. However, due to the small size of experimental Pl and the high crystallinity of samples at low aH_2O, analytical problems related to the contamination of Pl analyses cannot be avoided, for instance the low X^{fl}_{H2Oini} (≤0.2) samples at 1050 °C. Thus, the detection of other elements in the analyses (e.g., Fe, Ti and Mg) of plagioclase vary in a wide range, from 0.1 to 3.2 wt.%, and consequently may affect significantly the estimated An content.

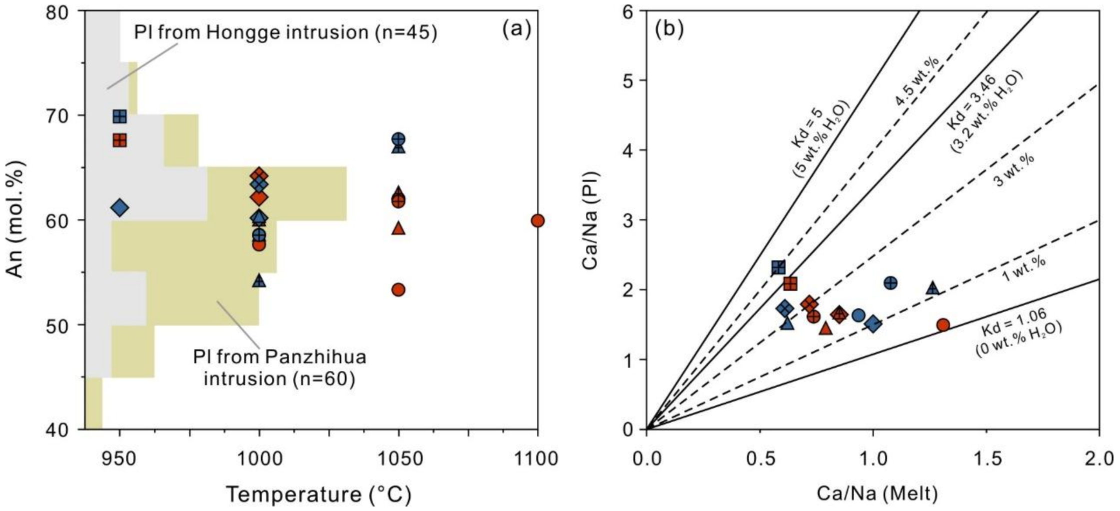

Fig. 3.7. (a) Anorthite content (An) variation in plagioclase as a function of temperature and X^{fl}_{H2Oini}. (b) Ca/Na ratios in Pl and coexisting melt for different water content. The solid lines are determined by Feig et al. (2006). The dashed lines are assumed according to the water contents in our experimental melts. Symbols as per Fig. 3.1.

The Ca/Na partitioning between coexisting Pl and melt is illustrated in Fig. 3.7b. Continuous lines represent constant values of $\mathrm{Kd}^{\mathrm{Pl-melt}}_{\mathrm{Ca-Na}}$ expressed by the following equation:

$$\mathrm{Kd}^{\mathrm{Pl-melt}}_{\mathrm{Ca-Na}} = \frac{\left(\frac{\mathrm{Ca}}{\mathrm{Na}}\right)\mathrm{Pl}}{\left(\frac{\mathrm{Ca}}{\mathrm{Na}}\right)\mathrm{melt}} \text{ in mole} \qquad (3)$$

The determined $\mathrm{Kd}^{\mathrm{Pl-melt}}_{\mathrm{Ca-Na}}$ values for given melt H_2O contents marked by the solid lines (Fig. 3.7b) are from Feig et al. (2006). Our data are plotted in Fig. 3.7b and the dashed lines are the values interpolated for three different water content (1, 3 and 4.5 wt.%). Our results confirm that the $\mathrm{Kd}^{\mathrm{Pl-melt}}_{\mathrm{Ca-Na}}$ increases with the water content in the melts, in good agreement with the study of Feig et al. (2006) as well as other water-controlled experiments (e.g., Sisson and Grove, 1993). We also conclude that the effects of pressure and fO_2 on $\mathrm{Kd}^{\mathrm{Pl-melt}}_{\mathrm{Ca-Na}}$ are negligible, and that the composition of Pl is mainly controlled by the Ca/Na ratio of the coexisting melt and the aH_2O in the system (e.g., Botcharnikov et al., 2008; Almeev et al., 2012).

3.4.4.6 Chromite

As the earliest crystallized phase, Chr was observed only in reducing conditions and high-temperature runs (≥1100 °C). Based on the discrimination diagram of spinel group minerals (Fig. 3.8), Chr in our system is mainly Fe^{3+}-rich and Al-rich, ranging in composition between Cr#66-83 [Cr# = Cr/(Cr+Al) in mole %] and Mg#20-41 [Mg# = $Mg/(Mg+Fe^{2+})$ in mole %]. Compared to the natural Chr compositions from Fe-Ti oxides bearing layered intrusions in ELIP, the experimental Chr is relatively higher in Cr content, which may be due to the high Cr content added in the starting composition. The Fe^{2+}# [$100 \times Fe^{2+}/(Fe^{2+}+Mg)$ in mole] and Cr# of Chr is often used as a parameter to discuss the petrogenesis of primitive basaltic magmas (e.g., Barnes and Roeder, 2001). On the Fe^{2+}# vs. Cr# diagram (Fig. 3.9a), all experimental Chr are plotted in the Emeishan picrite range, showing no apparent trends. The effect of fO_2 on Chr composition is more apparent in a plot explicitly considering the Fe^{3+} component, which was calculated stoichiometrically (Supplementary Table 3.2). In a Fe^{3+}# [$100 \times Fe^{3+}/(Fe^{3+}+Cr+Al)$ in mole] vs. Fe^{2+}# diagram (Fig. 3.9b), it can be noted that Fe^{3+}# increases with increasing fO_2, since the most oxidizing samples among those carried out at reducing conditions are obtained at water-saturated conditions. Most of the Chr of the Emeishan picrite range are plotting in the field of the experiments that were conducted at the most reducing conditions (and at low aH_2O).

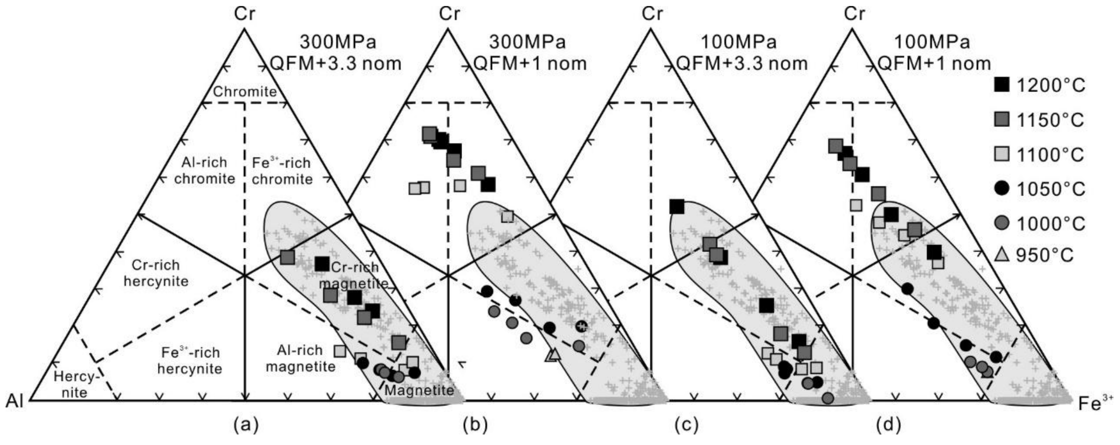

Fig. 3.8. Compositional variations of experimental chromite and magnetite under different pressures and redox conditions. Grey fields represent the chromite and magnetite composition ranges in nature samples from Panzhihua and Hongge intrusion.

3.4.4.7 Magnetite-ulvöspinel solid solution

Mt compositions vary widely, including Cr-rich, Al-rich, and nearly pure Mt endmember as shown in Fig. 3.8. There is a clear trend showing that high temperature Mt has the highest Cr content. The components of ulvöspinel in Mt are calculated following Stormer (1983) and vary from X_{usp} 0.06 to 0.85 (Supplementary Fig. 3.4). Despite the scatter of the data, there is a general linear trend of X_{Mt} ($X_{Mt} = 1 – X_{usp}$) vs. ΔQFM (Fig. 3.10a) that is comparable to the trend obtained for Mt compositions from the experiments with ferrobasaltic systems dry and hydrous conditions (Toplis and Carroll, 1995; Botcharnikov et al., 2008). It should be stressed that our experimental Mt at oxidizing condition deviates from the variation trend defined by Toplis and Carroll (1995) and Botcharnikov et al. (2008) based on experiments relevant for Skaergaard intrusion and Columbia ferrobasalts, possibly due to high Cr content in Mt which influence the X_{Mt} content. The concentration of MgO in Mt varies from ~3.5-9.5 wt.% and is higher in oxidizing experiments (Supplementary Fig. 3.5a). The concentration of Al_2O_3 in Mt changes from ~2.8-10.3 wt.% and has no notable relationship with fO_2 (Supplementary Fig. 3.5b). In addition, at a given temperature, aH_2O shows a positive correlation with the MgO content of Mt while the Al_2O_3 content of Mt decreases with increasing aH_2O.

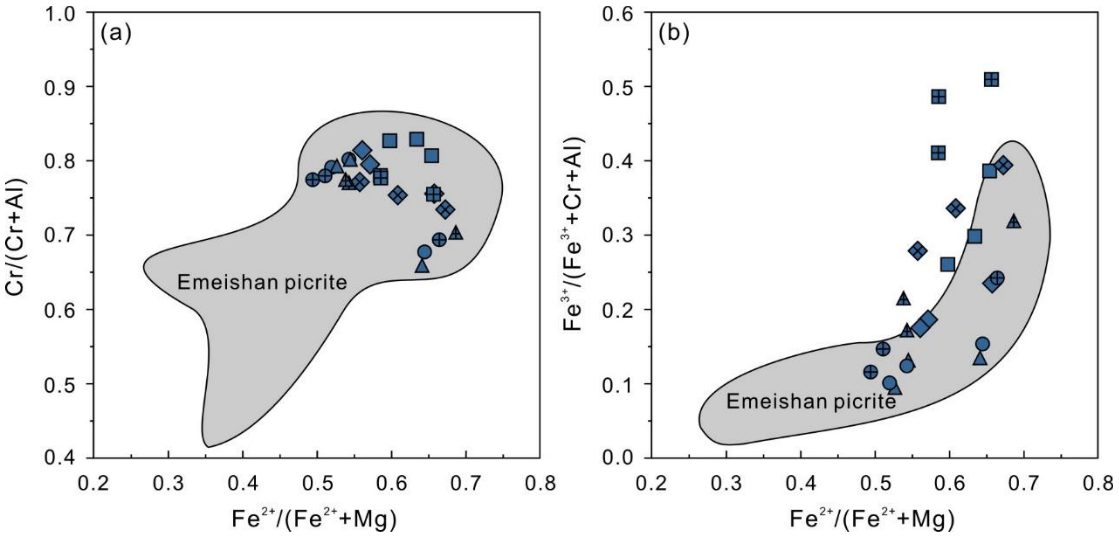

Fig. 3.9. Comparison of experimental chromite with natural spinel observed in Emeishan picrite (grey fields represent the variation range of chromite from natural picrites according to Kamenetsky et al. 2012). Symbols as per Fig. 3.1.

3.4.4.8 Ilmenite-hematite solid solution

The composition of ilmenite-hematite series vary in a wide range, and the mole fraction of Ilm (X_{Ilm}) changes from 0.31 to 0.94. The evolution trend of X_{Ilm} as a function of fO_2 is comparable to the results from Toplis and Carroll (1995). The Ilm-rich compositions (defined as ilmenite) are produced at reduced conditions (< QFM + 0.5), while Hm-rich ones (defined as hematite) appear in oxidized runs (> QFM + 0.5) but the latter show more steep variation with changing of fO_2 (Fig. 3.10b). In contrast to the magnetite-ulvöspinel solid solution, higher MgO content in Ilm (4.6-6.7 wt.%) than in Hm (2.4-4.7 wt.%) is observed (Supplementary Fig. 3.6a). Besides, Al_2O_3 contents in the ilmenite-hematite solid solution display a reversal trend as a function of fO_2 compared to MgO, changing from ~0.4-0.6 wt.% in Ilm and ~0.8-2.8 wt.% in Hm (Supplementary Fig. 3.6b). Additionally, aH_2O positively correlates with MgO concentration in Ilm, while no apparent relationship between aH_2O and MgO content in Hm is observed. No detectable relationship between fO_2 or aH_2O and Al_2O_3 content in Ilm-Hm solid solution is found.

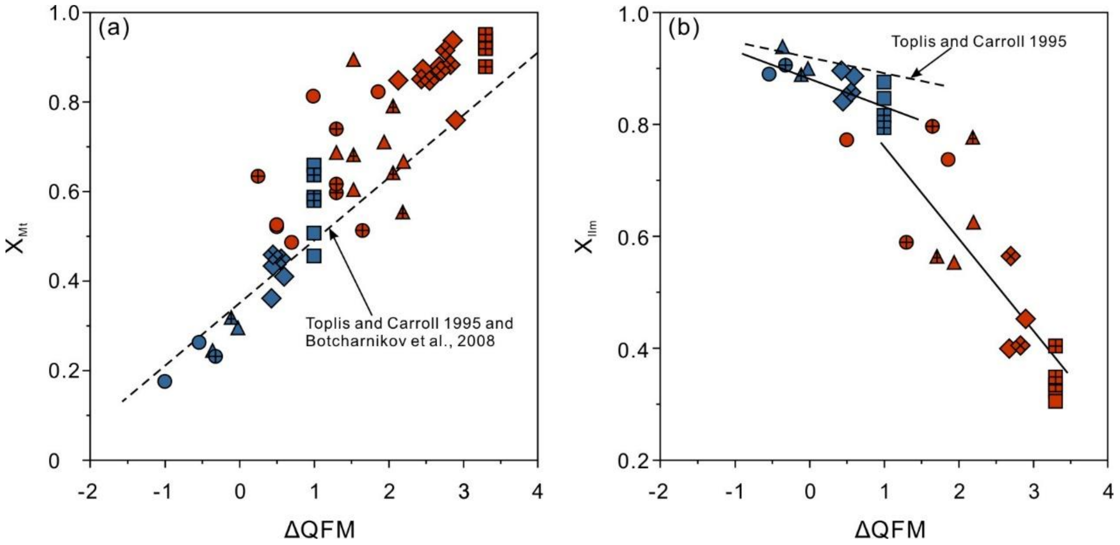

Fig. 3.10. Mole fractions of (a) Mt in magnetite-ulvöspinel solid solution and (b) Ilm in ilmenite-hematite solid solution, as a function of redox conditions (ΔQFM) and X^{fl}_{H2Oini}. Dashed lines in (a) and (b) are linear fits of all data points. Symbols as per Fig. 3.1.

3.4.4.9 Pseudobrookite

In natural rocks, pseudobrookite commonly occurs as oxidation products of ilmenites in basalts (Haggerty, 1981). At 100 MPa and temperatures below 1050 ℃, the endmember of Psb component varies between 31 and 54 mol % (ideal formula: $Fe_2^{3+}TiO_5$, Supplementary Table 3.2 and Supplementary Fig. 3.2c). Actually, crystallization of Psb is an uncommon feature for most of the phase equilibria experiments of basaltic systems, even those at highly oxidized conditions (e.g., Dall’agnol et al., 1999; Sato et al., 1999; Berndt et al., 2005; Botcharnikov et al., 2008). It seems that the high TiO_2 content is the key factor to trigger the precipitation of Psb as shown both in Koepke et al. (2003) and this study. Specifically, Psb is stable under 100 MPa in our experiments, which could indicate that the presence of this phase is enhanced by low pressure. Under higher pressure, rutile instead of Psb is more preferentially stable (e.g., Hellman and Green, 1979; Liou et al., 1998). However, the TiO_2 concentrations of the melt is relatively low, which prevents the crystallization of rutile at 300 MPa. Thus at this pressure, neither pseudobrookite nor rutile is observed, even at oxidizing conditions.

3.4.4.10 Other phases (apatite and amphibole)

Apatite usually shows a hexagonal shape or is present as needles in our experimental products. Among all our experimental samples, amphibole is only observed in one run at 950 ℃ and 300 MPa under reducing conditions. The amphibole is a Mg-rich pargasite according to the classification of Leake et al. (2003). Since no more data is available, we cannot make further interpretations of the effects of fO_2 or aH_2O.

3.5 Discussion

3.5.1 Effect of H_2O on Calcium (Ca) partitioning between olivine and melt

Calcium is a minor element in olivine, and its partitioning coefficient is thought to rely on Fo content in olivine and CaO content in melts, while the effects of T, P, and fO_2 are negligible. Accordingly, Libourel (1999) developed a model to calculate the Ca partition coefficient between olivine and melt and provide constraints on the conditions of Ol crystallization (e.g., Jurewicz and Watson, 1988; Kamenetsky et al., 2006). The equation provided by Libourel (1999) is mainly based on dry experiments and is described by following equation:

$$\ln D*_{\mathrm{CaO}}^{\mathrm{Ol-melt}} = -1.24\ X_{\mathrm{Fo}}^{3} + 3.33\ X_{\mathrm{Fo}}^{2} - 6.55\ X_{\mathrm{Fo}} + 2.05 \qquad (4)$$

However, the $\ln D*_{\mathrm{CaO}}^{\mathrm{Ol-melt}}$ values estimated in hydrous systems and obtained at various aH_2O indicate a systematic shift (e.g., Berndt et al., 2005; Feig et al., 2006; Botcharnikov et al., 2008; Fig. 3.11a-b) when compared to equation (4) and Feig et al. (2006) proposed that this deviation could be caused by an effect of water on the Ca partition coefficient. We combined data from our and other hydrous experiments published so far (Berndt et al., 2005; Feig et al., 2006; Botcharnikov et al., 2008; Feig et al., 2010; Almeev et al., 2013; Husen et al., 2016), which covered a wide range of Fo content in Ol (~40 to 95), fO_2 (~QFM - 2 to QFM + 4.1), aH_2O (~0 to 1) and pressure (100 to 700 MPa) to further constrain the Ca partition coefficient. After removing of experimental data with unrealistically high water contents which exceed the solubility at the investigated pressures (>5 wt.% at 200 MPa, data points of Feig et al., 2006, surrounded by a dashed ellipse in Fig. 3.11a, b), a new equation based on the regression of all data plotted in Fig. 3.11a-b with melt water content <3.5 wt.% is proposed (dashed line in Fig. 3.11c):

$\ln D*_{\mathrm{CaO}}^{\mathrm{Ol-melt}} = -1.24\ X_{\mathrm{Fo}}^{3} + 3.33\ X_{\mathrm{Fo}}^{2} - 6.55\ X_{\mathrm{Fo}} + 1.85(\pm 0.2)$ (5)

Previous study (Libourel, 1999) pointed out that the $\ln D*_{\mathrm{CaO}}^{\mathrm{Ol-melt}}$ value can be used to assess whether a natural olivine is in equilibrium with its host melt. However, according to our new model, it is obvious that olivine equilibrium with hydrous melt could also have obvious low $\ln D*_{\mathrm{CaO}}^{\mathrm{Ol-melt}}$ value (high to ~0.4) than olivine equilibrium with dry melt at the same Fo content. Hence, to determine the equilibration between olivine and its host melt, single $\ln D*_{\mathrm{CaO}}^{\mathrm{Ol-melt}}$ value is not enough and other factors should be taken into consideration, e.g., $\mathrm{Kd}_{\mathrm{Ol-melt}}^{\mathrm{Fe-Mg}}$ value. To the contrary, using the equation (4) from Libourel (1999) and this new equation (5), $\ln D*_{\mathrm{CaO}}^{\mathrm{Ol-melt}}$ value could be used to determine the water conditions in the melt if $\mathrm{Kd}_{\mathrm{Ol-melt}}^{\mathrm{Fe-Mg}}$ value (~0.3) suggests an equilibrium. For instance, H_2O content in volcanic rocks from ELIP is believed to be similar to those related to non-subduction-related plumes, however, recent studies on picrites from ELIP display an island arc-like H_2O content (up to 3.4 wt.%; Liu et al., 2017). With this new calibration, the no zoned Ol compositions from Emeishan picrites ($\mathrm{Kd}_{\mathrm{Ol-melt}}^{\mathrm{Fe-Mg}}$ value ~0.31, Tao et al., 2015) are mostly plotted in or close to the new calibrated range for hydrous system (Fig. 3.11c), correlated well with the previous studies on picrite water contents.

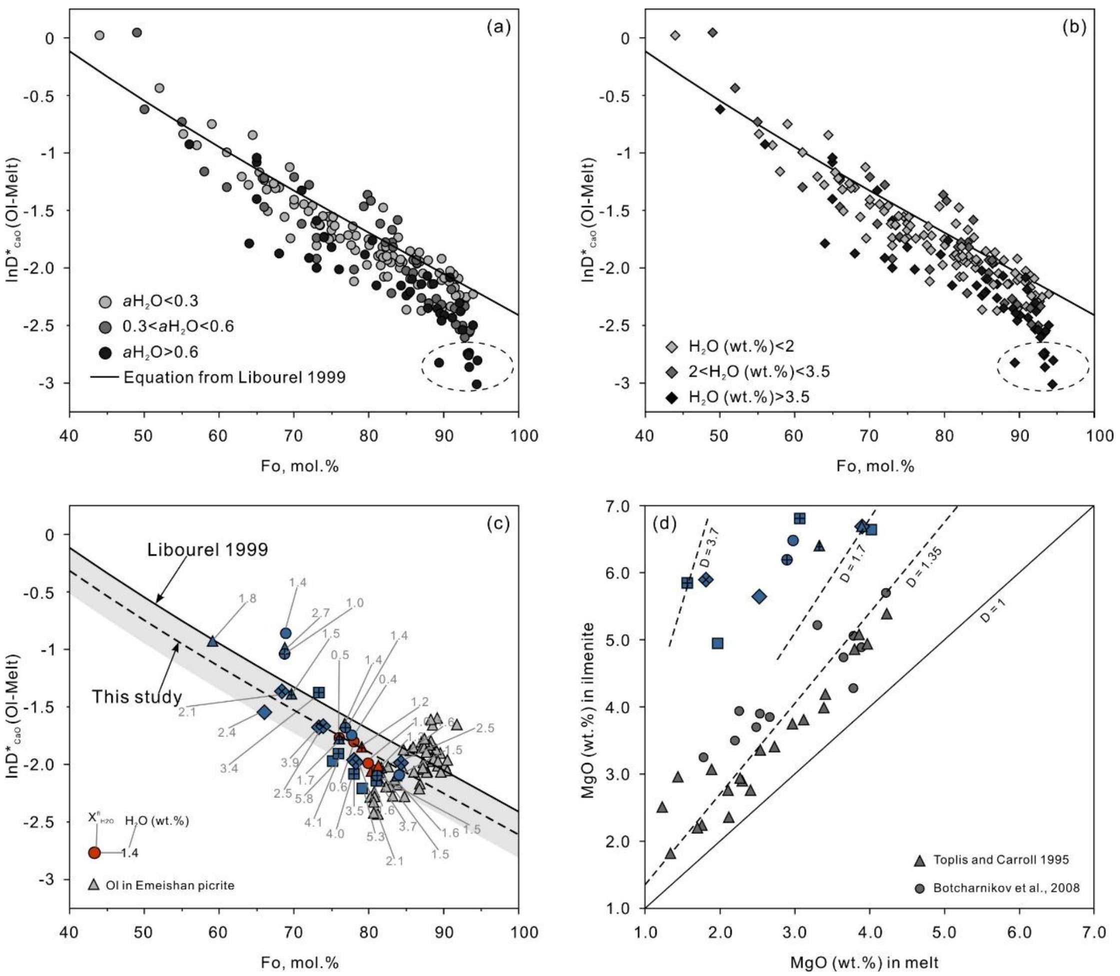

Fig. 3.11. The influence of aH_2O (a) and water content (b) of the melt on the Ca partitioning in Ol. The solid line in the plot belongs to the equilibrium study of Libourel (1999). (c) The new fitting line in this study with error range and the plot of Ca partitioning in our experimental Ol. No zoned olivine in Emeishan picrite is also plotted. (d) MgO partition coefficient between Ilm and coexisting melts in this study and comparison with previous studies. Symbols as per Fig. 3.1.

3.5.2 Mg partitioning between ilmenite and melt in the plagioclase-depleted basaltic system

MgO contents in Ilm could be used to estimate MgO content in its equilibrated silicate melt (e.g., Charlier et al., 2007). Previous studies indicated that the D_{MgO}^{Ilm} (= MgO_{Ilm}/MgO_{melt} in wt.%) is independent of pressure and fO_2 (e.g., Cawthorn and Biggar, 1993; Snyder et al., 1993; Vander Auwera and Longhi, 1994; Toplis and

Carroll, 1995) and varies in a relatively limited range, from ~ 1.3 to 1.5. Phosphorous had been proved by to be able to affect the D_{MgO}^{Ilm}, i.e., decrease of D_{MgO}^{Ilm} with increasing P_2O_5 content (Toplis et al., 1994). Nevertheless, the D_{MgO}^{Ilm} in our experiments had yielded higher values (~1.7 to 3.7 in Fig. 3.11d). We interpret that the deviation in D_{MgO}^{Ilm} due to the melt MgO content is already low when Ilm starts to crystallize. Broad crystallization of Cpx instead of Pl in our experiments, especially under anhydrous conditions, could strongly decrease the melt MgO contents and leads much higher D_{MgO}^{Ilm} . Thus in a Pl-depleted basaltic system (e.g., low aluminum basalts), using D_{MgO}^{Ilm} value at ~ 1.5 to estimate the MgO content in the melts could overestimate the MgO content of the magma. Previous studies on Fe-Ti oxide ore-bearing intrusions in ELIP suggested that the Fe-Ti oxides accumulation occurs at the early stage due to the sudden hydration or oxidization of parental magma (e.g., Pang et al., 2008a; Howarth and Prevec, 2013b). Applying the obtained new D_{MgO}^{Ilm} values from this study, we could recalculate the MgO contents in the melts through compositions of Ilm in the ore layers from the two most giant Panzhihua and Hongge intrusion in ELIP (Luan et al., 2014b; Cao et al., 2019). Assuming the D_{MgO}^{Ilm} = 2 at the initial crystallization stage of Ilm in our experiments, the calculated results are ~4 wt.% MgO content in Panzhihua melt and ~5 wt.% MgO content in Hongge melt. Comparing the primary MgO content (~8 wt.%) in the parental high-Ti basaltic magma, it is evident that the parental magma experienced extensive fractional crystallization before reaching Fe-Ti oxides accumulation in the melts.

3.5.3 Apatite saturation in high-Ti basalts

Apatite is a common cumulate/accessory mineral in layered intrusions and phosphorus plays an important role in Fe-Ti oxide ore mineralization processes (e.g., Skaergaard, Sept-Iles, Bushveld, and Panxi layered intrusions or Complex). Thus, the presence of apatite in such rocks is of interest because it provides a potential constraint on the composition of the liquid with which the minerals were in equilibrium. Previous studies indicate that apatite solubility is almost insensitive to pressure, water content, and oxygen fugacity (e,g., Watson, 1980; Tollari et al., 2006, 2008) and controlled mainly by temperature and melt compositions (e.g., Harrison and Watson, 1984; Tollari et al., 2006, 2008). To test the apatite saturation in our system, two models are applied to estimate the phosphorus content in the melt. Tollari et al. (2006) defined an equation which predicts the P_2O_5 content of silicate liquids saturated in either whitlockite or fluorapatite:

$$\mathrm{M}_{\mathrm{P2O5}}^{\mathrm{melt-sat}} = \exp[\mathrm{T}\times(\frac{-0.8579}{139.00-M_{SiO2}^{melt}} + 0.0165) - 3.3333\ln(\mathrm{M}_{\mathrm{CaO}}^{\mathrm{melt}})] \qquad (6)$$

and Harrison and Watson (1984) described the apatite solubilities from melts by the expression:

$$\ln\mathrm{D}_{\mathrm{P}}^{\mathrm{Ap/melt}} = [8400 + ((\mathrm{SiO_2} - 0.5)\times 2.64\times 10^4))/\mathrm{T}] - [3.1 + (12.4\times(\mathrm{SiO_2} - 0.5))] \text{ (7)}$$

where M represents the molar percentage of the relevant oxides (e.g., M_{SiO2} from 10% to 80%) and SiO_2 is the weight fraction of silica in the melt. T is temperature in Kelvin. Using these two equations, we calculated the required P content for apatite saturation in our experimental melts and it is obvious that the predicted P contents from Tollari et al. (2006) are systematically higher than the detected P contents in experimental products in which melt and apatite are coexisting (Fig. 3.12). In contrast, Harrison and Watson (1984) model provides better estimations for P contents when apatite reached saturation in our experiments. One of the possible reason explaining the large gap between the empirical prediction of Tollari et al. (2006) and experimental results might be due to the significantly higher Cpx/Pl ratio in our system than experiments in the experiments of Tollari et al. (2006), which significantly changed the CaO and SiO_2 contents in the residual melts. Although apatite is a late crystallizing phase in our experiments, this discrepancy between empirical calculations and experiments indicates that models proposed for basaltic systems are not suitable to estimate the maximum P_2O_5 contents in residual melts in high-Ti basaltic systems. Considering that phosphorus may play an important role in the formation of immiscible silicate liquid, the application of available apatite solubility models should be applied with caution to estimate maximum P_2O_5 contents in melts.

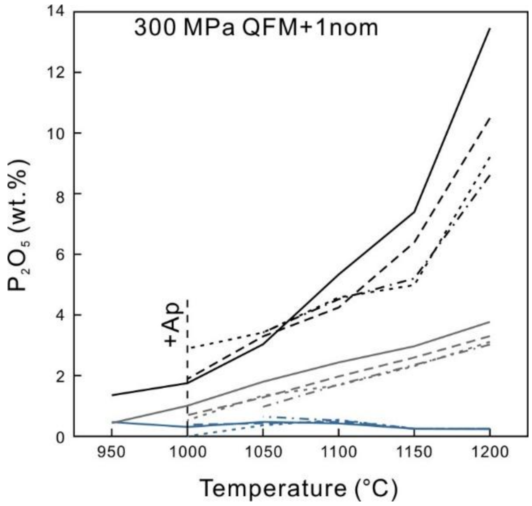

Fig. 3.12. Values of P_2O_5 (wt.%) required to saturate Ap in experimental melts of this study. Solid, dashed and dotted lines in dark color represent the calculated P_2O_5 (wt.%) contents in different initial X^{fl}_{H2Oini} according to equation (6). Lines in grey color illustrate the P_2O_5 content required for Ap saturation according to equation (7). Lines in blue represent the detected P_2O_5 (wt.%) contents in experimental melts under 300 MPa and intrinsic fO_2 at QFM + 1.

3.5.4 Comparison of the experimental conditions with estimations from thermobarometers and oxybarometers

Thermodynamic parameters (e.g., T, P, fO_2) in magmatic systems are the key factors to explore phase equilibria as well as mineral-melt and fluid-melt partition coefficients. The most commonly used and reliable way to reconstruct magmatic conditions is via thermobarometry and oxybarometry. In the past thirty years, abundant thermobarometers and oxybarometers were calibrated relying on numerous experimental studies (e.g., Putirka et al., 2003; Putirka, 2008; Ghiorso and Evans, 2008; Arató and Audétat, 2017). According to the application conditions, these thermometers and oxybarometers can be distingished into three types: single mineral (e.g., Nimis 1995; Nimis and Ulmer, 1998; Ridolfi et al., 2010; Wang et al., 2021), mineral-liquid (e.g., Putirka et al., 1996, 2003; Neave and Putirka, 2017), and mineral-mineral types (e.g., Brey and Köhler, 1990; Putirka, 2005). However, as pointed out by several previous studies (e.g., Feige et al., 2006; Botcharnikov et al., 2008), some commonly used models were unable to reproduce the experimental conditions for those runs with high aH_2O. Based on our experimental results in which Cpx and Mt are often observed, we can compare the Cpx-related thermobarometers (Fig. 3.13) and Mt-related thermometers and oxybarometers (Fig. 3.14) with experimental conditions.

Most of the calculated temperatures from the Cpx-liquid thermobarometer of Putirka (2008) is within the error predicted by the model (± 45 ℃, Fig. 3.13a, c, e), showing the good reliability of this model to evaluate temperatures. However, the applications of our analytical data to test the Cpx only or the Cpx-Opx thermobarometers indicate that they do not predict accurately the temperature conditions of the experiments (Fig. 3.13a, c). The comparison of calculated pressure and experimental pressures (Fig. 3.13b, d, f) indicates that none of the thermobarometers (Cpx only, Cpx-liquid, Cpx-Opx) are suitable to predict pressures variations within ± 100 MPa. Our data fit within the precision of the pressures estimated with the Opx-Cpx thermobarometer which is, however, very large (± 280 MPa). The Cpx-liquid thermobarometer tends to overestimate pressure when applied to our compositions. Cpx, Opx and melt compositions are not a simple function controlled only by P and T, but are also buffered by the other phases that are present. Hence, it is not surprising that the single Cpx thermobarometer has a larger uncertainty compared to the other thermobarometers based on two co-existing phases.

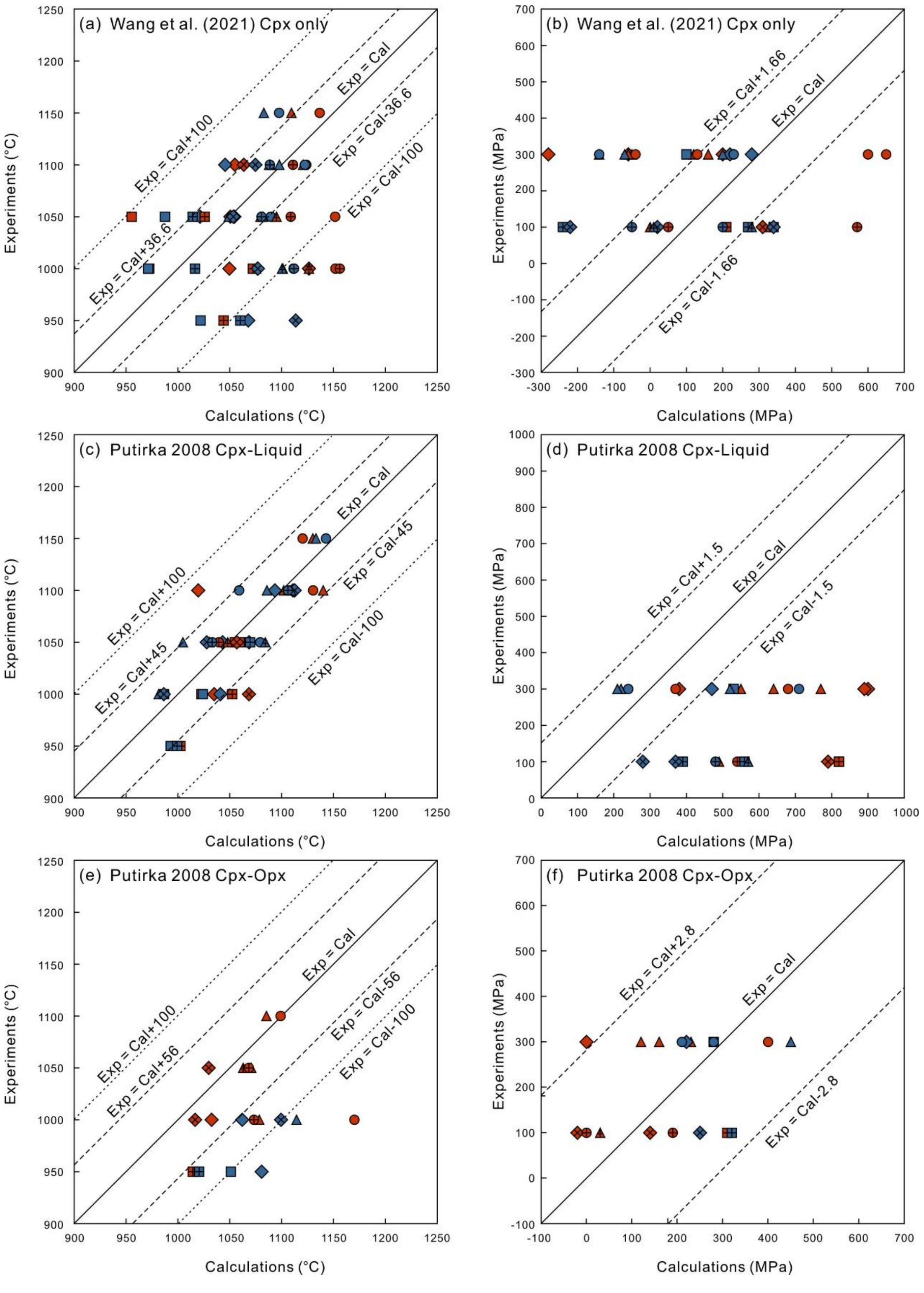

Fig. 3.13. Single Cpx thermometer (a) and barometer (b) according to Wang et al. (2021). Cpx-Liquid thermometer (c) based on equation 34 and barometer (d) based on equation 32c from Putirka (2008). Cpx-Opx thermometer (e) based on equation 36 and barometer (f) based on equation 39 from Putirka (2008). The solid lines in each panels represent experimental results equal to calculation results. The dashed lines show the suggested standard error of estimations

from literatures. The dotted lines illustrate the temperature differences within 100 ℃.

The compositions of ilmenite and magnetite can be used to check the thermometers developed so far with oxides. The single Mt thermometer of Canil and Lacourse (2020) trends to slightly overestimate temperatures (Fig. 3.14a), however, most of the calculated temperatures still show good agreements with experimental conditions (<100 ℃) which confirms a high reality of using Mg content in magnetite as a thermometer. In comparison, temperatures predicted by the Mt-Ilm thermometer (Ghiorso and Evans, 2008) displayed larger uncertainties compared to the calculation results using same dataset from Canil and Lacourse (2020) model, especially for the oxidizing experiments (Fig. 3.14b, c). One possible explanation for the differences between our data and the Mt-Ilm model is the presence of high Cr content in our system. According to the crystal structure of Mt, Cr^{3+} mainly replaces Fe^{3+} in Mt. Thus, both Fe^{3+} and total Fe content in Mt are decreasing due to high Cr partition coefficient in Mt. The Mt-Ilm thermometer was made using either $Fe^{2+}Ti \Leftrightarrow (Fe^{3+})$ exchange or $Fe^{2+} \Leftrightarrow Mg$ exchange between two oxides (Ghiorso and Evans, 2008), thus, high Cr content in Mt could obvious influence the elements exchange between two oxides and in consequence, influencing the accuracy of the Mt-Ilm thermometer. Hereby, we would rather suggest that the single Mt thermometer provides better temperature prediction in natural system.

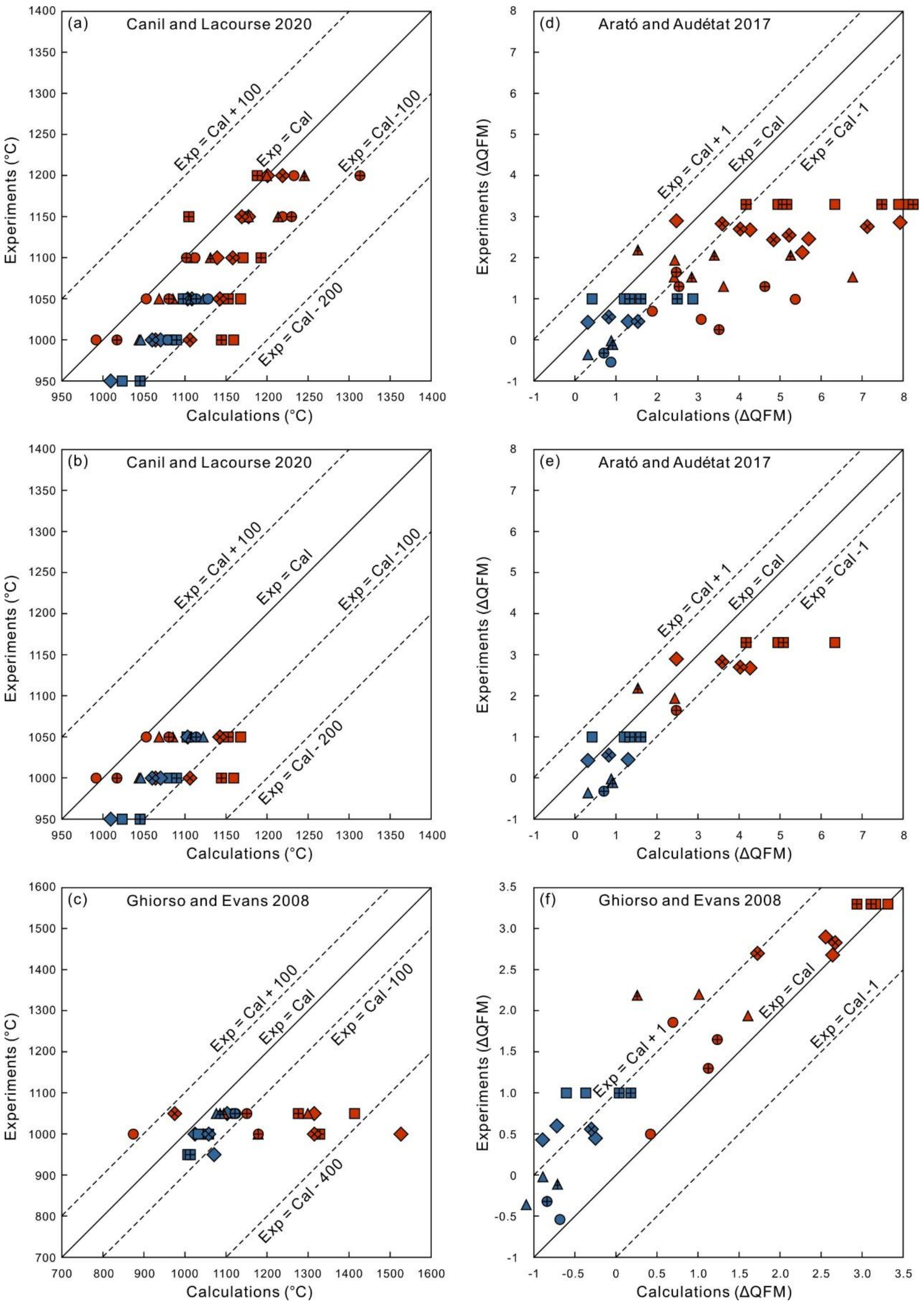

Fig. 3.14. (a) Single Mt thermometer according to Canil and Lacourse (2020) and (b) Single Mt thermometer only applied on Mt-Ilm co-existing samples. (c) Mt-Ilm thermometer based on Ghiorso and Evans (2008) for the same Mt-Ilm co-existing samples from (b). (d) Mt-Liquid oxybarometer according to Arató and Audétat (2017) and (e) Mt-Liquid oxybarometer only

applied on Mt-Ilm co-existing samples. (f) Mt-Ilm barometer based on Ghiorso and Evans (2008) for the same Mt-Ilm co-existing samples from (e).

Oxygen fugacity is an important parameter controlling Fe-Ti oxides composition, thus, elements distribution between oxides and melts or within oxides pairs can be used as an oxybarometer to explore the potential fO_2 in natural system. The two commonly used oxybarometers rely on the compositions of coexisting Mt-melt (Arató and Audétat, 2017) and coexisting Mt-Ilm equilibration (Ghiorso and Evans, 2008). Applying the Mt-melt oxybarometer on our samples, it is obvious that the calculated fO_2 is quite far away from the experimental conditions (Fig. 3.14d). However, with temperatures decreasing, especially when ilmenite reached saturation (≤ 1050 °C), the gap between the calculated and experimental fO_2 becomes smaller (Fig. 3.14e). For the Mt-Ilm coexisting samples in our experiments, the Mt-Ilm oxybarometer shows no obvious advantages over Mt-melt oxybarometer (Fig. 3.14e, f), as most of the calculations are about one log unit lower than experimental conditions. Considering that these two oxybarometers were all calibrated with Cr-depleted Mt, there is no doubt that there would be a larger uncertainty for the calculation results using Cr-rich Mt from our system. In addition, the Mt-melt oxybarometer was mainly determined with dacitic and rhyolitic melt compositions and temperature range from 750-1100 ℃ which could help to explain why the predictions are less ideal our high-temperature experiments with basaltic melt compositions.

3.5.5 Liquid line of descent (LLD) and application to the felsic magmatism in ELIP

The evolution of experimental melts as a function of melt MgO contents is plotted in Fig. 3.15. According to the previous studies, in ELIP, there are abundant felsic intrusions temporally and spatially close to the high-Ti basalts. Sr-Nd isotopes indicate that these felsic intrusions are genetically related to the high-Ti basalts, especially syenite intrusions emplaced simultaneously with the Fe-Ti oxide ore-bearing layered intrusions (Shellnutt and Iizuka, 2011). To explore the potential relationships between the mafic and felsic magmas, the compositions of syenite intrusions close to the three main Fe-Ti oxide ore-bearing layered intrusions (Baima, Hongge and Panzhihua, Supplementary Table 3.3) are also plotted in Fig. 3.15.

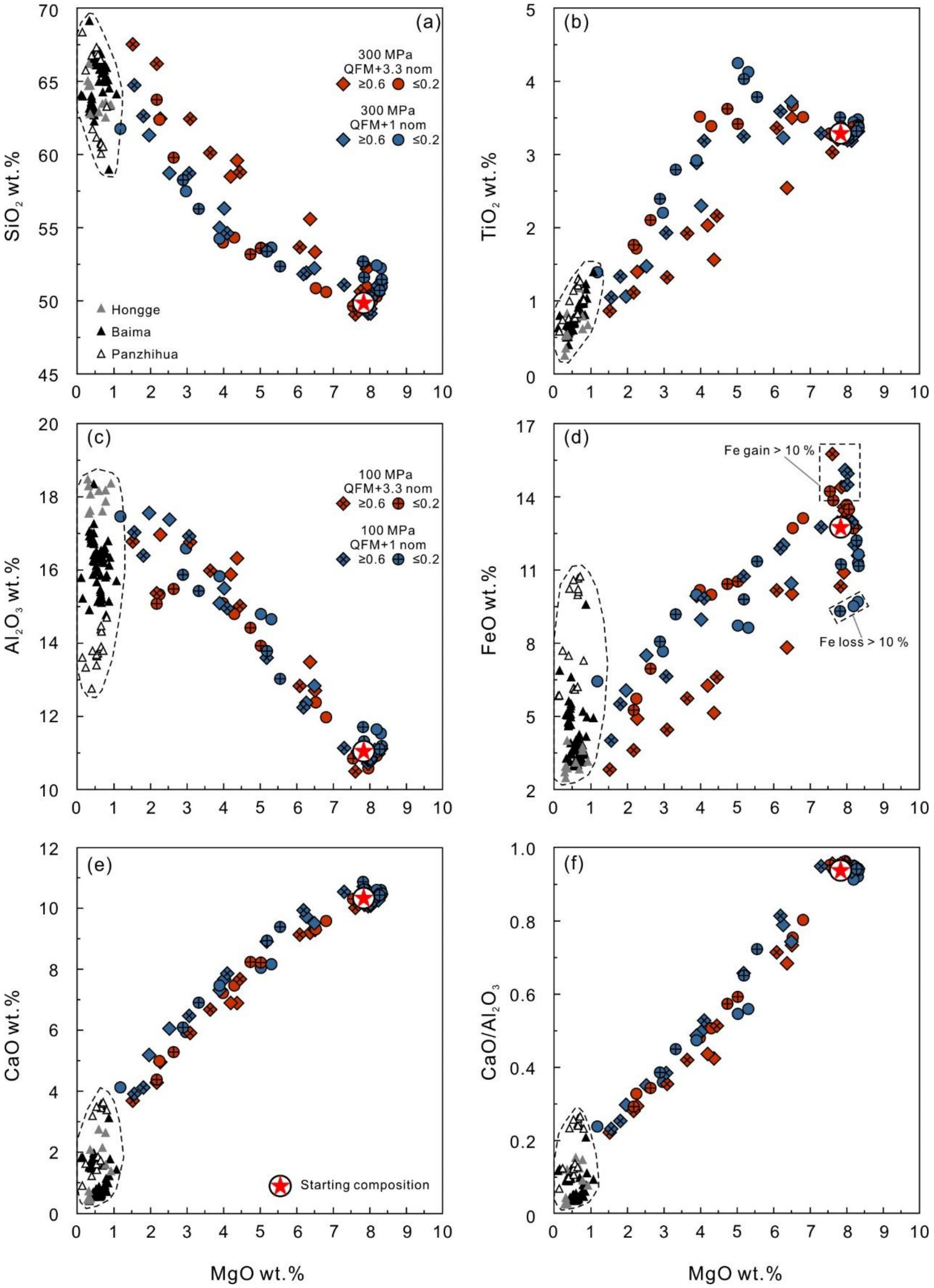

Fig. 3.15. Liquid lines of descent of experimental melts as a function of melt MgO content at

hydrous ($X^{fl}_{H2Oini} \geq 0.6$) and low $a$$H_2O$ ($X^{fl}_{H2Oini} \leq 0.2$) conditions. The triangles in dark, grey and white colors represent the compositions of contemporaneous syenite intrusions from Baima, Hongge and Panzhihua (data sources are from Shellnutt and Zhou, 2008; Shellnutt et al., 2009; Zhong et al., 2011; Shellnutt, 2021 and our unpublished syenite data).

Overall, SiO_2 contents of the experimental melts increase with decreasing melt MgO contents and define LLD's which are nonlinear (Fig. 3.15a). Furthermore, for any specific MgO content, melt SiO_2 contents of hydrous-oxidizing experiments are always higher than other for reducing counterpart experiments. One possible reason is the high proportion of Fe-Ti oxides under hydrous-oxidizing conditions. The TiO_2 contents of residual melts display a bell-shaped evolution for different experimental series dictated by (1) fO_2 conditions controlling Fe-Ti oxides crystallization and (2) aH_2O influencing silicate minerals crystallization (Fig. 3.15b). The low fO_2-aH_2O experiments display a significant increase of TiO_2 (up to ~4 wt.%) until Ilm saturation is reached. In contrast, the hydrous and oxidizing experiments evolve towards lower TiO_2 contents from the beginning of the crystallization sequence. The low aH_2O-oxidizing and hydrous-reducing experiments have an approximately constant TiO_2 content until about 4 wt.% melt MgO and TiO_2 contents decrease with decreasing MgO contents.

Al_2O_3 content increases with decreasing MgO in both series and reaches their maximum at the onset of Pl precipitation (Fig. 3.15c); a higher maximum is reached in hydrous experiments (17.6 wt.%) as a result of delayed Pl crystallization. Eliminating the samples with high Fe gain or loss from capsules (> 10%), the experimental melts show a general depletion of FeO from 13.5 to 2.8 wt.% with progressive magma differentiation (Fig. 3.15d). It is noteworthy that FeO contents in hydrous-oxidized melts decrease much faster than in low aH_2O melts or reduced melts. This is related to the extensive crystallization of Fe-Ti oxides as a consequence of high fO_2 in hydrous-oxidizing experiments. Since Cpx is the dominant phase in all experimental samples, CaO contents (Fig. 3.15e) and CaO/Al_2O_3 ratios (Fig. 3.15f) show similar decreasing trends at all experimental conditions.

It is noteworthy that for the selected major elements in Fig. 3.15, the compositional fields of Hongge and Baima syenite intrusions lie close to the end of the compositional fields defining the differentiation trend of high-Ti basalts in ELIP. In contrast, compositions of Panzhihua syenite intrusion do not match the prolongation of the experimental trend to low MgO contents, especially for Al_2O_3, FeO and CaO/Al_2O_3 ratios (Fig. 3.15c, d, f). Zhong et al. (2007) suggested that these felsic intrusions were formed by extensive fractional crystallization of basaltic parental magmas, whereas Shellnutt and Zhou (2007, 2008) and Shellnutt et al. (2009) argued that these intrusions were generated by remelting of underplated cumulate material. Based on our experiments, the composition of Hongge syenite intrusion displays the closest fitness with the experimental LLD, especially for the reducing experiments. Using MELTS simulation, Shellnutt (2021) modelled the fractional crystallization of high-Ti basalts at 500 MPa and fO_2 of QFM and QFM + 1. Modelling results showed that the Hongge syenite is likely produced by crystal accumulation during emplacement, similar to what was observed in our reducing experiments. Evidence from both MELTS modelling and our experimental results strongly suggests that the Hongge syenite was formed by fractional crystallization of high-Ti basalts. Although the composition of Baima syenite intrusion is also plotted close to the experimental LLD, Al_2O_3, FeO and CaO content still illustrate an obvious offset from the differentiation trend defined by experiments (Fig. 3.15c, d, e). Through SHRIMP zircon U-Pb techniques, the Baima syenite was dated at 252±2.5 Ma, which is about 8-10 Ma younger than the Baima Fe-Ti oxide ore-bearing layered intrusion (262±3, Shellnutt and Zhou, 2008). Combined with trace elements signatures (e.g., positive Eu anomalies and enrichment of light rare earth elements) and Sr-Nd isotope ratios, the Baima syenite intrusion was suggested to be formed by remelting of underplated mafic magmas injected into the crust during ELIP magmatism instead of fractional crystallization of high-Ti basalts. As for Panzhihua syenite, although the age of the syenite intrusion is indistinguishable from those of the

Panzhihua gabbroic intrusion (Zhong et al., 2011), the significantly positive $\varepsilon_{Hf}(t)$ values of syenites are higher than those of the upper gabbros of the associated mafic intrusion, which shows that they cannot be derived by fractional crystallization of these bodies. In contrast, the similar of Nd isotope ratios between Panzhihua syenite intrusions and major cyclic units of Panzhihua mafic layered intrusions, suggesting that their parental magmas share a common source and the Panzhihua syenite intrusions were generated by fractionation from mafic magmas in the deep-seated magma chamber (possibly near the crust-mantle boundary). In addition, FeO, CaO and CaO/Al_2O_3 ratio (Fig. 3.15d, e, f) in Panzhihua syenite display two different groups which was proposed generated by the emplacement of two distinct syenitic melts from differentiation of newly underplated basaltic magmas ponded at depth (Zhong et al., 2009). The different behavior between experimental melts and syenite intrusion compositions clearly tell us that although the syenite intrusions in the Panxi region might have close compositions, the genesis could be totally different from each other.

3.5.6 Melt evolution within mineral component space and constrains for the differentiation condition of high-Ti basalts

Applying the projections of Tormey et al. (1987) and Grove (1993), normative mineral compounds were recalculated from residual melt compositions and plotted onto the Cpx (diopside + hedenbergite)-Ol (forsterite + fayalite)-Qtz (Fig. 3.16a) and Pl (anorthite + albite)-Cpx (diopside + hedenbergite)-Qtz (Fig. 3.16b) pseudo-ternary diagrams through Pl (+ Ap + Fe-Ti oxides) and Ol (+ Ap + Fe-Ti oxides). Phenocrysts in the LZS high-Ti basalts and surrounded lavas are mainly Cpx, Pl and Ol (Qi et al., 2008), thus, only experimental melts saturated with Cpx, Cpx + Pl, Cpx + Ol, and Cpx + Pl + Ol are plotted in the triangular diagrams. In the projection from the Pl apex on the basalt tetrahedron (Fig. 3.16a), experimental melts conducted at 300 and 100 MPa exhibit a similar continuous strong decrease of normative Cpx and minor decrease of Ol accompanied by an enrichment in Qtz, illustrating the differentiation trend away from the Cpx-Ol side-line towards the Qtz corner. This trend is consistent with extensive crystallization of mafic silicates with ongoing cooling (Fig. 3.2c-d) and with the dominant Cpx phenocrysts observed in natural high-Ti basalts (Qi et al., 2008). In the Pl + Cpx + Qtz diagram (Fig. 3.16b), the experimental melts can be clarified into two distinct evolutions according to the occurrence of Ol in the crystallized phases. It is obvious that the Ol-bearing melts has relatively low fO_2 compared to those melts without Ol. Under low fO_2 conditions (< ΔQFM + 2), although aH_2O varies from nominally dry to water-saturated conditions, experimental melts are significantly displaced towards "Pl-enriched" compositions and evolve toward the Pl apex nearly parallel to the Cpx-Pl join, except for the most differentiated compositions which finally evolve towards silica-enriched compositions. In contrast, although high fO_2 hydrous melts (> ΔQFM + 2) are also shifted towards compositions that increase in Pl component (Supplementary Table 3.2), due to the high aH_2O which suppresses the crystallization of Pl, the melts evolution trend moves close to the increase of silica saturation (Fig. 3.2f; Table 3.2). According to the previous experimental studies of high-Ti basalts (e.g., Botcharnikov et al., 2008), hydrous experimental melts are significantly displaced towards "Pl-enriched" compositions and evolve toward the Pl apex nearly parallel to the Cpx-Pl join in the projection from Qtz, as a result of the delayed crystallization of Pl. However, in our system, obvious reversal trend is observed that the low aH_2O melts evolve toward the Pl apex instead of hydrous melts. One possible explanation is that due to the low Al_2O_3 content in our starting high-Ti basalts, Pl is unsaturated in most of our experimental samples, thus, the saturation of Pl in experimental melts is mainly controlled by the crystallinities. Early crystallization of Cpx, Ol, and Fe-Ti oxides both promote the Al_2O_3 and SiO_2 content in the melt which benefits to the saturation of Pl.

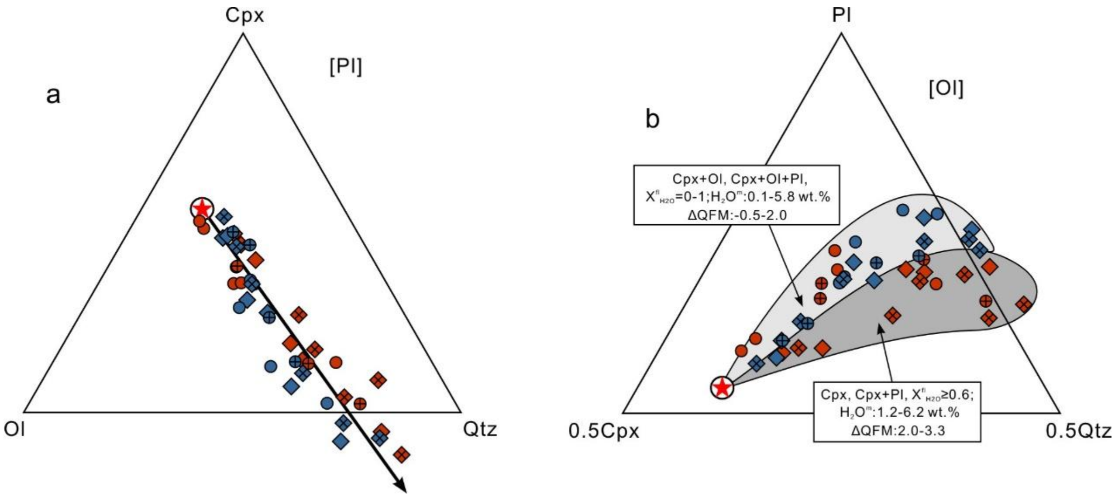

Fig. 3.16. Melts compositions of 300 MPa and 100 MPa saturated with Cpx, Cpx+Ol, Cpx+Pl and Cpx+Pl+Ol and comparison projected onto pseudoternary plots: (a) Cpx-Ol-Qtz projected from Pl, and (b) Pl-Cpx-Qtz projected from Ol. All calculations were performed according to the method used by Tormey et al. (1987) and Grove (1993). Symbols as per Fig. 3.15.

The effect of fO_2 on differentiation trends is also reflected in the FeO/MgO weight ratio versus melt SiO_2 content (Fig. 3.17). The experimental melts obtained under low fO_2 show an increase in melt FeO/MgO ratio with increasing SiO_2 content. These melts follow a tholeiitic differentiation trend after the classification of Miyashiro (1974). In contrast, the oxidized melts coexisting with Fe-Ti oxides over a wide range of conditions are consequently depleted in FeO following a calc-alkaline differentiation trend. In particular, strongly oxidized melts obtained in experiments with high X^{fl}_{H2Oini} (diamonds in Fig. 3.17) follow an evolution trend at almost constant FeO/MgO, which is common for calc-alkaline series (in SiO_2 range below 65 wt.%). Taking our experimental data into account, we can constrain the differentiation condition of LZS high-Ti basalts, assuming that the layered intrusions such as Baima, Hongge and Panzhihua represent the upper magma reservoirs from which Emeishan high-Ti basalts were extracted. In the shallow range of 100-300 MPa, pressure variations have a negligible influence on the evolution path. Compared to pressure, fO_2 is expected to play a dominant role in influencing the evolution trends. The most striking observation in this study is that the high-Ti basalts in ELIP could evolve in a large water activity range, from nominally dry to water-saturated conditions, which might be the critical factor controlling the precipitation of Fe-Ti oxides in ore-bearing layered intrusions. According to the Cpx and Pl phenocrysts in LZS basalts and comagmatic lavas, we proposed that the LZS high-Ti basalts most probably differentiated in an oxidized hydrous condition.

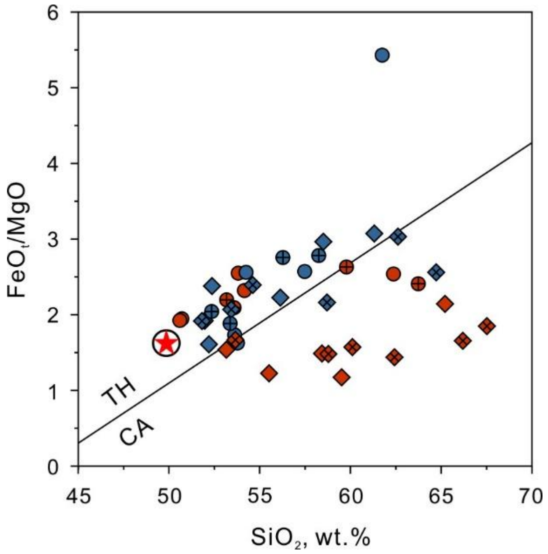

Fig. 3.17. The relationship between FeO/MgO ratio and SiO_2 content of the melt for the experimental data as a function of X^{fl}_{H2Oini}. Continuous lines are based on the discrimination criteria of Miyashiro (1974) for tholeiitic and calc-alkaline rock series. Symbols as per Fig. 3.15.

3.5.7 Implication for the crystallization conditions of the Hongge and Panzhihua layered intrusions

In ELIP, Panzhihua and Hongge are two of the most giant Fe-Ti oxide ore-bearing mafic-ultramafic layered intrusions. Although both are believed to have similar high-Ti basaltic parental magmas (e.g., Zhou et al., 2005; Zhong et al., 2006; Wang et al., 2008; Zhang et al., 2009; Hou et al., 2012), the differences in lithology and occurrence of Fe-Ti oxides mineralization indicate that the parental magmas experienced distinct crystallization processes (Table 3.3). Given that the crystallization sequence is close to the observations in the layered intrusions in ELIP, the phase equilibria obtained under different P-T-fO_2-aH_2O conditions in this study

(Fig. 3.1) can be applied to constrain the physical-chemical conditions for their formation. The mineral phase stability fields according to our experimental results and the simplified stratigraphic columns with mineral assemblages for Panzhihua and Hongge layered intrusions are illustrated in Fig. 3.18.

Table 3.3 Comparison of Panzhihua and Hongge Fe-Ti-oxide ore-bearing layered intrusions in ELIP

Intrusion name	Panzhihua	Hongge
Rock type	Gabbro (±Apatite)	Clinopyroxenite (±Olivine), gabbro
Hydrous mineral content	< 2 %	Up to 15 % in some section
Mineralization position	Lower Zone	Middle Zone

As shown in Fig. 3.18b, the mineral assemblages at the bottom of Panzhihua and Hongge are clinopyroxene + plagioclase and clinopyroxene + olivine, respectively. When compared to the experimental products and assuming the same parental magma (starting material for the experiments), it indicates that the high-Ti basalts started to crystallize at different temperature. Even if the Panzhihua melts were nearly dry, the maximum temperature for coexisting Cpx + Pl is ~ 1100 ℃ (Fig. 3.18a, c, oxidizing experiments). Moreover, in contrast to Hongge intrusion, cumulus olivine is absent at many positions in the stratigraphic column in Panzhihua, especially the lower part. This strongly suggests that the prevailing fO_2 during the formation of the Panzhihua intrusion should be relatively higher as olivine is more stable at reducing conditions (Fig. 3.1). For Hongge intrusion, Cpx + Ol can occur at temperatures as high as 1150 ℃ and the conditions should be most probably reducing to allow a large Cpx + Ol stability field. Furthermore, the fO_2 range for the parental magma could be constrained from the Pl-Cpx-Qtz triangle diagram (Fig. 3.16b), in which melts coexisting with olivine, either Cpx + Ol or Cpx + Ol + Pl, are only obtained in the fO_2 range at ~ ΔQFM - 0.5 to + 2 (light grey colored field in Fig. 3.16b). Hence, the most probable initial fO_2 ranges for Panzhihua and Hongge intrusion corresponds to ~ + 1 <

ΔQFM < + 2 and -1 < ΔQFM < + 1, respectively. It is worth noting that the mineral assemblage observed in the stratigraphic column of Hongge intrusion indicates that the fO_2 was gradually increasing with magma differentiation from bottom to the top. From the Lower Zone to the Middle Zone, the cumulate layers change from olivine clinopyroxenite layers to clinopyroxenite layers with minor cumulus olivine. Based on the phase equilibria in this study (Fig. 3.18a), the stability field of Ol decreases with increasing fO_2 at relatively constant aH_2O. Thus, the fO_2 of Hongge intrusion shows an obvious increasing trend during the crystallization process. According to the phase relationships from this study and previous studies (e.g., Toplis and Carroll, 1995; Botcharnikov et al., 2008), the variation of prevailing fO_2 will significantly influence the stability and proportions of Fe-Ti oxides in crystallizing magmas (Fig. 3.2). Hence, we can tentatively propose that due to the relatively more oxidizing condition at early stages, the Fe-Ti oxide ore layers are already observed in the Lower Zone in the Panzhihua intrusion. In contrast, Fe-Ti oxides ore layers are observed in the Middle Zone of the Hongge intrusion as a result of gradual increasing of fO_2 (Fig. 3.18b).

The stability of plagioclase is strongly affected by the prevailing aH_2O in the system (Botcharnikov et al., 2008; Almeev et al., 2012). This has been experimentally confirmed again by this study, as reflected by the fact that high aH_2O could suppress the crystallization of plagioclase (Fig. 3.1). Since plagioclase is the major cumulus phase in the Panzhihua intrusion, the prevailing aH_2O in the case of Panzhihua is expected to be relatively low. In the case of Hongge, the absence of Pl in the Lower and Middle Zone suggests more hydrous crystallizing conditions. This inference is further supported by the presence of high proportions of poikilitic amphibole in Hongge intrusion.

The emplacement depth of these Fe-Ti oxide ore-bearing layered intrusions is ambiguous, as their plutonic petrographic features and the contact with coeval continental flood basalts do not agree (e.g., Song et al., 2013; Luan et al., 2014b). Nevertheless, the experimentally-constrained phase relations could provide several key information. Particularly, amphibole only crystallized under 300 MPa in our experiments, thus the presence of interstitial and poikilitic amphibole which has an magmatic origin in both Hongge and Panzhihua (Pang et al., 2010; Howarth et al., 2013; Luan et al., 2014a, 2014b; Wang et al., 2020) strongly indicate that the crystallization pressure is greater than 100MPa. Besides, in Hongge intrusion, olivine is observed to crystallize together with magnetite and formed magnetite-dunite layers in the Middle Zone of Hongge intrusion (Wang et al., 2020). According to the experiments, the crystallization field of only olivine + oxide is only observed at 100 MPa. Hence, the crystallization pressure of Hongge intrusion is at least no greater than 300 MPa (possibly in the range of 200-300 MPa). Furthermore, based on the pressure effect on the phase proportions of plagioclase and olivine in our experiments, i.e., lower pressure prefers to crystallize more Pl and less Ol, we believe that the crystallization pressure of Panzhihua intrusion may be lower than that of Hongge intrusion (possibility in the range of 100-200 MPa).

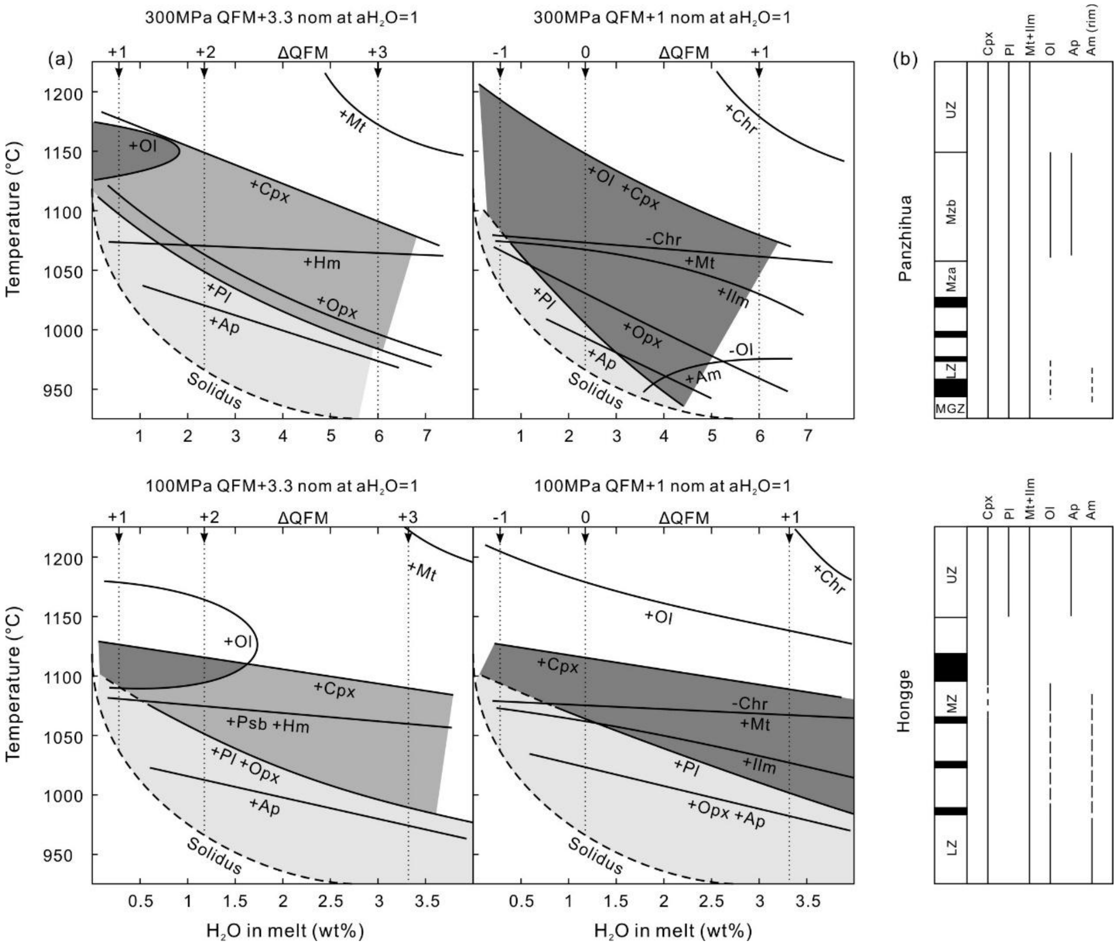

Fig. 3.18. (a) Different mineral cotectics as a function of P-T-fO_2-aH_2O conditions for the high-Ti basalts in this study. The dark grey colored fields represent the coexisting field of Ol+Cpx. The medium grey colored fields illustrate the single crystallizing conditions of Cpx. The light grey fields mark the co-crystallizing conditions of Cpx+Pl and it is worth noting that in the reducing experiments Cpx and Pl in the light grey fields also co-crystallized with Ol. (b) Mineral assemblages in different lithological zones of Panzhihua and Hongge layered intrusion. Solid lines represent the continuous occurrence of mineral phase while dashed lines illustrate the discontinuous occurrence of mineral phases. Abbreviations: LZ-Lower Zone; MZ-Middle Zone; UZ-Upper Zone; MGZ-Marginal Zone; Mza-Middle Zone a; Mzb-Middle Zone b. Other abbreviations for minerals as per Fig. 3.1.

In summary, although the parental magma of Fe-Ti oxide ore-bearing layered intrusions in ELIP is similar in composition, the different P-T-fO_2-aH_2O conditions (Table 3.4) control the diversity of crystallization and mineralization process in these layered intrusions. Thermodynamic modellings, such as MELTS (Ghiorso and Sack, 1995), are always applied to track the differentiation process of layered intrusions in ELIP (e.g., Zhang et al., 2012; Song et al., 2013; Luan et al., 2014b; Liao et al., 2015). However, our study indicates that during the formation of these layered intrusions, the P-T-fO_2-aH_2O conditions are not constant. Hence, such modelling results, especially those with constant fO_2 conditions, should be treated with caution when applied to the natural samples.

Table 3.4 Crystallization conditions of Panzhihua and Hongge Fe-Ti-oxide ore-bearing layered intrusions in ELIP

Intrusion name	Panzhihua	Hongge
Temperature	< 1100 ℃	< 1150 ℃
Pressure	100-200 MPa	200-300 MPa
Oxygen fugacity	QFM+1 to QFM+2	QFM-1 to QFM+1
Water content	Low	High

3.6 Conclusions

The systematic experiments performed at various aH_2O and fO_2 conditions at 300 and 100 MPa using high-Ti basalts as a starting material allowed us to bracket the possible differentiation conditions for the parental magma of Fe-Ti oxide ore-bearing layered intrusions in ELIP. According to the experimental results, the parental high-Ti basalts experienced crystallization at a temperature range from ~ 1150 to 950 ℃ and a depth of about 3-10 km (about 100 to 300 MPa). Water actively could vary widely, from nominally dry to water-saturated conditions. Oxygen fugacity is relatively low, ranging from QFM - 1 to QFM + 2. Furthermore, phase equilibria obtained in this study can be used to determine the different P-T-fO_2-aH_2O conditions of the two giant Panzhihua and Hongge Fe-Ti oxide ore-bearing layered intrusions in ELIP. Through comparison of crystallization sequence and mineral cotectics in natural and experimental samples, Panzhihua intrusion formed in a relatively oxidized, low T-P-aH_2O conditions whereas Hongge intrusion started to crystallize at relatively reduced conditions with a progressive evolution to oxidizing conditions which could be related to the high aH_2O that was prevailing.

Chapter 4: Hydrothermal reworking as a mechanism forming high-grade Fe-Ti-V ores in layered intrusions

Dachuan Wang[1], Tong Hou[2], Roman Botcharnikov[3], Stefan Weyer[1], Sarah-Lynn Haselbach[1], Zhaochong Zhang[2], Meng Wang[2], Ingo Horn[1], François Holtz[1]

[1] *Institut für Mineralogie, Leibniz Universität Hannover, Callinstr. 3, 30167 Hannover, Germany*

[2] *State Key Laboratory of Geological Processes and Mineral Resources, China University of Geosciences, Beijing 100083, China*

[3] *Institut für Geowissenschaften, Johannes Gutenberg Universität Mainz, J.-J.-Becher-Weg 21, 55125 Mainz, Germany*

(submitted to Science Advances)

Abstract

The genesis of high-grade Fe-Ti-V oxide ores (up to >90 vol.%) in layered intrusions remains highly debated. Here we show that hydrothermal dissolution and re-precipitation of Fe-Ti-V oxides played a critical role in the formation of high-grade massive ores using textural-compositional evidence and *in-situ* iron isotope data (δ^{56}Fe) on Fe-Ti-V oxide deposits hosted in the Hongge layered intrusion. Both magnetite and ilmenite exhibit reaction textures, with magnetite exhibiting two contrasting generations and ilmenite exhibiting chemical zonation. The δ^{56}Fe data for primary magnetite (-0.23 to 0.63 ‰) and ilmenite (-1.08 to -0.27 ‰) significantly exceed the typical δ^{56}Fe igneousrange. Secondary magnetite formed in major massive ore layers, displays extremely low δ^{56}Fe values (-1.24 to -0.09 ‰), indicating precipitation from hydrothermal fluids. According to mass balance modelling, ~20-30 % of the Fe in primary oxides was hydrothermally removed and re-precipitated into the major ore layers, which is expected to significantly increase ore tonnages and grades.

4.1 Introduction

Layered intrusions are large sill-like igneous bodies, which exhibit compositional, mineralogical and textural layering as a result of magma differentiation processes. Iron (Fe) ores, often hosted in layered intrusions (Eales and Cawthorn, 1996; Miller and Ripley, 1996; Parks and Hill, 1986; Wilson et al., 1996; Zhou et al., 2005) are one of the major sources for Fe, Ti (titanium) and V (vanadium) metals used in industry. However, the formation of thick massive Fe-Ti-V oxide layers (usually tens meters thick) in these intrusions is still under debate and several genetic models have been invoked, predominantly involving magmatic processes: (1) segregation of an immiscible Fe-rich silicate melt or Fe-Ti-V oxide melt from the magma (Zhou et al., 2005; Fischer et al., 2016); 2) early crystallization of Fe-Ti-V oxides with respect to silicates (Ganino et al., 2008, 2013; Pang et al., 2008a); 3) magma replenishment and mixing (Howarth and Prevec, 2013a), or (4) gravity sorting of Fe-Ti-V oxides (Cawthorn and Ashwal, 2009). However, all these magmatic models cannot satisfactorily explain the formation of massive ores (>60 vol.% Fe-Ti-V oxides; up to 60 m thick layers) containing nearly pure monomineralic layers with >90 vol.% Fe-Ti-V oxides). This is because certain amounts of silicate minerals would inevitably crystallize together with Fe-Ti-V oxides due to either the presence of Si and Al in the immiscible Fe-rich liquids (Wang et al., 2017) or small cotectic proportions of Fe-Ti-V oxides in the (ferro-) basaltic systems (Toplis and Carroll, 1995).

Most magmatic rocks in layered intrusions show clear signatures of hydrothermal fluid activities: (1) hydrothermal replacement textures (dissolution/precipitation textures, Arai and Akizawa, 2014; Yudovskaya et al., 2019), (2) presence of secondary minerals in or adjacent to the ores (Bindeman et al., 2008; Wotzlaw et al., 2012; Li et al., 2014), (3) distinctive core-rim trace element patterns recognized in cumulus minerals (Zirner et al., 2015; Xing and Wang, 2017), (4) fluid inclusions in minerals (Li et al., 2019) and (5) stable isotope compositions (Schannor et al., 2018). Although the importance of hydrothermal processes in magmatic layered intrusions is commonly discussed, the detailed mechanism controlling hydrothermal reworking and quantitative estimations of the mobilization and re-precipitation of iron in layered intrusions are poorly constrained.

In this study, we combine petrographic observations with *in-situ* elemental- and iron isotope analyses of Fe-Ti-V oxides from Hongge Fe-Ti-V oxide deposit to explore the importance of hydrothermal processes in the formation of nearly monomineralic thick massive ore layers. Hongge Fe-Ti-V deposit is the largest Fe-Ti-V deposit in Panxi region, southwestern China (Supplementary Fig. 4.1), and has been invoked as a classical example for magmatic enrichment of Fe-Ti-V oxides (Bai et al., 2021). However, our petrological and geochemical observations clearly indicate that hydrothermal fluids modified the mineralogy of the magmatic rocks and may be involved in the iron ore formation processes, as evidenced by the presence of hydrous minerals (e.g., chlorite, serpentine, talc, and tremolite, Luan et al., 2014a, 2014b) in close association with the ores and occurrence of extensive networks of hydrothermal veins that crosscut the intrusion (see Supplementary Figs. 4.2, 4.3 for details).

4.2 Results

4.2.1 The Hongge Fe-Ti-V oxide deposit and its hosting layered intrusion

The Hongge Fe-Ti-V oxide deposit is hosted in a sill-like mafic-ultramafic layered intrusion which was emplaced into the Mesoproterozoic marine facies schists and meta-sandstones in the north, and in Neoproterozoic dolomitic limestones and granitic gneisses in the south (Bai et al., 2021). Part of the intrusion at the north-eastern corner is overlain by thick layers of flood basalts (Luan et al., 2014b). The northern and western parts of the intrusion are in contact with late Permian alkaline granites and syenites (Supplementary Fig. 4.1c, Shellnutt and Jahn, 2010; Shellnutt et al., 2011b). Based on the analysis of drill cores, Hongge layered intrusion can be divided into three lithological zones with eleven stratigraphic units

(Supplementary Fig. 4.4), mainly composed of different proportions of olivine, clinopyroxene, plagioclase and Fe-Ti-V oxides (Wang et al., 2020). The Upper Zone (UZ) is referred to as gabbro zone without any visible ore layers. The Middle Zone (MZ) is composed of four units, which contain magnetite dunite/clinopyroxenite layers on top and Fe-Ti-V oxide ore layers at the bottom within each unit. Thick massive ore layers (up to ~60 m) including monomineralic ore layers occur only at the top of the MZ and are predominantly composed of magnetite and ilmenite. The four units of the Lower Zone (LZ) are mainly dominated by different proportions of coarse-grained cumulus olivine and clinopyroxene while oxides occur as interstitial phases.

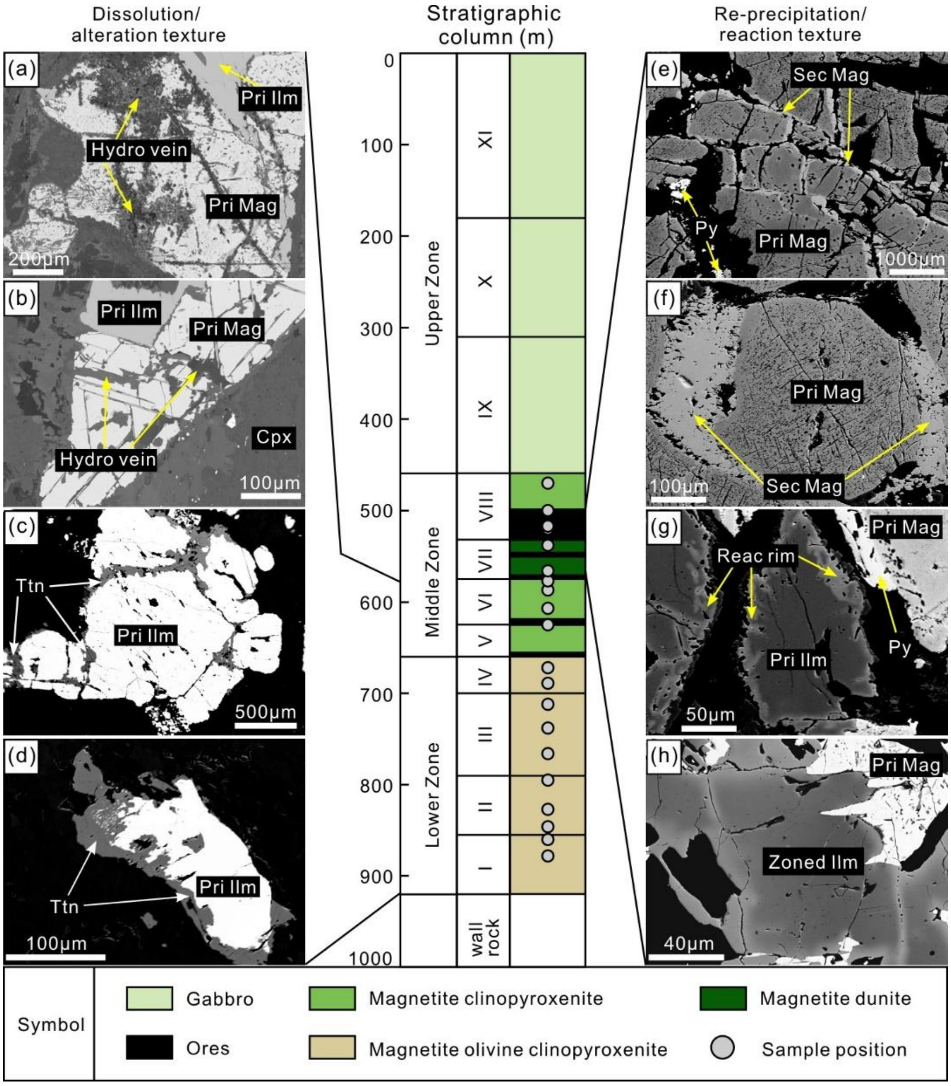

Fig. 4.1. Fe-Ti-V oxides reaction textures in Unit I to VI (a-d) and in Unit VII and bottom Unit VIII (e-h). (a-b) The primary magnetite is cut by hydrothermal veins. Secondary minerals include

epidote, talc, serpentine and amphibole. (c-d) Primary ilmenite is cut by veins and replaced by secondary titanite. (e-f) Secondary magnetite with high porosity surrounding the primary magnetite along sharp contact. (g) Primary ilmenite with irregular reaction rims. The reaction rims exhibit large compositional difference compared to the unreacted part. (h) Zonation in the primary ilmenite with progressive compositional variations. Abbreviations: Pri Mag=Primary magnetite; Pri Ilm=Primary ilmenite; Ttn=Titanite; Sec Mag=Secondary magnetite; Reac rim=Reaction rim; Zoned Ilm=Zoned ilmenite; Hydro vein=Hydrothermal vein; Py=Pyrite.

4.2.2 Textures of silicate and Fe-Ti-V oxide minerals

All samples show that alteration textures of primary silicate minerals are widely developed (Supplementary Fig. 4.4). Primary plagioclase crystals in the UZ are replaced by zoisite and albite. Olivine and clinopyroxene in the MZ and LZ are replaced by serpentine, amphibole, chlorite and epidote. The alteration of olivine to serpentine is particularly evident in the magnetite-bearing dunite layers adjacent to the thick massive ore layers. In addition, hydrothermal clinopyroxene which is enriched in Ca and Mg content was also commonly observed in the LZ and MZ (see Supplementary Information). In contrast to primary magmatic clinopyroxene that contains exsolution of magnetite, no oxide exsolutions are observed in the hydrothermal clinopyroxene. According to the alteration mineral assemblages in Hongge intrusion, the metamorphic reactions mainly occurred at temperature lower than 500 ℃.

Magnetite and ilmenite were significantly affected by dissolution and/or reaction processes. Notably, two generations of magnetite can be distinguished based on compositional and textural characteristics, whereas ilmenite exhibits significant morphological and compositional modifications within a single crystal (Fig. 4.1). The stratigraphic position, chemical composition and textural characteristics of both primary and secondary Fe-Ti-V oxides are shown in the Supplementary Figs. 4.5-4.7 and Supplementary Tables 4.1-4.4. The most important observations are summarized as follows:

(1) Dissolution/alteration textures of magnetite and ilmenite are observed in the rocks dominated by silicate layers containing relatively thin ore layers (<5 m) with Fe-Ti-V oxides proportion <60 vol.%; see Units I to VI in the LZ and MZ, respectively (Fig. 4.1a-d). Magnetite contains abundant exsolution lamella of ilmenite, has jagged edges and is often enclosed by coronas of secondary minerals and it is also cut by hydrothermal veins (Fig. 4.1a, b). Ilmenite is partially replaced by titanite or crosscut by titanite veins (Fig. 4.1c, d).

(2) Re-precipitation/reaction textures of magnetite and ilmenite are observed in the magnetite-bearing dunite layers (Unit VII, MZ) and in the thick massive ore layers (bottom Unit VIII, MZ; Fig. 4.1e-h). Distinct secondary magnetite is formed around the primary magnetite with a relatively sharp contact (Fig. 4.1e, f). Notably, this secondary magnetite has a high porosity and it shows an absence of unmixing lamellae (Fig. 4.1f). Chemically, an enrichment of secondary magnetite in Fe (up to ~92 wt.% FeO) is accompanied by a depletion in Ti, V, Al, Mn and Cr, emphasizing a significant compositional difference between primary and secondary magnetite phases (Supplementary Fig. 4.6a-f). However, it is worth noting that Cr and V content in primary and secondary magnetite of Unit VIII are similar (also see Supplementary Information). Ilmenite in Units VII and VIII, MZ displays reaction textures and clear core-rim compositional differences (Fig. 4.1g) or zonation with smooth but large chemical gradients (Fig. 4.1h). The rim of ilmenite is enriched in Fe and depleted in Ti + Mg when compared with the cores (Supplementary Fig. 4.6g-i).

(3) The relative proportion of ilmenite over magnetite within ore layers is significantly lower than that in the other silicate-rich layers (Fig. 4.2a; Supplementary Table 4.5).

4.2.3 *In-situ* iron isotopes of primary and secondary Fe-Ti-V oxides

The Fe isotopic compositions of Fe-Ti-V oxides have been systematically investigated using *in-situ* LA-MC-ICP-MS analysis (Supplementary Tables 4.6, 4.7).

The results show that primary magnetite with dissolution textures, which is observed in Units I and VI (Fig. 4.1a, b), has relatively high δ^{56}Fe values, ranging from +0.14 to +0.63 ‰ (green circles in Fig. 4.2b), and shows no detectable Fe isotopic zoning within a single grain. In contrast, primary magnetite, surrounded by secondary magnetite that is only observed in Unit VII and at the bottom of Unit VIII (Fig. 4.1e, f), shows relatively low δ^{56}Fe values (from -0.23 to +0.20 ‰; blue circles in Fig. 4.2b). Importantly, secondary magnetite in Units VII and VIII has extremely low δ^{56}Fe values (from -1.24 to -0.09 ‰; red circles in Fig. 4.2b) compared to primary magnetite of the same units.

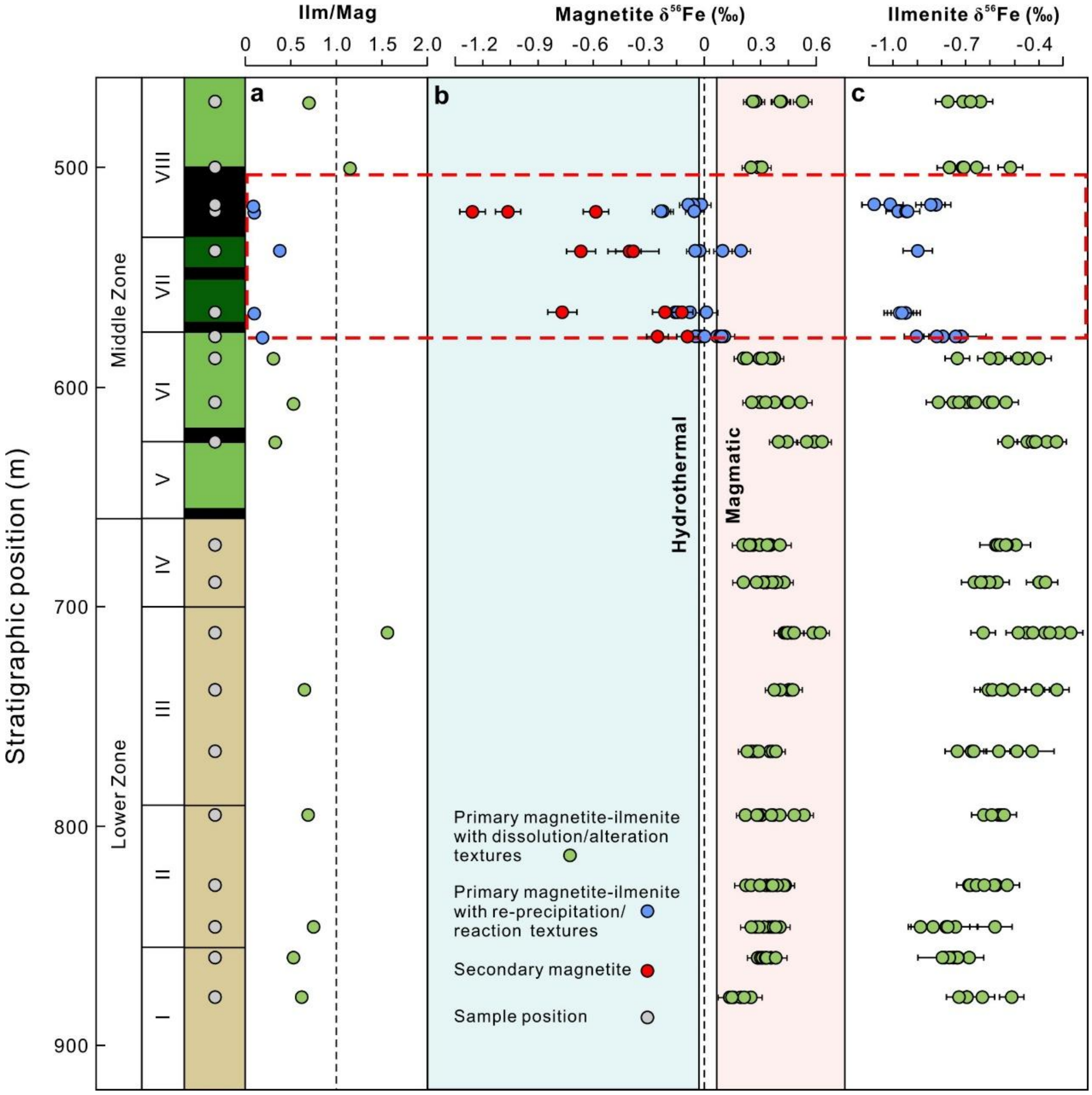

Fig. 4.2. Ratio of ilmenite/magnetite modal proportions in the samples (a) and *in-situ* Fe isotope variations for magnetite (b) and ilmenite (c) along the stratigraphic column (data are reported in

Supplementary Tables 4.5-4.7). Each circle represents one individual analyzed spot and each bar represents the range of δ^{56}Fe in one spot including 2σ errors. The red dashed rectangle marks the range of samples from magnetite-bearing dunite and from the thick massive ores. The Fe isotope range characteristic for magmatic magnetite is shown as a light pink area (extends to ~0.9 ‰) and hydrothermal magnetite is outlined as the light blue area according to Troll et al. (2019). Symbols for different lithological units in stratigraphic column as per Fig. 4.1. Abbreviations: Mag=magnetite, Ilm=ilmenite.

Ilmenite across the intrusion displays low δ^{56}Fe values ranging from -1.08 to -0.27 ‰, with extremely low δ^{56}Fe values in Unit VII and at the bottom of Unit VIII (-1.08 to -0.72 ‰; Fig. 4.2c). These minima in δ^{56}Fe are recorded in ilmenite from the ore layers and closely correspond to the lowest δ^{56}Fe values of secondary magnetite. Similar to magnetite, ilmenite grains are rather homogeneous in Fe isotopic composition. The δ^{56}Fe values in reaction rims or Fe isotope zonation of ilmenite could not be determined because laser beam size was larger than the width of the rims. It is noteworthy that ilmenite displays similar Fe isotope variation patterns to those of primary magnetite throughout the stratigraphic column (except in Lower Zone Unit I; Fig. 4.2b, c). In other words, both primary magnetite and ilmenite demonstrate coeval evolution of Fe isotopic signatures.

4.2.4 Temperatures estimated by Fe isotope thermometry and magnetite-ilmenite equilibria

According to our *in-situ* Fe isotope data, most of the primary magnetite-ilmenite pairs plot along with an equilibrium fractionation trend (Fig. 4.3a). Applying magnetite-ilmenite Fe isotope equilibrium fractionation thermometry (Polyakov and Mineev, 2000; Polyakov et al., 2007), the calculated Fe isotope equilibrium temperatures are in the range of ~300-450 ℃ but most of them plot within an interval of 350 to 450 ℃ (Fig. 4.3a, Supplementary Table 4.6). These temperatures are consistent with the temperatures (<500 ℃) estimated above for the assemblages of secondary silicate minerals (chlorite, calcite, epidote, amphibole, etc). In all cases, the calculated temperatures are significantly lower than temperatures that would be expected for isotopic equilibrium at typical magmatic conditions of mafic layered intrusions (1200-950 ℃, light yellow area in Fig. 4.3a, Zhang et al., 2012; Chen et al., 2014). Recent studies for Baima intrusion (another layered intrusion in Panxi region) pointed out that the Fe isotope equilibrium temperatures of Fe-Ti-V oxides could extend to ~650-550 ℃ due to Fe-Ti exchanges (sub-solidus re-equilibration processes (Chen et al., 2014; light purple area in Fig. 4.3a). This temperature range is still significantly higher than that observed for Hongge.

In addition to the Fe isotope thermometer, we estimated the equilibrium temperature with various geothermometers using the chemical composition of ilmenite and magnetite (Supplementary Table 4.5). Temperatures calculated using QUILF thermometry (Anderson et al., 1993) are consistently higher (~695-460 ℃) than those for primary magnetite-ilmenite pairs using Fe isotope fractionation, particularly for samples in massive ore layers (Fig. 4.3b). Besides, the two-iron oxide geothermometry model of Ghiorso and Evans (Ghiorso and Evans, 2008) had shown a similar trend with that of QUILF but indicated that the mineral equilibrium temperatures in the lower units (~532-344 ℃) are closer to the Fe isotope equilibrium temperatures (Supplementary Fig. 4.8a). The highest calculated temperatures (~758-638 ℃) from two-iron oxide equilibrium were also recognized for massive Fe-Ti-V oxide ore layers. Geothermometry using Mg content in magnetite (X_{Mg}^{Mag}, Canil and Lacourse, 2020) provided the highest temperature estimations among the three geothermometers, with a temperature ranging from ~850 to 450 ℃ in the lower units and ~980-780 ℃ in the massive Fe-Ti-V oxide ore layers (Supplementary Fig. 4.8b). The equilibrium temperatures of secondary magnetite and reaction rims of ilmenite were also estimated using the three mineral thermometers resulting in the temperature ranges from ~500-440 ℃, ~380-330 ℃ and 680-520 ℃, respectively. Although there are some temperature differences among the results from the three geothermometers (Fig. 4.3b; Supplementary Fig. 4.8a-b), the temperatures show systematic trends from low hydrothermal temperature of primary Fe-Ti-V oxides in Unit I to VI and secondary Fe-Ti-V oxides in Unit VII and VIII, which agrees with temperature estimated from the Fe isotope equilibrium, to maximum magmatic temperature of the primary Fe-Ti-V oxides in the ore layers.

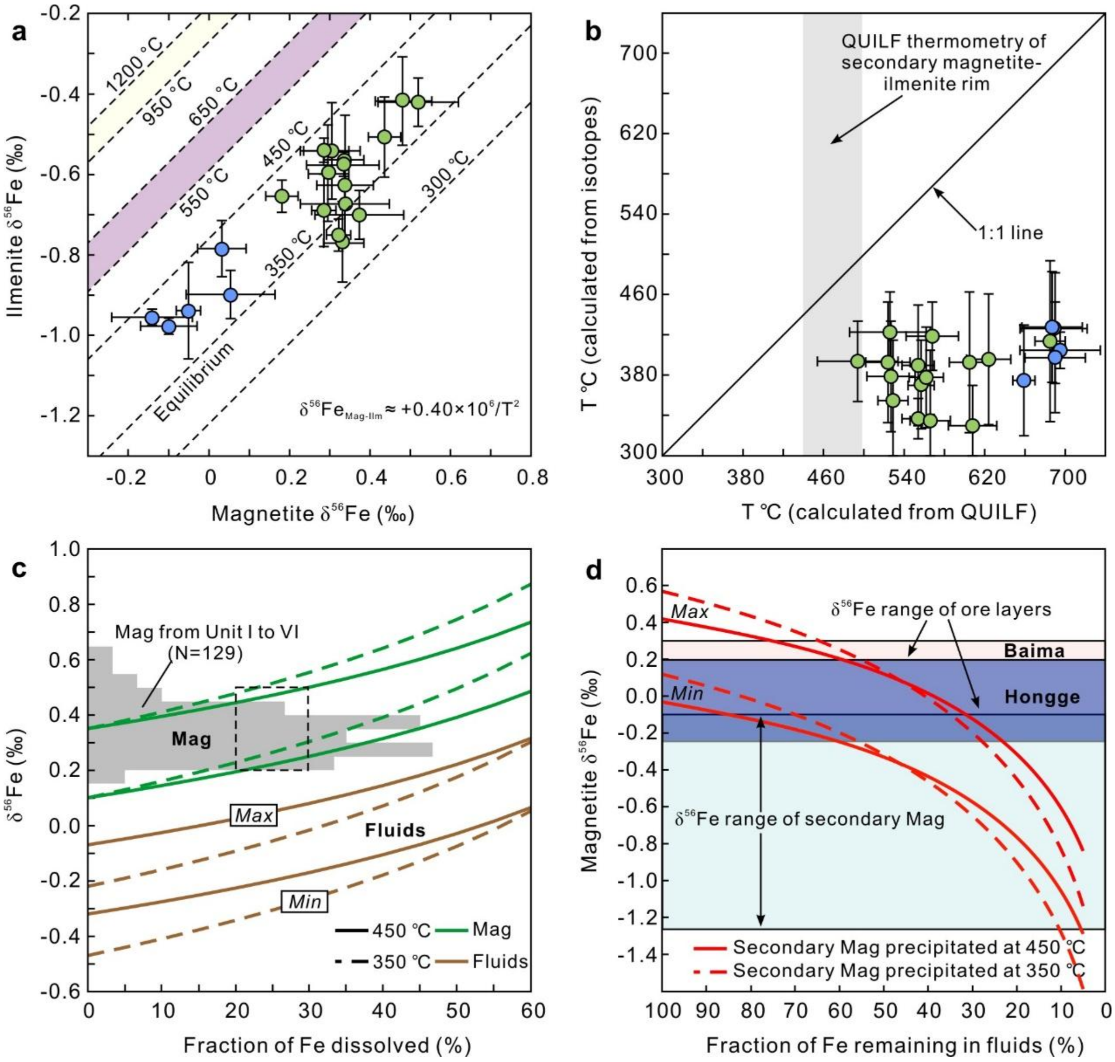

Fig. 4.3. Temperatures calculated using Fe isotope and chemical equilibria in magnetite and ilmenite. Modelling calculations for hydrothermal dissolution and re-precipitation processes. (a) Fe isotope compositions and isotope fractionation isotherms (dashed lines) for primary magnetite and ilmenite pairs from Hongge Fe-Ti-V oxide deposit. The light yellow region indicates expected Fe isotope equilibrium fractionation at magmatic temperatures (1200-950 ℃, Zhang et al., 2013; Chen et al., 2014). The light purple area represents the range of sub-solidus re-equilibrium temperatures (650-550 ℃, Chen et al., 2014). Each circle represents the average value of analysis within the single thin section (see Supplementary Table 4.6). (b) Comparison of primary

magnetite-ilmenite equilibrium temperatures between QUILF thermometry and Fe isotope thermometry (Supplementary Tables 4.5, 4.6). The grey field represents elemental equilibrium temperatures according to the secondary magnetite-ilmenite reaction rims through QUILF thermometry in thick massive ores (bottom of Unit VIII) and heavily altered magnetite-bearing dunite layers (Unit VII). (c) Modelled Fe isotope variations for primary magnetite during hydrothermal dissolution process. The histogram of δ^{56}Fe for primary magnetite from Unit I to VI is provided on the vertical axis to show the main Fe isotope variation range (data are from Supplementary Table 4.6). The solid and dashed lines are illustrated for modelling results at 450 ℃ and 350 ℃, respectively. The green color represents magnetite Fe isotope variations during Fe dissolution process while the brown color is used for potential Fe isotope values of hydrothermal fluids which are assumed to be in equilibrium with magnetite during the dissolution process. The dashed box scales for the possible fraction of Fe loss during the dissolution process. (d) Modelled Fe isotope values for secondary magnetite during Fe re-precipitation process. The bottom light blue area represents the δ^{56}Fe range of secondary magnetite analyzed in this study (data are from Supplementary Table 4.7). The upper light pink area represents the δ^{56}Fe range of unaltered magmatic magnetite from ore layer samples in Baima Fe-Ti-V oxide deposit (Liu et al., 2014b). The middle dark blue area represents the δ^{56}Fe range of primary magnetite from thick massive ores (bottom of Unit VIII) and adjacent heavily altered magnetite-bearing dunite layers (Unit VII) in the Hongge Fe-Ti-V deposit. Abbreviation: Mag=magnetite.

4.3 Discussion

Petrological and geochemical results outlined above suggest significant modification of primary magmatic rocks and Fe-Ti-V oxides. Across the Hongge layered intrusion, the Fe-Ti-V oxides exhibit characteristic reaction textures, coexistence with alteration minerals and hydrothermal veins, two generations of magnetite, contrasting chemical composition and zonation of ilmenite, change in the proportion of magnetite and ilmenite, coeval variation of Fe isotope compositions of coexisting magnetite and ilmenite, extremely low δ^{56}Fe values in oxides from the ore layers as well as systematic and large disagreement between Fe isotope and mineral equilibrium temperatures. These observations point to a significant influence of the late stage, presumably hydrothermal processes on the formation and re-distribution of Fe-Ti-V oxides within the Hongge layered intrusion.

Hydrothermal processes at the late stages of magmatic evolution in layered intrusions can be controlled by the contribution from magmatic fluids exsolved from crystalizing magma as well as by external fluids probably originating from the rocks hosting the intrusion. Previous studies indicate that the Hongge intrusion is located in a within-plate tectonic setting and its parental magmas were derived from Emeishan mantle plume with low water contents (<0.5 wt.%, Luan et al., 2014b). After cooling and formation of typical cumulate layers of the intrusion, most of magmatic water should be either trapped by rare water-bearing minerals (e.g., amphibole) or extracted by residual melts and efficiently removed from the main part of the intrusion. Thus, fluids involved in the hydrothermal activity are expected to be predominantly external in origin. This conclusion is further confirmed by the C-H-O isotopic signatures of the fluid inclusions from Hongge intrusion. Isotopic compositions of H_2O and CO_2 released from Hongge magnetite, clinopyroxene and apatite at 400-800 ℃ have $\delta^{13}C$ (-13.7 ‰ to -17.9 ‰ on average) and $\delta^{18}O$ (16.2 ‰ to 19.2 ‰ on average) values that are similar to those of wall rocks (Hekou Formations with $\delta^{13}C$ from -19 ‰ to -28 ‰ and $\delta^{18}O$ from 5 ‰ to 25 ‰, Yang et al., 1999; Xing and Wang, 2012). In addition, abundant H_2O released from the inclusions hosted in magnetite at the 400-800 ℃ temperature interval has relatively low δD values ranging from -90 ‰ to -115 ‰, also indicating the involvement of fluids from the wall rocks (Xing and Wang, 2017). Other studies of Ganino et al. (2013) and Yu et al. (2015) also confirmed involvement of external fluids during the solidification and evolution of the Hongge layered intrusion. Thus, the most plausible source for the fluids would be the hosting rocks released fluids through contact metamorphism. The wall rocks at Hongge mainly comprise dolomitic limestone, metasandstone and metamudstone (Bai et al., 2021), which can potentially release significant amounts of H_2O and CO_2 that may contribute to the formation of hydrothermal fluids around the intrusion. Chlorine is a particularly important component of hydrothermal solutions because it can form relatively soluble complex ions with many cations that are otherwise extremely insoluble in aqueous solutions. Assuming metasedimentary source of the fluids, fluids might contain relatively high Cl concentrations, which agrees with high Cl content in apatite (Supplementary Table 4.9) occurring in assemblages with other metasomatic minerals (e.g., chlorite, hydrothermal clinopyroxene; Supplementary Table 4.10). Typically, such hydrothermal fluids (see detailed description in Supplementary Information) are enriched in light Fe isotopes (e.g. δ^{56}Fe = ~ -1.26 to -0.14 ‰, Sharma et al., 2001; Beard et al., 2003; Rouxel et al., 2008; Li et al., 2017) and hence, reaction of such fluids with primary magmatic minerals may significantly affect their chemical and isotopic compositions.

The petrographic observations presented above clearly indicate that hydrothermal processes played an important role in the reworking of primary magmatic rocks of Hongge intrusion. Magnetite-ilmenite isotopic re-equilibration under hydrothermal conditions can occur through two main mechanisms (Dziony et al., 2014). The first mechanism is the interaction of magnetite/ilmenite assemblage with a percolating Fe^{2+}-bearing fluid. Application of experimentally determined and calculated isotope fractionation factors (β-factors) for $FeCl_2^0$, ilmenite and magnetite (Polyakov and Mineev, 2000; Polyakov et al., 2007; Hill et al., 2010) predict an increase of δ^{56}Fe values for magnetite and a decrease of δ^{56}Fe values for ilmenite during the hydrothermal re-equilibration process (Supplementary Fig. 4.10). The second mechanism, which is more commonly invoked, is a hydrothermal dissolution and re-precipitation process because most fluids and especially Cl-rich fluids have strong capabilities for dissolving ferrous Fe (Supplementary Fig. 4.11a). In the Hongge samples, widespread dissolution/alteration textures of primary magnetite and ilmenite in samples of Units I to VI (Fig. 4.1a-d) suggest that the second mechanism played a dominant role, and a considerable amount of Fe may have been dissolved in and remobilized by fluids as $FeCl_2$ species (Scholten et al., 2019).

Magnetite dissolution processes have been discussed in abundant studies and the

Fe loss can be estimated with the Rayleigh model (Rouxel et al., 2008; Zhu et al., 2018). According to the modelling results shown in Fig. 4.3c, ~20-30 % of primary magnetite in Unit I to VI of the Hongge intrusion may have been dissolved. Compared to Fe, Ti is essentially immobile in the hydrothermal fluids between 300-500 ℃ (Supplementary Fig. 4.11b, Dolejš and Manning, 2010). Hence, it is reasonable to assume that the hydrothermal fluids mainly remobilized Fe, without significant changes in Ti content of the initial rocks.

Previous studies showed that Fe solubility in hydrothermal fluids decreases with decompression and increasing temperature (Supplementary Fig. 4.11a, Simon et al., 2004). Assuming that the inner part of intrusion is always hotter than the cooling margins of the intrusion, it can force effective hydrothermal fluid circulation and vertical migration of fluids through the intrusive body. Fluids ascending in temperature gradient will be heated and will experience decompression, with both factors negatively affecting solubility of magnetite in the fluid. It is apparent that during hydrothermal dissolution process, other mobile cautions (e.g., Na, Si, Ca and Mg) may also experience mass transfer (Martin, 2012), which is supported by different types of alterations of silicates (see discussion in Supplementary Information). However, the solubility of silicate minerals in the fluids increases with increasing temperature, in contrast to the solubility of magnetite (see Supplementary Fig. 4.11a). The interplay between such opposite solubility behaviour of Fe-Ti-V oxides and that of silicate minerals can result in progressive dissolution and removal of silicate minerals (as shown experimentally in basalt-fluid system, Martin, 2012) with concomitant precipitation of magnetite along the stratigraphic column. The removal of silicates will provide required space for precipitating secondary magnetite. This process will be most efficient at P-T-fO_2 conditions where fluids will reach magnetite saturation, localizing its precipitation within a given layer of the intrusion. Thus, with such a mechanism, iron dissolved from the rocks of deeper and colder units will be transported by hydrothermal fluids upwards and precipitated, when magnetite saturation is reached. This eventually may result in the formation of monomineralic Fe-Ti-V oxide ore layers of up to 60 meter thick.

Although hydration of olivine could also produce secondary magnetite that is compositionally similar to the re-precipitated secondary magnetite, texture and isotope evidence support Fe re-precipitation from hydrothermal fluids in Hongge intrusion. Firstly, secondary magnetite formed by hydration of olivine mainly crystallized within or surrounded the olivine remnants, showing discontinuous thin veins (supplementary Fig. 4.12b). However, in the case of Hongge intrusion, the majority of secondary magnetite veins are thick and continuous, cementing primary oxides, indicating a hydrothermal re-precipitation origin (supplementary Fig. 4.12c). Secondly, previous research has shown that secondary magnetite formed by olivine hydration always has high positive δ^{56}Fe values (Scott et al., 2017). This is not the case for Hongge as the Fe isotope values of secondary magnetite are negative. Such values are similar to those of magnetite reported in hydrothermally altered oceanic basalts (Dziony et al., 2014) and low-temperature hydrothermal magnetite (Troll et al., 2019). Therefore, we can conclude that in Hongge intrusion, most of the secondary magnetite was precipitated from hydrothermal fluids.

The Fe precipitation process from the hydrothermal fluids can be also modelled applying the Rayleigh distribution and the modelled δ^{56}Fe values of secondary magnetite are displayed in Fig. 4.3d. It is evident that the predicted δ^{56}Fe values agree with the measured values of secondary magnetite after ca. 20 % of precipitation. Since the δ^{56}Fe of secondary magnetite is significantly lower than the δ^{56}Fe of primary magmatic magnetite (corresponding to the ore layers of Baima deposit without detectable hydrothermal reworking in Fig. 4.3d), isotopic re-equilibration between primary and secondary magnetite would easily drive δ^{56}Fe of primary magnetite towards lower or even negative values as observed in Unit VII and bottom of Unit VIII. In the case of ilmenite, due to the low solubility and mobility of Ti in the hydrothermal fluids (Dolejš and Manning, 2010), no secondary ilmenite was observed in Unit VII and at bottom of Unit VIII but Fe in ilmenite could still experience isotopic exchange with hydrothermal fluids by diffusion. There is evidence that

Fe-carrying fluids also reacted with primary ilmenite directly through Fe-Mg exchange, forming narrow Fe-rich rims or zonation (Fig. 4.1g, h; Supplementary Tables 4.3, 4.4) which were, however, unsuitable for accurate Fe isotope analyses. As light Fe isotope diffuse faster than heavy Fe isotopes (Oeser et al., 2014), Fe-Mg exchange diffusion between primary ilmenite and such Fe-rich rims would further drive Fe isotope compositions of ilmenite towards lighter values. Therefore, we suggest that the low Fe isotope values of primary magnetite and ilmenite in the thick massive ore layers and adjacent layers were generated by isotope re-equilibration in the course of abundant hydrothermal reactions and re-precipitation of secondary magnetite.

Fe-Ti oxide thermometry shows that primary magnetite and core of ilmenite within the ore layers recorded high and almost magmatic temperatures in contrast to hydrothermal temperatures in the units below and above the Middle Zone (see Supplementary Fig. 4.8). Temperature estimated from the compositions of secondary magnetite is also in the hydrothermal range. The higher temperature recorded by primary oxides in the ores is presumably due to precipitation of secondary magnetite, which could isolate the inner primary magnetite from further chemical exchange of Fe, Ti and Mg with primary ilmenite in the ore layers. Precipitation of secondary magnetite not only leads to re-equilibration of Fe isotopes in magnetite and ilmenite, but more importantly, this hydrothermal dissolution-transport-precipitation process can promote efficient Fe enrichment and significant increase in both grades and tonnages of the oxide ores. According to mass balance calculations, hydration-formed secondary magnetite could increase oxides content by no more than 7 vol.%, which is clearly insufficient to form thick layers of massive ores, particularly monomineralic Fe-Ti-V oxide ores. In comparison, hydrothermal reworking and Fe re-precipitation have the potential to increase oxides content by 17-27 vol.%, which is significantly greater than the potential contribution of olivine hydration. Thus, hydrothermal Fe re-precipitation is obviously required for the formation of thick massive ore layers. Although the precise proportions of hydration-formed and hydrothermally re-precipitated secondary magnetite are unknown, mass balance calculations indicate that the combined effect could range from 24-34 vol.% enrichment. Regardless of how rough our estimates are, hydrothermal reworking is a critical process in the formation of high-grade Fe-Ti-V ores in magmatic layered intrusions.

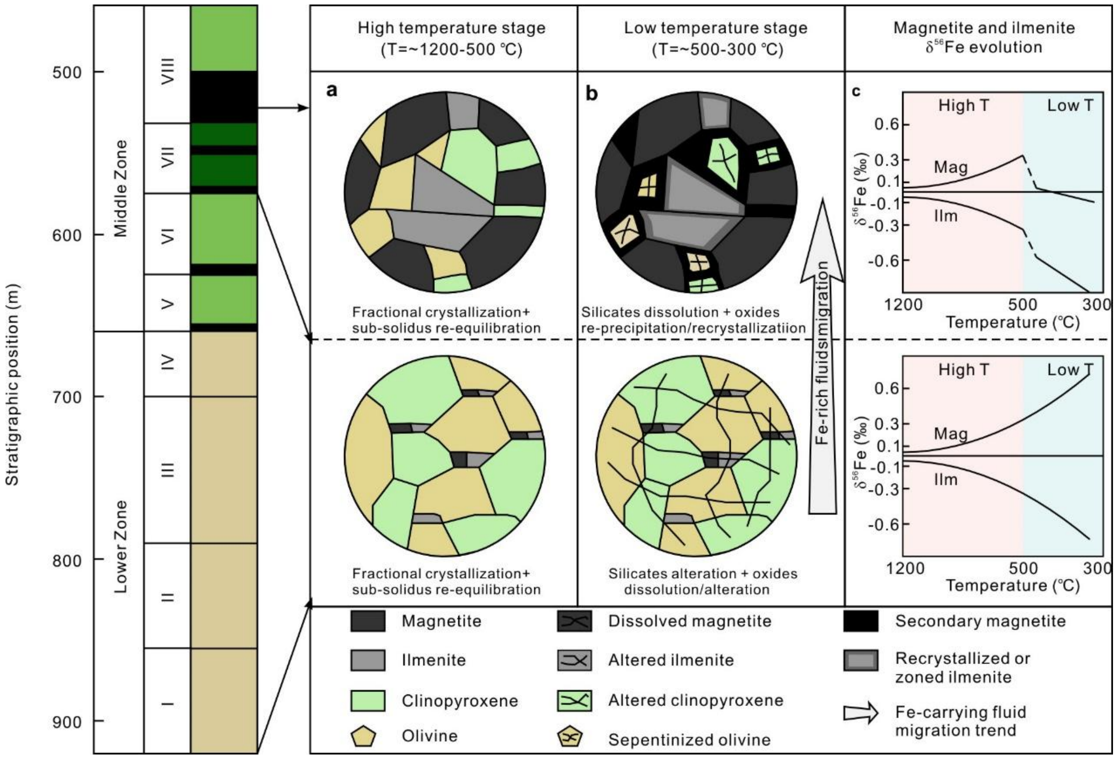

Fig. 4.4. Conceptual model of hydrothermal reworking illustrates the formation processes of thick massive ores. (a) Formation of primary silicates-bearing ore layers (upper) and their hosting silicates layers (lower) in layered intrusions at magmatic and sub-solidus temperatures (1200-500 ℃). Under these conditions, the ore layers are mainly disseminated with relatively low oxide proportion of only ~50-60 vol.%. (b) Through hydrothermal reworking under low temperatures (500-300 ℃), abundant Fe in the silicate layers (lower) could be dissolved and carried upwards by the hydrothermal fluids. Due to heating towards the inner part of the intrusion and decompression of ascending fluid, it can reach saturation with magnetite and re-precipitate secondary magnetite (upper). Simultaneously, the silicate minerals in the primary ore layers can be dissolved and transported away by heating and ascending fluids. At optimal P-T conditions, this combination of mobilization processes will result in a significant “upgrade” of the primary disseminated ore layers into massive ore layers or even monomineralic ore layers. (c) The Fe isotope evolution during different stages, i.e., primary magnetite-ilmenite in the hosting silicates

layers (lower) and thick massive ore layers (upper) from magmatic to hydrothermal stage. The dashed part of the lines represents the discontinuous sharp decrease of the Fe isotopes of primary magnetite and ilmenite in thick massive ore layers due to hydrothermal precipitation of secondary magnetite. Symbols for different lithological units in stratigraphic column as per Fig. 4.1. Abbreviations: Mag=magnetite, Ilm=ilmenite.

Based on petrographic observations and Fe isotope compositions of Fe-Ti-V oxides, we propose a new magmatic-hydrothermal model for the formation of thick massive ores layers in the Hongge intrusion. At the magmatic stage, either due to silicate liquid immiscibility (Zhou et al., 2005) or fractional crystallization (Pang et al., 2008a), silicate and Fe-Ti-V oxide minerals crystallized together as primary silicate-bearing ore layers (<60 vol.% Fe-Ti-V oxides) in the MZ and Fe-Ti-V oxide-bearing silicate layers (~10-20 vol.% Fe-Ti-V oxides) in the LZ (Fig. 4.4a). During a hydrothermal stage, the upward flow of fluids could dissolve/alter the igneous minerals and remobilize Fe, Si, Na and other elements in the lower units. Due to temperature gradient from the margin (cooler) to the inner part (hotter) of the Hongge intrusion, the hydrothermal fluids will migrate upwards and transport Fe until magnetite saturation is reached. Meanwhile, the Si-rich material (such as olivine and clinopyroxene) could be partly dissolved and transported by hydrothermal fluids away from the hot middle zone of the intrusion. Such a reworking process will produce strong alteration of olivine in Unit VII and thick secondary magnetite veins in Unit VII and bottom of Unit VIII. This hydrothermal reworking process could be most efficient at optimal P-T-fO_2 conditions corresponding to the upper MZ layer in the Hongge intrusion, resulting in the formation of thick massive or even monomineralic Fe-Ti-V oxide ore layers (Fig. 4.4b). Our model is in accordance with the observed Fe isotopic compositions of minerals through the intrusion (Fig. 4.4c) and may be applicable to other Fe-Ti-V oxide deposits with extremely enriched ore layers hosted by layered intrusions. Therefore, we propose that hydrothermal reworking could play a key role in the formation of World-class Fe-Ti-V oxides deposits hosted by layered intrusions.

4.4 Methods

4.4.1 Sampling and mineral composition analyses

Twenty samples from MZ and LZ, which are considered to have direct genetic relationships with ore-forming processes, were collected for *in-situ* Fe isotope analyses. The 34 samples with the representative Fe-Ti-V oxides textures are selected for microprobe analyses with an interval at ~20-30 m along the drill core. Back-scattered electron images (BSE) were typically captured under the working condition with 15 kV accelerating voltage and 15 nA beam current using Cameca electron microprobe.

The major and trace elements of magnetite and ilmenite were analyzed with a Cameca SX100 electron microprobe at the Institute of Mineralogy, Leibniz Universität Hannover (Germany). Analytical conditions were set at an accelerating voltage of 15 kV and beam current of 100 nA. The beam size was fixed at 5 μm during the whole analysis. The counting times were 10 s on the peak for each element. Standards used for calibrations include quartz (Si), Woll MAC (Ca), chromite (Cr) and synthetic TiO_2, Fe_2O_3, MgO, Al_2O_3, Mn_3O_4, V and NiO. PAP procedure was applied for late correction of raw data. The precision for oxide concentrations was better than 1 %.

4.4.2 *In-situ* Fe isotope determinations by fs-LA-MC-ICP-MS

A high mass resolution MC-ICP-MS (Thermo Scientific Neptune Plus) connected to a Spectra-Physics Solstice femtosecond laser ablation system was applied to measure Fe isotope compositions at the Institute of Mineralogy, Leibniz Universität Hannover (Germany). The UV femtosecond laser ablation system is based on a 100 femtosecond Ti-sapphire regenerative amplifier system (Hurricane I, Spectra-Physics) and is described in detail by Horn and Blanckernurg (2007). The measurements of Fe isotopes were conducted following the analytical protocol of Horn et al. (2006) and Oeser et al. (2014). Raster-mode was used during mineral analyses and repetition rates varied between 5 and 20 Hz depending on the FeO content of Fe-Ti-V oxides to keep a relatively constant signal intensity of between 10 and 20 V on mass ^{56}Fe. For mass bias correction, a 2 ppm Ni solution was added via a quartz glass spray chamber (double pass Scott design) - which was equipped with an ESI PFA-ST nebulizer and connected with the Laser ablation sample, before introduction into the plasma for simultaneous isotope analyses. Additionally, a sample-standard-bracketing method was applied to correct for the instrumental mass bias drift. Each analysis was performed for a period of 160 s, including 40 s for background analyses (with laser off) and 120 s for sample analyses. The pure Fe-metal IRMM-014 was used as bracketing standard. The raw data were processed with LamTool excel tool. Isotope compositions are reported as δ^{56}Fe values relative to IRMM-014 standard and were determined as follows:

$$\delta^{56}\mathrm{Fe} = [\frac{\left(\frac{^{56}\mathrm{Fe}}{^{54}\mathrm{Fe}}\right)_{\mathrm{sample}}}{\left(\frac{^{56}\mathrm{Fe}}{^{54}\mathrm{Fe}}\right)_{\mathrm{IRMM-014}}} -1] \times 1000.$$

As no natural standards for magnetite and ilmenite exist, a secondary standard material, JM Puratronic iron standard (99.995 %, Puratronic, Johnson Matthey, lot No. FE495007IF2; δ^{56}Fe = 0.09 ± 0.05 ‰, Horn et al., 2006) was used to check the performance and stability of the analytical setup. The Fe isotope composition for Puratronic relative to IRMM-014 well agrees with previously determined values (Supplementary Table 4.8) ensuring high precision and accuracy of the *in-situ* Fe isotope analysis conducted in this study. Several previous studies have shown that all investigated minerals can be accurately and reliably analyzed with fs-LA-MC-ICP-MS relative to iron metal (Horn and Blanckenburg, 2007; Steinhoefel et al., 2009; Dziony et al., 2014; Oeser et al., 2014; Günther et al., 2017). All individual samples analyzed in this study, including magnetite, ilmenite, and metal plot along a mass-dependent fractionation line (Supplementary Fig. 4.7) which proves high reliability for the *in-situ* analyses.

4.4.3 Equilibrium temperatures calculated in Fig. 4.3a

Based on the previous experimental studies for magnetite and ilmenite (Polyakov and Mineev, 2000; Polyakov et al., 2007), the β^{56}Fe factor (reduced isotopic partition function ratio) of magnetite and ilmenite were determined as,

$10^3\ln\beta_{\mathrm{Mt}}^{56} \approx 0.64394\times10^6/T^2$, and $10^3\ln\beta_{\mathrm{Ilm}}^{56} \approx (0.37934/1.5)\times10^6/T^2$:

where T is the absolute temperature in Kelvin. Hence, the possible iron isotope thermometer of magnetite-ilmenite have been calibrated as:

$10^3\ln\beta_{Mt\text{-}Ilm} = 10^3\ln\beta_{Mt} - 10^3\ln\beta_{Ilm} = \Delta^{56}\mathrm{Fe}_{\mathrm{Mt\text{-}Ilm}} = \delta^{56}\mathrm{Fe}_{\mathrm{Mt}} - \delta^{56}\mathrm{Fe}_{\mathrm{Ilm}} \approx [0.64394 - (0.37934/1.5)]\times10^6/T^2 \approx 0.40\times10^6/T^2$ (1),

4.4.4 Magnetite-ilmenite mineral equilibrium temperature in Fig. 4.3b

Program QUILF (Andersen et al., 1993) is a software package that can be used to assess the equilibrium conditions among Ti-magnetite, ilmenite, augite, pigeonite, orthopyroxene, olivine and quartz through the QUILF (**Q**uartz - **U**lvöspinel - **Il**menite - **F**ayalite) equilibrium:

$SiO_2 + 2Fe_2TiO_4 = 2FeTiO_3 + Fe_2SiO_4$ (2)

Depending on the assemblage, various physical-chemical parameters could be estimated (e.g., temperature, pressure, oxygen fugacity, etc). The calculations were performed with ilmenite, magnetite and co-existing clinopyroxene and olivine. Pressure and silica activity were set at 100 MPa and 0.6 according to the previous studies (Pang et al., 2008a). It is worth noting that for the samples in Unit VII and bottom Unit VIII, where thick massive Fe-Ti-V oxide ore layers formed, we still used only magnetite-ilmenite pairs to estimate the temperature due to the absence of silicates or heavy alteration of primary clinopyroxene and olivine. With these mineral assemblage, QUILF equilibria could easily provide reliable information of temperature and oxygen fugacity with low uncertainties.

4.4.5 Rayleigh fractionation model in Fig. 4.3c

The equations that governs magnetite Fe isotope Rayleigh fractionation processes in Fig. 4.3c are,

$$\delta^{56}\mathrm{Fe}_{\mathrm{Mt\ (hydrothermal\ dissolution)}} = (1000 + \delta^{56}\mathrm{Fe}_{\mathrm{Mt\text{-}primary}}) \times f^{\alpha^{\mathrm{Fluid-Mt}}-1} - 1000 \qquad (3)$$

where the fractionation factor $\alpha^{\mathrm{Fluid\text{-}Mt}}$ is scaled by Polyakov et al. (2007) and Hill et al. (2010). Since the primary magnetite in Hongge Fe-Ti-V oxide deposit has been strongly modified by hydrothermal fluids and has no clue to identify their primary magmatic Fe isotope value, thus the range of $\delta^{56}\mathrm{Fe}_{\mathrm{Mt\text{-}primary}}$ is selected from the Fe isotope ranges (0.1 to 0.35 ‰) in unaltered Baima Fe-Ti-V deposit (Chen et al., 2014) in the same region and f represents the fraction of Fe remaining in the primary magnetite. Meanwhile, assuming the hydrothermal fluids were in equilibrium with magnetite during the dissolution process, the Fe isotope values of hydrothermal fluids can be scaled by the following equation,

$$\delta^{56}\mathrm{Fe}_{\mathrm{Fluids}} = \delta^{56}\mathrm{Fe}_{\mathrm{Mt\ (hydrothermal\ dissolution)}} - \Delta^{56}\mathrm{Fe}_{\mathrm{Mt\text{-}Fluids}} \qquad (4),$$

where $\Delta^{56}\mathrm{Fe}_{\mathrm{Mt\text{-}Fluids}} \approx 1000\ln(\alpha^{\mathrm{Mt-Fluids}})$.

Model lines in Fig. 4.3c at 450 ℃ and 350 ℃ describe Rayleigh fractionation process for a fractionation factor $\alpha^{\mathrm{Mt-Fluids}}$ of 1.00042 and 1.00057 or $\alpha^{\mathrm{Fluids-Mt}}$ of 0.99958 and 0.99943, respectively.

4.4.6 Rayleigh fractionation model in Fig. 4.3d

For the re-precipitation process of secondary magnetite in Fig. 4.3d, the Fe isotope range of hydrothermal fluids obtained from equation (4) during hydrothermal dissolution process is selected as the starting values ($\delta^{56}\mathrm{Fe}_{\mathrm{Fluid\text{-}start}}$ = ~ -0.45 to 0 ‰). The Fe isotope variations of hydrothermal fluids during Fe re-precipitation process can be calculated according to the Rayleigh equation,

$$\delta^{56}\mathrm{Fe}^{f}_{\mathrm{Fluid}} = (\delta^{56}\mathrm{Fe}_{\mathrm{Fluid\text{-}start}} + 1000) \times f^{\alpha^{\mathrm{Mt-Fluid}}-1} - 1000 \qquad (5),$$

where the fractionation factor $\alpha^{\text{Mt-Fluid}}$ is calculated from Polyakov et al. (2007) and Hill et al. (2010) and *f* is the fraction of Fe remaining in the fluids.

The "snapshot" $\delta^{56}\text{Fe}\,^{f}_{\text{secondary Mt}}$ at a given fraction *f* can then be determined by Equation (6),

$$\delta^{56}\text{Fe}\,^{f}_{\text{secondary Mt}} = \delta^{56}\text{Fe}_{\text{Fluid}} + \Delta^{56}\text{Fe}_{\text{Mt-Fluid}} \qquad (6)$$

where $\Delta^{56}\text{Fe}_{\text{Mt-Fluids}} \approx 1000\ln(\alpha^{\text{Mt-Fluids}})$. The fractionation factor $\alpha^{\text{Mt-Fluids}}$ for modelling at 450 ℃ and 350 ℃ is the same as mentioned in Fig. 4.3c.

4.4.7 Mass balance calculations

Assuming that the shape of the Hongge layered intrusion is an ideal cylinder, the thickness of lower units could be used to represent the volume of lower units. In this studied drill core, the thickness (Tn) from Unit I to VI is approximately 350 meters, and magnetite volume proportions (Pr) range from ~6 to 30 % (average ~15 %, Supplementary Table 4.5). As a result, the total volume of Fe loss ($T_{\text{Fe-L}}$) during the hydrothermal dissolution process can be calculated using a simple mass balance equation:

$$T_{\text{Fe-L}} = \text{Tn} \times \text{Pr} \times \text{F} \qquad (7)$$

where F is the fraction of Fe loss (20-30 %) calculated from Fig. 4.3c. Using the previously mentioned parameters (Tn: 350 meter, Pr: 15 %; F: 20-30 %) in equation (7), the calculated results show that the dissolved Fe is an important Fe source with the potential to form ~10-16 meter thick ore layers.

Mass balance could also be used to estimate the volume of secondary magnetite formed by hydration of olivine. The highest FeO content for olivine (Fo=72.5) in the Hongge intrusion is ~ 25 wt.% and the molecular formula of this olivine is ~$(Mg_{1.45}Fe_{0.55})SiO_4$. Assuming that this is the primary olivine composition in the massive ore layers before hydration and the proportion of primary olivine is estimated as 40 vol.%, the maximum volume proportion of secondary magnetite formed by hydration is only ~7 % (=40 %×0.55/3) based on Fe atomic number balance between olivine (0.55) and magnetite (3). Considering the density of magnetite (~4.3-4.8 g/cm^3) is much higher than olivine (~3.3-3.8 g/cm^3), the actual hydration-formed secondary magnetite should be less than 7 %. Thus, without hydrothermal Fe re-precipitation, hydration-formed secondary magnetite could enhance at most 7 vol.% of the oxides in the ore layers.

If we assume that all of the dissolved Fe re-precipitates as secondary magnetite into the primary silicate-bearing ore layers, the total thickness of the hydrothermally formed layers should correspond to the amount of Fe dissolved in the fluids. Because calculated dissolved Fe has the potential to form 10-16 meter thick ore layers, potential hydrothermal contributions could range from 10/60 to 16/60, which can be expressed directly as 17-27 vol.%. When the two sources of secondary magnetite are combined, the volume percentage of oxides in the ore layers may increase by 24-34 vol.% in total.

Conclusions

In this Ph.D. project, systematic mineralogical, petrological and geochemical studies were conducted on the drill core samples from Hongge Fe-Ti-V oxide ore-bearing layered intrusion. Besides, experimental simulations on the Hongge parental magmas (ELIP high-Ti basalts) were applied to constrain the crystallization and Fe-Ti-V oxide mineralization conditions. These findings provide new insights into the formation of Fe-Ti-V oxide deposits in layered intrusions and are summarized below.

1. The open magma chamber processes in Hongge layered intrusion

The Hongge layered intrusion, which is only about 1,700 meters thick, contains about 60-100 meter thick massive monomineralic Fe-Ti-V oxide ore layers. Mass balance calculations indicate that the required Fe content in the Hongge magma is far beyond the proposed parental magma compositions of Emeishan high-Ti basalts. Mineralogical studies on the cumulus silicate minerals (including olivine, clinopyroxene, and plagioclase) reveal that the forsterite content (Fo) of olivine and anorthite content (An) of plagioclase show several reversals as well as phase proportion changes. Besides, the Mg# of clinopyroxene keeps nearly constant, without any fractional crystallization trend. In addition, the Cr, V, and P contents in bulk rocks show several reversals. Both mineral and bulk rock compositional reversals suggest that the Hongge layered intrusion cannot be formed in a closed magma chamber with a single injection of magma. Instead, there are more primitive magmas periodically recharged into the Hongge magma chamber through an open system. Multiple replenishing magmas provides enough Fe, Ti, and V supply during the ore formation processes, which is critical for the formation of World-class Fe-Ti-V oxide deposits.

2. Crystallization conditions of the Hongge layered intrusion

Crystallization experiments using a proposed high-Ti basaltic composition were conducted in variable T-P-fO_2-aH_2O conditions using IHPVs. The compositions of experimental minerals illustrated good comparisons with the Hongge natural samples, suggesting that the phase equilibria experiments can be used to determine the crystallization condition of Hongge layered intrusion. According to phase relationships, the crystallization condition of Hongge layered intrusion can be constrained at temperature ~1150-1000 ℃, pressure 200-300 MPa, and high water content. The fO_2 of Hongge intrusion was relatively low at the initial crystallization stage in Lower Zone, and with the addition of fluids (mainly H_2O), an increasing trend could be observed from Lower Zone (~QFM - 1) to the Middle Zone (~QFM + 1). The increase of fO_2 is the key factor triggering the formation of thick massive Fe-Ti-V oxide ore layers in the Upper Middle Zone.

3. Hydrothermal reworking as an important mechanism to form Hongge high-grade Fe-Ti-V oxide ore layers

Previous studies and our experiments show that thick massive ore layers, especially monomineralic ore layers, cannot be formed solely by magmatic processes. Through detailed petrological observations in this study, Hongge magnetite and ilmenite exhibit dissolution textures in the lower Units and re-precipitation/reaction textures in the massive ore layers in the upper Units. *In-situ* Fe isotope data for primary magnetite (-0.23 to 0.63 ‰) and ilmenite (-1.08 to -0.27 ‰) significantly exceed the typical δ^{56}Fe igneousrange. In contrast, secondary magnetite formed in major massive ore layers, displays extremely low δ^{56}Fe values (-1.24 to -0.09 ‰), indicating precipitation from hydrothermal fluids. Rayleigh modeling on Fe isotopes shows that about 20-30 % of Fe could be hydrothermally remobilized from the lower Units and subsequently re-precipitated into the thick massive ore layers. According to the mass balance calculations, the hydrothermal reworking could enhance up to ~30 vol.% of Fe-Ti-V oxides, which played a critical role in the formation of high-grade Fe-Ti-V oxide ores in layered intrusions. Our new magmatic-hydrothermal model shows that the Fe-Ti-V deposits in layered intrusions are not a pure magmatic origin but instead a combined control of magmatic and hydrothermal processes.

References

Abbott, R. N. (1978). Peritectic reactions in the system An-Ab-Or-Qz-H_2O. Canadian Mineralogist, 16, 245-256.

Akimoto, S., Nagata, T., & Katsura, T. (1957). The $TiFe_2O_5$—Ti_2FeO_5 solid solution series. Nature, 179(4549), 37-38.

Ali, J. R., Lo, C. H., Thompson, G. M., & Song, X. (2004). Emeishan Basalt Ar–Ar overprint ages define several tectonic events that affected the western Yangtze platform in the Mesozoic and Cenozoic. Journal of Asian Earth Sciences, 23(2), 163-178.

Ali, J. R., Thompson, G. M., Zhou, M. F., & Song, X. (2005). Emeishan large igneous province, SW China. Lithos, 79(3-4), 475-489.

Ali, J. R., & Aitchison, J. C. (2006). Positioning Paleogene Eurasia problem: Solution for 60–50 Ma and broader tectonic implications. Earth and Planetary Science Letters, 251(1-2), 148-155.

Almeev, R. R., Holtz, F., Koepke, J., Parat, F., & Botcharnikov, R. E. (2007). The effect of H_2O on olivine crystallization in MORB: Experimental calibration at 200 MPa. American Mineralogist, 92(4), 670-674.

Almeev R. R., Holtz, F., Koepke J., & Parat F. (2012). Experimental calibration of the effect of H_2O on plagioclase crystallization in basaltic melt at 200 MPa. American Mineralogist, 97(7), 1234–1240.

Almeev, R. R., Holtz, F., Ariskin, A. A., & Kimura, J. I. (2013). Storage conditions of Bezymianny Volcano parental magmas: results of phase equilibria experiments at 100 and 700 MPa. Contributions to Mineralogy and Petrology, 166(5), 1389-1414.

Andersen, D. J., Lindsley, D. H., & Davidson, P. M. (1993). QUILF: A Pascal program to assess equilibria among Fe-Mg-Mn-Ti oxides, pyroxene, olivine, and quartz. Computers & Geosciences, 19(9), 1333–1350.

Angerer, T., Hagemann, S. G., & Danyushevsky, L. (2013). High-grade iron ore at

Windarling, Yilgarn Craton: a product of syn-orogenic deformation, hypogene hydrothermal alteration and supergene modification in an Archean BIF-basalt lithostratigraphy. Mineralium Deposita, 48(6), 697-728.

Arai, S., & Akizawa, N. (2014). Precipitation and dissolution of chromite by hydrothermal solutions in the Oman ophiolite: New behavior of Cr and chromite. American Mineralogist, 99(1), 28–34.

Aranovich, L. Y., & Newton, R. C. (1999). Experimental determination of CO_2-H_2O activity-composition relations at 600–1000 ℃ and 6–14 kbar by reversed decarbonation and dehydration reactions. American Mineralogist, 84(9), 1319-1332.

Arató, R., & Audétat, A. (2017). FeTiMM—A new oxybarometer for mafic to felsic magmas. Geochemical Perspectives Letters, 5, 19-23.

Bai, Z. J., Zhong, H., Naldrett, A. J., Zhu, W. G., & Xu, G. W. (2012). Whole-rock and mineral composition constraints on the genesis of the giant Hongge Fe-Ti-V oxide deposit in the Emeishan Large Igneous Province, Southwest China. Economic Geology, 107(3), 507-524.

Bai, Z. J., Zhong, H., Li, C., Zhu, W. G., He, D. F., & Qi, L. (2014). Contrasting parental magma compositions for the Hongge and Panzhihua magmatic Fe-Ti-V oxide deposits, Emeishan Large Igneous Province, SW China. Economic Geology, 109(6), 1763-1785.

Bai, Z. J., Zhong, H., Hu, R. Z., Zhu, W. G., & Hu, W. J. (2019). Composition of the chilled marginal rocks of the Panzhihua layered intrusion, Emeishan Large Igneous Province, SW China: Implications for parental magma compositions, sulfide saturation history and Fe–Ti oxide mineralization. Journal of Petrology, 60(3), 619-648.

Bai, Z. J., Zhong, H., Hu, R. Z., & Zhu, W. G. (2021). World-Class Fe-Ti-V Oxide Deposits Formed in Feeder Conduits by Removing Cotectic Silicates. Economic Geology, 116(3), 681-691.

Baragar, W. R. A., & Annells, R. N. (1969). The geochemistry of Coppermine River basalts (Vol. 69, p. 43). Geological Survey of Canada.

Barling, J., Weis, D., & Demaiffe, D. (2000). A Sr-, Nd-and Pb-isotopic investigation of the transition between two megacyclic units of the Bjerkreim–Sokndal layered intrusion, south Norway. Chemical Geology, 165(1-2), 47-65.

Barnes, S. J. (1986). The effect of trapped liquid crystallization on cumulus mineral compositions in layered intrusions. Contributions to Mineralogy and Petrology, 93(4), 524-531.

Barnes, S. J., & Hoatson, D. M. (1994). The Munni Munni complex, Western Australia: stratigraphy, structure and petrogenesis. Journal of Petrology, 35(3), 715-751.

Barnes, S. J., & Roeder, P. L. (2001). The range of spinel compositions in terrestrial mafic and ultramafic rocks. Journal of petrology, 42(12), 2279-2302.

Barnes, S. J., Maier, W. D., & Ashwal, L. D. (2004). Platinum-group element distribution in the main zone and upper zone of the Bushveld Complex, South Africa. Chemical Geology, 208(1-4), 293-317.

Beard, B. L., Johnson, C. M., Von Damm, K. L., & Poulson, R. L. (2003). Iron isotope constraints on Fe cycling and mass balance in oxygenated Earth oceans. Geology, 31(7), 629–632.

Berndt, J., Liebske, C., Holtz, F., Freise, M., Nowak, M., Ziegenbein, D., Hurkuck, W., & Koepke, J. (2002). A combined rapid-quench and H_2-membrane setup for internally heated pressure vessels: Description and application for water solubility in basaltic melts. American Mineralogist, 87(11-12), 1717-1726.

Berndt, J., Koepke, J., & Holtz, F. (2005). An experimental investigation of the influence of water and oxygen fugacity on differentiation of MORB at 200 MPa. Journal of Petrology, 46(1), 135-167.

Bindeman, I. N., Brooks, C. K., McBirney, A. R., & Taylor, H. P. (2008). The low-δ^{18}O late-stage ferrodiorite magmas in the Skaergaard Intrusion: Result of liquid immiscibility, thermal metamorphism, or meteoric water incorporation into magma? The Journal of Geology, 116(6), 571–586.

Botcharnikov, R. E., Behrens, H., & Holtz, F. (2006). Solubility and speciation of C–O–H fluids in andesitic melt at T= 1100–1300 ℃ and P= 200 and 500 MPa. Chemical Geology, 229(1-3) 125-143.

Botcharnikov, R. E., Almeev, R. R., Koepke, J., & Holtz, F. (2008). Phase relations and liquid lines of descent in hydrous ferrobasalt—implications for the Skaergaard intrusion and Columbia River flood basalts. Journal of Petrology, 49(9), 1687-1727.

Boudreau, A. E. (2016). The Stillwater Complex, Montana–Overview and the significance of volatiles. Mineralogical Magazine, 80(4), 585-637.

Boudreau, A. (2019). Hydromagmatic processes and platinum-group element deposits in layered intrusions (p. 284). Cambridge: Cambridge University Press.

Boven, A., Pasteels, P., Punzalan, L. E., Liu, J., Luo, X., Zhang, W. Guo, Z., & Hertogen, J. (2002). ^{40}Ar/^{39}Ar geochronological constraints on the age and evolution of the Permo-Triassic Emeishan volcanic province, southwest China. Journal of Asian Earth Sciences, 20(2), 157-175.

Brey G. P., & Köhler, T. (1990). Geothermobarometry in four-phase lherzolites II. New thermobarometers, and practical assessment of existing thermobarometers. Journal of Petrology, 31(6), 1353-1378.

Cameron, E. N. (1978). The lower zone of the eastern Bushveld Complex in the Olifants River trough. Journal of Petrology, 19(3), 437-462.

Campbell, I. H. (1978). Some problems with the cumulus theory. Lithos, 11(4), 311-323.

Campbell, I. H. (1996). Fluid dynamic processes in basaltic magma chambers. In Developments in petrology (Vol. 15, pp. 45-76). Elsevier.

Canil, D., & Lacourse, T. (2020). Geothermometry using minor and trace elements in igneous and hydrothermal magnetite. Chemical Geology, 541, 119576.

Cao, Y., Wang, C. Y., Huang, F., & Zhang, Z. (2019). Iron isotope systematics of the Panzhihua mafic layered intrusion associated with giant Fe‐Ti oxide deposit in the Emeishan large igneous province, SW China. Journal of Geophysical

Research: Solid Earth, 124(1), 358-375.

Cawthorn, R. G., & McCarthy, T. S. (1980). Variations in Cr content of magnetite from the upper zone of the Bushveld Complex—evidence for heterogeneity and convection currents in magma chambers. Earth and Planetary Science Letters, 46(3), 335-343.

Cawthorn, R. G., & Biggar, G. M. (1993). Crystallization of titaniferous chromite, magnesian ilmenite and armalcolite in tholeiitic suites in the Karoo Igneous Province. Contributions to Mineralogy and Petrology, 114(2), 221-235.

Cawthorn, R. G. (1996). Re-evaluation of magma compositions and processes in the uppermost Critical Zone of the Bushveld Complex. Mineralogical Magazine, 60(398), 131-148.

Cawthorn, R. G., Barnes, S. J., Ballhaus, C., & Malitch, K. N. (2005). Platinum group element, chromium, and vanadium deposits in mafic and ultramafic rocks. Economic Geology, 100(S), 215-249.

Cawthorn, R. G., & Ashwal, L. D. (2009). Origin of anorthosite and magnetitite layers in the Bushveld Complex, constrained by major element compositions of plagioclase. Journal of Petrology, 50(9), 1607–1637.

Charlier, B., Duchesne, J. C., & Vander Auwera, J. (2006). Magma chamber processes in the Tellnes ilmenite deposit (Rogaland Anorthosite Province, SW Norway) and the formation of Fe–Ti ores in massif-type anorthosites. Chemical Geology, 234(3-4), 264-290.

Charlier, B., Skår, Ø., Korneliussen, A., Duchesne, J. C., & Vander Auwera, J. (2007). Ilmenite composition in the Tellnes Fe–Ti deposit, SW Norway: fractional crystallization, postcumulus evolution and ilmenite–zircon relation. Contributions to Mineralogy and Petrology, 154(2), 119-134.

Charlier, B., Namur, O., Malpas, S., de Marneffe, C., Duchesne, J. C., Vander Auwera, J., & Bolle, O. (2010). Origin of the giant Allard Lake ilmenite ore deposit (Canada) by fractional crystallization, multiple magma pulses and mixing. Lithos, 117(1-4), 119-134.

Charlier, B., Namur, O., Bolle, O., Latypov, R., & Duchesne, J. C. (2015). Fe–Ti–V–P ore deposits associated with Proterozoic massif-type anorthosites and related rocks. Earth-Science Reviews, 141, 56-81.

Chen, L. M., Song, X. Y., Hu, R. Z., Yu, S. Y., He, H. L., Dai, Z. H., She, Y. W., & Xie, W. (2017). Controls on trace-element partitioning among co-crystallizing minerals: Evidence from the Panzhihua layered intrusion, SW China. American Mineralogist, 102(5), 1006-1020.

Chung, S. L., & Jahn, B. M. (1995). Plume-lithosphere interaction in generation of the Emeishan flood basalts at the Permian-Triassic boundary. Geology, 23(10), 889-892.

Churakov, S. V., & Gottschalk, M. (2003). Perturbation theory based equation of state for polar molecular fluids: II. Fluid mixtures. Geochimica et Cosmochimica Acta, 67(13), 2415-2425.

da Silva, M. M., Holtz, F., & Namur, O. (2017). Crystallization experiments in rhyolitic systems: The effect of temperature cycling and starting material on crystal size distribution. American Mineralogist: Journal of Earth and Planetary Materials 102(11), 2284-2294.

Dall'Agnol, R., Scaillet, B., & Pichavant, M. (1999). An experimental study of a lower Proterozoic A-type granite from the Eastern Amazonian Craton, Brazil. Journal of Petrology, 40(11), 1673-1698.

Dare, S. A., Barnes, S. J., Beaudoin, G., Méric, J., Boutroy, E., & Potvin-Doucet, C. (2014). Trace elements in magnetite as petrogenetic indicators. Mineralium Deposita, 49(7), 785-796.

DePaolo, D. J., & Wasserburg, G. J. (1979). Sm-Nd age of the Stillwater Complex and the mantle evolution curve for neodymium. Geochimica et Cosmochimica Acta, 43(7), 999-1008.

Devine, J. D., Gardner, J. E., Brack, H. P., Layne, G. D., & Rutherford, M. J. (1995). Comparison of microanalytical methods for estimating H_2O contents of silicic volcanic glasses. American Mineralogist, 80(3-4), 319-328.

Dolejš, D., & Manning, C. E. (2010). Thermodynamic model for mineral solubility in aqueous fluids: theory, calibration and application to model fluid-flow systems. Geofluids, 10(1-2), 20–40.

Dong, H., Wang, K., & Liu, B. (2021). Amphibole geochemistry of the Baima layered intrusion, SW China: Implications for the evolution of interstitial liquid and the origin of Fe-Ti oxide ores. Ore Geology Reviews, 139, 104436.

Duan, Z., & Zhang, Z. (2006). Equation of state of the H_2O, CO_2, and H_2O–CO_2 systems up to 10 GPa and 2573.15 K: Molecular dynamics simulations with ab initio potential surface. Geochimica et Cosmochimica Acta, 70(9), 2311-2324.

Dziony, W., Horn, I., Lattard, D., Koepke, J., Steinhoefel, G., Schuessler, J., & Holtz, F. (2014). In-situ Fe isotope ratio determination in Fe-Ti oxides and sulfides from drilled gabbros and basalt from the IODP Hole 1256D in the eastern equatorial Pacific. Chemical Geology, 363, 101–113.

Eales, H. V., & Cawthorn, R. G. (1996). The bushveld complex. In Developments in petrology (Vol. 15, pp. 181-229). Elsevier.

Enkin, R. J., Yang, Z., Chen, Y., & Courtillot, V. (1992). Paleomagnetic constraints on the geodynamic history of the major blocks of China from the Permian to the present. Journal of Geophysical Research: Solid Earth, 97(B10), 13953-13989.

Erdmann, S., Scaillet, B., Martel, C., & Cadoux, A. (2014). Characteristic textures of recrystallized, peritectic, and primary magmatic olivine in experimental samples and natural volcanic rocks. Journal of Petrology, 55(12), 2377-2402.

Feig, S. T., Koepke, J., & Snow, J. E. (2006). Effect of water on tholeiitic basalt phase equilibria: an experimental study under oxidizing conditions. Contributions to Mineralogy and Petrology, 152(5), 611-638.

Feig, S. T., Koepke, J. & Snow, J. E. (2010). Effect of oxygen fugacity and water on phase equilibria of a hydrous tholeiitic basalt. Contributions to Mineralogy and Petrology, 160(4), 551-568.

Fischer, L. A., Wang, M., Charlier, B., Namur, O., Roberts, R. J., Veksler, I. V., Cawthorn, G., & Holtz, F. (2016). Immiscible iron-and silica-rich liquids in the

Upper Zone of the Bushveld Complex. Earth and Planetary Science Letters, 443, 108-117.

Fischer, L. A. (2018). The Upper zone of the Bushveld Complex, South Africa: Parental magma and crystallization processes (Doctoral dissertation, Hannover: Institutionelles Repositorium der Leibniz Universität Hannover).

Freise, M., Holtz, F., Nowak, M., Scoates, J. S., & Strauss, H. (2009). Differentiation and crystallization conditions of basalts from the Kerguelen large igneous province: an experimental study. Contributions to Mineralogy and Petrology, 158(4), 505-527.

Frost, B. R., Lindsley, D. H., & Andersen, D. J. (1988). Fe–Ti oxide–silicate equilibria: assemblages with fayalitic olivine. American Mineralogist, 73(7-8), 727–740.

Frost, B. R. (1991). Magnetic petrology: factors that control the occurrence of magnetite in crustal rocks. In: Lindsley, D.H. (Ed.), Oxide Minerals: Petrologic and Magnetic Significance, vol. 25. Mineralogical Society of America, Washington, pp. 489–509.

Gaetani, G. A., & Grove, T. L. (1998). The influence of water on melting of mantle peridotite. Contributions to Mineralogy and Petrology, 131(4), 323-346.

Ganino, C., Arndt, N. T., Zhou, M. F., Gaillard, F., & Chauvel, C. (2008). Interaction of magma with sedimentary wall rock and magnetite ore genesis in the Panzhihua mafic intrusion, SW China. Mineralium Deposita, 43(6), 677-694.

Ganino, C., Harris, C., Arndt, N. T., Prevec, S. A., & Howarth, G. H. (2013). Assimilation of carbonate country rock by the parent magma of the Panzhihua Fe-Ti-V deposit (SW China): evidence from stable isotopes. Geoscience Frontiers, 4(5), 547-554

GEOROC (2008). Geochemistry of rocks of the oceans and continents. Mainz: MPI für Chemie. Available at http://georoc.mpchmainz.gwdg.de/georoc/.

Ghiorso, M. S., & Sack, R. O. (1995). Chemical mass transfer in magmatic processes IV. A revised and internally consistent thermodynamic model for the interpolation and extrapolation of liquid-solid equilibria in magmatic systems at elevated temperatures and pressures. Contributions to Mineralogy and Petrology, 119(2), 197-212.

Ghiorso, M. S., & Evans, B. W. (2008). Thermodynamics of rhombohedral oxide solid solutions and a revision of the Fe-Ti two-oxide geothermometer and oxygen-barometer. American Journal of science, 308(9), 957-1039.

Green, T. H., & Ringwood, A. E. (1966). Origin of the calc-alkaline igneous rock suite. Earth and Planetary Science Letters, 1(5), 307-316.

Grove, T. L., Baker, M. B., & Kinzler, R. J. (1984). Coupled CaAl-NaSi diffusion in plagioclase feldspar: Experiments and applications to cooling rate speedometry. Geochimica et Cosmochimica Acta, 48 (10), 2113-2121.

Grove, T. L. (1993). Corrections to expressions for calculating mineral components in “Origin of calc-alkaline series lavas at medicine lake volcano by fractionation, assimilation and mixing” and “Experimental petrology of normal MORB near the kane fracture zone: 22°-25° N, mid-atlantic ridge”. Contributions to Mineralogy and Petrology, 114(3), 422-424.

Günther, T., Klemd, R., Zhang, X., Horn, I., & Weyer, S. (2017). In-situ trace element and Fe-isotope studies on magnetite of the volcanic-hosted Zhibo and Chagangnuoer iron ore deposits in the Western Tianshan, NW China. Chemical Geology, 453, 111-127.

Guo, F., Fan, W., Wang, Y., & Li, C. (2004). When did the Emeishan mantle plume activity start? Geochronological and geochemical evidence from ultramafic-mafic dikes in southwestern China. International Geology Review, 46(3), 226-234.

Haggerty, S. E., & Lindsley, D. H. (1970). Stability of the pseudobrookite (Fe_2TiO_5)-ferropseudobrookite ($FeTi_2O_5$) series. Carnegie Inst. Washington Year Book 68, 247-249.

Haggerty, S. E. (1981). Oxidation of opaque mineral oxides in basalts. In: Rumble III, D. (Ed.), Oxide Minerals. Rev. Mineral., vol. 3. Mineralogical Society of America, Washington, DC, United States, pp. Hg1– Hg98.

Hamilton, M. A., Pearson, D. G., Thompson, R. N., Kelley, S. P., & Emeleus, C. H. (1998). Rapid eruption of Skye lavas inferred from precise U–Pb and Ar–Ar dating of the Rum and Cuillin plutonic complexes. Nature, 394(6690), 260-263.

Hanski, E., Kamenetsky, V. S., Luo, Z. Y., Xu, Y. G., & Kuzmin, D. V. (2010). Primitive magmas in the Emeishan large igneous province, southwestern China and northern Vietnam. Lithos, 119(1-2), 75-90.

Harrison, T. M., & Watson, E. B. (1984). The behavior of apatite during crustal anatexis: equilibrium and kinetic considerations. Geochimica et Cosmochimica Acta, 48(7), 1467-1477.

Hauri, E. (2002). SIMS analysis of volatiles in silicate glasses, 2: isotopes and abundances in Hawaiian melt inclusions. Chemical Geology, 183(1-4), 115-141.

Hellman, P. L., & Green, T. H. (1979). The role of sphene as an accessory phase in the high-pressure partial melting of hydrous mafic compositions. Earth and Planetary Science Letters, 42(2), 191-201.

Henderson, P., & Suddaby, P. (1971). The nature and origin of the chrome-spinel of the Rhum layered intrusion. Contributions to Mineralogy and Petrology, 33(1), 21-31.

Hill, P. S., Schauble, E. A., & Young, E. (2010). Effects of changing solution chemistry on Fe^{3+}/Fe^{2+} isotope fractionation in aqueous Fe-Cl solutions. Geochimica et Cosmochimica Acta, 74(23), 6669–6689.

Holloway, J. R., & Burnham, C. W. (1972). Melting relations of basalt with equilibrium water pressure less than total pressure. Journal of Petrology, 13(1), 1-29.

Holness, M. B., Tegner, C., Nielsen, T. F., Stripp, G., & Morse, S. A. (2007). A textural record of solidification and cooling in the Skaergaard intrusion, East Greenland. Journal of Petrology, 48(12), 2359-2377.

Holness, M. B., Tegner, C., Nielsen, T. F., & Charlier, B. (2017). The thickness of the mushy layer on the floor of the Skaergaard magma chamber at apatite saturation. Journal of Petrology, 58(5), 909-932.

Horn, I., von Blanckenburg, F., Schoenberg, R., Steinhoefel, G., & Markl, G. (2006). In situ iron isotope ratio determination using UV-femtosecond laser ablation with application to hydrothermal ore formation processes. Geochimica et Cosmochimica Acta, 70(14), 3677-3688.

Horn, I., & von Blanckenburg, F. (2007). Investigation on elemental and isotopic fractionation during 196 nm femtosecond laser ablation multiple collector inductively coupled plasma mass spectrometry. Spectrochimica Acta Part B: Atomic Spectroscopy, 62(4), 410-422.

Hou, T., Zhang, Z., Kusky, T., Du, Y., Liu, J., & Zhao, Z. (2011). A reappraisal of the high-Ti and low-Ti classification of basalts and petrogenetic linkage between basalts and mafic–ultramafic intrusions in the Emeishan Large Igneous Province, SW China. Ore Geology Reviews, 41(1), 133-143.

Hou, T., Zhang, Z., Encarnacion, J., & Santosh, M. (2012). Petrogenesis and metallogenesis of the Taihe gabbroic intrusion associated with Fe–Ti-oxide ores in the Panxi district, Emeishan Large Igneous Province, southwest China. Ore Geology Reviews, 49, 109-127.

Hou, T., Zhang, Z., Encarnacion, J., Santosh, M., & Sun, Y. (2013). The role of recycled oceanic crust in magmatism and metallogeny: Os–Sr–Nd isotopes, U–Pb geochronology and geochemistry of picritic dykes in the Panzhihua giant Fe–Ti oxide deposit, central Emeishan large igneous province, SW China. Contributions to Mineralogy and Petrology, 165(4), 805-822.

Howarth, G. H., & Prevec, S. A. (2013a). Trace element, PGE, and Sr–Nd isotope geochemistry of the Panzhihua mafic layered intrusion, SW China: Constraints on ore-forming processes and evolution of parent magma at depth in a plumbing-system. Geochimica et Cosmochimica Acta, 120, 459-478.

Howarth, G. H., & Prevec, S. A. (2013b). Hydration vs. oxidation: Modelling implications for Fe–Ti oxide crystallisation in mafic intrusions, with specific reference to the Panzhihua intrusion, SW China. Geoscience Frontiers, 4(5), 555-569.

Howarth, G. H., Prevec, S. A., & Zhou, M. F. (2013). Timing of Ti-magnetite crystallisation and silicate disequilibrium in the Panzhihua mafic layered intrusion: Implications for ore-forming processes. Lithos, 170, 73-89.

Hunter, R. H., & Sparks, R. S. J. (1987). The differentiation of the Skaergaard intrusion. Contributions to Mineralogy and Petrology, 95(4), 451-461.

Hunter, R. H. (1996). Texture development in cumulate rocks. In Developments in Petrology (Vol. 15, pp. 77-101). Elsevier.

Husen, A., Almeev, R. R., & Holtz, F. (2016). The effect of H_2O and pressure on multiple saturation and liquid lines of descent in basalt from the Shatsky Rise. Journal of Petrology, 57(2), 309-344.

Irving, A. J., & Wyllie, P. J. (1975). Subsolidus and melting relationships for calcite, magnesite and the join $CaCO_3$-$MgCO_3$ 36 kb. Geochimica et Cosmochimica Acta, 39(1), 35-53.

Johnson, C., Beard, B., & Weyer, S. (2020). Iron Geochemistry: An Isotopic Perspective. Ch. 4 (Springer, Cham).

Jurewicz, A. J., & Watson, E. B. (1988). Cations in olivine, Part 2: Diffusion in olivine xenocrysts, with applications to petrology and mineral physics. Contributions to Mineralogy and Petrology, 99(2), 186-201.

Kamenetsky, V. S., Elburg, M., Arculus, R., & Thomas, R. (2006). Magmatic origin of low-Ca olivine in subduction-related magmas: co-existence of contrasting magmas. Chemical Geology, 233(3-4), 346-357.

Kamenetsky, V. S., Chung, S. L., Kamenetsky, M. B., & Kuzmin, D. V. (2012). Picrites from the Emeishan Large Igneous Province, SW China: a compositional continuum in primitive magmas and their respective mantle sources. Journal of Petrology, 53(10), 2095-2113.

Kerans, C. (1983). Timing of location of the Muskox intrusion: constraints from Coppermine homocline cover strata. Canadian Journal of Earth Sciences, 20(5), 673-683.

Kerr, R. C., & Tait, S. R. (1985). Convective exchange between pore fluid and an overlying reservoir of denser fluid: a post-cumulus process in layered intrusions. Earth and Planetary Science Letters, 75(2-3), 147-156.

Klemm, D. D., Henckel, J., Dehm, R. M., & Von Gruenewaldt, G. (1985). The geochemistry of titanomagnetite in magnetite layers and their host rocks of the eastern Bushveld Complex. Economic Geology, 80(4), 1075-1088.

Knipping, J. L., Bilenker, L. D., Simon, A. C., Reich, M., Barra, F., Deditius, A. P., Wälle, M., Heinrich, C. A., Holtz, F., & Munizaga, R. (2015). Trace elements in magnetite from massive iron oxide-apatite deposits indicate a combined formation by igneous and magmatic-hydrothermal processes. Geochimica et Cosmochimica Acta, 171, 15-38.

Koepke, J., Berndt, J., & Bussy, F. (2003). An experimental study on the shallow-level migmatization of ferrogabbros from the Fuerteventura Basal Complex, Canary Islands. Lithos, 69(3-4), 105-125.

Kress, V. C., & Carmichael, I. S. (1991). The compressibility of silicate liquids containing Fe_2O_3 and the effect of composition, temperature, oxygen fugacity and pressure on their redox states. Contributions to Mineralogy and Petrology, 108(1), 82-92.

Kruger, F. J., & Smart, R. (1987). Diffusion of trace elements during bottom crystallization of double-diffusive convection systems: the magnetitite layers of the Bushveld Complex. Journal of Volcanology and Geothermal Research, 34(1-2), 133-142.

Kruger, W., & Latypov, R. (2022). In situ crystallization of non-cotectic and foliated igneous rocks on a magma chamber floor. Communications Earth & Environment, 3(1), 1-12.

Leake, B. E., Woolley, A. R., Birch, W. D., Burke, E. A., Ferraris, G., Grice, J. D., Hawthorne, F. C., Kisch, H. J., Krivovichew, V. G., Schumacher, J. C., Stephenson, N. C. N., & Whittaker, E. J. (2003). Nomenclature of amphiboles: additions and revisions to the International Mineralogical Association’s 1997 recommendations. The Canadian Mineralogist, 41(6), 1355-1362.

Lee, C. A. (1996). A review of mineralization in the Bushveld Complex and some other layered intrusions. Developments in petrology, 15, 103-145.

Li, H., Li, L., Zhang, Z., Santosh, M., Liu, M., Cui, Y., Yang, X., Chen, J. & Yao, T. (2014). Alteration of the Damiao anorthosite complex in the northern North China Craton: implications for high-grade iron mineralization. Ore Geology Reviews, 57, 574–588.

Li, L. X., Li, H. M., Zi, J. W., Rasmussen, B., Sheppard, S., Wilde, S. A., & Meng, J. (2019). Role of fluids in Fe-Ti-P mineralization of the Proterozoic Damiao anorthosite complex, China: Insights from baddeleyite-zircon relationships in ore and altered anorthosite. Ore Geology Reviews, 115, 103186.

Li, X., Wang, J., & Wang, H. (2017). Fe isotopic compositions of modern seafloor hydrothermal systems and their influence factors. Journal of Chemistry, 2017

Li, X., Zhang, C., Almeev, R. R., & Holtz, F. (2020). GeoBalance: An Excel VBA program for mass balance calculation in geosciences. Geochemistry, 80(2), 125629.

Liao, M., Tao, Y., Song, X., Li, Y., & Xiong, F. (2015). Multiple magma evolution and ore-forming processes of the Hongge layered intrusion, SW China: Insights from Sr–Nd isotopes, trace elements and platinum-group elements. Journal of Asian Earth Sciences, 113, 1082-1099.

Libourel, G. (1999). Systematics of calcium partitioning between olivine and silicate melt: implications for melt structure and calcium content of magmatic olivines. Contributions to Mineralogy and Petrology, 136(1), 63-80.

Liou, J. G., Zhang, R., Ernst, W. G., Liu, J., & McLimans, R. (1998). Mineral parageneses in the Piampaludo eclogitic body, Gruppo di Voltri, western Ligurian Alps. Schweizerische Mineralogische und Petrographische Mitteilungen, 78(2), 317-335.

Liu, D., Shen, F. K., & Zhang, G. Z. (1985). Layered intrusions of the Panxi area, Sichuan province. In: Zhang, Y. X. (Ed.), Corpus of the Panxi Paleorift Studies in China. Geological Publishing House, Beijing, pp. 85–118.

Liu, P. P., Zhou, M. F., Chen, W. T., Boone, M., & Cnudde, V. (2014a). Using multiphase solid inclusions to constrain the origin of the Baima Fe–Ti–(V) oxide deposit, SW China. Journal of Petrology, 55(5), 951-976.

Liu, P. P., Zhou, M. F., Luais, B., Cividini, D., & Rollion-Bard, C. (2014b). Disequilibrium iron isotopic fractionation during the high-temperature magmatic differentiation of the Baima Fe-Ti oxide-bearing mafic intrusion, SW China. Earth and Planetary Science Letters, 399, 21–29.

Liu, J., Xia, Q. K., Kuritani, T., Hanski, E., & Yu, H. R. (2017). Mantle hydration and the role of water in the generation of large igneous provinces. Nature Communications, 8(1), 1-8.

Luan, Y., Song, X. Y., Chen, L. M., Zheng, W. Q., Tian, X. L., & Ran, Q. Y. (2014a). Mineralogical features and petrogenetic significances of the hornblende and phlogopite of the Hongge layered intrusion, Sichuan Province. Acta Petrologica Sinica, 30(5): 1457-1471 (in Chinese with English abstract).

Luan, Y., Song, X. Y., Chen, L. M., Zheng, W. Q., Zhang, X. Q., Yu, S. Y., She, Y. W., Tian, X. L., & Ran, Q. Y. (2014b). Key factors controlling the accumulation of the Fe–Ti oxides in the Hongge layered intrusion in the Emeishan Large Igneous Province, SW China. Ore Geology Reviews, 57, 518-538.

Ma, Y., Ji, X. T., Li, J. C., Huang, M., & Kan, Z. Z. (2003). Mineral resources of the Panzhihua region. Sichuan Science and Technology Press, Chengdu, 275 pp. (in Chinese).

Maier, W. D., Barnes, S. J., Gartz, V., & Andrews, G. (2003). Pt-Pd reefs in magnetitites of the Stella layered intrusion, South Africa: A world of new exploration opportunities for platinum group elements. Geology, 31(10), 885-888.

Marsh, B. D. (1989). Magma chambers. Annual Review of Earth and Planetary Sciences, 17, 439-474.

Mathison, C. I., & Ahmat, A. L. (1996). The Windimurra Complex, Western Australia. In Developments in Petrology (Vol. 15, pp. 485-510). Elsevier.

Martin, R. F. (2012). The petrogenesis of anorogenic felsic magmas and AMCG suites: Insights on element mobility and mutual cryptic contamination from polythermal experiments. Lithos, 151, 35–45.

McBirney, A. R., & Noyes, R. M. (1979). Crystallization and layering of the Skaergaard intrusion. Journal of Petrology, 20(3), 487-554.

McBirney, A. R. (1996). The Skaergaard intrusion. In Developments in Petrology (Vol. 15, pp. 147-180). Elsevier.

Miller, Jr J. D., & Ripley, E. M. (1996). Layered intrusions of the Duluth complex, Minnesota, USA. Layered intrusions, 257-301.

Mills, R. D., & Glazner, A. F. (2013). Experimental study on the effects of temperature cycling on coarsening of plagioclase and olivine in an alkali basalt. Contributions to Mineralogy and Petrology, 166(1), 97-111.

Miyashiro, A. (1974). Volcanic rock series in island arcs and active continental margins. American journal of science, 274(4), 321-355.

Morse, S. A. (1980). Kiglapait mineralogy II: Fe-Ti oxide minerals and the activities of oxygen and silica. Journal of Petrology, 21(4), 685-719.

Naldrett, A. J., Cameron, G., Gruenewaldt, G. V., & Sharpe, M. R. (1987). The formation of stratiform PGE deposits in layered intrusions. In Origins of igneous layering (pp. 313-397). Springer, Dordrecht.

Namur, O., Charlier, B., Toplis, M. J., Higgins, M. D., Liégeois, J. P., & Vander Auwera, J. (2010). Crystallization sequence and magma chamber processes in the ferrobasaltic Sept Iles layered intrusion, Canada. Journal of Petrology, 51(6), 1203-1236.

Namur, O., Charlier, B., & Holness, M. B. (2012). Dual origin of Fe–Ti–P gabbros by immiscibility and fractional crystallization of evolved tholeiitic basalts in the Sept Iles layered intrusion. Lithos, 154, 100-114.

Namur, O., Humphreys, M. C., & Holness, M. B. (2014). Crystallization of interstitial liquid and latent heat buffering in solidifying gabbros: Skaergaard intrusion, Greenland. Journal of Petrology, 55(7), 1389-1427.

Namur, O., & Humphreys, M. C. (2018). Trace element constraints on the differentiation and crystal mush solidification in the Skaergaard intrusion, Greenland. Journal of Petrology, 59(3), 387-418.

Naslund, H. R., & McBirney, A. R. (1996). Mechanisms of formation of igneous layering. In Developments in petrology (Vol. 15, pp. 1-43). Elsevier.

Neave, D. A., & Putirka, K. D. (2017). A new clinopyroxene-liquid barometer, and implications for magma storage pressures under Icelandic rift zones. American Mineralogist, 102(4), 777-794.

Nimis, P. (1995). A clinopyroxene geobarometer for basaltic systems based on crystal-structure modeling. Contributions to Mineralogy and Petrology, 121(2), 115-125.

Nimis, P., & Ulmer, P. (1998). Clinopyroxene geobarometry of magmatic rocks Part 1: An expanded structural geobarometer for anhydrous and hydrous, basic and ultrabasic systems. Contributions to Mineralogy and Petrology, 133(1), 122-135.

Oeser, M., Weyer, S., Horn, I., & Schuth, S. (2014). High-precision Fe and Mg isotope ratios of silicate reference glasses determined in situ by femtosecond LA-MC-ICP-MS and by solution nebulisation MC-ICP-MS. Geostandards and Geoanalytical Research, 38(3), 311-328.

Oeser, M., Dohmen, R., Horn, I., Schuth, S., & Weyer, S. (2015). Processes and time scales of magmatic evolution as revealed by Fe-Mg chemical and isotopic zoning in natural olivines. Geochimica et Cosmochimica Acta, 154, 130–150.

Osborn, E. F. (1978). Change in phase relations in response to change in pressure from 1 atm to 10 kbar for the system Mg_2SiO_4-iron oxide-$CaAl_2Si_2O_8$-SiO_2: Carnegie Inst. Washington. Year Book, 77, 784-790.

Panxi Geological Party. (1984). Mineralization and Exploration Forecasting of V–Ti Magnetite Deposits in the Panzhihua–Xichang Region (in Chinese).

Pang, K. N., Zhou, M. F., Lindsley, D., Zhao, D., & Malpas, J. (2008a). Origin of Fe–Ti oxide ores in mafic intrusions: evidence from the Panzhihua intrusion, SW China. Journal of Petrology, 49(2), 295-313.

Pang, K. N., Li, C., Zhou, M. F., & Ripley, E. M. (2008b). Abundant Fe–Ti oxide inclusions in olivine from the Panzhihua and Hongge layered intrusions, SW China: evidence for early saturation of Fe–Ti oxides in ferrobasaltic magma. Contributions to Mineralogy and Petrology, 156(3), 307-321.

Pang, K. N., Li, C., Zhou, M. F., & Ripley, E. M. (2009). Mineral compositional constraints on petrogenesis and oxide ore genesis of the late Permian Panzhihua layered gabbroic intrusion, SW China. Lithos, 110(1-4), 199-214.

Pang, K. N., Zhou, M. F., Qi, L., Shellnutt, G., Wang, C. Y., & Zhao, D. (2010). Flood basalt-related Fe–Ti oxide deposits in the Emeishan large igneous province, SW China. Lithos, 119(1-2), 123-136.

Pang, K. N., Zhou, M. F., Qi, L., Chung, S. L., Chu, C. H., & Lee, H. Y. (2013). Petrology and geochemistry at the Lower zone-Middle zone transition of the Panzhihua intrusion, SW China: Implications for differentiation and oxide ore genesis. Geoscience Frontiers, 4(5), 517-533.

Parks, J., & Hill, R. E. T. (1986). Phase compositions and cryptic variation in a 2.2-km section of the Windimurra layered gabbroic intrusion, Yilgarn Block, Western Australia; a comparison with the Stillwater Complex. Economic Geology, 81(5), 1196-1202.

Parsons, I., & Becker, S. M. (1987). Layering, compaction and post-magmatic processes in the Klokken intrusion. In Origins of igneous layering (pp. 29-92). Springer, Dordrecht.

Peate, I. U., & Bryan, S. E. (2009). Pre-eruptive uplift in the Emeishan?. Nature Geoscience, 2(8), 531.

Philpotts, A. R. (1967). Origin of certain iron-titanium oxide and apatite rocks. Economic Geology, 62(3), 303-315.

Polyakov, V. B., & Mineev, S. D. (2000). The use of Mössbauer spectroscopy in stable isotope geochemistry. Geochimica et Cosmochimica Acta, 64(5), 849–865.

Polyakov, V. B., Clayton, R. N., Horita, J., & Mineev, S. D. (2007). Equilibrium iron isotope fractionation factors of minerals: reevaluation from the data of nuclear inelastic resonant X-ray scattering and Mössbauer spectroscopy. Geochimica et Cosmochimica Acta, 71(15), 3833–3846.

Putirka, K., Johnson, M., Kinzler, R., Longhi, J. & Walker, D., (1996). Thermobarometry of mafic igneous rocks based on clinopyroxene-liquid equilibria, 0–30 kbar. Contributions to Mineralogy and Petrology, 123(1), 92-108.

Putirka, K. D., Mikaelian, H., Ryerson, F., & Shaw, H. (2003). New clinopyroxene-liquid thermobarometers for mafic, evolved, and volatile-bearing lava compositions, with applications to lavas from Tibet and the Snake River Plain, Idaho. American Mineralogist, 88(10), 1542-1554.

Putirka, K. D. (2005). Igneous thermometers and barometers based on plagioclase+ liquid equilibria: Tests of some existing models and new calibrations. American Mineralogist, 90(2-3), 336-346.

Putirka, K. D. (2008). Thermometers and barometers for volcanic systems. Reviews in Mineralogy and Geochemistry, 69(1), 61-120.

Qi, L., & Zhou, M. F. (2008). Platinum-group elemental and Sr–Nd–Os isotopic geochemistry of Permian Emeishan flood basalts in Guizhou Province, SW China. Chemical Geology, 248(1-2), 83-103.

Qi, L., Wang, C. Y., & Zhou, M. F. (2008). Controls on the PGE distribution of Permian Emeishan alkaline and peralkaline volcanic rocks in Longzhoushan, Sichuan Province, SW China. Lithos, 106(3-4), 222-236.

Reynolds, I. M. (1985). Contrasted mineralogy and textural relationships in the uppermost titaniferous magnetite layers of the Bushveld Complex in the Bierkraal area north of Rustenburg. Economic Geology, 80(4), 1027-1048.

Ridolfi, F., Renzulli, A., & Puerini, M. (2010). Stability and chemical equilibrium of amphibole in calc-alkaline magmas: an overview, new thermobarometric formulations and application to subduction-related volcanoes. Contributions to Mineralogy and Petrology, 160(1), 45-66.

Roeder, P. L., & Emslie, R. (1970). Olivine-liquid equilibrium. Contributions to mineralogy and petrology, 29(4), 275-289.

Rouxel, O., Shanks III, W. C., Bach, W., & Edwards, K. J. (2008). Integrated Fe-and S-isotope study of seafloor hydrothermal vents at East Pacific Rise 9-10 N. Chemical Geology, 252(3-4), 214–227.

Sato, H., Nakada, S., Fujii, T., Nakamura, M., & Suzuki-Kamata, K. (1999). Groundmass pargasite in the 1991–1995 dacite of Unzen volcano: phase stability experiments and volcanological implications. Journal of Volcanology and Geothermal Research, 89(1-4), 197-212.

Scaillet, B., Pichavant, M., Roux, J., Humbert, G., & Lefevre, A. (1992). Improvements of the Shaw membrane technique for measurement and control of fH_2 at high temperatures and pressures. American Mineralogist, 77(5-6), 647-655.

Scaillet, B., Pichavant, M., & Roux, J. (1995). Experimental crystallization of leucogranite magmas. Journal of Petrology, 36(3), 663-705.

Scaillet, B., & Macdonald, R. A. Y. (2003). Experimental constraints on the relationships between peralkaline rhyolites of the Kenya Rift Valley. Journal of Petrology, 44(10), 1867-1894.

Schannor, M., Veksler, I., Hecht, L., Harris, C., Romer, R., & Manyeruke, T. (2018). Small-scale Sr and O isotope variations through the UG2 in the eastern Bushveld Complex: The role of crustal fluids. Chemcial Geology, 485, 100–112.

Scholten, L., Schmidt, C., Lecumberri-Sanchez, P., Newville, M., Lanzirotti, A., Sirbescu, M., & Steele-MacInnis, M. (2019). Solubility and speciation of iron in hydrothermal fluids. Geochimica et Cosmochimica Acta, 252, 126-143.

Schuessler, J. A., Botcharnikov, R. E., Behrens, H., Misiti, V., & Freda, C. (2008). Amorphous materials: properties, structure, and durability: oxidation state of iron in hydrous phono-tephritic melts. American Mineralogist, 93(10), 1493-1504.

Schwab, R. G., & Küstner, D. (1981). Die Gleichgewichtsfugazitäten technologisch und petrologisch wichtiger Sauerstoffpuffer. Neues Jahrbuch für Mineralogie. Abhandlungen, 140(2), 111-142.

Scoates, J. S., & Wall, C. J. (2015). Geochronology of layered intrusions. In Layered intrusions (pp. 3-74). Springer, Dordrecht.

Scott, S. R., Sims, K., Frost, B., Kelemen, P., Evans, K., & Swapp, S. (2015). On the hydration of olivine in ultramafic rocks: Implications from Fe isotopes in serpentinites. Geochimica et Cosmochimica Acta, 215, 105–121 (2017).

Sharma, M., Polizzotto, M., & Anbar, A. D. (2001). Iron isotopes in hot springs along the Juan de Fuca Ridge. Earth and Planetary Science Letters, 194(1-2), 39–51.

Shellnutt, J. G., & Zhou, M. F. (2007). Permian peralkaline, peraluminous and metaluminous A-type granites in the Panxi district, SW China: their relationship to the Emeishan mantle plume. Chemical Geology, 243(3-4), 286-316.

Shellnutt, J. G., & Zhou, M. F. (2008). Permian, rifting related fayalite syenite in the Panxi region, SW China. Lithos, 101(1-2), 54-73.

Shellnutt, J. G., Zhou, M. F., & Zellmer, G. F. (2009). The role of Fe–Ti oxide crystallization in the formation of A-type granitoids with implications for the Daly gap: an example from the Permian Baima igneous complex, SW China. Chemical Geology, 259(3-4), 204-217.

Shellnutt, J. G., & Jahn, B. M. (2010). Formation of the Late Permian Panzhihua plutonic-hypabyssal-volcanic igneous complex: implications for the genesis of Fe–Ti oxide deposits and A-type granites of SW China. Earth and Planetary Science Letters, 289(3-4), 509-519.

Shellnutt, J. G., Wang, K. L., Zellmer, G. F., Iizuka, Y., Jahn, B. M., Pang, K. N., Qi, L., & Zhou, M. F. (2011a). Three Fe-Ti oxide ore-bearing gabbro-granitoid complexes in the Panxi region of the Emeishan large igneous province, SW China. American Journal of Science, 311(9), 773-812.

Shellnutt, J. G., Jahn, B. M., & Zhou, M. F. (2011b). Crustal-derived granites in the Panzhihua region, SW China: implications for felsic magmatism in the Emeishan Large Igneous province. Lithos, 123(1-4), 145-157.

Shellnutt, J. G., & Iizuka, Y. (2011). Mineralogy from three peralkaline granitic plutons of the Late Permian Emeishan large igneous province (SW China):

evidence for contrasting magmatic conditions of A-type granitoids. European Journal of Mineralogy, 23(1), 45-61.

Shellnutt, J. G., Denyszyn, S., & Mundil, R. (2012). Precise age determination of mafic and felsic intrusive rocks from the Permian Emeishan large igneous province (SW China). Gondwana Research, 22(1), 118-126.

Shellnutt, J. G., & Pang, K. N. (2012). Petrogenetic implications of mineral chemical data for the Permian Baima igneous complex, SW China. Mineralogy and Petrology, 106(1), 75-88.

Shellnutt, J. G. (2014). The Emeishan large igneous province: a synthesis. Geoscience Frontiers, 5(3), 369-394.

Shellnutt, J. G., Pham, T. T., Denyszyn, S. W., Yeh, M. W., & Tran, T. A. (2020). Magmatic duration of the Emeishan large igneous province: insight from Northern Vietnam. Geology, 48(5), 457-461.

Shellnutt, J. G. (2021). A cumulate syenite in the upper part of the Hongge-layered mafic–ultramafic intrusion, Emeishan large igneous province, SW China. International Journal of Earth Sciences, 110(8), 2979-3000.

Shishkina, T. A., Botcharnikov, R. E., Holtz, F., Almeev, R. R., & Portnyagin, M. V. (2010). Solubility of H_2O-and CO_2-bearing fluids in tholeiitic basalts at pressures up to 500 MPa. Chemical Geology, 277(1-2), 115-125.

Simon, A. C., Pettke, T., Candela, P. A., Piccoli, P. M., & Heinrich, C. A. (2004). Magnetite solubility and iron transport in magmatic-hydrothermal environments. Geochimica et Cosmochimica Acta, 68(23), 4905–4914.

Sisson, T. W., & Grove, T. L. (1993). Experimental investigations of the role of H_2O in calc-alkaline differentiation and subduction zone magmatism. Contributions to Mineralogy and Petrology, 113(2), 143-166.

Snyder, D., Carmichael, I. S., & Wiebe, R. A. (1993). Experimental study of liquid evolution in an Fe-rich, layered mafic intrusion: Constraints of Fe-Ti oxide precipitation on the T-fO_2 and T-ρ paths of tholeiitic magmas. Contributions to Mineralogy and Petrology, 113(1), 73-86.

Sparks, R. S. J., Huppert, H. E., Kerr, R. C., McKenzie, D. P., & Tait, S. R. (1985). Postcumulus processes in layered intrusions. Geological Magazine, 122(5), 555-568.

Song, X. Y., Zhou, M. F., Hou, Z. Q., Cao, Z. M., Wang, Y. L., & Li, Y. (2001). Geochemical constraints on the mantle source of the upper Permian Emeishan continental flood basalts, southwestern China. International Geology Review, 43(3), 213-225.

Song, X. Y., Zhou, M. F., Tao, Y., & Xiao, J. F. (2008). Controls on the metal compositions of magmatic sulfide deposits in the Emeishan large igneous province, SW China. Chemical Geology, 253(1-2), 38-49.

Song, X. Y., Keays, R. R., Xiao, L., Qi, H. W., & Ihlenfeld, C. (2009). Platinum-group element geochemistry of the continental flood basalts in the central Emeisihan Large Igneous Province, SW China. Chemical Geology, 262(3-4), 246-261.

Song, X. Y., Qi, H. W., Hu, R. Z., Chen, L. M., Yu, S. Y., & Zhang, J. F. (2013). Formation of thick stratiform Fe‐Ti oxide layers in layered intrusion and frequent replenishment of fractionated mafic magma: evidence from the Panzhihua intrusion, SW China. Geochemistry, Geophysics, Geosystems, 14(3), 712-732.

Steinhoefel, G., Horn, I., & von Blanckenburg, F. (2009). Micro-scale tracing of Fe and Si isotope signatures in banded iron formation using femtosecond laser ablation. Geochimica et Cosmochimica Acta, 73(18), 5343-5360.

Stormer, J. C. (1983). The effects of recalculation on estimates of temperature and oxygen fugacity from analyses of multicomponent iron-titanium oxides. American Mineralogist, 68(5-6), 586-594.

Tao, Y., Li, C., Hu, R., Ripley, E. M., Du, A., & Zhong, H. (2007). Petrogenesis of the Pt–Pd mineralized Jinbaoshan ultramafic intrusion in the Permian Emeishan large igneous province, SW China. Contributions to Mineralogy and Petrology, 153(3), 321-337.

Tao, Y., Putirka, K., Hu, R. Z., & Li, C. (2015). The magma plumbing system of the

Emeishan large igneous province and its role in basaltic magma differentiation in a continental setting. American Mineralogist, 100(11-12), 2509-2517.

Thy, P., Lesher, C. E., & Tegner, C. (2009). The Skaergaard liquid line of descent revisited. Contributions to Mineralogy and Petrology, 157(6), 735-747.

Tollari, N., Toplis, M. J., & Barnes, S. J. (2006). Predicting phosphate saturation in silicate magmas: an experimental study of the effects of melt composition and temperature. Geochimica et Cosmochimica Acta, 70(6), 1518-1536.

Tollari, N., Baker, D. R., & Barnes, S. J. (2008). Experimental effects of pressure and fluorine on apatite saturation in mafic magmas, with reference to layered intrusions and massif anorthosites. Contributions to Mineralogy and Petrology, 156(2), 161-175.

Toplis, M. J., Libourel, G., & Carroll, M. R. (1994). The role of phosphorus in crystallisation processes of basalt: an experimental study. Geochimica et Cosmochimica Acta, 58(2), 797-810.

Toplis, M. J., & Carroll, M. R. (1995). An experimental study of the influence of oxygen fugacity on Fe-Ti oxide stability, phase relations, and mineral—melt equilibria in ferro-basaltic systems. Journal of Petrology, 36(5), 1137-1170.

Toplis, M. J., & Carroll, M. R. (1996). Differentiation of ferro-basaltic magmas under conditions open and closed to oxygen: implications for the Skaergaard intrusion and other natural systems. Journal of Petrology, 37(4), 837-858.

Tormey, D. R., Grove, T. L., & Bryan, W. B. (1987). Experimental petrology of normal MORB near the Kane Fracture Zone: 22–25 N, mid-Atlantic ridge. Contributions to Mineralogy and Petrology, 96(2), 121-139.

Troll, V. R., Weis, F. A., Jonsson, E., Andersson, U. B., Majidi, S. A., Högdahl, K., Harris, C., Millet, M. A., Chinnasamy, S. S., Kooijman, E., & Nilsson, K. P. (2019). Global Fe–O isotope correlation reveals magmatic origin of Kiruna-type apatite-iron-oxide ores. Nature Communications, 10(1), 1-12.

Vander Auwera, J., & Longhi, J. (1994). Experimental study of a jotunite (hypersthene monzodiorite): constraints on the parent magma composition and crystallization conditions (P, T, fO_2) of the Bjerkreim-Sokndal layered intrusion (Norway). Contributions to Mineralogy and Petrology, 118(1), 60-78.

van der Laan, S. R., & Koster van Groos, A. F. (1991). Pt-Fe alloys in experimental petrology applied to high-pressure research on Fe-bearing systems. American Mineralogist, 76(11-12), 1940-1949.

Veksler, I. V., & Hou, T. (2020). Experimental study on the effects of H_2O upon crystallization in the Lower and Critical Zones of the Bushveld Complex with an emphasis on chromitite formation. Contributions to Mineralogy and Petrology, 175(9), 1-17.

Villiger, S., Ulmer, P., Müntener, O., & Thompson, A. B. (2004). The liquid line of descent of anhydrous, mantle-derived, tholeiitic liquids by fractional and equilibrium crystallization—an experimental study at 1.0 GPa. Journal of Petrology, 45(12), 2369-2388.

Von Gruenewaldt, G. (1993). Ilmenite-apatite enrichments in the Upper Zone of the Bushveld Complex: a major titanium-rock phosphate resource. International Geology Review, 35(11), 987-1000.

Wager, L. R., Brown, G. M., & Wadsworth, W. J. (1960). Types of igneous cumulates. Journal of Petrology, 1(1), 73-85.

Wager, L. R., & Brown, G. M. (1968). Layered igneous rocks: Oliver and Boyd. Edinburgh and London, 588.

Wall, C. J., Scoates, J. S., Friedman, R. M., & Meurer, W. P. (2010). Refining the precise age and duration of magmatism related to the Stillwater Complex. Ontario Geological Survey, Miscellaneous Release Data, 269(4).

Wallace, P. J. (2002). Volatiles in submarine basaltic glasses from the Northern Kerguelen Plateau (ODP Site 1140): Implications for source region compositions, magmatic processes, and plateau subsidence. Journal of Petrology, 43(7), 1311-1326.

Wang, C. Y., Zhou, M. F., & Zhao, D. (2008). Fe–Ti–Cr oxides from the Permian Xinjie mafic–ultramafic layered intrusion in the Emeishan large igneous province, SW China: crystallization from Fe-and Ti-rich basaltic magmas. Lithos, 102(1-2), 198-217.

Wang, D., Hou, T., Wang, M., & Holtz, F. (2020). New constraints on the open magma chamber processes in the formation of giant Hongge Fe-Ti-V oxide deposit. Lithos, 374, 105704.

Wang, M., Veksler, I., Zhang, Z., Hou, T., & Keiding, J. K. (2017). The origin of nelsonite constrained by melting experiment and melt inclusions in apatite: The Damiao anorthosite complex, North China Craton. Gondwana Research, 42, 163-176.

Wang, X., Hou, T., Wang, M., Zhang, C., Zhang, Z., Pan, R., Marxer, F., & Zhang, H. (2021). A new clinopyroxene thermobarometer for mafic to intermediate magmatic systems. European Journal of Mineralogy, 33(5), 621-637.

Watson, E. B. (1980). Apatite and phosphorus in mantle source regions: an experimental study of apatite/melt equilibria at pressures to 25 kbar. Earth and Planetary Science Letters, 51(2), 322-335.

Wilmart, E., Demaiffe, D., & Duchesne, J. C. (1989). Geochemical constraints on the genesis of the Tellnes ilmenite deposit, Southwest Norway. Economic Geology, 84(5), 1047-1056.

Wilson, A. H. (1996). The great dyke of Zimbabwe. In Developments in Petrology (Vol. 15, pp. 365-402). Elsevier.

Wilson, J. R., Robins, B., Nielsen, F. M., Duchesne, J. C., & Vander Auwera, J. (1996). The Bjerkreim-Sokndal layered intrusion, Southwest Norway. In Developments in Petrology (Vol. 15, pp. 231-255). Elsevier.

Wotzlaw, J. F., Bindeman, I. N., Schaltegger, U., Brooks, C. K., & Naslund, H. R. (2012). High-resolution insights into episodes of crystallization, hydrothermal alteration and remelting in the Skaergaard intrusive complex. Earth and Planetary Science Letters, 355, 199–212.

Wu, Y. D., Yang, J. H., Stagno, V., Nekrylov, N., Wang, J. T., & Wang, H. (2022). Redox heterogeneity of picritic lavas with respect to their mantle sources in the

Emeishan large igneous province. Geochimica et Cosmochimica Acta, 320, 161-178.

Xiao, L., Xu, Y. G., Chung, S. L., He, B., & Mei, H. (2003). Chemostratigraphic correlation of Upper Permian lavas from Yunnan Province, China: extent of the Emeishan large igneous province. International Geology Review, 45(8), 753-766.

Xiao, L., Xu, Y. G., Mei, H. J., Zheng, Y. F., He, B., & Pirajno, F. (2004a). Distinct mantle sources of low-Ti and high-Ti basalts from the western Emeishan large igneous province, SW China: implications for plume–lithosphere interaction. Earth and Planetary Science Letters, 228(3-4), 525-546.

Xiao, L., Xu, Y.G., Xu, J.F., He, B., & Pirajno, F. (2004b). Chemostratigraphy of flood basalts in the Garze-Litang region and Zongza block: implications for western extension of the Emeishan Large Igneous Province, SW China. Acta Geologica Sinica-English Edition, 78(1), 61-67.

Xing, C. M., Wang, C. Y., & Zhang, M. J. (2012). Volatile and CHO isotopic compositions of giant Fe-Ti-V oxide deposits in the Panxi region and their implications for the sources of volatiles and the origin of Fe-Ti oxide ores. Science China Earth Sciences, 55(11): 1782-1795.

Xing, C. M., & Wang, C. Y. (2017). Cathodoluminescence images and trace element compositions of fluorapatite from the Hongge layered intrusion in SW China: A record of prolonged crystallization and overprinted fluid metasomatism. American Mineralogist: Journal of Earth and Planetary Materials, 102(7), 1390-1401.

Xu, Y., Chung, S. L., Jahn, B. M., & Wu, G. (2001). Petrologic and geochemical constraints on the petrogenesis of Permian–Triassic Emeishan flood basalts in southwestern China. Lithos, 58(3-4), 145-168.

Xu, Y., Mei, H., Xu, J., Huang, X., Wang, Y., & Chung, S. L. (2003). Origin of two differentiation trends in the Emeishan flood basalts. Chinese Science Bulletin, 48(4), 390-394.

Xu, Y. G., He, B., Huang, X., Luo, Z., Chung, S. L., Xiao, L., Zhu, D., Fan, W. M., Xu, J., & Wang, Y. J. (2007). Identification of mantle plumes in the Emeishan Large Igneous Province. Episodes Journal of International Geoscience, 30(1), 32-42.

Yang, J. D., Sun, W., Wang, Z., Xue, Y., & Tao, X. (1999). Variations in Sr and C isotopes and Ce anomalies in successions from China: evidence for the oxygenation of Neoproterozoic seawater? Precambrian Research, 93(2-3), 215-233.

Yao, Z., & Mungall, J. E. (2022). Magnetite layer formation in the Bushveld complex of South Africa. Nature communications, 13(1), 1-11.

Yu, S. Y., Song, X., Ripley, E., Li, C., Chen, L., She, Y., & Luan, Y. (2015). Integrated O–Sr–Nd isotope constraints on the evolution of four important Fe–Ti oxide ore-bearing mafic–ultramafic intrusions in the Emeishan large igneous province, SW China. Chemical Geology, 401, 28-42.

Yuan, Q., Namur, O., Fischer, L. A., Roberts, R. J., Lü, X., & Charlier, B. (2017). Pulses of plagioclase-laden magmas and stratigraphic evolution in the Upper Zone of the Bushveld Complex, South Africa. Journal of Petrology, 58(8), 1619-1643.

Yudovskaya, M. A., Costin, G., Shilovskikh, V., Chaplygin, I., McCreesh, M., & Kinnaird, J. (2019). Bushveld symplectic and sieve-textured chromite is a result of coupled dissolution-reprecipitation: a comparison with xenocrystic chromite reactions in arc basalt. Contributions to Mineralogy and Petrology, 174(9), 1–21.

Zhang, X. Q., Song, X. Y., Chen, L. M., Xie, W., Yu, S. Y., Zheng, W. Q., Deng Y. F., Zhang J. F., & Gui, S. G. (2012). Fractional crystallization and the formation of thick Fe–Ti–V oxide layers in the Baima layered intrusion, SW China. Ore Geology Reviews, 49, 96-108.

Zhang, X. Q., Song, X. Y., Chen, L. M., Yu, S. Y., Xie, W., Deng, Y., Zhang, J. F., & Gui, S. G. (2013). Chalcophile element geochemistry of the Baima layered intrusion, Emeishan Large Igneous Province, SW China: implications for sulfur saturation history and genetic relationship with high-Ti basalts. Contributions to

Mineralogy and Petrology, 166(1), 193-209.

Zhang, Y., Ni, H., & Chen, Y. (2010). Diffusion data in silicate melts. Reviews in Mineralogy and Geochemistry, 72(1), 311-408.

Zhang, Z., Mahoney, J. J., Mao, J., & Wang, F. (2006). Geochemistry of picritic and associated basalt flows of the western Emeishan flood basalt province, China. Journal of Petrology, 47(10), 1997-2019.

Zhang, Z., Zhi, X., Chen, L., Saunders, A. D., & Reichow, M. K. (2008). Re–Os isotopic compositions of picrites from the Emeishan flood basalt province, China. Earth and Planetary Science Letters, 276(1-2), 30-39.

Zhang, Z., Mao, J., Saunders, A. D., Ai, Y., Li, Y., & Zhao, L. (2009). Sr, Nd, Pb and O isotopes of clinopyroxenes from the three typical mafic–ultramafic layered intrusions in the Emeishan large igneous province, SW China. Lithos, 113, 369-392.

Zhang, Z., Hou, T., Santosh, M., Li, H., Li, J., Zhang, Z., Song, X., & Wang, M. (2014). Spatio-temporal distribution and tectonic settings of the major iron deposits in China: An overview. Ore Geology Reviews, 57, 247-263.

Zhang, Z., Santosh, M., & Li, J. (2015). Iron deposits in relation to magmatism in China. Journal of Asian Earth Sciences, 113, 951-956.

Zhang, Z., Qin, J., Lai, S., Long, X., Ju, Y., Wang, X., & Zhu, Y. (2020). Origin of Late Permian amphibole syenite from the Panxi area, SW China: high degree fractional crystallization of basaltic magma in the inner zone of the Emeishan mantle plume. International Geology Review, 62(2), 210-224.

Zhong, H., Zhou, X. H., Zhou, M. F., Sun, M., & Liu, B. G. (2002). Platinum-group element geochemistry of the Hongge Fe–V–Ti deposit in the Pan-Xi area, southwestern China. Mineralium Deposita, 37(2), 226-239.

Zhong, H., & Zhu, W.G. (2006). Geochronology of layered mafic intrusions from the Pan–Xi area in the Emeishan large igneous province, SW China. Mineralium Deposita, 41(6), 599-606.

Zhong, H., Zhu, W., Qi, L., Zhou, M., Song, X., & Zhang, Y. (2006). Platinum-group element (PGE) geochemistry of the Emeishan basalts in the Pan-Xi area, SW China. Chinese Science Bulletin, 51(7), 845-854.

Zhong, H., Zhu, W. G., Chu, Z. Y., He, D. F., & Song, X. Y. (2007). SHRIMP U–Pb zircon geochronology, geochemistry, and Nd–Sr isotopic study of contrasting granites in the Emeishan large igneous province, SW China. Chemical Geology, 236(1-2), 112-133.

Zhong, H., Zhu, W. G., Hu, R. Z., Xie, L. W., He, D. F., Liu, F., & Chu, Z. Y. (2009). Zircon U–Pb age and Sr–Nd–Hf isotope geochemistry of the Panzhihua A-type syenitic intrusion in the Emeishan large igneous province, southwest China and implications for growth of juvenile crust. Lithos, 110(1-4), 109-128.

Zhong, H., Campbell, I. H., Zhu, W. G., Allen, C. M., Hu, R. Z., Xie, L. W., & He, D. F. (2011). Timing and source constraints on the relationship between mafic and felsic intrusions in the Emeishan large igneous province. Geochimica et Cosmochimica Acta, 75(5), 1374-1395.

Zhong, Y. T., He, B., Mundil, R., & Xu, Y. G. (2014). CA-TIMS zircon U–Pb dating of felsic ignimbrite from the Binchuan section: Implications for the termination age of Emeishan large igneous province. Lithos, 204, 14-19.

Zhong, Y., Mundil, R., Chen, J., Yuan, D., Denyszyn, S. W., Jost, A. B., Payne, J. L., He, B., Shen, S., & Xu, Y. (2020). Geochemical, biostratigraphic, and high-resolution geochronological constraints on the waning stage of Emeishan Large Igneous Province. GSA Bulletin, 132(9-10), 1969-1986.

Zhou, M. F., Malpas, J., Song, X. Y., Robinson, P. T., Sun, M., Kennedy, A. K., Lesher, C. M., & Keays, R. R. (2002a). A temporal link between the Emeishan large igneous province (SW China) and the end-Guadalupian mass extinction. Earth and Planetary Science Letters, 196(3-4), 113-122.

Zhou, M. F., Yan, D. P., Kennedy, A. K., Li, Y., & Ding, J. (2002b). SHRIMP U–Pb zircon geochronological and geochemical evidence for Neoproterozoic arc-magmatism along the western margin of the Yangtze Block, South China. Earth and Planetary Science Letters, 196(1-2), 51-67.

Zhou, M.F., Robinson, P.T., Lesher, C.M., Keays, R.R., Zhang, C.J., & Malpas, J. (2005). Geochemistry, petrogenesis and metallogenesis of the Panzhihua gabbroic layered intrusion and associated Fe–Ti–V oxide deposits, Sichuan Province, SW China. Journal of Petrology, 46(11), 2253-2280.

Zhou, M. F., Arndt, N. T., Malpas, J., Wang, C. Y., & Kennedy, A. K. (2008). Two magma series and associated ore deposit types in the Permian Emeishan large igneous province, SW China. Lithos, 103(3-4), 352-368.

Zhou, M. F., Chen, W. T., Wang, C. Y., Prevec, S. A., Liu, P. P., & Howarth, G. H. (2013). Two stages of immiscible liquid separation in the formation of Panzhihua-type Fe-Ti-V oxide deposits, SW China. Geoscience Frontiers, 4(5), 481-502.

Zhu, Z. Y., Jiang, S. Y., Mathur, R., Cook, N. J., Yang, T., Wang, M., Ma, L., & Ciobanu, C. L. (2018). Iron isotope behaviour during fluid/rock interaction in K-feldspar alteration zone-a model for pyrite in gold deposits from the Jiaodong Peninsula, East China. Geochimica et Cosmochimica Acta, 222, 94–116.

Zirner, A. L., Marks, M. A., Wenzel, T., Jacob, D. E., & Markl, G. (2015). Rare earth elements in apatite as a monitor of magmatic and metasomatic processes: The Il ḿaussaq complex, South Greenland. Lithos, 228, 12–22.

Supplementary Material

Supplementary Information for Chapter 3: "Experimental constraints on the crustal differentiation of high-Ti basalts in Emeishan Large Igneous Province, SW China: Implications for the formation of Fe-Ti oxide ore-bearing layered intrusions"

Dachuan Wang[1], Tong Hou[2], Roman Botcharnikov[3], Sarah Haselbach[1], Andreas Klügel[4], Meng Wang[2], Zhaochong Zhang[2], François Holtz[1]

[1]Institut für Mineralogie, Leibniz Universität Hannover, Hannover, Germany; [2]State Key Laboratory of Geological Processes and Mineral Resources, China University of Geosciences, Beijing, China; [3]Institut für Geowissenschaften, Johannes Gutenberg Universtät Mainz, Mainz, Germany; [4]Fachbereich Geowissenschaften, Universtät Bremen, Germany

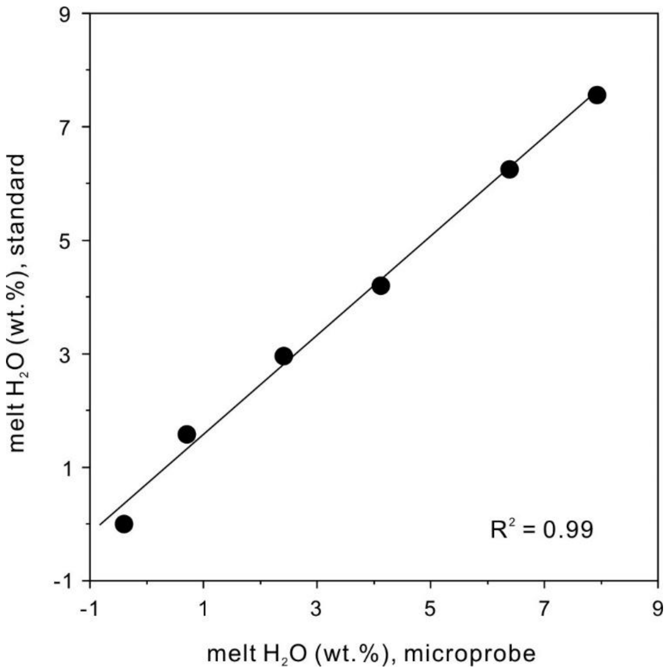

Supplementary Fig. 3.1. Comparison between theoretical H_2O in melt and actual microprobe analyses.

H_2O in melt (wt.%) = 0.8742 × H_2O microprobe (wt.%) where H_2O microprobe is “H_2O by difference” (100 % - microprobe total).

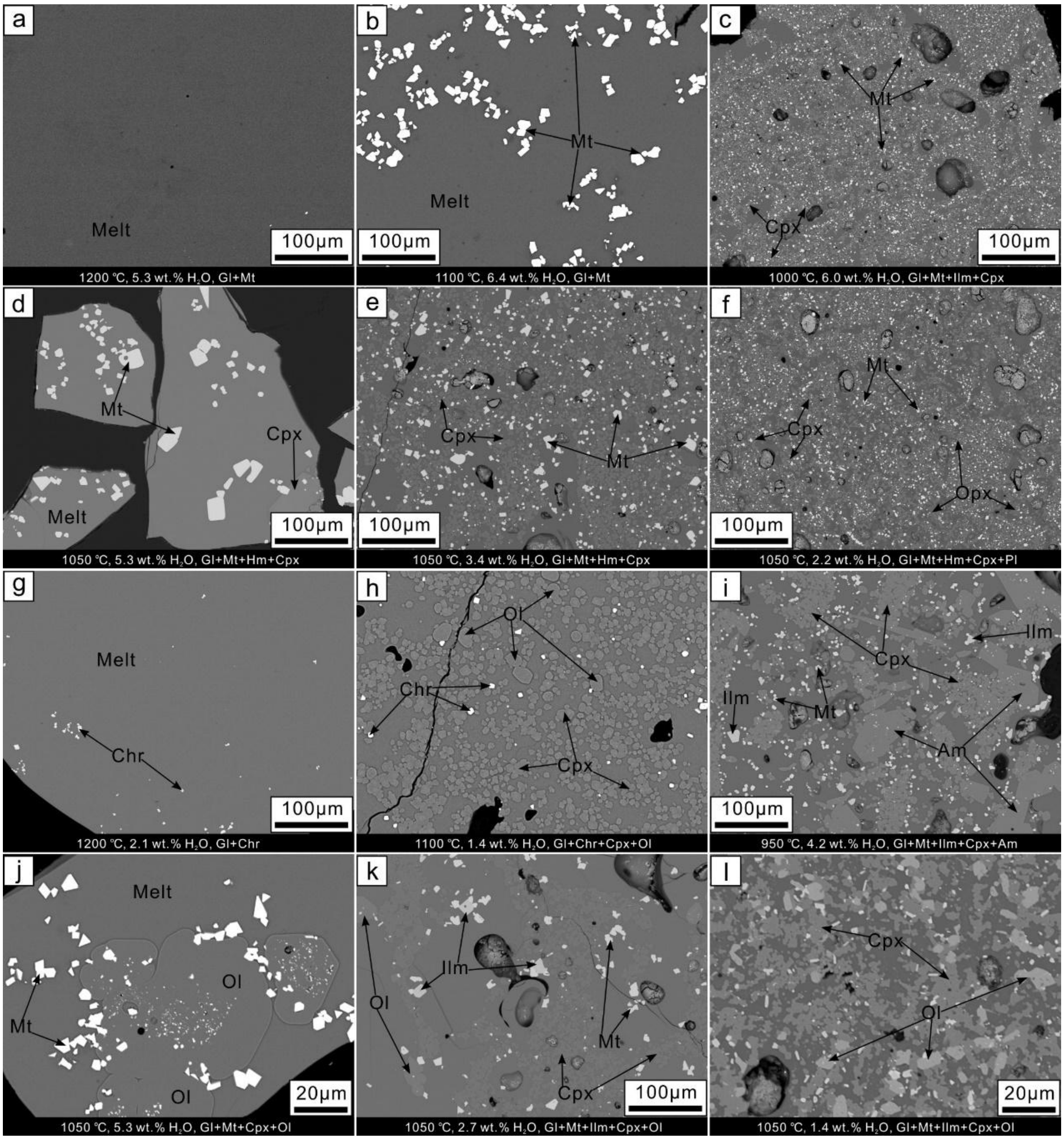

Supplementary Fig. 3.2. Scanning electron microscope images of selected run products obtained in crystallization experiments at 300 MPa in the temperature range of 1200-950 ℃. (a-c) Water-saturated experiments for different temperatures at intrinsic *f*O_2 of QFM + 3.3. (d-f) 1050 ℃ and intrinsic *f*O_2 of QFM + 3.3 experiments with different X^{fl}_{H2Oini} (=1, 0.6, 0.2). (g-i) Water-saturated experiments for different temperatures at intrinsic *f*O_2 of QFM + 1. (j-l) 1050 ℃ and intrinsic *f*O_2 of QFM + 1 experiments with different X^{fl}_{H2Oini} (=1, 0.6, 0). Phase abbreviations: Mt-magnetite; Cpx-clinopyroxene; Opx-orthopyroxene; Chr-chromite; Ilm-ilmenite; Am-amphibole.

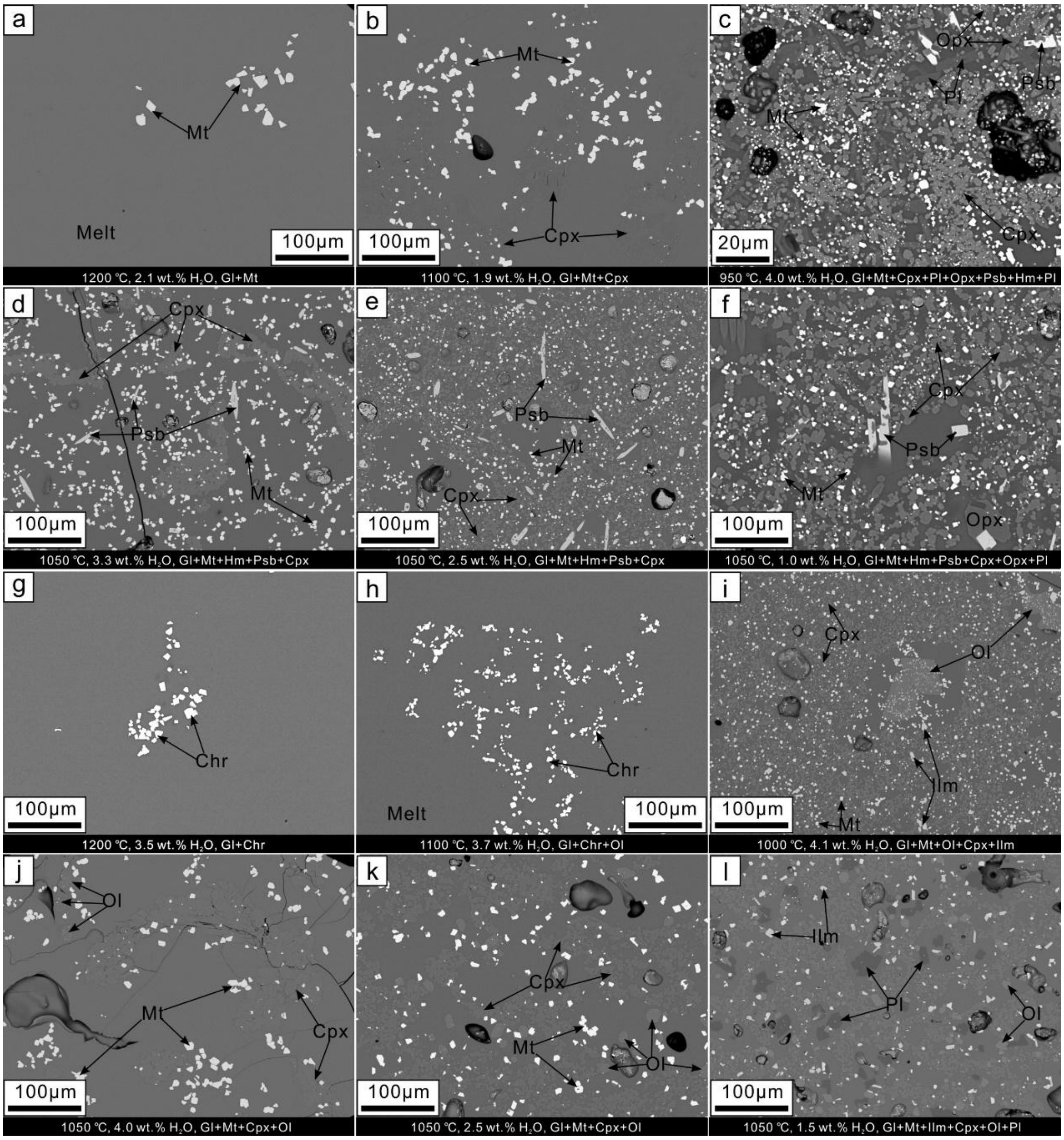

Supplementary Fig. 3.3 Scanning electron microscope images of selected run products obtained in crystallization experiments at 100 MPa in the temperature range of 1200-950 ℃. (a-c) Water-saturated experiments for different temperatures at intrinsic fO_2 of QFM + 3.3. (d-f) 1050 ℃ and intrinsic fO_2 of QFM + 3.3 experiments with different X^{fl}_{H2Oini} (=1, 0.6, 0). (g-i) Water-saturated experiments for different temperatures at intrinsic fO_2 of QFM + 1. (j-l) 1050 ℃ and intrinsic fO_2 of QFM + 1 experiments with different X^{fl}_{H2Oini} (=1, 0.6, 0.2). Phase abbreviations: Mt-magnetite; Cpx-clinopyroxene; Opx-orthopyroxene; Chr-chromite; Ilm-ilmenite; Am-amphibole; Psb-pseudobrookite; Pl-plagioclase.

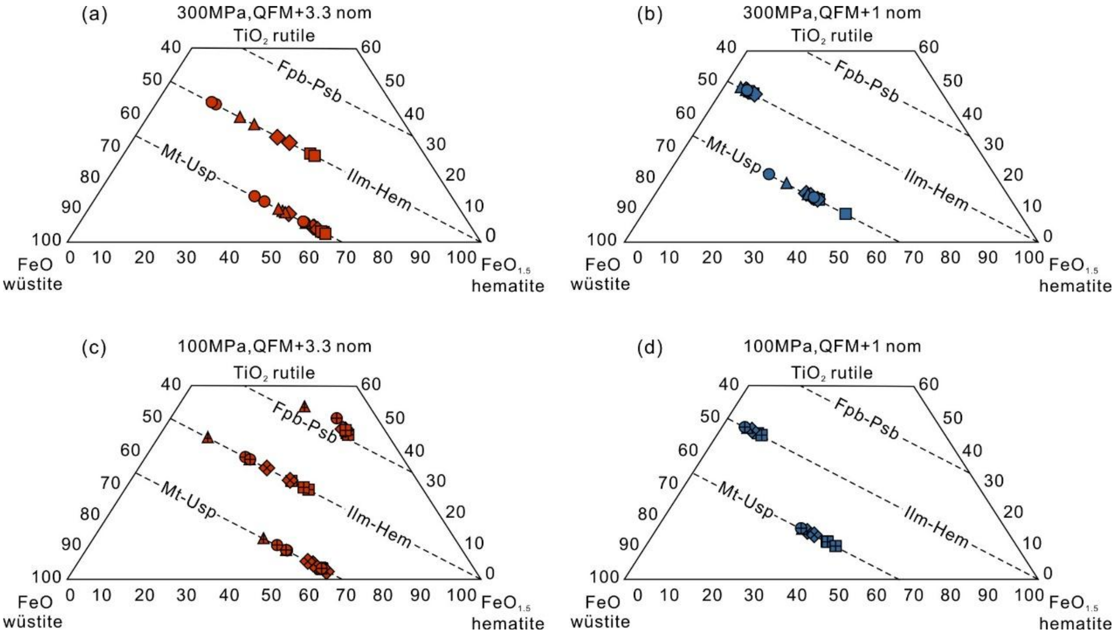

Supplementary Fig. 3.4. Compositions of the Fe-Ti oxides in the FeO-Fe_2O_3-TiO_2 diagram. Dashed lines correspond to the ferropseudobrookite-pseudobroolite, ilmenite-hematite and magnetite-ulvöspinel solid solution, respectively. Symbols as per Fig. 3.1.

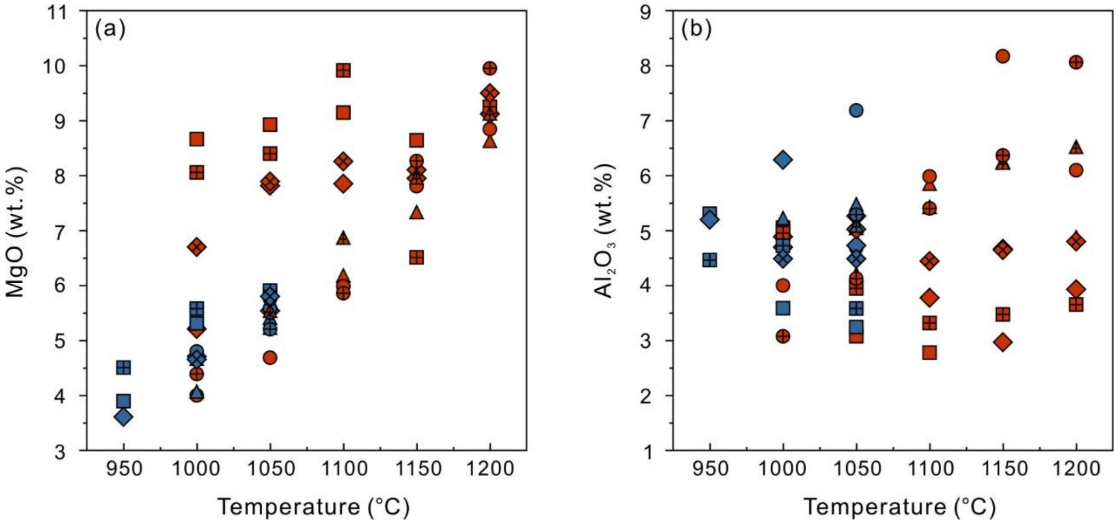

Supplementary Fig. 3.5. MgO content (a) and Al_2O_3 content (b) in magnetite-ulvöspinel solid solution as a function of temperature and water activity. Symbols as per Fig. 3.1.

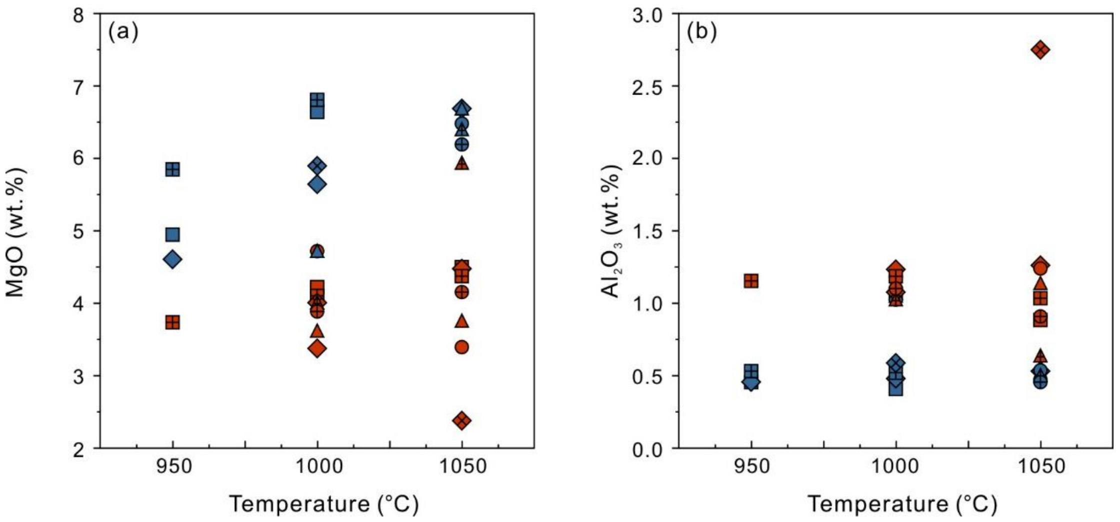

Supplementary Fig. 3.6. MgO content (a) and Al_2O_3 content (b) in Ilm-Hm solid solution as a function of temperature and water activity. Symbols as per Fig. 3.1.

Supplementary Information for Chapter 4: “Hydrothermal reworking as a mechanism forming high-grade Fe-Ti-V ores in layered intrusions**”**

Dachuan Wang[1], Tong Hou[2], Roman Botcharnikov[3], Stefan Weyer[1], Sarah-Lynn Haselbach[1], Zhaochong Zhang[2], Meng Wang[2], Ingo Horn[1], François Holtz[1]

[1] Institut für Mineralogie, Leibniz Universität Hannover, Callinstr. 3, 30167 Hannover, Germany

[2] State Key Laboratory of Geological Processes and Mineral Resources, China University of Geosciences, Beijing 100083, China

[3] Institut für Geowissenschaften, Johannes Gutenberg Universität Mainz, J.-J.-Becher-Weg 21, 55125 Mainz, Germany

Panxi regional geology and Hongge ore deposit geology

Panxi (Panzhihua to Xichang) region in southwestern China (Supplementary Fig. 4.1a) is the largest Fe-Ti-V metallogenic province worldwide, reserving ~20 and 30 % of global Ti and V resources (Bai et al., 2021). It is an important part of the Permian (~260 Ma) Emeishan Large Igneous Province (Xu et al., 2001; Zhou et al., 2002a). The basement in this region is mainly composed of Proterozoic rocks, including 1) Paleo- to Mesoproterozoic low-grade metasedimentary rocks interbedded with felsic and mafic metavolcanic rocks, and 2) Neoproterozoic granitic and metamorphic rocks. The Emeishan flood basalts were widely distributed (Chung and Jahn, 1995; Song et al., 2001; Su et al., 2001) and covered these basement rocks. Moreover, from north to south, four coeval large mafic-ultramafic layered intrusions (i.e., Baima, Xinjie, Hongge and Panzhihua) host World-class Fe-Ti-V oxide deposits (Supplementary Fig. 4.1b, Zhong et al., 2001). Thick Fe-Ti-V oxide ore bodies are mainly located in the lower or middle part of these layered intrusions, composed of gabbros and clinopyroxenites (Wang et al., 2008). In addition, these layered intrusions are all close adjacent to late Permian alkaline granites and syenites (~250-260 Ma, Shellnutt and Jahn, 2010; Luan et al., 2014b) and a series of faults with NS-, NE-, and NW-trends cut the intrusions and the adjacent footwall rocks.

Hongge layered intrusion hosts the largest Fe-Ti-V oxide ore deposit in Panxi region, reserving ~4.5 billion tons Fe-Ti-V oxides ores with 1.83×10^9 t Fe, 1.96×10^8 t Ti and 1.45×10^7 t V. The intrusion is ~ 16 km long, 5 to 10 km wide and 0.6-2.7 km thick (Luan et al., 2014b), with a total outcrop area of ~60 km^2 (Supplementary Fig. 4.1c). Footwall rocks mainly include Mesoproterozoic and Neoproterozoic meta-sandstone, meta-mudstone and dolomitic limestone. In addition, the Hongge intrusion is also in contact with the Permian Emeishan flood basalts in the northeastern and Permian syenite in the southwest of the open pit.

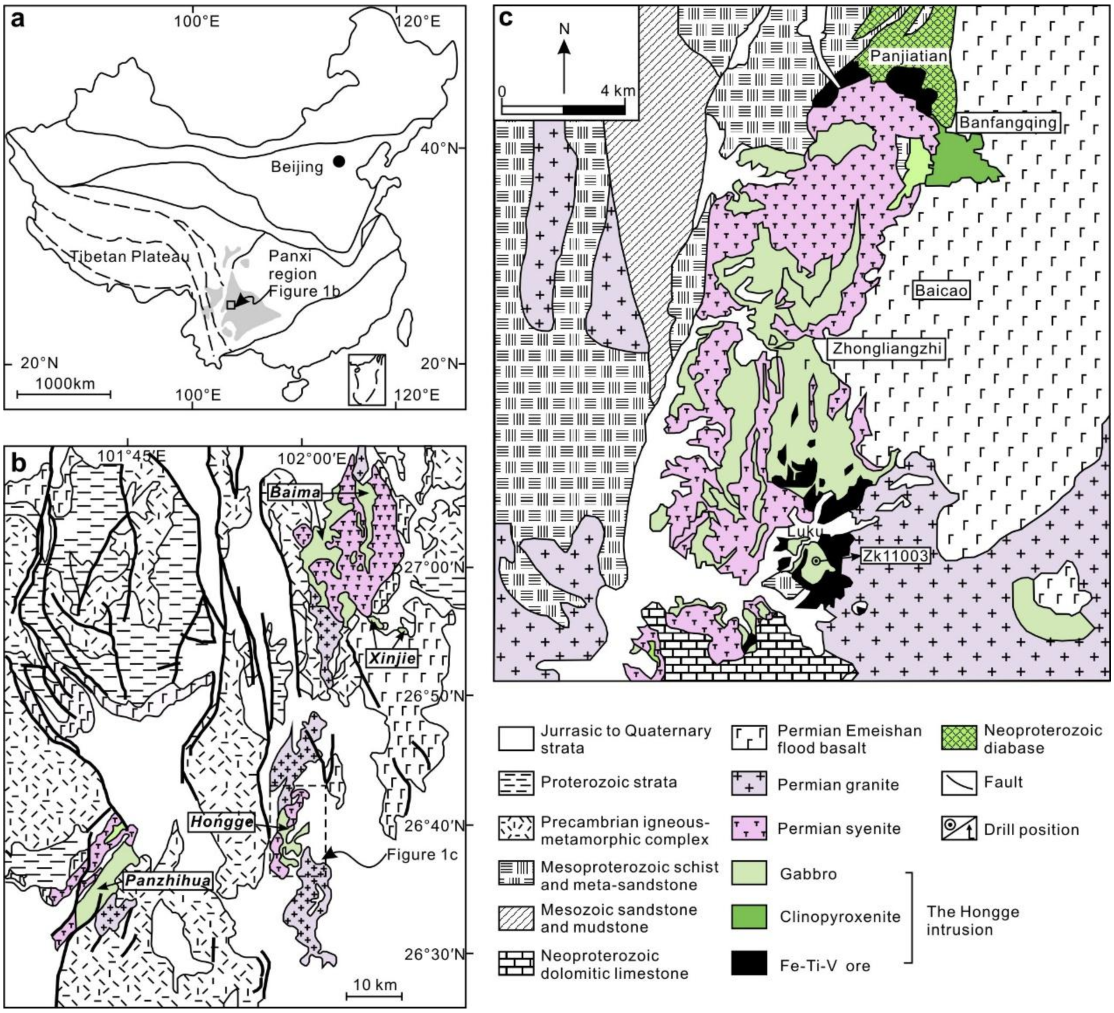

Supplementary Fig. 4.1. Regional and ore deposit geology of Hongge Fe-Ti-V oxide deposit in Southwestern China. (a) Location of Panxi region in Southwestern China. (b) Panxi regional geology and distribution of the four main Fe-Ti-V oxide deposits, modified from Zhong et al. (2011). From north to south, these deposits are named as Baima, Xinjie, Hongge and Panzhihua, respectively. (c) Sketch geological map of Hongge Fe-Ti-V oxide deposit, modified from Luan et al. (2014b), showing the location of the studied drill core (ZK11003).

Field and petrologic evidence for hydrothermal reworking in Hongge intrusion

Hydrothermal reworking has widely documented in both the silicate and oxide textures. Besides these microstructures, field and petrologic observations provide broader evidence for the fluid-rock interactions during hydrothermal reworking (Supplementary Figs. 4.2-4.3), including:

1) On the scale of open pit, long dykes and veins, predominantly composed of albite, cut across the entire UZ (Supplementary Fig. 4.2a-b), as do magnetite clinopyroxenite layers (Supplementary Fig. 4.2c-e) and massive Fe-Ti-V oxide ore layers (Supplementary Fig. 4.2f), with strong alterations in the contact gabbroic rocks.

2) On the scale of hand specimens, hydrothermal veins were discovered in each of the major stratigraphic units, varying from a few millimeters to centimeters in thickness (Supplementary Fig. 4.3). Major vein minerals are similar to those found in mafic igneous rocks metamorphosed under the greenschist facies. Albite, serpentine, amphibole, calcite, epidote, clinopyroxene, and some clay minerals are among the mineral assemblages, which limit the major hydrothermal temperature range to 300-500 ℃.

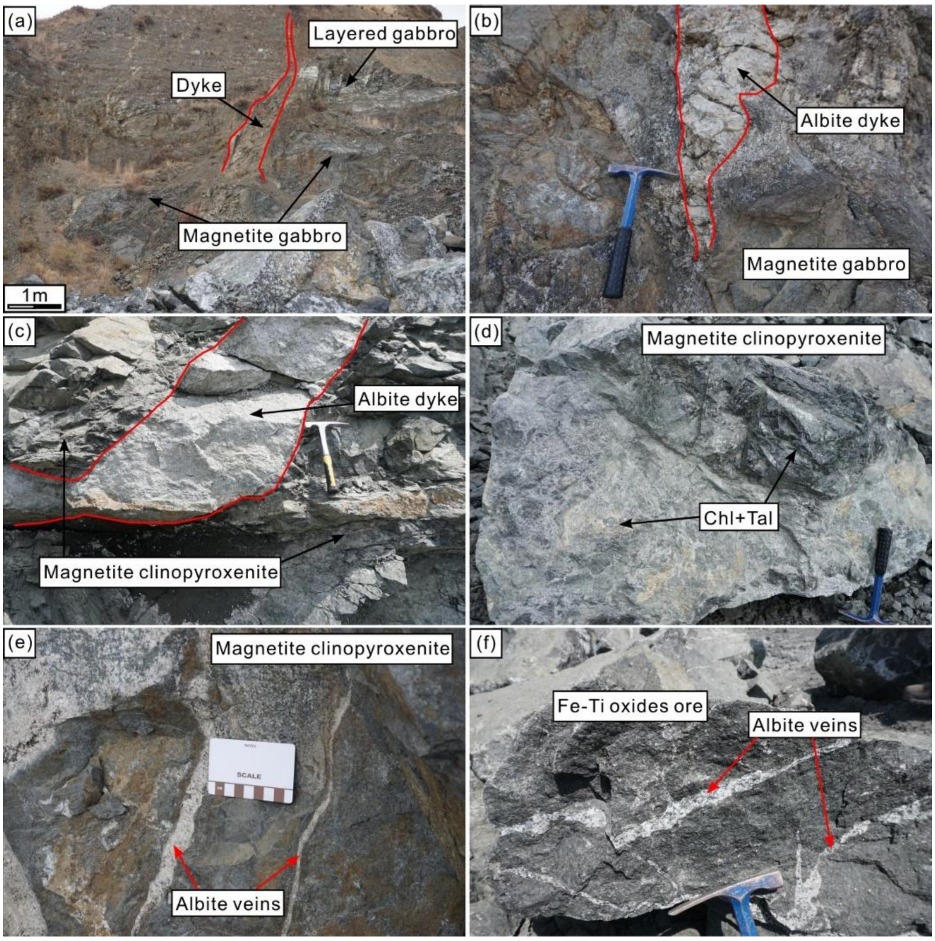

Supplementary Fig. 4.2. Representative field observations in the Hongge open pit. (a) A dyke cuts across the layered gabbro layers and magnetite gabbros in the Upper Zone of Hongge intrusion. (b) and (c) Albite dykes cut across the magnetite gabbros and magnetite clinopyroxenites. Strong deformation and hydrothermal alteration are observed in these dykes and adjacent areas. (d) Alteration minerals in the surface of magnetite clinopyroxenite. (e-f) Albite veins cut across the magnetite clinopyroxene layer and Fe-Ti-V oxides ore. Abbreviations: Tal=talcum; Chl=chlorite.

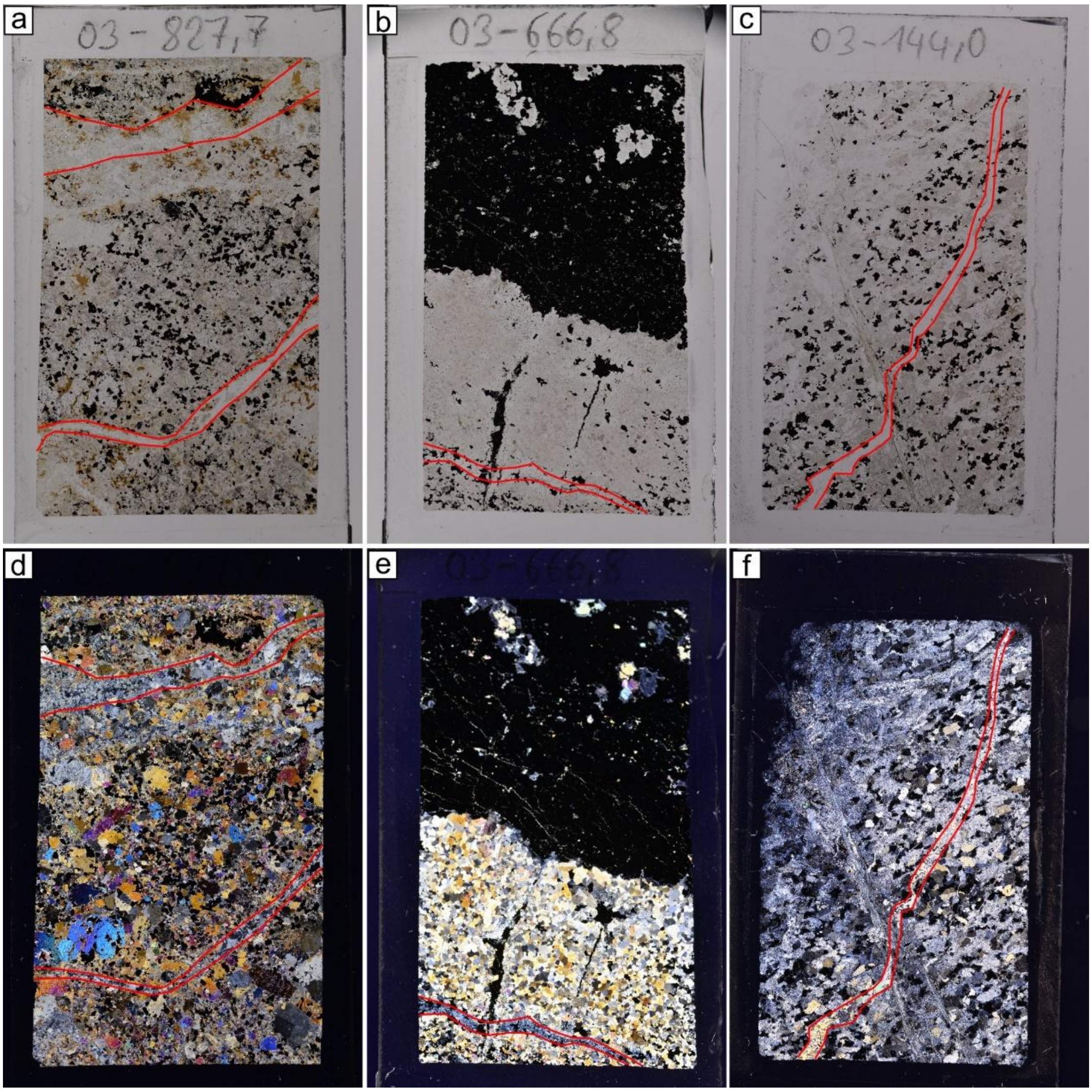

Supplementary Fig. 4.3. Representative hydrothermal veins in LZ, MZ and UZ. (a) Albite veins in olivine magnetite layers in LZ. The hydrothermal clinopyroxene is separated within and adjacent to the vein. (b) Serpentine and hydrothermal clinopyroxene veins in magnetite clinopyroxenite layers in MZ. (c) Calcite veins in altered gabbro layers in UZ. (d-e) The hydrothermal veins in sample a-c under plane-polarized light.

Description of the studied drill core (ZK11003)

The drill core studied was selected from a drilling location in the southern part of the Hongge Fe-Ti-V oxide deposit (Supplementary Fig. 4.1c). The drill core covers all of the main zones and units of the Hongge intrusion, based on our previous mineralogy and petrology studies (Wang et al., 2020). The Hongge intrusion can be divided into three main lithological zones with eleven units from top to bottom. The Upper Zone (UZ) includes three units and is about 460 meters thick with multiple layers of gabbros, magnetite gabbros and apatite magnetite gabbros (Supplementary Fig. 4.4a-c). No visible mineralization is observed in the UZ. The Middle Zone (MZ), which is ~200 meters thick, contains four units. Each of the units is repeated with magnetite-bearing clinopyroxenite/dunite layers on top (Supplementary Fig. 4.4d-f) and ore layers with a variable thickness at the bottom (Supplementary Fig. 4.4g, h). Notably, the ore layers in Unit V to VII are mainly disseminated ore layers with abundant silicate minerals (~40-50 vol.%). Thick massive ore layers (Fe-Ti-V oxides vol.% >60 % and thickness up to ~ 60 meters) which are the main target in this study only occur at the bottom of Unit VIII and are predominantly composed of magnetite and ilmenite (Supplementary Fig. 4.4i). The four units of Lower Zone (LZ) are ~ 260 meters thick and predominantly formed with magnetite olivine clinopyroxenite layers (Supplementary Fig. 4.4j-l). Hydrous minerals (e.g., amphibole; Supplementary Fig. 4.4j) are observed in certain layers in the LZ with a high proportion (up to ~ 15 %). Similar to UZ, no economical ore layers were found in the LZ from the studied drill core.

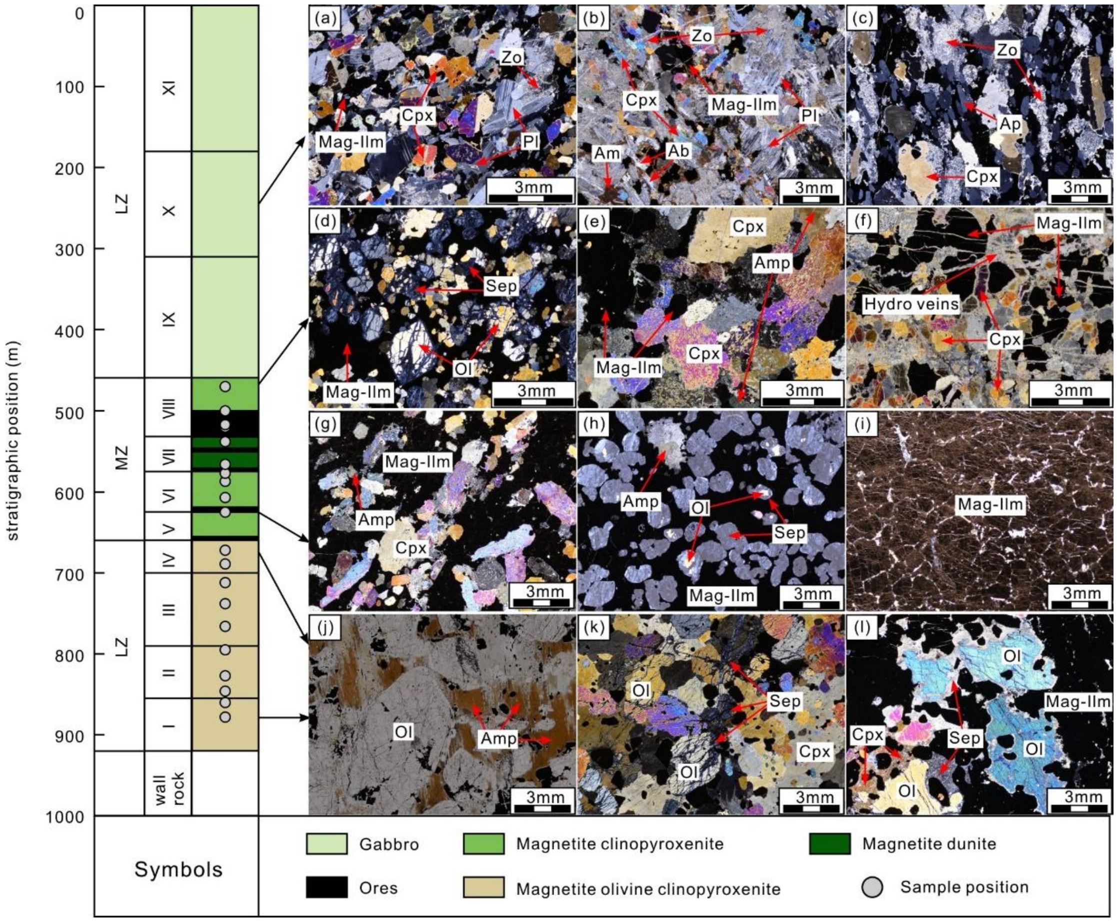

Supplementary Fig. 4.4. Stratigraphic column of Hongge intrusion according to the studied drill core and representative samples in different zones or units. (a) Fresh magnetite gabbro in the UZ. (b) Altered gabbro in Unit IX of UZ. (c) Apatite gabbroic rocks in the UZ. In these different types of gabbros, plagioclase is partly or significantly replaced by zoisite. (d) The representative magnetite dunite layer in the MZ. Almost all olivine crystals in (d) are partly replaced by serpentine at the rim or cut across by serpentine veins. (e-f) Two types of magnetite clinopyroxenite layers on top of each unit in MZ. Some clinopyroxene was altered into amphibole (e) or cemented by hydrothermal veins which are filled by albite or serpentine (f). (g-i) Different types of ore layers in the MZ, including disseminated ore layers with clinopyroxene (g) or olivine (h) and massive ore layers without obvious silicate minerals (i). Silicate minerals in the disseminated ore are strongly altered, i.e., almost all the olivine in Unit VII was replaced by serpentine. (j-l) Different magnetite olivine clinopyroxenite layers in the LZ. (j) Considerable amounts of hydrous minerals (e.g., amphibole) can be found in the samples from several layers. (k) Cumulus olivine with serpentine alteration and clinopyroxene in the LZ and interstitial Fe-Ti-V oxides. (l) Replacement of olivine by serpentine was observed in the LZ. Abbreviations:

LZ=Lower Zone; MZ=Middle Zone; UZ=Upper Zone; Amp=amphibole, Ap=apatite, Pl=plagioclase, Mag=magnetite, Ilm=ilmenite, Cpx=clinopyroxene, Ol=olivine, Sep=serpentine, Zo=zoisite, Hydro veins=hydrothermal veins.

Major and trace element compositions of magnetite and ilmenite

Depending on the textures and habitus, two types of magnetite had been identified in our samples, including primary magnetite (Fig. 4.1a-b) and secondary magnetite (Fig. 4.1e-f). Their chemical compositions are presented in Supplementary Tables 4.1, 4.2.

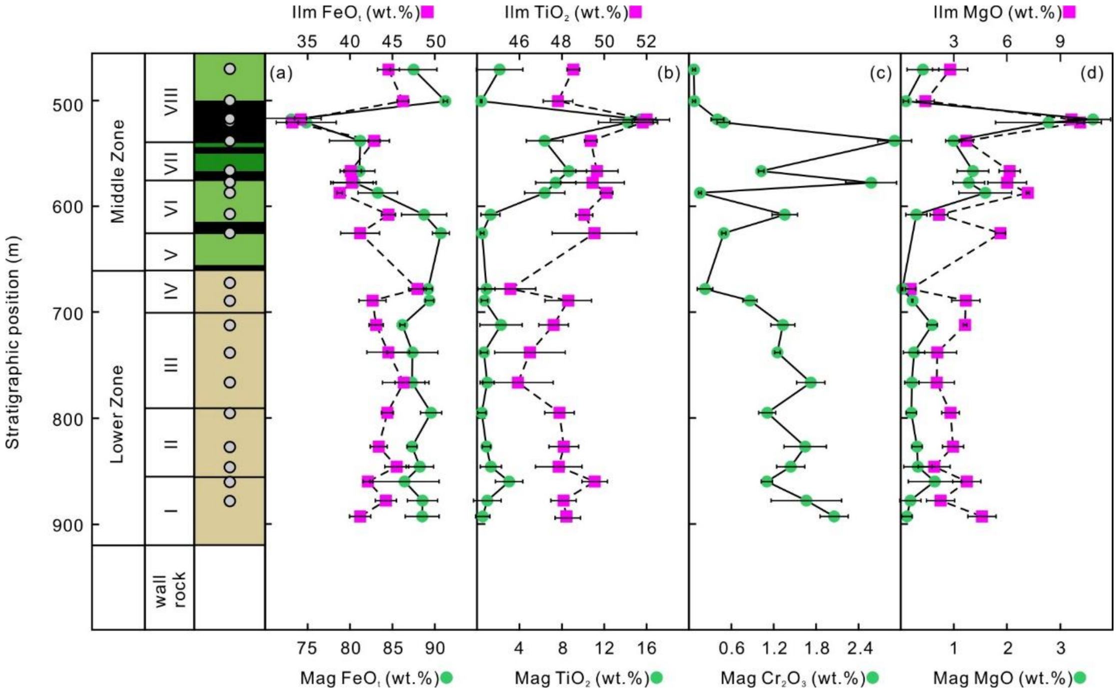

Supplementary Fig. 4.5. Representative element variations of primary magnetite and ilmenite along the stratigraphic position. Data are from Supplementary Table 4.1. Symbols for different lithological units in stratigraphic column as per Supplementary Fig. 4.4. Error bars represent 1δ standard deviation. Abbreviations: Mag=magnetite; Ilm=ilmenite.

For the primary magnetite with dissolution textures (Fig. 4.1a-b; Supplementary Table 4.1), their FeO_t contents in the magnetite clinopyroxenite layers and magnetite olivine clinopyroxenite layers from LZ and MZ are relatively high, varying from 85.99 to 91.26 wt.%. In contrast, significantly lower values (~74.85-83.08 wt.%) were observed in the magnetite of magnetite dunite layers or thick massive ore layers

(Supplementary Fig. 4.5a). The TiO_2 contents in primary magnetite vary from 0.45 to 14.25 wt.% and the highest concentrations were also found in the magnetite dunite layers and thick massive ore layers in the MZ (Supplementary Fig. 4.5b). Cr_2O_3 contents in primary magnetite are relatively high and show several reversals from the bottom upwards, ranging from 0.07 to 2.89 wt.% (Supplementary Fig. 4.5c). Al_2O_3, MgO, and V_2O_3 contents are mainly lower than 3 wt.%. Compared to the primary magnetite, secondary magnetite (Fig. 4.1e, f) is compositionally restricted, i.e., near-pure magnetite. FeO_t in secondary magnetite is high up to ~92.00 wt.% while TiO_2, V_2O_3, Al_2O_3, Cr_2O_3, and MnO are extremely low (Supplementary Fig. 4.6a-f; Supplementary Table 4.2).

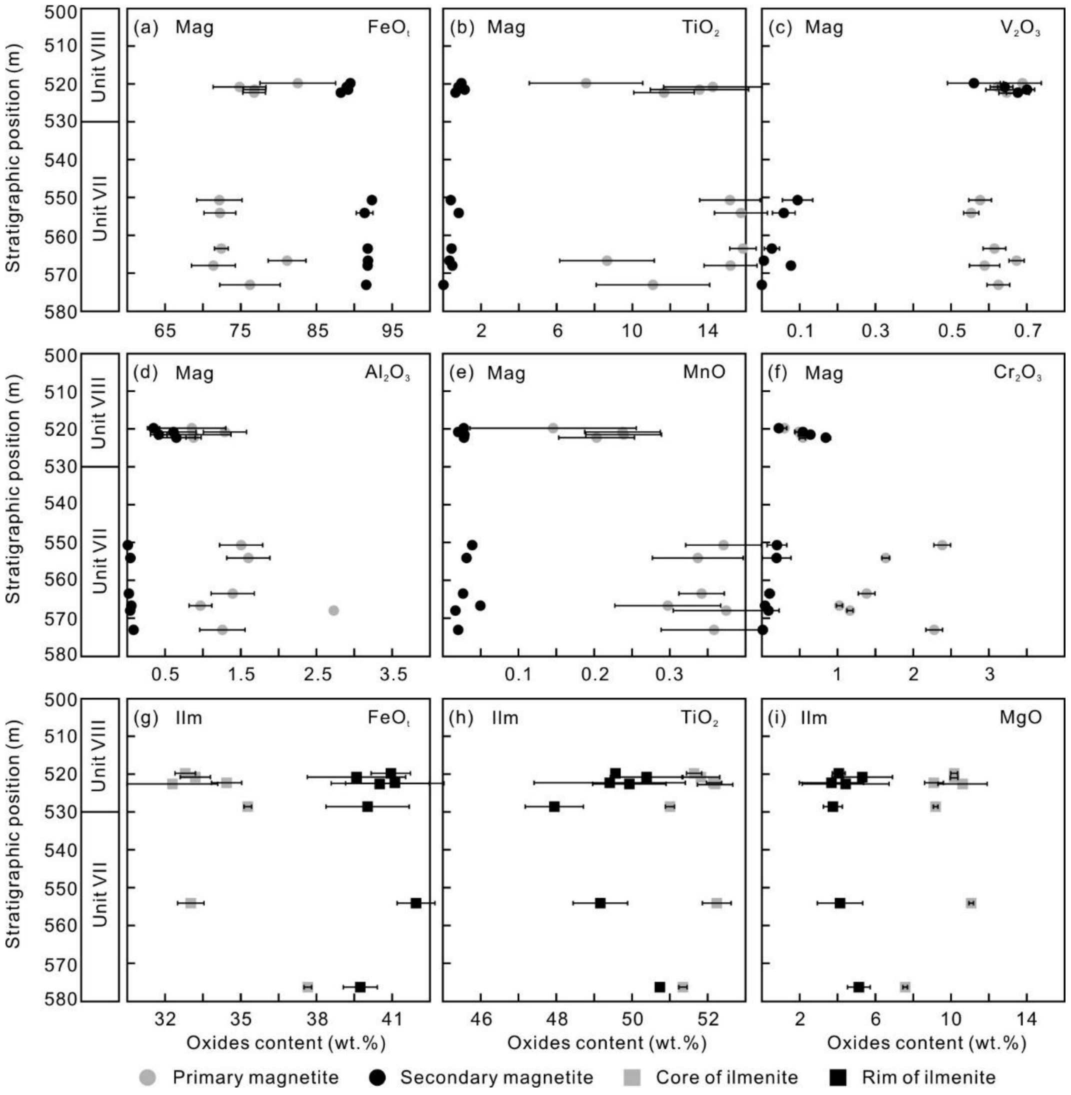

Supplementary Fig. 4.6. Elemental comparison for primary and secondary Fe-Ti-V oxides. (a-f)

Elemental differences between primary magnetite and secondary magnetite in the magnetite dunite layers and thick massive ores. Data are from Supplementary Table 4.2. (g-i) Core and rim composition differences in primary ilmenite with reaction textures in the magnetite dunite layers and thick massive ores. Error bars represent 1δ standard deviation. Data are from Supplementary Table 4.3.

Similar to magnetite, three types of ilmenites are identified, including 1) primary ilmenite with reaction textures in Unit I to VI (Fig. 4.1c-d), 2) primary ilmenite with reaction texture concentrated in Unit VII and bottom Unit VIII (Fig. 4.1g), and 3) zoned ilmenite only occurring in the thick massive ores (Fig. 4.1h). The FeO_t and TiO_2 of primary ilmenite crystals are ranging from 33.20 to 47.97 wt.% and 45.57 to 52.00 wt.%, respectively (Supplementary Fig. 4.5a-b; Supplementary Table 4.1). MgO contents vary from 0.56 to 10.16 wt.% and the highest value is observed in a thick massive ore layer (Supplementary Fig. 4.5d). Primary ilmenites with reaction rims have clear and sharp compositional differences between core and rim. Compared to the core compositions, the rims are more enriched in FeO_t content and depleted in TiO_2 and MgO content (Supplementary Fig. 4.6g-i; Supplementary Table 4.3). Notably, from the core to the rim, zoned ilmenite shows a gradually increasing trend for FeO_t, MnO, and decreasing trend for MgO contents. The TiO_2 content in zoned ilmenite does not vary strongly. Only a minor difference could be observed between core and rim (Supplementary Fig. 4.7; Supplementary Table 4.4).

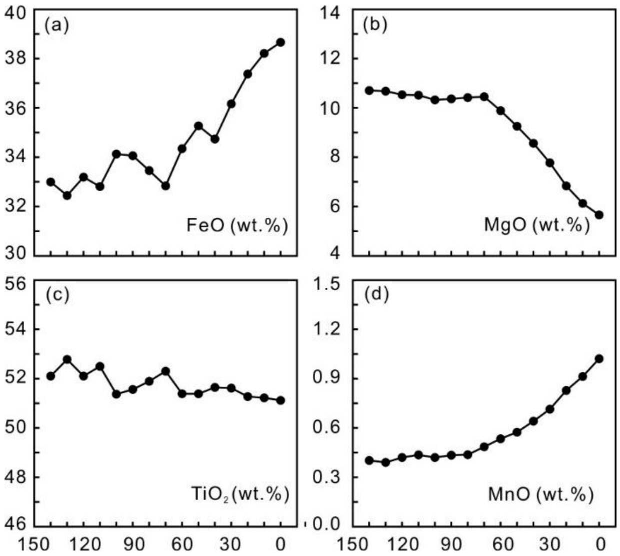

Supplementary Fig. 4.7. Elemental profile in zoned ilmenite according to sample 515.0 (step length was set at 10 μm, profile starting position was set from the most outside rim at 0). Data are from Supplementary Table 4.4.

Temperatures estimated from magnetite-ilmenite geothermometry and magnetite Mg geothermometry

According to magnetite-ilmenite pairs developed by Ghiorso and Evans (2008), temperature estimated from geothermometer can be made using either the $Fe^{2+}Ti$<=>$(Fe^{3+})_2$ exchange or Fe^{2+}<=>Mg exchange between the two-iron oxides. The comparison of the two temperature estimates allows for the evaluation of the internal consistency of coexisting iron oxide compositions as well as the extent of disequilibrium. Temperatures derived from this model are found to be consistent with experimental phase relations for cummingtonite stability in silicic volcanics. Web-based software implementing the new thermodynamic model, the two-oxide geothermometer, and oxygen barometer is available at https://gitlab.com/ENKI-portal/app-fe-ti-oxide-geotherm. The two-iron oxide geothermometry model showed a similar trend but indicated that the mineral equilibrium temperatures in the lower units (~532-344 ℃) are closer to the Fe isotope equilibrium temperatures. The highest two-oxide equilibrium temperatures (~758-638 ℃) were also calculated for massive ore layers (Supplementary Fig. 4.8a).

Magnetite Mg geothermometry is based on the Mg content in magnetite (Canil and Lacourse, 2020). The X_{Mg} [=Mg/(Mg+Fe_{tot}) in mole] of magnetite is strongly dependent on T, and can be formulated into an empirical geothermometer:

$$T_{\text{Mg-magnetite}}\ (℃) = \frac{-8344(\pm 320)}{\mathrm{Ln}X\mathrm{Mg}-4.1(\pm 0.28)} - 273 \qquad r^2 = 0.83 \qquad (1)$$

with a temperature error less than 50 ℃. Geothermometry with magnetite (X_{Mg}^{Mag}) provided the highest temperature estimations with a temperature range from ~850 to 450 ℃ in the lower units and ~980-780 ℃ in the massive ore layers (Supplementary Fig. 4.8b). The equilibrium temperatures of secondary magnetite and reaction rims of ilmenite were also estimated using the two mineral thermometers resulting in the temperature ranges from ~380-330 ℃ and 680-520 ℃, respectively. It is obvious that the magnetite geothermometry using Mg content provides much higher temperature estimation than the other two thermometers using magnetite-ilmenite pairs. According to the kinetics experiments of Fe-Ti oxides re-equilibration (Hou et al., 2020), Fe-Ti re-equilibrated much faster than Mg-Mn during sub-solidus re-equilibration. Thus, magnetite thermometer using Mg content would keep more information about magmatic stage while magnetite-ilmenite thermometers are sensitive to the late-stage modification and record the temperature of late-stage activities.

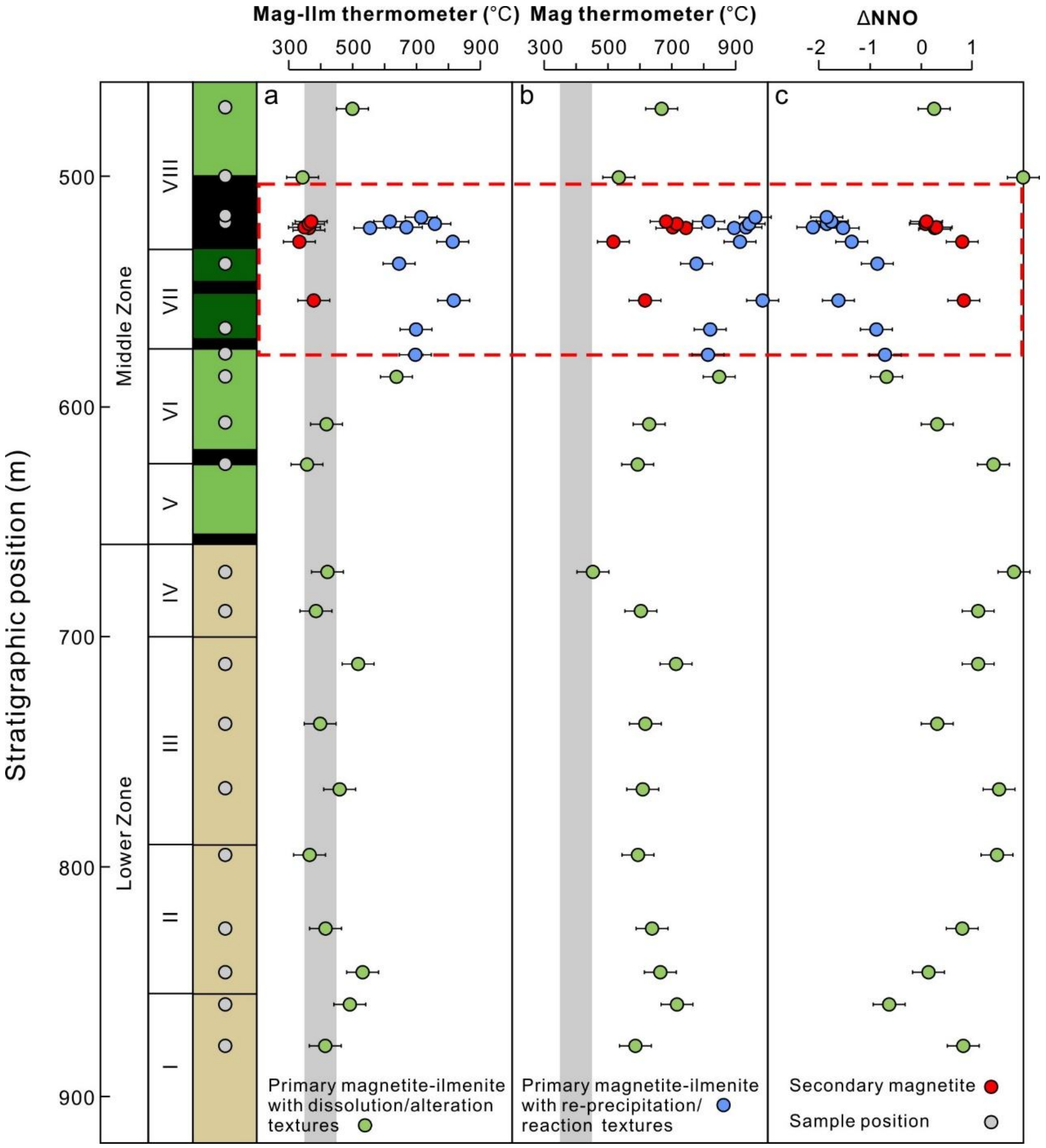

Supplementary Fig. 4.8. Temperatures and oxygen fugacity calculated using chemical equilibria in magnetite and ilmenite. (a) Temperature calculated according to Ghiorso and Evans (2008) model. (b) Equilibrium temperature estimated based on Mg content in magnetite (Canil and Lacourse, 2020). (c) Oxygen fugacity calculated with magnetite and ilmenite according to Ghiorso and Evans (2008) model. The grey areas represent the temperature range estimated from Fe isotope fractionation. Data are from Supplementary Table 4.5.

Distribution of Cr and V in primary and secondary magnetite

As stated in the main text, an enrichment of Fe in secondary magnetite (up to ~92 wt.% FeO) is accompanied by a depletion in Ti, V, Al, Mn, and Cr, highlighting a significant compositional difference with primary magnetite (Supplementary Fig. 4.6a-f). Nonetheless, the Cr and V content in primary and secondary magnetite from Unit VIII are similar (Supplementary Fig. 4.6), contradicting the general trend. Although experimental data for the partitioning of trace elements between magnetite and fluids are lacking, Nadoll et al. (2014) believe that the same factors that control trace elements in magnetite under magmatic conditions (fluid/melt composition, temperature, pressure, oxygen fugacity) should also apply equally to magnetite under lower-temperature hydrothermal conditions.

Previous research has found that the V content in magnetite is strongly related to oxygen fugacity (Toplis and Corgne, 2002; Wijbrans et al., 2015). According to Ghiorso and Evans's (2008) model, oxygen fugacity could also be constrained by magnetite-ilmenite pairs. The silicate layers in the lower units clearly have much higher oxygen fugacity than the massive ore layers (Supplementary Fig. 4.8c). Furthermore, there is a clear decreasing trend for oxygen fugacity with fractional crystallization of Fe-Ti-V oxides from Unit VII to the bottom of Unit VIII. In contrast to the temperature relationship between primary and secondary magnetite, secondary magnetite in Unit VII and Unit VIII has significantly higher oxygen fugacity than primary magnetite. The higher oxygen fugacity in both the silicate layers of the lower units and the secondary magnetite layers of the massive ore layers indicates that the fluids oxidized everything during hydrothermal reworking. Because V is compatible in magnetite (Wijbrans et al., 2015), primary magnetite in Unit VIII is expected to have lower V content than primary magnetite in Unit VII during the fractional crystallization processes. However, because the partition coefficient for V between magnetite and melt increases with decreasing oxygen fugacity (Toplis and Corgne, 2002; Wijbrans et al., 2015), the decreasing trend for V content in primary magnetite in bottom of Unit VIII may be halted due to the decreasing oxygen fugacity from Unit VII to bottom of Unit VIII. This is most likely why the V content of primary magnetite from Unit VII and the bottom of Unit VIII is similar. The partition coefficient for V between magnetite and fluids is also thought to increase as oxygen fugacity decreases (Nadoll et al., 2014). As shown in Supplementary Fig. 4.8c, the fluids oxidized the entire Hongge intrusion during hydrothermal reworking, hence V is less mobile in oxidized fluids. As a result, the secondary magnetite in Unit VII has a low V content. However, as oxygen fugacity decreases, the partition coefficient for V between magnetite and fluids increases, and the V content in secondary magnetite from bottom of Unit VIII may be higher than secondary magnetite from Unit VII.

Concerning chromium (Cr), we propose that because of its high compatibility in magnetite (Dare et al., 2014), crystallization of magnetite in rocks below Unit VIII could quickly lead to a decrease in Cr content in the residual melt, as evidenced by a rapid depletion of bulk rock Cr content (Wang et al., 2020). Thus, prior to the formation of secondary magnetite, the primary magnetite that crystallized in bottom Unit VIII had a very low Cr content (much lower than magnetite in Unit VII). Cr is considered relatively immobile during hydrothermal alteration (Dare et al., 2014), and Cr is present at low concentrations in hydrothermal fluids during the dissolution of primary magnetite. As a result, secondary magnetite precipitated from the fluids always has low Cr content. Finally, while the Cr contents of primary and secondary magnetite were similar at the bottom of Unit VIII, their concentrations were controlled by different mechanisms.

Potential composition of hydrothermal fluids in Hongge intrusion

The potential composition of hydrothermal fluids could be approximately estimated through the nature of fluid-source rocks and hydrous mineral assemblages in the post-magmatic veins. Because the wall rocks at Hongge are primarily made up of dolomitic limestone, metasandstone, and metamudstone, certain amounts of Mg, Ca, and CO_2 may be dissolved into the fluids. Albite, serpentine, amphibole, clinopyroxene, and some clay minerals are hydrous phases in hydrothermal veins, indicating that the fluids are also rich in sodium (Na). The presence of apatite with relatively high Cl concentrations in hydrothermal mineral assemblages suggests the presence of chloride-bearing fluids. Thus, we hypothesize that the major components of hydrothermal fluids could include Cl, Na, Ca, Mg and CO_2.

Mass transport during hydrothermal dissolution

SiO_2 is highly soluble in most hydrothermal fluids and according to the hydration reaction of olivine:

$3(Mg,Fe)_2SiO_2 + 9H_2O \rightarrow (Fe,Mg)_3Si_2O_5(OH)_4 + Fe_3O_4 + 3Mg(OH)_2 + 4H_2 + SiO_{2(aqueous)}$ (2)

abundant Si was dissolved into the fluids while Fe and Mg which were released from olivine and formed magnetite veins and brucite around olivine remnant (Supplementary Fig. 4.4k). In addition, replacement of olivine by chlorite has also been observed. Hence, according to the composition of chlorite (Supplementary Table 4.10), Si and Fe had also been dissolved into the hydrothermal fluids while Mg is inferred to stay in the residues during hydrothermal reworking.

Primary clinopyroxene in the LZ and MZ had reacted with the hydrothermal fluids, forming hydrothermal clinopyroxene, as mentioned in the main text. Secondary clinopyroxene has much higher Mg# (up to 90) than primary clinopyroxene and is enriched in Ca-Mg content but depleted in Fe-Na content (Supplementary Table 4.10). As a result, Mg and Ca were less mobile than Fe during hydrothermal reworking. Mg and Ca immobility during hydrothermal alteration may be related to Ca and Mg enrichment in the hydrothermal fluids. Na is known to be highly mobile in hydrothermal fluids (Rosasco and Roedder, 1979), as evidenced by albite dykes and rocks in the middle of UZ (stratigraphically above the thick massive ore layers) composed of altered gabbros with plagioclase almost completely replaced by albite. As a result, it is reasonable to assume that the hydrothermal fluids mainly remobilized Fe and Na from the initial igneous protolith with little mobilization of Ti, Ca, and Mg.

Brief descriptions for Supplementary Figs. 4.9-4.12

All the *in-situ* Fe isotope values of Puratronic standard (secondary standard), magnetite and ilmenite samples are plotted in Supplementary Fig. 4.9a-c. It is apparent that all the analyses are plotted along the Fe isotope fractionation line, showing a high accuracy during the analyses. In addition, a comparison of Puratronic standard during different analytical days with suggested values from Horn et al. (2006) is shown in Supplementary Fig. 4.9d. All the Puratronic standard values are within the standard deviations, confirming a reliable tuning of the MC-ICP-MS during the analyses.

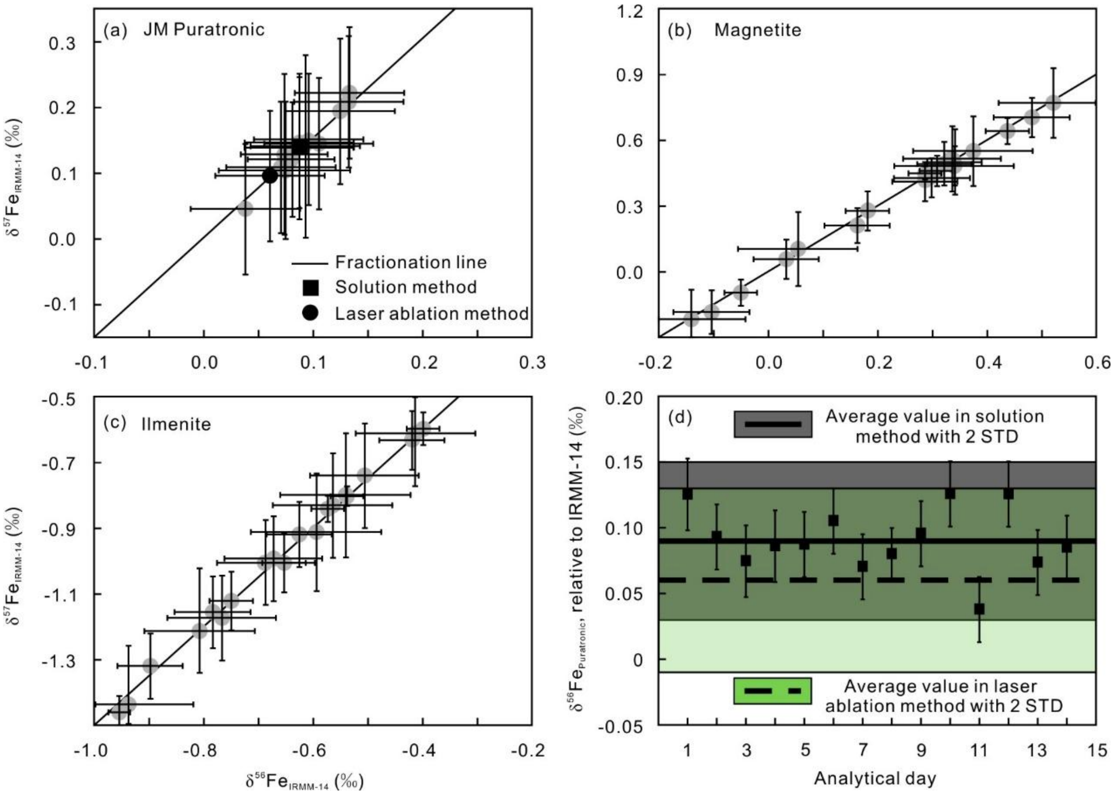

Supplementary Fig. 4.9. δ^{57}Fe vs. δ^{56}Fe of blind standard and Fe-Ti-V oxides. (a) Fe isotopic compositions of Puratronic blind standard. (b-c) *In-situ* magnetite and ilmenite analyses plotted along a mass-dependent fractionation line. Each grey circle represents the average value of thin sections during analyses (Data are from Supplementary Tables 4.6, 4.8). (d) Fe isotope variations of Puratronic standard during different analytical days (reference values are from Horn et al. 2006).

The Fe isotope fractionations among magnetite, ilmenite and Fe-bearing hydrothermal fluids were determined by abundant previous studies. A brief illustration for the Fe isotope fractionation of these three species is shown in Supplementary Fig. 4.10.

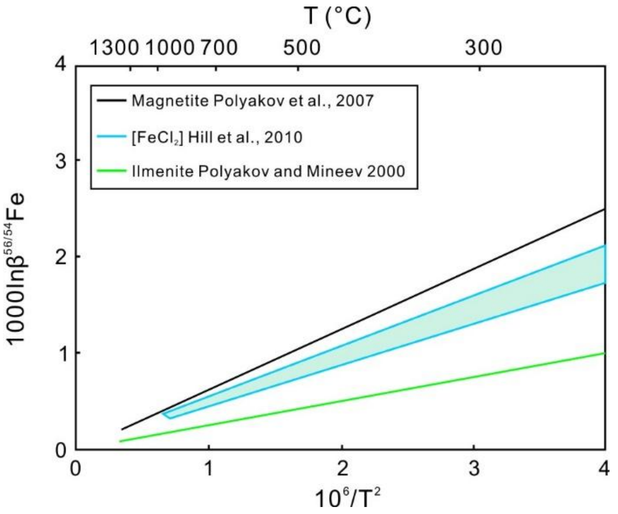

Supplementary Fig. 4.10. Compiled reduced partition function ratios for ^{56}Fe-^{54}Fe exchange from 300 to 1300 °C. The equilibrium fractionation factor α between two phases of interest (A and B) can be calculated according to $\alpha_{A\text{-}B} = \beta_A/\beta_B$ or $1000\ln\alpha_{A\text{-}B} = 1000\ln\beta_A - 1000\ln\beta_B = \Delta_{A\text{-}B}$ [modified from Dziony et al. (2014)].

Iron, titanium and silica solubility are both depended on both pressure, temperature and salinity of hydrothermal fluids. The different solubilities of these elements help to constraint the most optimal P-T-fO_2 conditions during hydrothermal dissolution and re-precipitation processes (Supplementary Fig. 4.11).

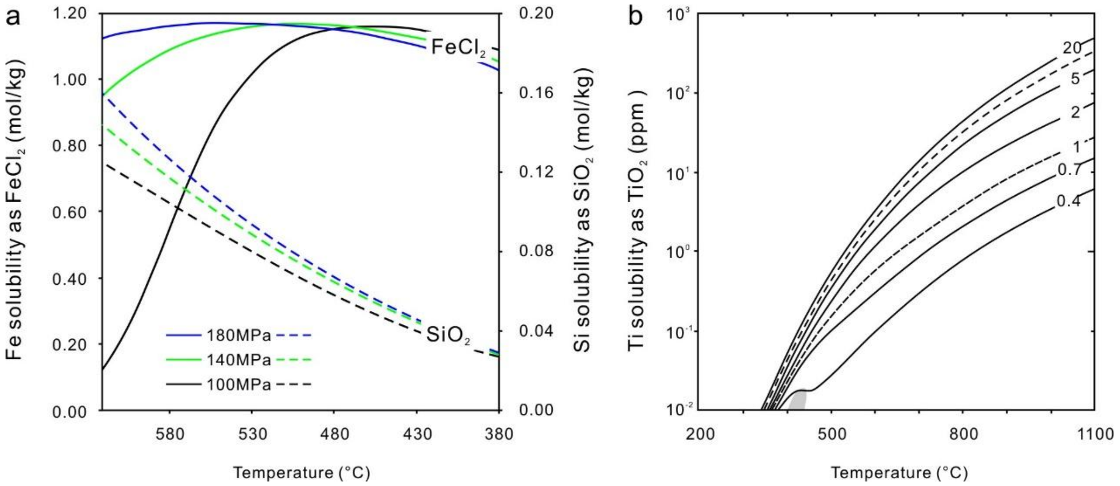

Supplementary Fig. 4.11. (a) Iron (Fe) and silica (Si) solubility in hydrothermal fluids under different temperature-pressure conditions [modified from Akinfiev and Diamond (2009) and Rojas et al. (2018)]. (b) Titanium (Ti) solubility in hydrothermal fluids under different temperature-pressure conditions [modified from Dolejš and Manning (2010)].

A representable ore layer sample from Unit VII (Supplementary Fig. 4.12a) illustrates clear hydration-formed secondary magnetite (Supplementary Fig. 4.12b) and hydrothermal re-precipitated secondary magnetite (Supplementary Fig. 4.12c). It is clearly that the secondary magnetite from hydration of olivine is much thinner than the secondary magnetite from hydrothermal re-precipitation.

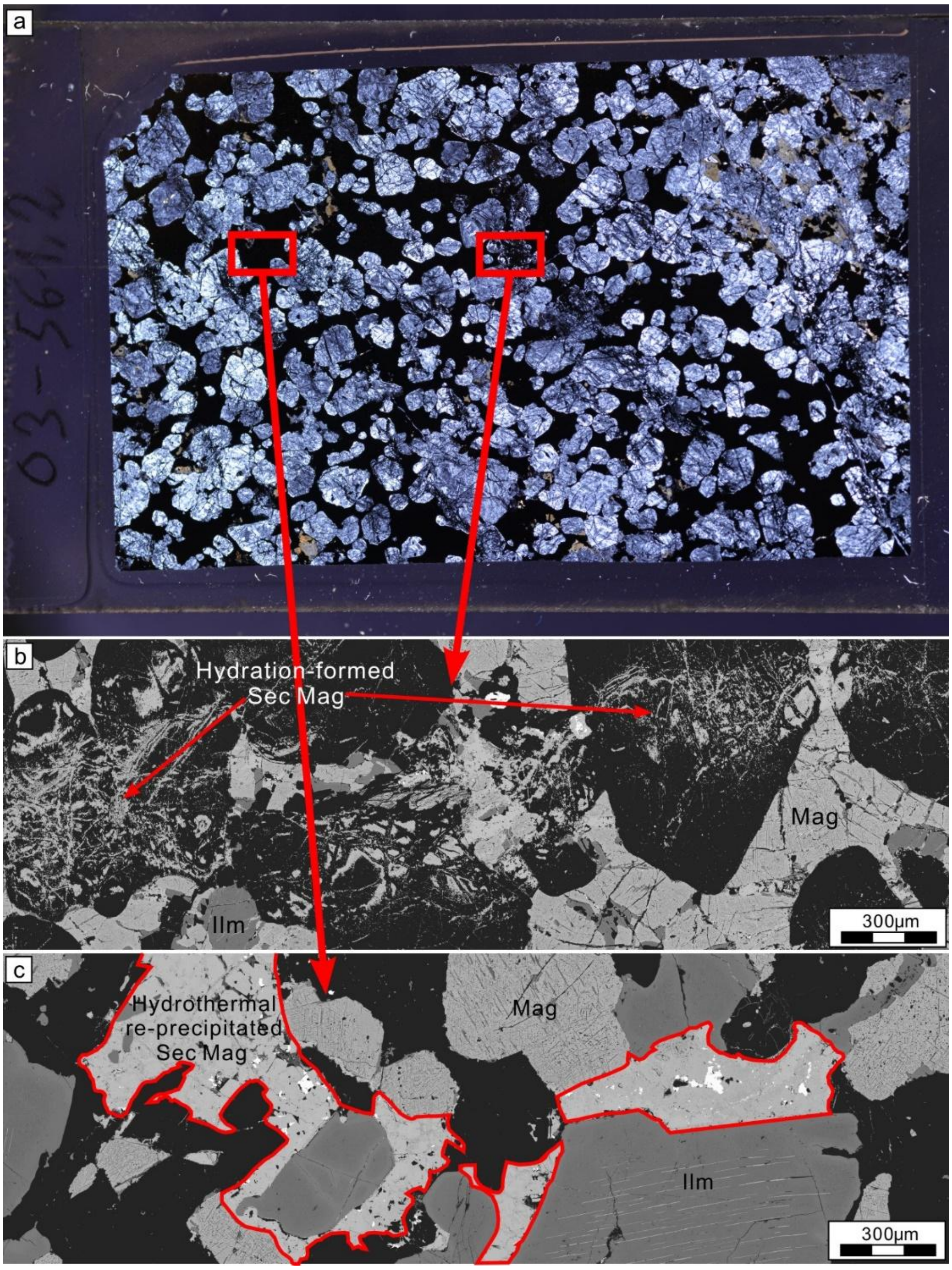

Supplementary Fig. 4.12. An example from the ore layers in Unit VII to illustrate the two types of secondary magnetite. (a) The full image of the sample. (b) Secondary magnetite veins produced by hydration of olivine. (c) Secondary magnetite produced by hydrothermal re-precipitation. Abbreviations: Mag=magnetite; Ilm=ilmenite; Sec Mag=secondary magnetite.

Additional References

Akinfiev, N. N, & Diamond, L. W. (2009). A simple predictive model of quartz solubility in water–salt–CO_2 systems at temperatures up to 1000 ℃ and pressures up to 1000 MPa. *Geochim. Cosmochim. Acta* **73,** 1597-1608.

Hou, T., Botcharnikov, R., Moulas, E., Just, T., Berndt, J., Koepke, J., Zhang, Z., Wang, M., Yang, Z., & Holtz, F. (2020). Kinetics of Fe–Ti oxide re-equilibration in magmatic systems: implications for thermo-oxybarometry. Journal of Petrology, 61(11-12), egaa116.

Nadoll, P., Angerer, T., Mauk, J. L., French, D., & Walshe, J. (2014). The chemistry of hydrothermal magnetite: A review. Ore Geology Reviews, 61, 1-32 (2014).

Rojas, P. A., Barra, F., Deditius, A., Reich, M., Simon, A., Roberts, M., & Rojo, M. (2018). New contributions to the understanding of Kiruna-type iron oxide-apatite deposits revealed by magnetite ore and gangue mineral geochemistry at the El Romeral deposit, Chile. Ore Geology Reviews, 93, 413-435.

Rosasco, G. J., & Roedder, E. (1979). Application of a new Raman microprobe spectrometer to nondestructive analysis of sulfate and other ions in individual phases in fluid inclusions in minerals. Geochimica et Cosmochimica Acta, 43(12), 1907-1915.

Toplis, M. J., & Corgne, A. (2002). An experimental study of element partitioning between magnetite, clinopyroxene and iron-bearing silicate liquids with particular emphasis on vanadium. Contributions to Mineralogy and Petrology, 144(1), 22-37.

Wijbrans, C. H., Klemme, S., Berndt, J., & Vollmer, C. (2015). Experimental determination of trace element partition coefficients between spinel and silicate melt: the influence of chemical composition and oxygen fugacity. *Contrib. to Mineral. Petrol.* **169**(4), 1-33.

Electronic Supplement-List of Supplementary Tables

Electronic supplement is available for this thesis.

Supplementary Table 2.1 Bulk rock compositions for samples in the Hongge layered intrusion

Supplementary Table 2.2 Compositions of cumulus minerals in the Hongge layered intrusion

Supplementary Table 2.3 Modal proportions obtained via scanning electron microscope in the Hongge layered intrusion

Supplementary Table 3.1 Comparison of Emeishan high-Ti basalts with other basaltic systems

Supplementary Table 3.2 Compositions of experimental phases

Supplementary Table 3.3 Compositions of Panzhihua, Hongge and Baima syenite intrusions

Supplementary Table 4.1 Major and trace elements of primary magnetite and ilmenite

Supplementary Table 4.2 Major and trace elements comparsion between primary magnetite and secondary magnetite

Supplementary Table 4.3 Major and trace elements comparison between primary ilmenite core and reaction rim

Supplementary Table 4.4 Composition profiles of representative zoned ilmenite (step length was set at 10 µm)

Supplementary Table 4.5 Mode proportions of selected samples and equilibrium temperatures of primary magnetite-ilmenite pairs and secondary magnetite-ilmenite reaction rims through different thermometers

Supplementary Table 4.6 *In-situ* Fe isotope compositions of primary magnetite and ilmenite

Supplementary Table 4.7 Representative Fe isotope compositions of secondary magnetite

Supplementary Table 4.8 *In-situ* Fe isotope compositions of Puratronic standard

Supplementary Table 4.9 Representative apatite compositions

Supplementary Table 4.10 Representative hydrothermal mineral compositions in the Hongge layered intrusion

Curriculum Vitae

Personal details

Name: Dachuan Wang
Address: Wilhelmshaverner Strasse 16,
30167, Hannover, Germany
E-mail: d.wang@mineralogie.uni-hannover.de

Tel: +49(0)1629781726
Gender: Male
Nationality: Chinese
Date of birth: 31.12.1991
Family status: Single

Education

Since 10/2017-today	Ph.D. student at the Institute of Mineralogy, LUH
09/2014-07/2017	Master of Geological Engineering, major in Economic Geology. China University of Geosciences (Beijing) Thesis: *A Study on the geological features and genesis of Beizhan iron deposit in western Tianshan, China*
09/2010-07/2014	Bachelor of Science, major in Ore deposit exploration China University of Geosciences (Beijing) Thesis: *The petrographic evolution and ore mineralization of Tiemulike iron deposit in western Tianshan, China*

Research interests

- Experimental petrology and geochemistry
- Layered intrusions
- Fe-Ti-V oxide deposits

List of Publications

Journal Articles

Wang, D., Hou, T., Wang, M., Holtz, F. (2020). New constraints on the open magma chamber processes in the formation of giant Hongge Fe-Ti-V oxide deposit. **Lithos**, 374, 105704.

Wang, D., Hou, T., Botcharnikov, R., Weyer, S., Haselbach, S., Zhang, Z., Wang, M., Holtz, F. Hydrothermal reworking as a mechanism forming high-grade Fe-Ti-V ores in layered intrusions. Submitted to **Science Advances**.

Abstracts

Wang D, Hou T, Botcharnikov R and Holtz F. 2020. Mineral chemistry of cumulus plagioclase and clinopyroxene: new constraints on the parental magma composition and differentiation of the Panzhihua Fe-Ti oxide ore-bearing intrusion. DMG online meeting. ***Poster***

Wang D, Hou T and Holtz F. 2021. Fe remobilization and formation of thick massive ore layers in giant Hongge Fe-Ti deposit. GOOD Meeting, Clausthal. ***Oral***